Refinement of high-spatial resolution zircon U-Pb geochronological methodologies

Ph.D. Thesis
2021

Eoghan Corbett



Trinity College Dublin
Coláiste na Tríonóide, Baile Átha Cliath
The University of Dublin

To Nana

I declare that this thesis has not been submitted as an exercise for a degree at this or any other university and it is entirely my own work.

I agree to deposit this thesis in the University's open access institutional repository or allow the library to do so on my behalf, subject to Irish Copyright Legislation and Trinity College Library conditions of use and acknowledgement.

_____

Eoghan Paraic Corbett

Refinement of high-spatial resolution zircon U-Pb geochronological methodologies

Eoghan P. Corbett

SUMMARY

Zircon [ZrSiO4] is a naturally occurring mineral commonly used in geochronological, isotope and elemental geochemical studies. It can form as an accessory phase in a wide variety of magmatic and metamorphic conditions and is remarkably stable both physically and chemically over geological timescales. It will often reliably preserve isotopic and geochemical information even under extreme pressure and temperature conditions. If a zircon remains isotopically undisturbed since its initial '*closure'* (i.e. crystallisation), an absolute age for its formation can be determined by the U-(Th-)Pb (parent/daughter) ratio. However, owing to its incorporation of tandem uranium ($^{238}U \rightarrow {}^{206}Pb$) and actinium-series ($^{235}U \rightarrow {}^{207}Pb$) decay schemes, it is also possible to determine instances when the integrity of its U-Pb systematics were compromised in the past. In addition to its incorporation of radionuclides, zircon also has a tendency to incorporate useful temperature- or process-sensitive trace elements, including the rare earth elements (REE), yttrium (Y) and titanium (Ti). A discrete record of age, temperature and process histories within zircon is often preserved within sharply defined and compositionally distinct intra-crystalline zones/domains which occur at a micron to sub-micron scale and which can only be sampled using *in-situ* high-spatial resolution techniques.

Chapter 2 of this thesis contributes directly to the field of high-spatial resolution techniques, by the application of a novel method of high-resolution *in-situ* zircon U-Pb determination, which dramatically reduces the crater depth by comparison with conventional, high-frequency static laser ablation protocols (by up to 96.5%) and produces ages indistinguishable from those derived by benchmark isotope-dilution thermal ionisation mass-spectrometry (ID-TIMS). The approach to laser ablation analysis described herein, in addition to improving the depth-resolution of analysis, may help to overcome downhole fractionation and plasma loading effects.

The second study of this thesis contained in *chapter 3*, contributes towards an improved understanding of processes occurring during laser sampling of zircon. It presents the likely cause of a zircon matrix-dependent bias present in U-Pb age determination by LA-ICP-MS, which becomes apparent in a comparison of mirrored halves of the same Plešovice zircon crystal in which one half has been subjected to an artificial annealing process at 1100˚C for 96 h. A comparison of equivalent sampling locations reveals a poor approximation of the laser spot mask, sub-parallel crater walls and non-stoichiometric U-Pb sampling within the annealed matrix. We propose that relative changes in the optical and thermo-physical properties of the annealed zircon matrix are responsible for the systematic offset

towards younger apparent ages, away from the accepted age by ~22 Ma (i.e. 6.7%).

The final contribution of this thesis (*Chapter 4*) examines the phenomenon of anomalous apparent age distribution within zircon which has experienced multiple metamorphic episodes. Recrystallisation of radiation damage domains occurs in the wake of an inwardly progressing reaction front catalysed by the percolation of fluids. As a result, the recorded age information, has been decoupled from the expected core-to-rim textural succession of growth usually observed under cathodoluminescence (CL). The viability of two potential fluid-mediated mechanisms for intra-crystalline element mobilisation is considered with respect to numerous textural, chemical, micro-structural, and isotopic observations, which when combined contributes to an understanding of how partial resetting of isotope systematics in zircon may occur. A recognition of the characteristic features associated with such a process, allows for reacted and un-reacted domains to be distinguished thereby allowing meaningful ages (pertaining to discrete intra-crystalline domains) to be determined from zircons, which might otherwise be disregarded in an analysis of such rocks.

ACKNOWLEDGEMENTS

I have been part of the Geology Department at Trinity College Dublin almost a decade, so expectedly this list of people to whom I owe thanks is long, and yet, it remains a non-exhaustive one. There are just too many people to thank.

In my first year as an undergraduate science student, I spent most of my allotted credits on Biology oriented subjects. Little did I realise, that the 20 or so credits I spent choosing Junior Freshman Geology would have lead me here. There is no doubt that I continued studying Geology after my Freshman year (and for many years after that), because of the calibre of the teachers I have been so lucky to have learned by. The first thank you has to be for Chris Nicholas, without whose colourful illustrations, meticulous teaching materials and the tantalising promise of a 'dinosaur lecture', got me hooked in my first year.

Trinity's emphasis on field geology was not lost on me either. It all clicked for me on the Wexford field trip under the guidance of both Patrick Wyse Jackson and Geoff Clayton, when I "got my eye in" and started piecing the past back together. No mention of field trips is complete without thanking the following people; to Chris Nicholas for the countless excursions in Dublin, Arran and Clare; to Ian Sanders for all the trips to Dublin's south side; to Dave Chew helping to 'build character' in a multitude of wet and windy locations and for his supervision of our undergraduate mapping dissertation in Greece; to John Graham for all his experience, himself a testament to grit and character; to Emma Tomlinson for all her wisdom on volcanics in Spain; and to Quentin, for hiring me after the Spain trip…

The same gratitude applied to all the afore mentioned back in the classroom setting as well. I must also thank Balz Kamber, for igniting my interest in all things Archaean and for his fascinating classes. Thanks as well to Patrick Wyse Jackson for all of his encouragement and kindness through the years and especially for affording me opportunities to demonstrate and teach undergraduates and visiting students both in the field and classroom. This is the work I valued most during my Ph.D.

I am especially grateful to have learned by some of the Emeritus Professors; Ian Sanders, whose lectures on acetate were legendary far and wide and who established firmly my fascination in Geology. George Sevastopulo, thank not only for the wisdom imparted in class, but more so for the example you set. To John Graham, for the grounding in sedimentary petrology. Gentlemen all.

The Geology Department would not have been the same without the presence over the years of Frank, Maura, Neil, Noel and Cora. Thank you all for your help and laughs over the years. Thanks especially to Sarah and Frances, for all their 'behind the scenes' work and who have always been there to answer any of my queries. I would also like to thank the staff ant the CMA/iCrag lab, Colin, Leona, Paul and Foteini without whose help and assistance this Ph.D. would not have been possible.

Life in the department would not have been the same without all of my peers through the years. The list of you is far too long, for those of you in the early years and for those of you who I got to know more recently, thanks for all the laughs, lunches, pints and late night boogies down in the depths of The Globe.

Of my friends I have to mention both Gary and Brendan especially, I owe a lot of this to you boys.

For my time in the states, thank you to all my colleagues and peers I got to know over there. I owe a big debt of gratitude to Loretta Corcoran, without whose dedication and training I would not have gotten far. I owe an enormous thank you to Tony Simonetti, who was extremely welcoming, encouraging, attentive and helpful supervisor. I want to thank you for your trust and for the opportunities you afforded me, in my appointment as a candidate, as well as in my scientific endeavours and for those opportunities of fieldwork/teaching in Death Valley. I am very grateful to have worked with you and I am sure we will collaborate further into the future.

This leads me to my single biggest thank you. Thank you Quentin, you have been a fantastic supervisor and mentor over the duration of my time in the Department. From the trust you placed in me from the beginning as a research assistant to now. I would not have made it to this point without your encouragement, example and guidance through all the ups and downs, successes and failures.

I would especially like to thank everyone who helped me and my family through after my accident, both inside and outside of college. I am beyond grateful to be in a position to finish this Ph.D. I would not have made it through without your support.

To Mark, Emer and Gary, the Core4, you really are the best friends anyone could wish for. Having a good laugh at all that we've done together over the years and the prospect of all our future escapades has really pulled me through. To my cousins, aunts and uncles, thank you all. I wouldn't be doing this if it weren't for all the scrabbling around on rocks, poking in rock-pools and horsing around in the wilds of Co. Clare. Thanks especially to Cian, for all the morale boosting, dinners and 'WeWork' spaces offered throughout our most recent antics in West Clare. To my Nana, this one is for you. Thanks for all your inextinguishable support, interest, care and love that you offer all of us every day and in everything we do.

To my family, Mam and Dad, thanks for always being there in support of everything I choose to do. Getting to this point has been largely down to you both, so thanks for all the love, support and encouragement from the very beginning. It has been a longer, tougher road than expected but we got there in the end. To Clí, you are the kindest person I know and best sister in the world. Thanks for always being there. To Dónal, thanks for all you interest over the years. I look forward to sharing in some long awaited adventures. And Sadie, you have no idea how much you mean to all of us or how you pulled me through everything. The light of our world and a joy to see growing up.

TABLE OF CONTENTS

CHAPTER 1 INTRODUCTION 1

1.1. Thesis Context 1
1.1.1. Radioactivity and radionuclides 1
1.1.2. Natural clocks 3
1.1.3. Zircon as a mineral chronometer 4
1.1.4. Technological developments in mass-spectrometry and micro-sampling; towards high-spatial resolution. 7
1.2. Thesis Structure 10
1.3. Content Prelude 10
1.4. References 12

CHAPTER 2 SHALLOW SAMPLING BY MULTI-SHOT LASER ABLATION AND ITS APPLICATION WITHIN U-PB ZIRCON GEOCHRONOLOGY 18

2.1. Abstract 18
2.2. Introduction 19
2.3. Materials and methods 20
2.3.1. Instrumentation 20
2.3.2. Pre-treatment and sample preparation 22
2.3.3. Analytical procedure and timeline 23
2.3.4. Signal integration and data reduction 24
2.3.5. Linear drift and mass bias correction 26
2.3.6. Uncertainty propagation and data rejection 26
2.4. Results 27
2.4.1. External precision 27
2.4.2. Internal precision 28
2.4.3. Age determinations of validation samples 28
2.4.4. NICE script comparison 34
2.4.5. Monitoring time-dependent fractionation 35
2.4.6. Monitoring time-dependent fractionation 35
2.4.7. Sample volume estimates 37
2.4.8. Thermal annealing 40
2.5. Discussion 40
2.5.1. Accuracy and precision 40
2.5.2. Thermal annealing as a pre-treatment 40
2.5.3. Applications in geochronology 41
2.6. Conclusions 41
2.7. Acknowledgments 42
2.8. References 43
2.9. Supporting information and supplementary figures 48
2.9.1. Annotated copy of the NICE Python script (v.2) 48
2.9.2. Supplementary SE-SEM images of crater geometries 57

CHAPTER 3 EFFECTIVE OPTICAL OPACITY AND RADIATION DAMAGE IN ZIRCON; MATRIX DEPENDENT CONTROLS ON U-PB LA-ICP-MS 70

3.1. Abstract 70
3.2. Introduction 71
3.3. Experimental 72
3.3.1. Sample Preparation 72
3.3.2. Instrumentation 72
3.3.3. U-Pb data reduction 76
3.4. Results and discussion 77
3.4.1. Textural and structural comparison 77
3.4.2. Radionuclide composition 80
3.4.3. Age determination 82
3.4.4. Downhole fractionation correction: 87
3.4.5. Radiation damage 88

3.4.6. Crater geometry: 90
3.4.7. Downhole fractionation and crater geometry 93
3.4.8. Matrix dependent ablation behaviour 97
3.5. Conclusion 101
3.6. Acknowledgements 102
3.7. References: 103
3.8. Supporting information and supplementary figures 107
3.8.1. Identification of inclusions present within Plešovice zircon 107
3.8.2. WRS-1348 Age plots 108

CHAPTER 4 ANOMALOUS AGE DISTRIBUTION, ISOCHRON EVOLUTION AND TRACE ELEMENT MOBILISATION IN CRYSTALLINE ZIRCONS AS EVIDENCE FOR FLUID MEDIATED STRUCTURAL RE-EQUILIBRATION. 109
4.1. Abstract 109
4.2. Introduction 110
4.3. Geological setting and samples 113
4.3.1. Regional Geology 113
4.4. Sample details 115
4.5. Analytical Methods 115
4.6. Results and discussion 117
4.6.1. Isotopic disturbance and textural decoupling 117
4.7. Textural observations 120
4.7.1. CL imaging 120
4.7.2. BSE imaging 121
4.7.3. Structural order and lattice orientation 121
4.7.4. The occurrence of non-formula elements 125
4.8. Anomalous age zonation revealed by scanning ion imaging 127
4.8.1. General observations 127
4.9. Age determinations 134
4.10. Element redistribution during fluid-mediated recrystallisation 136
4.10.1. Evidence in support of CDR mechanism. 136
4.10.2. U concentration and secondary ion signal stability 137
4.11. Conceptual mechanism resulting anomalous age distributions 140
4.12. Conclusion 142
4.13. Acknowledgments 143
4.14. References 144
4.15. Supporting information and supplementary figures 153
4.15.1. Additional EBSD misorientation maps 153
4.15.2. Preliminary LA-ICP-MS mapping 154
4.15.3. Additional SII grids including isotopes of ^{204}Pb, ^{207}Pb and ^{208}Pb 155

CHAPTER 5 SYNTHESIS 157
5.1. Future work 159
5.2. References 162

CHAPTER 1

Introduction

1.1. THESIS CONTEXT

Geology is a field of science concerned with generative and transformative processes, which pertain to Earth and its context in the wider solar system. Such processes can be observed in the present at wide spatial scales and are largely assumed to be time invariant. The relative timing of events can be arranged in sequence, without any requisite knowledge of *when* these events occurred. However, the advent of radiometric dating in the early 20th century (Boltwood, 1907) has made it possible to determine the timing of events in absolute units of time (Ma, ka, etc.), throughout Earth's history. Importantly, by establishing *when* any single (and perhaps discrete) event occurred in absolute terms, it can be integrated into a wider planetary (or inter-planetary) context.

The science of radiometric dating is a relatively young branch of geology which has its basis in both the physics of radioactivity ('radio') and mass-spectrometric techniques ('metric'). The following introductory chapter will contextualise the work of this Ph.D. thesis in relation to the key concepts and relevant developments in the field of radiometric isotope geochronology. It begins by providing some overview on; the radioactivity of nuclides, isotope systems, 'natural clocks' and zircon as a mineral chronometer, historical developments in geochronology and concludes with a comment on the relative contribution towards the field of U-Pb geochronology this thesis hopes to provide.

1.1.1. Radioactivity and radionuclides

Radionuclides are atoms with an energetically unstable *parent* nucleus, which, by a process of radioactive decay, become energetically more stable. The nuclear transmutation of radionuclides by a combination of neutron-proton ratio change (as in β-decay) and/or reduction in atomic mass (as in α-decay), eventually results in a stable *daughter* product. At the level of a single nuclide/atom, a decay event cannot be predicted. Fortunately, the rate of decay is a probabilistic function and becomes predictable when a significant number of identical radionuclides are involved. Such a quantity of identical radionuclides is predicted to reduce by half after a single *half-life* ($T_{½}$) duration. The *half-life* ($T_{½}$) for a quantity of any given radionuclide can vary from almost instantaneous to far longer than the age of the universe. Radiometric dating as it pertains to geology, relies therefore upon radionuclides with an appropriate *half-life* duration (see Fig. 1.1).

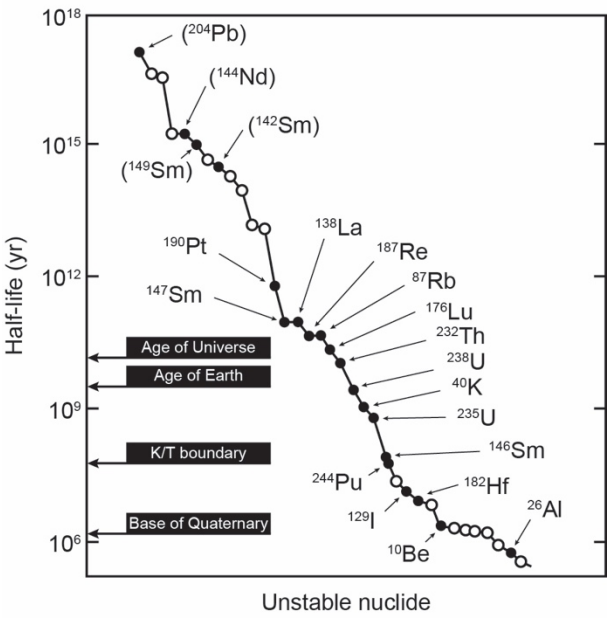


Figure 1.1 Nuclides charted on the basis of decreasing nuclear stability (x-axis) and corresponding half-life duration (y-axis). Geologically useful parent radionuclides are labelled. Some long-lived radionuclides are considered stable over geological time and are marked in brackets (after Dickin, 2018).

Of the primordial nuclides pertinent to radiometric geochronology, *parent-daughter* and *daughter-daughter* isotope couplings of U-Pb and Pb-Pb respectively, are among the most widely used. The uranium-series ($^{238}U \rightarrow {}^{206}Pb$) and actinium-series ($^{235}U \rightarrow {}^{207}Pb$) decay schemes both have *half-lives* which intersect some fraction of Earth history and terminate in specific stable "*radiogenic*" isotopes of Pb (Fig. 1.2). The uranium-series describes the decay chain of ^{238}U to a stable daughter product of ^{206}Pb, which when in secular equilibrium, has a *half-life* of 4.468 Gy. The actinium-series charts the decay of ^{235}U to ^{207}Pb, with ^{235}U having a *half-life* of 704 My.

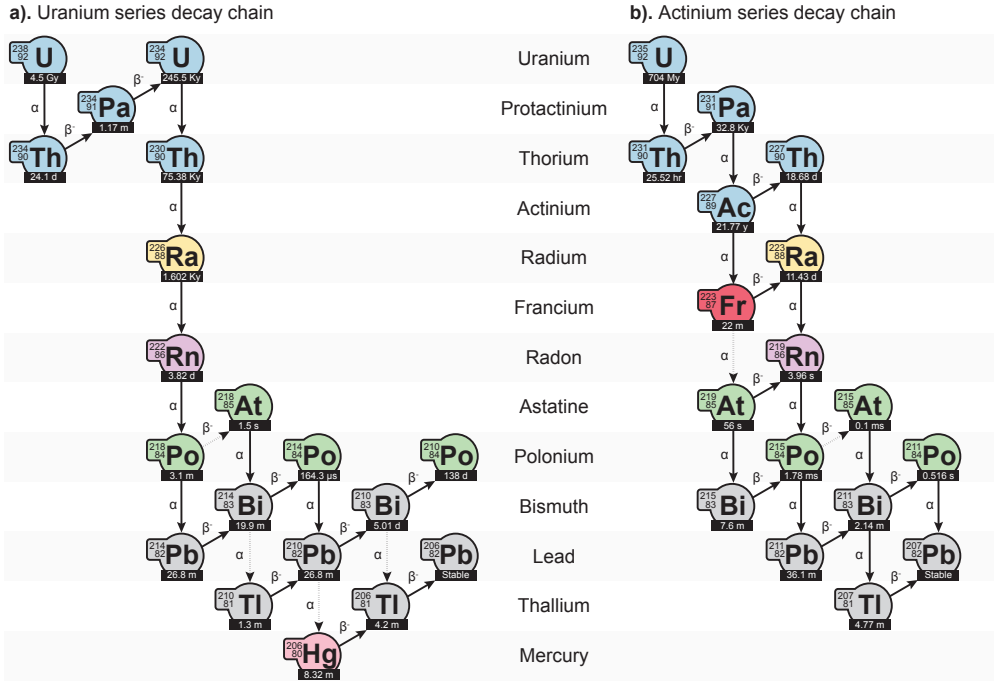


Figure. 1.2 (a) Uranium series decay chain begins with a parent isotope of uranium (^{238}U) and decays through several intermediary daughter products, eventually terminating in a stable daughter isotope of lead (^{206}Pb). The half-life of ^{238}U is 4.468 Gy. **(b)** The actinium series decay chain begins with ^{235}U and decays through several intermediary daughter products,

eventually terminating with stable daughter product, ^{207}Pb. The half-life of ^{235}U is 704 My. Both decay series have the potential to reach secular equilibrium at geological timescales, assuming a closed system is maintained.

Both decay series described are unique, insofar as there is no crossover of intermediate products/isotopes between the decay schemes. Furthermore, the *half-life* of the parent isotope is orders of magnitude longer than that of any of the intermediary daughter isotopes, as a result secular equilibrium can be reached over geological timescales i.e. The ingrowth production of stable isotopes of Pb in each case is proportional to the rate of decay of the parent, where isotopic equilibrium conditions are unperturbed in the hosting material.

1.1.2. Natural clocks

By incorporating sufficient quantities of a parent isotope into a mineral lattice during crystallisation and by hosting the ingrowth of radiogenic products thereafter, a mineral becomes a potential 'natural clock'. Several such radioactive-radiogenic isotope couplings exist in nature (e.g. $^{40}K/^{40}Ar$, $^{87}Rb/^{87}Sr$, $^{147}Sm/^{143}Nd$ and $^{187}Re/^{187}Os$) and can be hosted in several naturally occurring mineral phases. For any isotopic coupling to yield geologically meaningful ages the system must remain in secular equilibrium, exhibiting so-called 'closed' system behaviour through time. Processes including but not limited to; metasomatism, metamictisation, diffusion and/or recrystallisation, may disturb the flux of either end-member or intermediary products within a decay series, resulting in partial or complete resetting of an isotope system. It is often a non-trivial task to detect disequilibrium or 'open' system behaviour where it occurs (e.g. Eakin et al., 2016).

Minerals incorporating significant quantities of U during crystallisation contrastingly, benefit from receiving the tandem/parallel decay schemes of both uranium isotopes (Fig 1.2). The coexistence of parallel U-Pb decay schemes in a single host phase, affords an internal check of system integrity through time (Chew et al. 2017). Isotopic disturbance or lack-thereof can be represented graphically in *concordia space* for accessory mineral phases, which have a high $^{238}U/^{204}Pb$ ratio (e.g. zircon, titanite etc.). Assuming a time invariant rate of decay for both parent isotopes of U, an expression of correlative age can be charted by plotting both $^{206}Pb/^{238}U$ and $^{207}Pb/^{235}U$ ratios. A point at which both $^{238}U/^{206}Pb$ and $^{207}Pb/^{235}U$ ages are equal is said to be *concordant* and a line intersecting the locus of many such points describes a so-called 'concordia' curve (see Fig. 1.3). If a mineral chronometer remains isotopically undisturbed since its initial *closure* (i.e. crystallisation), both its $^{206}Pb/^{238}U$ and $^{207}Pb/^{235}U$ will evolve through time, along the trajectory of the concordia curve.

An isotopic disturbance of the system which results in a loss of intermediate or end-member products (e.g. Pb-loss), manifests as a non-corroboration of $^{206}Pb/^{238}U$ and $^{207}Pb/^{235}U$ ages (i.e. discordancy). Partial Pb loss from zircon, is probably the most widely know example and is typified by an array of points (a '*cord*') tangential to the concordia curve. The array of points lies on a straight line as both isotopes of Pb are chemically identical, thus their loss (or gain) is directly proportional to one another. The *intercepts* of a discordant array with the concordia curve, denotes the timing of

disequilibrium events since T_0. The capacity to monitor for and chart isotopic disturbances of the host phase through time, arguably make the U-Pb isotope coupling the most reliable and flexible of the radiometric clocks.

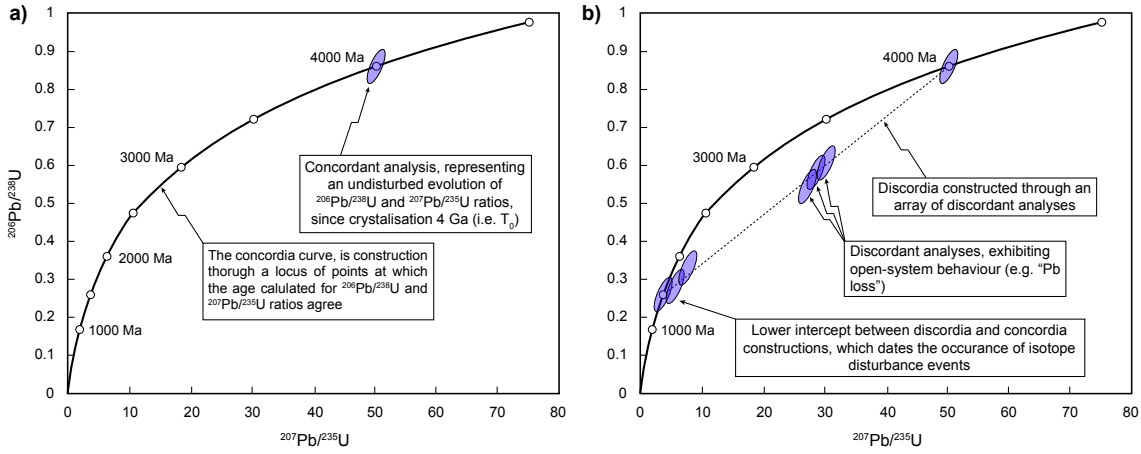


Figure. 1.3 A Wetherill Concordia (Wetherill, 1956) diagram is a graphical device, which displays the isotopic evolution of Pb/U ratios as the ingrowth of radiogenic Pb in a mineral chronometer proceeds from an initial starting point (T_0). The concordia curve itself charts the evolutionary course of sister ratios of $^{206}Pb/^{238}U$ and $^{207}Pb/^{235}U$, having equivalent ages. **(a)** A concordant analysis as shown, will have an isotopic Pb/U ratio which has evolved undisturbed since T_0. The mineral chronometer preserving this undisturbed isotopic signature remains a so-called closed system. **(b)** A departure from the concordia curve illustrates a disequilibrium of the measured Pb/U ratios, and have a multitude of causes. Instances of open-system behaviour such as that shown, are most often attributed to so-called "Pb-loss" events mediated in zircon either by an ancient or recent interaction with aqueous fluids in near-surface or low-grade conditions. An array of such discordant ellipses may allow the construction of a discordia line intercepting somewhere along the concordia curve. The locus of this intercept dates the timing of this mineralogical/geochemical disturbance. Recent "Pb-loss" events intercept concordia at the origin.

1.1.3. Zircon as a mineral chronometer

Commonly used U-Pb hosting accessory mineral phases used in the field of geochronology include, silicates; zircon [$ZrSiO_4$], titanite/sphene [CaTiSiO]. Oxide phases include; baddeleyite [ZrO_2] and rutile [TiO_2] and finally phosphates phases; monazite [$(La,Ce)PO_4$], apatite [$Ca_{10}(PO_4)_6(OH,F,Cl)_2$] and xenotime [$YPO_4$]. Amongst these, zircon is the most widely applied to high-precision U-Pb. The inherent advantages of zircon include its; incorporation of U and Th in trace concentrations (i.e. up to thousands of ppm); primary exclusion of *common* Pb during crystallisation; robust mechanical properties and its chemical stability over a wide temperature range (Peterman et al., 2016; Kusiak et al., 2015; Kogawa et al., 2012; Marsellos and Garver, 2010; Reddy et al., 2007; Watson et al., 1997). Zircon also has a tendency to incorporate useful temperature- or process-sensitive trace elements, including the rare earth elements (REE), yttrium (Y) and titanium (Ti) (Kogawa et al., 2012; Harley and Kelly, 2007). The mechanical and chemical properties of zircon and its ability to incorporate and retain minor and trace elements are largely governed by its crystal structure (Kogawa et al., 2012).

Zircon is a tetragonal orthosilicate mineral, with edge-sharing chains of ZrO_8 along its b-axis (see Fig. 1.4a) and polyhedral chains along its c-axis, consisting of alternating SiO_4 tetrahedra and ZrO_8 octahedra. The octahedral sites, usually consist of two interpenetrating ZrO_4 tetrahedra, both of which are distorted in one dimension being either elongated or shortened as in Fig. 1.4b (Nyman et al. 1984). The geometry formed as a result of these opposing chain structures, generates channels or voids which in chemically pure zircon remain unoccupied (Harley and Kelly, 2007). In natural zircon however, these interstices are more than likely occupied by impurities at parts per million (ppm) to tens of ppm levels (Hanchar et al. 2001; Hoskin et al. 2000).

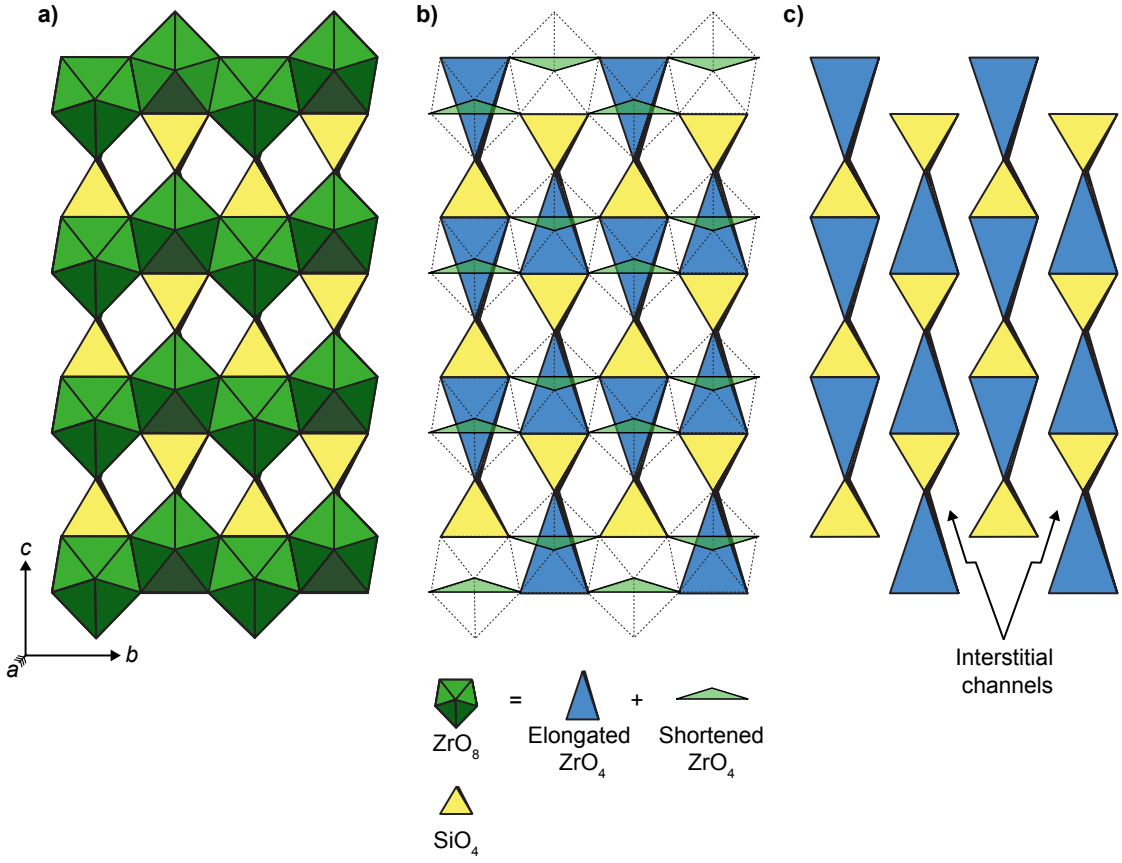


Figure 1.4. Projections of the zircon crystal lattice parallel to the a-axis. Each projection is made in the same orientation, with components being removed in each case for clarity. **(a)** The octahedral site (shown in green) is occupied in pure zircon by ZrO_8 and the tetrahedral site (shown in yellow) is occupied by SiO_4. **(b)** The octahedral site, is usually occupied by two interpenetrating ZrO_4 tetrahedra, one of which shares four edges with the SiO_4 tetrahedra and is elongated in one dimension along the c-axis (blue), the other (green) is shortened in the a-axis dimension and shares two edges with adjacent SiO_4. **(c)** A view, which highlights the interstitial voids parallel to the c-axis, which allow for the accommodation of incompatible divalent cations (e.g. Pb^{2+}). Modified after; Harley and Kelly, 2007.

The open structure of zircon is largely afforded by the c-axis parallel void space between chains of alternating SiO_4 and ZiO_8 polyhedra (see Fig. 1.4c). This void space is not only important for the accommodation of incompatible and radiogenic ingrowth cations, but it also confers the ability to maintain very low absolute thermal expansion and compressibility under extreme temperature and pressure (P-T) conditions. The minimal volume expansion which occurs in the zircon lattice (about 0.6%

from room temperature to its stability limit of 1690°C) is almost fully accommodated along the c-axis by an increase in the Zr−O bond length (Harley and Kelly, 2007). Zircon is also highly incompressible, however preferential shortening of the same c-axis parallel Zr−O bonds during compression, results in anisotropic stability of the structure. Zircon is extremely physically durable therefore over a large range of physical conditions, due to its ability to accommodate strain along its interstitial c-axis channels, provided that they are relatively free of impurities (Harley and Kelly, 2007).

The zircon lattice structure provides stoichiometric sites that can accommodate 5^+ ions (e.g. P, on the 4-fold coordinated Si site), 4^+ ions (Hf, U, Th and Ti replacing the Zr site in 6-fold coordination), and 3^+ ions (REE, also replacing the Zr site) (Crowley et al., 2014; Schaltegger et al., 2014; Finch and Hanchar 2003). The suitability for primary substitution by cations is governed by both their ionic radius and charge. Substitutions which incur minimal strain across either or both Si^{4+} and Zr^{4+} sites will be favoured (Harley and Kelly, 2007). Large quantities of Pb^{2+} (including *common* ^{204}Pb) are not accommodated within the cation sites of zircon during initial crystallisation, as it is divalent under the conditions prevalent during crystallisation (Watson, 1997). The large ionic radius of Pb^{2+} (1.29 Å) is prohibitive for direct substitution into either 4-fold coordinated site (Kogawa et al., 2012; Shannon, 1976). Any initial incorporation of Pb^{2+} into cation sites is thought to require coupled substitution with a charge compensating cation, such as P^{5+} or H^+, hence the low likelihood of its initial inclusion during crystallisation (Kogawa et al., 2012; Hoskin and Schaltegger, 2003; Cherniak and Watson, 2003; Cherniak and Watson, 2000). Incompatible divalent cations (e.g. Pb^{2+}, Fe^{2+}, Mo^{2+}) are likely to be accommodated largely within interstitial voids in the lattice, including radiogenic isotopes of Pb (Schaltegger et al., 2014). This initial exclusion of Pb^{2+} during crystallisation, affords zircon low initial U/Pb ratios enabling direct calculation of $^{206}Pb/^{238}U$ and $^{207}Pb/^{235}U$ ages, without necessarily requiring any initial Pb correction.

Cation diffusivities in zircon are controlled by formation and migration of intrinsic Zr vacancies within its structure, endowing it with some of the slowest known mineral cation diffusivities (Cherniak and Watson, 2003; Cherniak and Watson, 2000). Zircon crystal lattice, therefore preserves a chemical fingerprint either since its formation or since the latest significant resetting of its chemistry (Harley and Kelly, 2007). Spectacular internal textural relationships are a common feature of zircon and are often indicative of their growth histories. Such textural relationships can occur on a micron to sub-micron scale, often delineating sharp contacts between compositionally distinct zones (Cherniak et al., 1997). These include but are not limited to; alternating “oscillatory” zones of phased magmatic growth, “sector” zonation (as viewed down the c-axis) and “fir-tree” zonation attributed to growth-rate related phenomena in magmatic zircon, inherited magmatic or metamorphic cores that are texturally distinct from subsequent magmatic or metamorphic overgrowths (see Corfu et al., 2003 and examples therein). These features can be imaged either by cathodoluminescence (CL) or backscatter electron (BSE) microscopy. The sluggish rate by which volume diffusion of tetravalent cations proceeds in crystalline zircon lattice accounts for the formation and preservation of these sharply contrasting domains even at the most extreme thermal conditions (Cherniak et al., 1997).

Empirically-derived volume diffusion parameters of U, Th and Pb indicate that these elements are essentially immobile within zircon at temperatures below *c*. 900°C (Meis and Gale, 1998; Cherniak et al., 1997). There is ample evidence to suggest however, that such elements, even those bound at primary tetravalent sites within the zircon lattice, are mobile at low temperature conditions (e.g. Timms et al., 2006; Geisler et al., 2003; Geisler et al., 2002). This seemingly contradictory behaviour has been variously observed, however little consensus has been reached on any causative mechanism(s) (as discussed by Kramers et al., 2009). Much of the attention on element mobility has focussed on the phenomenon of low temperature Pb loss. Relatedly therefore, the valency and specific locus of radiogenic Pb accommodation within the lattice structure are all topics of attention and debate (e.g. Villa and Hanchar, 2017; Kogawa et al., 2012; Kramers et al., 2009; Utsunomiya et al., 2004; Cherniak and Watson, 2003; Cherniak and Watson, 2000; Cherniak et al., 1997; Kober 1987). The properties of zircon are critically affected by the development of intracrystalline radiation damage due to self-irradiation (metamictization). Radiation damage is often associated development of fast-diffusion pathways variously observed in natural zircon and can enable enhanced diffusion of U, Th and Pb at low temperatures (Peterman et al., 2016; Kusiak et al., 2015; Reddy et al., 2006) . Furthermore, the accumulation of radiation damage may facilitate mineral-fluid interaction which in turn may enact a redistribution of elements in zircon grains (Seydoux-Guillaume et al., 2015). The inconsistency of element retention in zircon at low temperatures has cause for concern not only in the field of geochronology, but also in long term radioactive waste storage applications (Ewing et al. 1995). The ability to quantitatively assess the complex intracrystalline chemical information (e.g. trace element variation in zoned zircon), has only been made possible by the relatively recent development of high-spatial resolution micro-sampling techniques.

1.1.4. Technological developments in mass-spectrometry and micro-sampling; towards high-spatial resolution.

From its earliest developments into U-Pb zircon geochronology in the 1950s (e.g. Tilton et al., 1955; Vinogradov et al., 1952), thermal ionisation mass spectrometry (TIMS) has remained the paradigm of precision and accuracy and is the 'benchmark' method against which U-Pb ages determined by all other techniques are compared (Horstwood et al., 2016; Košler et al., 2013). Today, routine TIMS analysis following a process of zircon dissolution, isotope dilution (ID) and elemental separation by ion-exchange generate ages to within ≤0.1% precision for a single zircon grain. ID-TIMS is unmatched in this regard, due to the specific method by which ionisation is achieved. It necessarily requires the dissolution and purification of a single grain, for subsequent evaporation steps (i.e. thermal ionisation) carried out on a heated filament. Any internal chemical or structural complexities below the grain scale often present in grains with a complex history, cannot easily be disentangled by ID-TIMS (Cocherie and Robert, 2007).

The first response to this limitation was in the early 1970s, whereupon a secondary ion microprobe mass analyser was used to conduct *in-situ* Pb isotope analysis on lunar material (Anderson and Hinthorne, 1973). Following this work, a secondary ion mass spectrometer (SIMS) instrument was developed in Australia coined the SHRIMP (sensitive high resolution ion microprobe) (Clement et al.,

1977). It was developed specifically to target the age information encoded in complex mineral phases, such as those observed in zircon. By the end of the 1970s secondary ion mass spectrometer (SIMS) instruments specifically designed for U–Pb geochronology were developed and became available commercially (e.g. Hinthorne et al., 1979; Williams, 1979).

The first attempt at micro-sampling by laser ablation (LA) was conducted using an infra-red ruby laser coupled to an inductively coupled plasma mass spectrometer was in the mid-1980s (Gray, 1985). These first attempts showed not only the great potential of the laser ablation inductively coupled plasma mass spectrometry (LA-ICP-MS) technique, with respect to its detection capabilities and spatial resolution, but also its limitations; namely in analytical precision and accuracy. Plasma sources, have an intrinsic instability which causes a slight 'flicker' in the intensity of the resulting ion beam. This limits the precision of isotope ratio measurements, relative to that of TIMS. Initially, many of these advances were achieved using single detector (quadrupole) ICP-MS instruments, which sampled some of this intrinsic plasma noise (Woodhead et al., 2016). Subsequent studies (e.g. Longerich et al. 1996; Fryer et al. 1995; Jackson et al. 1992) showed that entirely new calibration strategies would have to be developed for *in-situ* solid sampling and significant improvements made in laser and ICP-MS in order to achieve the precision and accuracy required for applications such as isotopic dating of geological samples. In order to counteract the effect of plasma noise, peak hopping must take place at a high rate (for single-collector instruments) to compensate for signal drift and/or instability to the largest possible extent.

The subsequent development of multi-collector instrumentation (MC-ICP-MS) marked an important advance in mass spectrometry. MC-ICP-MS instruments allowed the simultaneous detection of multiple atomic masses, thereby countering some of the previous analytical problems associated with plasma noise. The advantages of LA-ICP-MS were recognised during these early years of its development and improvements in instrumentation lead to its widespread use in mid-1990s. Košler (2007) recalls that isotopic dating by SIMS was a well-established technique by the late-1990s with, LA-ICP-MS being regarded as a relatively novel method of elemental and isotopic measurements.

Soon LA-ICP-MS could routinely achieve precision and accuracy comparable with that of SIMS/SHRIMP in terms of isotopic ratio measurements (see Simonetti et al., 2005). The flexibility and short time required for an analysis (low running cost) lead to LA-ICP-MS being adopted worldwide (Chew et al., 2018; Woodhead et al., 2016). It is ideally suited in studies requiring large datasets such as detrital mineral provenance, which by other methods would be time/cost intensive (Pullen et al. 2014; Machado and Gauthier 1996). The flexibility of LA-ICP-MS lends itself towards applications in which; minimal sample destruction, the resolution of sub-grain complexities, and/or the retention of lithological context is required (Corbett et al., 2020). It is now possible to generate quantitative 2-dimensional element, trace element and isotope ratio raster maps by *in-situ* LA-ICP-MS, such methods offer a lateral resolution of features (e.g. polyphase growth domains) at a micron scale (Chew et al., 2017; Ubide et al., 2015).

There have been major advances in the field in terms of instrumentation and software, as well as in our fundamental understanding of laser-sample interactions, particle transport and ion behaviour since the inception of the method in the early-1990s. Despite such advances however, non-stoichiometric sampling of the target analyte due to laser induced elemental fractionation (LIEF) and differential matrix responses remain a concern for the method. Combined, these phenomena account for the stochastic variance (1–2%, 2σ) observed in zircon U-Pb ages determined by in-situ LA-ICP-MS techniques and those determined by the benchmark ID-TIMS method (Horstwood et al., 2016; Košler et al., 2013). Consequently, both LIEF and matrix effects are the focus of much recent research (e.g. Corbett et al., 2020; Marillo-Sialer et al., 2014; Allen and Campbell, 2012; Klötzli et al., 2009; Kuhn et al., 2003).

The application of atom probe tomography (APT) has been invaluable in the study of phenomena occurring at the nano scale, especially with respect to discordancy and mechanisms of trace elemental redistribution in zircon. By preparing a needle-like sample, a timed laser (or voltage) pulse applied to the sample allows for a sequential removal of ions from the needle tip, which are registered by a position-sensitive detector within a time-of-flight (TOF) mass-spectrometer allowing the resolution of zircon elemental and isotopic composition in 3-D with near-atomic-scale resolution (Blum et al., 2017). APT studies of ancient zircons have revealed accumulations/clusters of several trace elements, including Y, Yb, Dy, Lu, and radiogenic Pb, which are heterogeneously distributed at a nano-scale (e.g. Peterman et al., 2016; Piazolo et al., 2016; Reddy et al., 2016; Valley et al., 2015). The morphology and chemistry of these isolated accumulations is varied and unsurprisingly, multiple mechanisms for their formation have been proposed. Trace element redistribution by way of diffusion (during reheating) into amorphous domains created during alpha-recoil events (Valley et al., 2015), partitioning and/or trapping of trace elements within defect structures present within deformed, partially annealed and/or reconstituted zircon (Peterman et al., 2016; Piazolo et al., 2016; Reddy et al., 2016) have all been proposed. The Pb isotope composition of the observed accumulations/clusters in each case were of radiogenic origin irrespective of their mode of formation and are thus not features of initial zircon crystallisation. Thus observations made by APT have offered critical insights into the phenomenon of Pb mobility (and loss) in zircon. In some instances, a measurement of $^{207}Pb/^{206}Pb$ sampled from within the nano-scale accumulations/clusters can be used to constrain the timing of elemental redistribution (e.g. Valley et al., 2015).

There remain opportunities in the field of U-Pb zircon geochronology despite its widespread study and ubiquitous use. The proliferation of commercially available micro-sampling tools, especially the widespread availability of low cost LA-ICP-MS instrumentation in recent decades, has lead to the development of novel sampling protocols and a greater understanding of phenomena at a sub-grain scale. This Ph.D. aims further the development of high-spatial resolution protocols and expand their application. It also hopes to employ high-spatial resolution techniques to investigate outstanding questions and poorly understood phenomena regarding zircon U-Pb analysis.

1.2. THESIS STRUCTURE

This Ph.D. thesis is centred around three core chapters (chapters 2, 3 and 4), each of which were prepared as self-contained studies. The studies presented herein were prepared as independent contributions, being either published or prepared for publication in a peer-review journal. As such, each chapter will contain distinct introductions and conclusions apiece. The publication status of each study at the time of thesis submission, as well as an author list, are provided at the beginning of each chapter. Despite each of the core chapters containing self-referential conclusions, chapter 5 synthesises their principle findings/outcomes and offers an overarching conclusion with respect to the original impetus of the thesis.

1.3. CONTENT PRELUDE

Chapter 2 presents a novel method for zircon U-Pb age determination by LA-ICP-MS. This study builds upon the so-called 'single-shot' method of static-spot ablation pioneered by Cottle et al. (2009). Similar to previous studies (e.g. Cottle et al., 2009; Cottle et al., 2012) the method developed herein, applies several single laser pulses (1 Hz) to the sample-surface in delayed succession. These 'single-shots' generate mass peaks which are expectedly less intense and shorter in duration than those produced by conventional high-frequency LA-ICP-MS analysis. This presents some technical challenges for the precise and accurate determination of isotope ratios. Previous studies such as those mentioned above, focused their attention on resolving the mass peaks generated on a shot-to-shot basis by each laser pulse. This necessarily requires a highly sensitive mass-spectrometer and a sample transport configuration capable of delivering a dense 'packet' of analyte material to the plasma source (i.e. ultra-fast washout cell geometry). By contrast, the method described herein, places and emphasis on generating precise and accurate ages on a very minimal overall volume of ablated analyte. No specialised or modified instrumentation was used in this study. Furthermore, a sector-field single-collector instrument was used for the first time in this application. A large single-volume ablation cell geometry was used in combination with a short washout interval to generate elevated, albeit less distinct mass peaks for each laser pulse. A software application was designed, which is capable of defining, collating and determining U-Pb isotope ratios for a user defined number of laser pulses (applied in sequence to the same sample location). Age determinations made in this manner reproduce to within ~1% (2σ level) on sample volumes as low as 704 ± 23 μm^3 (on 91500 zircon standards). The multi-shot LA-ICP-MS protocol employed here also significantly reduces the effect depth-dependent fractionation as the resultant craters are extremely shallow (as shallow as 0.56 ± 0.02 μm on 91500 zircon standards) and maintain an aspect ratio of <<1.

Chapter 3 presents a likely cause of a zircon matrix-dependent bias present in U-Pb age determination by LA-ICP-MS. This bias was observed in a single Plešovice zircon crystal which was cut and prepared as two mirrored halves, with one half subjected to an artificial annealing process at 1100˚C for 96 h. Artificial annealing applied to radiation-damaged zircon prior to LA-ICP-MS, has often be proposed as a 'pre-treatment' promoting the recovery of structural order and crystal density. Hence, it is believed that biases associated with sample-standard matrix-(mis)matching may be eliminated and also that external precision

may potentially be improved (Allen and Campbell, 2012). Zircon matrices subjected to annealing in a study by Marillo-Sialer (2014) demonstrate a universal reduction of crater depth, however annealing does not enact a homogenising influence over ablation rate between similarly treated calibration standards, as might be expected. In this study, a comparison of counterpart ablated locations between annealed and untreated crystal halves reveals differential ablation behaviour and non-stoichiometric U-Pb sampling, resulting in a systematic apparent younging of the damage free annealed half from the accepted age by ~22 Ma (i.e. 6.7%). We propose that the presence of lattice defects as a result of self-irradiation in the untreated matrix, act as absorption centres for laser light, increasing optical opacity and shortening the absorption depth of incident photons. Furthermore, lattice defects in radiation damaged matrices may impede the dissipation of heat energy away from the site of photon absorption, thus confining thermal interactions to a smaller volume of material. The intrinsic optical and thermo-physical properties of a zircon matrix exert control over ablation behaviour, governing not only the crater geometry but also the particle size and distribution of the emission products of ablation (as observed by means of a U/Th proxy). Radiation damage may therefore promote efficient (i.e. near-surface) laser-matter coupling and consequently generate ablation products which have a more suitable size fraction for stoichiometric ionisation within the ICP.

Chapter 4 presents a detailed textural, micro-structural and isotopic analysis of 4 highly complex zircons isolated from shear zone adjacent granulite facies rocks of the Lewisian Gneiss Complex (LCG) of Northwest Scotland. It evaluates the relationship between anomalous apparent ages and observed textural, chemical and micro-structural features, proposing a fluid-mediated reaction mechanism for the observed isotopic disturbance and trace-element redistribution. It posits that a CDR reaction front catalysed in the presence of inwardly percolating hydrothermal fluids, enacted a structural re-equilibration after radiation damage producing a near-pristine recrystallised zircon matrix which has lost much of its secondarily-sited incompatible elements (including radiogenic Pb). Its inward progression is facilitated along fracture networks and/or an interconnected network of overlapping amorphous domains, wherein an exchange of elements takes place. Relict evidence of these exchange pathways still exists in surface expressions of micrometer sub-circular inclusion trails containing non-formula elements (e.g. Ca, Mg and Fe) and a patchy distribution of radiogenic Pb isotopes as observed under scanning ion imaging (SII). Secondary ion instability evidenced by an offset of measured and predicted uncertainties of $^{206}Pb/^{238}U$ are almost exclusively for user-define selections within the reacted domains may also suggest that the greater compatibility of U for primary inclusion in zircon, is responsible for the observed anomalous ages, by way of its preferential retention and redistribution during the recrystallisation reaction. Despite the pervasive alteration exhibited by these grains, it is still possible to isolate geologically meaningful ages from within domains interpreted to be un-reacted by diffusion reaction, as exemplified by an extraction of ages overlapping with previously determined protolith and tectonothermal events for the Lewisian.

1.4. REFERENCES

Allen, C.M., Campbell, I.H., 2012. Identification and elimination of a matrix-induced systematic error in LA–ICP–MS 206Pb/238U dating of zircon. Chemical Geology, 332–333, 157–165.

Andsersen, C.A, Hinthorne, J.R., 1973. Thermodynamic approach to the quantitative interpretation of sputtered ion mass spectra. Analytical Chemistry, 45, 1421-1438.

Boltwood, B.B., 1907. Ultimate disintegration products of the radioactive elements; Part II, Disintegration products of uranium. American Journal of Science, 23, 78-88.

Cherniak, D.J., Hanchar, J.M., Watson, E.B., 1997. Diffusion of tetravalent cations in zircon. Contributions to Mineralogy and Petrology, 127, 383-390.

Cherniak, D.J., Watson, E.B., 2000. Pb diffusion in zircon. Chemical Geology, 172, 5-24.

Cherniak, D.J., Watson, E.B., 2003. "Diffusion in zircon" in: Hanchar, J.M., Hoskin, P.W.O. (eds) Zircon. Mineralogical Society of America Reviews in Mineralogy & Geochemistry, 53, 113-143.

Chew, D.M., Petrus, J.A., Kenny, G.G., McEvoy, N., 2017. Rapid high-resolution U–Pb LA-Q-ICPMS age mapping of zircon. Journal of Analytical Atomic Spectrometry, 32, 262-276.

Chew, D.M., Drost, K., Petrus, J.A., 2018. Ultrafast, > 50 Hz LA-ICP-MS spot analysis applied to U–Pb dating of zircon and other U-bearing minerals. Geostandards and Geoanalytical Research, 43, 39–60.

Clement, S.W.J, Compston, W., Newstead, G., 1977. "Design of a large, high-resolution ion microprobe" in: Benninghoven, A. (ed.) Proceedings of the internation secondary ion mass spectroscopy conference, Münster, 1977. Springer, Heidelberg, 1-6.

Cocherie, A., Robert, M., 2007. Direct measurement of lead isotope ratios in low concentration environmental samples by MC-ICPMS and multi-ion counting. Chemical Geology, 243, 90–104.
Corbett, E.P., Simonetti, A., Shaw, P., Corcoran, L., Crowley, Q.G., Hoare, B.C., 2020. Shallow sampling by multi-shot laser ablation and its application within U-Pb zircon geochronology. Chemical Geology, 544.

Corbett, E.P., Simonetti, A., Shaw, P., Corcoran, L., Crowley, Q.G. and Hoare, B.C., 2020. Shallow sampling by multi-shot laser ablation and its application within U-Pb zircon geochronology. Chemical Geology, 544, 119568.

Corfu, F., Hanchar, J.M., Hoskin, P.W.O., Kinny, P., 2003 “Atlas of zircon textures” in: Hanchar, J.M., Hoskin, P.W.O. (eds) Zircon. Mineralogical Society of America Reviews in Mineralogy & Geochemistry, 53, 469-500.

Cottle, J.M., Horstwood, M.S.A., Parrish, R.R., 2009. A new approach to single shot laser ablation analysis and its application to in situ Pb/U geochronology. Journal of Analytical Atomic Spectrometry, 24, 1355–1363.

Cottle, J.M., Kylander-Clark, A.R., Vrijmoed, J.C., 2012. U–Th/Pb geochronology of detrital zircon and monazite by single shot laser ablation inductively coupled plasma mass spectrometry (SS-LA-ICPMS). Chemical Geology, 332–333, 136–147.

Crowley, Q.G.C., Heron, K., Riggs, N., Kamber, B.S., Chew, D., McConnell, B., Benn, K., 2014. Chemical abrasion applied to LA-ICP-MS U–Pb zircon geochronology. Minerals, 4, 503-518.

Dickin, A.P., 2018. “Nucleosynthesis and nuclear decay” in: Radiogenic Isotope Geochronology (3 ed.), Cambridge University Press, 2.

Eakin, M., Brownlee, S.J., Baskaran, M., Barbero, L., 2016. Mechanisms of radon loss from zircon: Microstructural controls on emanation and diffusion. Geochimica et Cosmochimica Acta, 184, 212-226.

Ewing, R.C., Lutze, W., Weber, W.J., 1995. Zircon: a host phase for the disposal of weapons plutonium. Journal of Material Research, 10, 243 – 246.

Finch, R.J., Hanchar, J.M., 2003. “Structure and chemistry of zircon and zircon-group minerals” in: Hanchar, J.M., Hoskin, P.W.O. (eds) Zircon. Mineralogical Society of America Reviews in Mineralogy and Geochemistry, 53, 1-25.

Fryer, B.J., Jackson, S.E. & Longerich, H.P., 1995. Design, operation and role of the laser-ablation microprobe coupled with an inductively-coupled plasma mass spectrometer (LAM-ICP-MS) in the Earth-Sciences. Canadian Mineralogist, 33, 303–312.

Geisler, T., Pidgeon R.T., van Bronswijk, W., Kurtz R., 2002. Transport of uranium, thorium, and lead in metamict zircon under low-temperature hydrothermal conditions. Chemical Geology, 191, 141–154.

Geisler T, Schleicher H, Pidgeon RT, Kurtz R, van Bronswijk W., 2003. Experimental hydrothermal alteration of partially metamict zircon. American Mineralogist, 88(10), 1496-1513.

Gray, A.L., 1985. Solid Sample Introduction by LA for ICP-MS. Analyst, 110, 551– 556.

Hanchar, J.M., Finch, R.J., Hoskin, P.W.O., Watson, E.B., Cherniak, D.J., Mariano, A.N., 2001. Rare earth elements in synthetic zircon: Part 1. Synthesis, and rare earth element and phosphorus doping. American Mineralogist, 86, 667-680.

Harley, S.L., Kelly, N.M., 2007. Zircon, Tiny but timely. Elements, 3, 13-18.

Hinthorne, J.R., Anderson, C.A., Conrad, R.L., Lovering, J.F., 1979. Single-grain $^{207}Pb/^{206}Pb$ and U/Pb age determinations with a 10 μm spatial resolution using the ion microprobe mass analyser (IMMA). Chemical Geology, 25, 271–303.

Horstwood, M.S.A, Košler, J., Gehrels, G., Jackson, S.E, McLean, N.M., Paton, C., Pearson, N.J., Sircombe, K.N., Sylvester, P., Vermeesch, P., Bowring, J.F, Condon, D.J., Schoene, B., 2016. Community-derived standards for LA-ICP-MS U–Th-Pb geochronology – uncertainty propagation, age interpretation and data reporting. Geostandards and Geoanalytical Research, 40, 311-332.

Hoskin, P.W.O., Black, L.P., 2000. Metamorphic zircon formation by solid-state recrystallization of protolith igneous zircon. Journal of Metamorphic Petrology, 18, 423-439.

Hoskin, P.W.O., Schaltegger, U., 2003. "The composition of zircon and igneous and metamorphic petrogenesis" in: Hanchar, J.M., Hoskin, P.W.O. (eds) Zircon. Mineralogical Society of America Reviews in Mineralogy & Geochemistry, 53, 27-62.

Jackson, S.E., Longerich, H.P., Dunning, G.R., Fryer, B.J.,1992. The application of laser-ablation microprobe-inductively coupled plasma-mass spectrometry (LAM-ICP-MS) to in situ trace element determination in minerals. Canadian Mineralogist, 30, 1049–1064.

Klötzli, U., Klötzli, E., Günes, Z., Košler, J., 2009. Accuracy of laser ablation U-Pb zircon dating: Results from a test using five different reference zircons. Geostandards and Geoanalytical Research, 33(1), 5–15.

Kober, B., 1987. Single-zircon evaporation combined with Pb+ emitter bedding for 207Pb/206Pb age investigations using thermal ion mass spectrometry, and implications to zirconology. Contributions to Mineralogy and Petrology, 96, 63–71.

Kogawa, M., Watson, B.E., Ewing, R.C., Utsunomiya, S., 2012. Lead in zircon at the atomic scale. American Mineralogist, 97, 1094–1102.

Košler, J., 2007. LA-ICP-MS; a new dating tool in Earth Science. Proceedings of the Geologists' Association, 118, 19–24.

Košler, J., Sláma, J., Belousova, E., Corfu, F., Gehrels, G.E., Gerdes, A., Horstwood, M.S.A., Sircombe K.N., Sylvester, P., Tiepolo, M., Whitehouse, M.J., Woodhead, J.D., 2013. U-Pb detrital zircon analysis - results of an inter-laboratory comparison. Geostandards and Geoanalytical Research, 37, 243-259.

Kramers, J., Frei, R., Newville, M., Kober, B., Villa, I., 2009. On the valency state of radiogenic lead in zircon and its consequences. Chemical Geology, 261, 4–10.

Kuhn, H.R., Guillong, M., Günther, D., 2004. Size-related vaporisation and ionisation of laser-induced glass particles in the inductively coupled plasma. Analytical and Bioanalytical Chemistry, 378(4), 1069–1074.

Kusiak, M.A., Dunkley D.J., Wirth, R., Whitehouse, M.J., Wilde, S.A., Marquardt, K., 2015. Metallic lead nanospheres discovered in ancient zircons. Proceedings of the National Academy of Sciences of the United States of America, 112(16), 4958–4963.

Longerich, H.P., Jackson, S.E., Günther, D., 1996. Inter-laboratory note. Laser ablation inductively coupled plasma mass spectrometric transient signal data acquisition and analyte concentration calculation., Journal of Analytical Atomic Spectrometry, 11(9), 899- 904.

Machado, N., Gauthier, G., 1996. Determination of 207Pb/206Pb ages on zircon and monazite by laser-ablation ICPMS and application to a study of sedimentary provenance and metamorphism in southeastern Brazil. Geochimica et Cosmochimica Acta, 60(24), 5063–5073.

Marillo-Sialer, E., Woodhead, J.D., Hergt, J., Grieg, A., Guillong, M., Gleadow, A., Evans, N., Paton, C., 2014. The zircon “matrix effect”: evidence for an ablation rate control on the accuracy of U–Pb age determinations by LA-ICP-MS., Journal of Analytical Atomic Spectrometry, 29(6), 981.

Marsellos, A.E., Garver, J.I., 2010. Radiation damage and uranium concentration in zircon as assessed by Raman spectroscopy and neutron irradiation. American Mineralogist, 95(8-9), 1192–1201.

Meis, C. and Gale, J.D., 1998. Computational study of tetravalent uranium and plutonium lattice diffusion in zircon. Materials Science and Engineering, 57, 52-61.

Nyman, H., Hyde, B.G., Anderson, S., 1984. Zircon, anhydrite, scheelite and some related structures containing bisdisphenoids. Acta Crystallographica, (B)40, 441-447.

Peterman, E.M., Reddy, S.M., Saxey, D.W., Snoeyenbos, D.R., Rickard, W.D.A., Fougerouse, D., Kylander-Clark, A.R.C., 2016. Nanogeochronology of discordant zircon measured by atom probe microscopy of Pb-enriched dislocation loops. Science Advances, 2(9) e1601318.

Pullen, A., Ibáñez-Mejía, M., Gehrels, G.E., Ibáñez-Mejía, J.C., Pecha, M., 2014. What happens when n= 1000? Creating large-n geochronological datasets with LA-ICP-MS for geologic investigations. Journal of Analytical Atomic Spectrometry, 29(6), 971.

Reddy, S.M., Timms, N.E., Pantleon, W., Trimby, P., 2007. Quantitative characterization of plastic deformation of zircon and geological implications. Contributions to Mineralogy and Petrology, 153, 625-645.

Schaltegger, U., Wotzlaw, J.F., Ovtcharova, M., Chiaradia, M., Spikings, R., 2014. Mass Spectrometry in Earth Sciences: The Precise and Accurate Measurement of Time. Chimia, 68, 124-128(5).

Seydoux-Guillaume, A.M., Bingen, B., Paquette, J.L. and Bosse, V., 2015. Nanoscale evidence for uranium mobility in zircon and the discordance of U–Pb chronometers. Earth and Planetary Science Letters, 409, 43-48.

Shannon, R.D., 1976. Revised effective ionic radii and systematic studies of interatomic distances in halides and chalcogenides. Acta Crystallographica, (A)32, 751-767.

Simonetti, A., Heaman, L.M., Hartlaub, R.P., Creaser, R.A., MacHattie, T.G., Böhm, C., 2005. U–Pb zircon dating by laser ablation-MC-ICP-MS using a new multiple ion counting Faraday collector array. Journal of Analytical Atomic Spectrometry, 20, 677–686.

Tilton, G., Patterson, C., Brown, H., Inghram, M., Hayden, R., Hess, D., Larsen, E.S. Jr., 1955. Isotopic composition and distribution of lead, uranium and thorium in a Precambrian granite. Geological Society of America Bulletin, 66, 1131-1148.

Timms N.E., Kinny, P.D., Reddy, S.M., 2006. Enhanced diffusion of Uranium and Thorium linked to crystal plasticity in zircon. Geochemical Transactions, 7(10).

Ubide, T., McKenna, C.A., Chew, D.M., Kamber, B.S., 2015. High-resolution LA-ICP- MS trace element mapping of igneous minerals: In search of magma histories. Chemical Geology, 409, 157–168.

Utsunomiya, S., Palenik, C.S., Valley, J.W., Cavosie, A.J., Wilde, S.A., Ewing, R.C., 2004. Nanoscale occurrence of Pb in an Archean zircon. Geochimica et Cosmochimica Acta, 68, 4679–4686.

Villa, I.M., Hanchar, J.M., 2017. Age discordance and mineralogy. American Mineralogist, 102, 2422–2439.

Vinogradov, A.P., Zadorozhnyi, I.K., Zykor, S.I., 1952. Isotopic composition of lead and the age of the earth. Doklady Akademii Nauk SSSR, 85, 1107-1110.

Watson, E.B., Cherniak, D.J., Hanchar, J.M., Harrison, T.M., Wark, D.A., 1997. The incorporation of Pb into zircon. Chemical Geology. 141, 19-31.

Wetherill, G.W., 1956. Discordant uranium-lead ages. 1. Transactions, American Geophysical Union, 37, 320–326.

Williams, P., 1979. The sputtering process and sputtered ion emission. Surface Science, 90, 588–634.

Woodhead, J.D., Horstwood, M.S.A., Cottle, J., 2016. Advances in isotope ratio determination by LA-ICP-MS. Elements, 12(5), 317-322.

CHAPTER 2

Shallow sampling by multi-shot laser ablation and its application within U-Pb zircon geochronology

Published in *Chemical Geology*, 2020, *544*, article 119568.

Co-authors: Antonio Simonetti[1], Phil Shaw[2], Loretta Corcoran[1], Quentin Crowley[3] and Brendan C. Hoare[3].

[1.] University of Notre Dame, USA
[2.] Nu Instruments – Ametek, UK
[3.] Trinity College Dublin, Ireland

2.1. ABSTRACT

The interaction of incident laser radiation and sample substrate is complex and difficult to predict. Natural zircons are often both structurally and chemically heterogeneous in 3-dimensional space. Encountering growth-related, structural micro-heterogeneities, inclusions and chemical complexities is almost inevitable during a static ablation of several tens of seconds. A multi-shot approach to laser ablation described here implements a minimal sample exposure time to incident laser radiation by applying multiple 1 Hz shots to a single sample location in delayed succession. This process can be conceptualised as a "slowing down" of a high-frequency (5-20 Hz) static laser ablation inductively coupled plasma mass spectrometry (LA-ICP-MS) analysis until each laser pulse is distinct albeit transient. The ability to integrate and collate signal pulses for a small number of consecutive laser shots, as opposed to continuously pulsing the laser, produces precise age determinations (< 1% reproducibility, 2σ level) on small sample volumes (704 ± 23 μm^3 on 91500 zircon standard). The multi-shot LA-ICP-MS protocol employed here significantly reduces the effect of 'downhole' fractionation as the resultant craters are extremely shallow (as shallow as 0.56 ± 0.02 μm on 91500 zircon standard) and maintain an aspect ratio of << 1. Further benefits include a reduced probability of thermally induced effects (e.g., substrate melting), plasma loading, and the potential for signal mixing (with depth) in a heterogeneous sample.

2.2. INTRODUCTION

Zircon U-Pb ages determined by the benchmark isotope dilution thermal ionization mass spectrometry (ID-TIMS) method, are often at variance (1–2%, 2σ) to those determined by in-situ laser ablation-inductively coupled plasma mass spectrometry (LA-ICP-MS) for the same sample set (Horstwood et al., 2016; Košler et al., 2013). Despite rapid advances in LA-ICP-MS instrumentation, techniques, pre-treatments and a converging consensus on how zircon U-Pb data-reduction protocols are to be employed (e.g., Horstwood et al., 2016), laser induced elemental fractionation (LIEF) arguably still remains the single greatest obstacle in achieving the analytical precision and accuracy associated with other, often more costly in-situ techniques (e.g., secondary ion mass spectrometry, SIMS; Chew et al., 2018).

Non-stoichiometric sampling of the target analyte due to LIEF has often been reported for high-frequency, static ablation protocols used extensively in U-Pb geochronological studies (e.g., Kuhn et al., 2004; Horn et al., 2000; Longerich et al., 1996; Fryer et al., 1995; Hirata and Nesbitt, 1995). Laser operational parameters directly affect the properties of laser-generated aerosols, particle-size distribution, dehydration, atomization and ionization efficiency, and hence directly influence the degree of fractionation occurring within the system (Kuhn et al., 2004; Horn and Günther, 2003; Koch et al., 2002; Guillong and Günther, 2002; Bleiner and Günther, 2001).

Various studies demonstrate a minimisation of LIEF by utilizing a short (157 or 193 nm) laser wavelength (e.g., Kroslakova and Günther, 2007; Jackson et al., 2004; Russo et al., 2000), maintaining focus above the material surface (Marillo-Sialer et al., 2014; Liu et al., 2000), careful adjustment of carrier gas flow and composition (Kroslakova and Günther, 2007; Horn and Günther, 2003; Günther and Heinrich, 1999), and avoiding melting or particle re-deposition over the sample surface by utilizing shorter pulse widths (Shaheen et al., 2012; Fernández et al., 2007; Eggins et al., 1998). The most practicable means by which LIEF can be minimised however, is by ensuring craters are of a critical aspect ratio (depth/diameter) < 1 (Mank and Mason, 2001, 1999).

For zircon, a high affinity of U (and Hf) for Zr results in its retention within the crater during a laser-induced phase transition of SiO_2 to ZrO_2 (Kuhn et al., 2009). Both Si and Pb show no such affinity and freely are mobilised out of ablation craters as condensate independently of their diameter (Kuhn et al., 2009; Košler et al., 2005). U retention during ablation was shown by Kuhn et al. (2009) to be crater-size dependent. Where an aspect ratio can be kept << 1, LIEF of this kind can be reduced well within the associated analytical uncertainty, eliminating the need to propagate any additional uncertainty (Horstwood, 2008).

Authors of similar, previous work to that presented here (e.g., Cottle et al., 2012, 2009) demonstrated the utility and potential of a single-shot approach to laser ablation for minimising sample destruction and improving depth resolution, by integrating discrete peaks generated by consecutive single laser pulses. The analytical procedure presented in this contribution differs from these previous works

insofar as shot-to-shot resolution is not the primary concern. A complete and ultra-fast washout of the analyte (and the associated small-volume ablation cell) is consequently not required. Instead, the relatively large volume of the standard ablation cell (~8 cm^3) is utilised in concert with a short washout duration (3 s) to maintain an elevated signal throughout an analysis, with only a partial washout between laser pulses. Hence fewer shots need be applied to the sample surface, as isotope ratio determination can be made for each 1 Hz laser shot. Herein lies the advantage of a multi-shot approach to laser ablation; the resulting depth achieved after either 30 or 10 shots is much shallower than a conventional laser analysis (e.g., up to 96.5% shallower than some other ablation protocols (Horstwood, 2008), and demonstrably minimises U-Pb 'downhole' fractionation. The approach to laser ablation analysis described here may help to overcome other sources of laser induced elemental fractionation (LIEF) such as, thermally induced effects (e.g., substrate melting), plasma loading effects and crucially, intra-crystalline signal mixing (with depth).

The analytical protocol reported here routinely produces weighted mean age determinations largely reproducible to ≤1% (2σ) on small sample volumes (as low as 704 ± 23 μm^3) with a 40 μm diameter spot, demonstrating an overall improvement in internal precision over that of a single-shot approach alone (Cottle et al., 2009). The multi-shot method outlined here is validated with results obtained on zircon standard reference materials and samples dated using benchmark ID- TIMS.

2.3. MATERIALS AND METHODS

2.3.1. Instrumentation

Ablations were performed using a UP-213 frequency quintupled deep UV (λ = 213 nm) solid-state Nd:YAG laser ablation sampling system (New Wave Research, USA). This was coupled to a Nu Attom High Resolution (HR)-ICP-MS instrument (Nu Instruments, UK), at the Midwest Isotope and Trace Element Research Analytical Center (MITERAC), University of Notre Dame, USA. Analytical set-up and operating parameters are summarised in Table 2.1. The sweep gas flow rates and temperatures within spray chamber and desolvating membrane were monitored and maintained with a Aridus II Desolvating Nebulising system (CETAC Technologies, USA). The sweep gas flow rate proved particularly influential in the resultant reproducibility of U/Pb ratios, given the small volumes of analyte being sampled. Ideal laser and sweep gas set-up and parameters were determined over the course of multiple analytical sessions by monitoring reproducibility on measured U/Pb ratios of NIST612 standard glass.

The Nu Attom HR-ICP-MS instrument was operated in low resolution, peak jump detector mode during a time-resolved analysis (TRA). In this mode, the magnet position is static or 'parked' at a mass of interest (i.e., 206) in the middle of the Pb-isotope range. The detector plate voltages can therefore achieve very fast and reliable scanning or peak jumping over the narrow mass range set by the operator, in this instance between masses 202 and 238. The *fastscan ion optics* facility of the Nu Attom allows for a maximal acquisition time at the top of each mass peak defined by the user in the TRA analysis file

during a sweep. The TRA used herein to derive ages operated at differing sweep and cycle settings depending on the shot count used. Dwell times were fixed at 500 μs on each mass of interest, namely; 202, 204, 206, 207, 208, 235 and 238. Magnet calibration and detector tuning were conducted prior to TRA by aspirating a tune solution containing 0.5 ppb U and Pb in dry plasma mode. A subsequent, secondary check of the tune conditions was carried out in-situ on NIST612 standard glass by laser ablation after He was introduced into the system (1 L min^{-1}). The working values used for NIST612 are from Woodhead and Hergt (2001).

Crater depth determinations and imaging were made using a Pro film3D (Filmetrics, USA) White Light Interferometer (WLI) and a TESCAN TIGER MIRA3 variable pressure field-emission scanning electron microscope (FE-SEM) equipped with a secondary electron detector at the iCRAG lab, Trinity College Dublin, respectively. The WLI technique optically measures surface roughness and texture, allowing a three-dimensional visualization and quantitative measurement of ablation crater depth and geometry to a vertical resolution of 0.176 μm. The cross-sectional depth of each crater was derived from five different linear transect measurements, conducted in differing orientations. The representative depth of an individual crater is given by the mean of these separate measurements (n = 5) and its associated uncertainty is derived from the range in measured values. A total of 20 craters were measured in this manner for every sample analysed to determine the mean resultant depth for a sample set. The uncertainty associated with these values was propagated by quadrature.

Laboratory and Sample Mount Preparation

Laboratory name(s)	Midwest Isotope and Trace Element Research Analytical Center (MITERAC), University of Notre Dame, USA; iCRAG lab, Trinity College Dublin, Ireland.
Sample type/mineral	Polished zircon
Sample preparation	Conventional mineral separation where appropriate, 25mm round resin mount, polished to ¼ μm finish

Laser ablation system

Make, Model and type	ESI/New Wave Research, UP-213 solid state laser, Nd:YAG
Wavelength (λ)	213 nm
Pulse width	3 ns
Fluence	~3 Jcm^{-2}
Repetition rate	1 Hz
Spot size	40 μm
Shot count	10 or 30
Sampling mode/pattern	Sequential single shot, static spot ablation
Washout interval	3 s

Transport regime and sweep gas flow

Laser cell volume	standard 'quick-change drawer' cell (~8 cm^3)
Transport tubing dimension	200 cm x 0.48 cm (ID) of Teflon lined Tygon® tubing
Cell atmosphere and transport gas composition	100% He in cell, Ar auxiliary gas combined via 'Y'-style connection 20 cm before entry into the ICP source
Sweep gas flow	1 $Lmin^{-1}$ (He)
Auxiliary gas flow	3 $Lmin^{-1}$ (Ar) at 110^{o}C, maintained by a CETAC Aridus II desolvating nebuliser, Nebuliser pressure 27.8 psi

ICP-MS Instrument

Make, Model and type	Nu Instruments, Nu Attom HR-ICP-MS, magnetic sector single collector
Detector mode	Static/parked magnet, peak jump detector mode, combined with FastScan Ion optics
Forward RF power	1300 W
Reflected power	≤ 3 W
Sweeps	10
Cycles	2500 (for a 10 shot analysis) or 10000 (for a 30 shot analysis)
Dwell time	500μs on each isotope
Measured masses	202, 204, 206, 207, 208, 235, 238

Data Processing

Gas blank/Baseline duration	Minimum 30 s
Calibration strategy	91500 was used as primary reference standard in brackets of n=5 either side of validation samples (n=10), except when Plešovice was used.
Data processing and plotting package(s)	Python based script add-ons operating within Nu Instruments, Nu Quant software platform; in-house Microsoft Excel© spreadsheet; IsoplotR online (Vermeesch, 2018)
Common-Pb correction	No common-Pb correction applied
LIEF correction	No LIEF correction applied
Uncertainty level and propagation	Ages are quoted at 2σ absolute, uncertainty propagation is by quadratic addition.

Table 2.1 Instrument set-up and operational parameters

2.3.2. Pre-treatment and sample preparation

Thermal pre-treatment by annealing was conducted on a sub-set of samples (summarised in Table 2.2), to investigate the effect of heat-treatment on resultant crater morphologies. Samples were heat-treated at either 850 °C for 48 h, or at 1100 °C for 96 h (Nasdala et al., 2006; Mattinson, 2005). Where a heat-treated sample was being analysed, a primary reference having received the same heat-treatment was used as an external standard.

Regardless of whether a thermal pre-treatment was conducted, it is necessary to ensure all sample surfaces are as clean as possible prior to analysis. Surface contamination (i.e., *common*-Pb) is a concern when sampling such low volumes of material. All samples were subject to several rounds of sonication and rinsing prior to being mounted in a two-part epoxy resin mount. After mounting and polishing, the mount was subject to a further round of cleaning, which involved; (1) several seconds rinsing with ethanol, (2) sonication in a sealed, ethanol filled vessel for 30 min, (3) rinsing with high-purity water, (4) sonication in sealed, high-purity water filled vessels for 30 min, (5) further rinsing with high-purity water, and (6) dried using electronics-safe, pressurised air. Similar care was taken to clean the ablation cell prior to the start of each analytical session.

Sample Name*	**Pre-treatment**	**Reference material information**
91500 (U)	Untreated	91500 (Wiedenbeck et al., 1995)
91500 (850/48)	850°C for 48 h	
91500 (1100/96)	1100°C for 96 h	
Plešovice (U)	Untreated	Plešovice (Sláma et al., 2008)
Plešovice (850/48)	850°C for 48 h	
Plešovice (1100/96)	1100°C for 96 h	
DD85-17 (U)	Untreated	DD85-17 Mafic Tonalite, Marmion batholith
DD85-17 (850/48)	850°C for 48 h	(Tomlinson et al., 2003)
DD85-17 (1100/96)	1100°C for 96 h	
DD81-29 (U)	Untreated	DD81-29 Heronry Lake Diorite Intrusion (Davis and
DD81-29 (850/48)	850°C for 48 h	Edwards, 1986)
DD81-29 (1100/96)	1100°C for 96 h	
WRS-1348 (U)	Untreated	WRS-1348 (Pointon et al., 2012)
Fish Canyon Tuff (U)	Untreated	Fish Canyon Tuff Zircon (Bachmann et al., 2007)

Table 2.2 Sample names, ages and pre-treatment descriptions for each of the studied samples. *Annealed sets of a given sample are labelled with an (850/48) or (1100/96) suffix pursuant to the treatment they received (e.g., DD85-17 (850/48) was heat treated at 850^{o}C for 48 h). Untreated samples are labelled with a (U) suffix.

2.3.3. Analytical procedure and timeline

All analytical sessions were structured with a sample-standard bracket technique consisting of five primary reference standard analyses on either side of 10 validation sample analyses (treated as "un-known"), until a total of 20 "unknown" analyses were conducted (i.e., 5-10-5-10-5). Each sample received a total of either 10 or 30 single-shots in sequence before moving onto the next location/sample. Where possible, laser spots were placed in order to avoid any cracks or inclusions visible on the sample surface. During a TRA, a baseline determination was made for up to 30 s prior to opening the laser shutter. During this time interval, the laser is continually fired at a repetition rate of 4 Hz against the laser shutter, to thermally stabilise or 'warm up' the laser head. The laser shutter opens for 1 s to allow a single (1 Hz) shot to strike the focussed sample surface, a 3 s washout interval then follows allowing a partial return to

baseline of the signal before the next laser shot. This partial return towards baseline is crucial as it maintains an elevated signal intensity whilst also allowing the *NICE script* Nu-Quant software add-on to decipher signal peaks. This cycle of firing and washout continues until either 10 or 30 consecutive laser shots have been fired in the same location. The duration of a multi-shot analysis conducted in this manner is ~3 to 8 min depending on the total shot count applied. A standard bracketed analytical session consisting of several such multi-shot analyses (n = 35) therefore, can take up to between 2 and 5 h. It should be noted that no pre-ablation shot or raster procedure was undertaken in this study to 'clean' the sample of potential surface common Pb contamination, as the ^{204}Pb ion signal remained below the limit of quantification (LOQ) throughout each analysis. As a precautionary measure the first 10% of shots are ignored within the Nu Quant software to avoid any potential for ^{204}Pb surficial contamination, but can still be integrated as part of the TRA at the user's discretion.

2.3.4. Signal integration and data reduction

Nu Quant is Nu Instruments software developed for processing data obtained using the Attom HR-ICP-MS. It allows the user to construct batch files containing several separate TRA files. Single and multi-shot analyses require each TRA to be processed using a *NICE script* add-on, which operates within the Nu Quant software platform. The Nu Quant software platform offers the freedom for users to construct and import their own Python-based *NICE scripts* for data reduction purposes. Two *NICE script* variants were developed for the purposes of multi-shot data reduction; version 2 (*v.2*), which utilises user defined ^{238}U signal threshold values to determine the start and end of each laser shot; and version 5 (*v.5*), whereby the software delineates signal pulses between the start of the signal for the first shot and the end of the signal for the final shot. Both require the user to input multiple parameters before the signals can be compiled. These iterations of the script contained the most robust algorithms tested within this study and are freely available as supplementary material to the online version of this publication.

2.3.4.1 *Version 2 (v.2)*

The start and end points of the 30s baseline/'gas-blank' measurement (acquired prior to firing the laser) are defined by the user in terms of "baseline start cycle" and "baseline end cycle", respectively. This selection of baseline continuum signal is used to subsequently perform a baseline subtraction calculation of the net acquired signal intensities. Ideally therefore, users should select as much of a representative baseline signal as possible. The user must also determine the "start peak trigger", a threshold value for the ^{238}U ion signal, which will define the start and end points of signal peaks. To avoid falsely triggering and integrating signal peaks too narrow to be real (i.e., signal noise), the user defines the minimum *channel width*, which constitutes a real peak. When necessary, the user can request that the software ignore the first number of shots/peaks during ratio computation so as to avoid integrating signals potentially affected by surface *common*-Pb contamination. Cycles satisfying the conditions defined by the user (i.e., above the minimum triggering threshold, based on ^{238}U ion signal intensity; and of sufficient channel width) are integrated as part of a multi-shot analysis. Ratios are calculated for a single peak by summing the total number of counts for each isotope across the entire *peak width*, and applying a

subtraction of the baseline average counts (for the same isotope) to this value. A summary of the data handling process for *v.2* is given in Fig. 2.1.

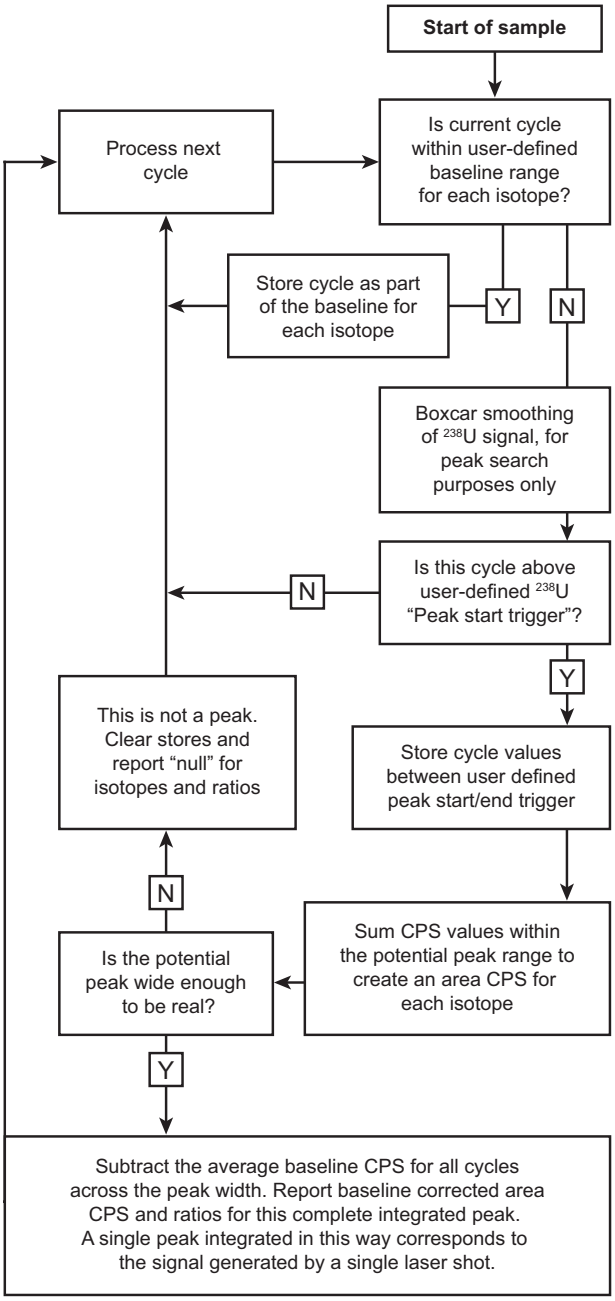


Figure 2.1 The operational work flow undertaken to crop and integrate 'peak tops' within the *NICE script v.2*.

2.3.4.2 *Version 5 (v.5)*

Version 5 of the *NICE script* add-on was used in this study when the cumulative counts on the least abundant isotope measured in a ratio pair (usually ^{207}Pb) integrated over the course of an analysis were low (i.e., for analyses of 10 shots and Fish Canyon Tuff (U); see *section 2.4.4*). Version 5 does not operate using a trigger value based on ^{238}U ion signal intensity to initiate a *peak search*. Instead the user defines the first and last cycles within a TRA that pertain to an on-peak measurement. Back-to-back peak brackets of a user defined width then divide the space between the first and last peak for an entire TRA. A representative TRA for both *NICE script* versions are illustrated in Fig. 2.2.

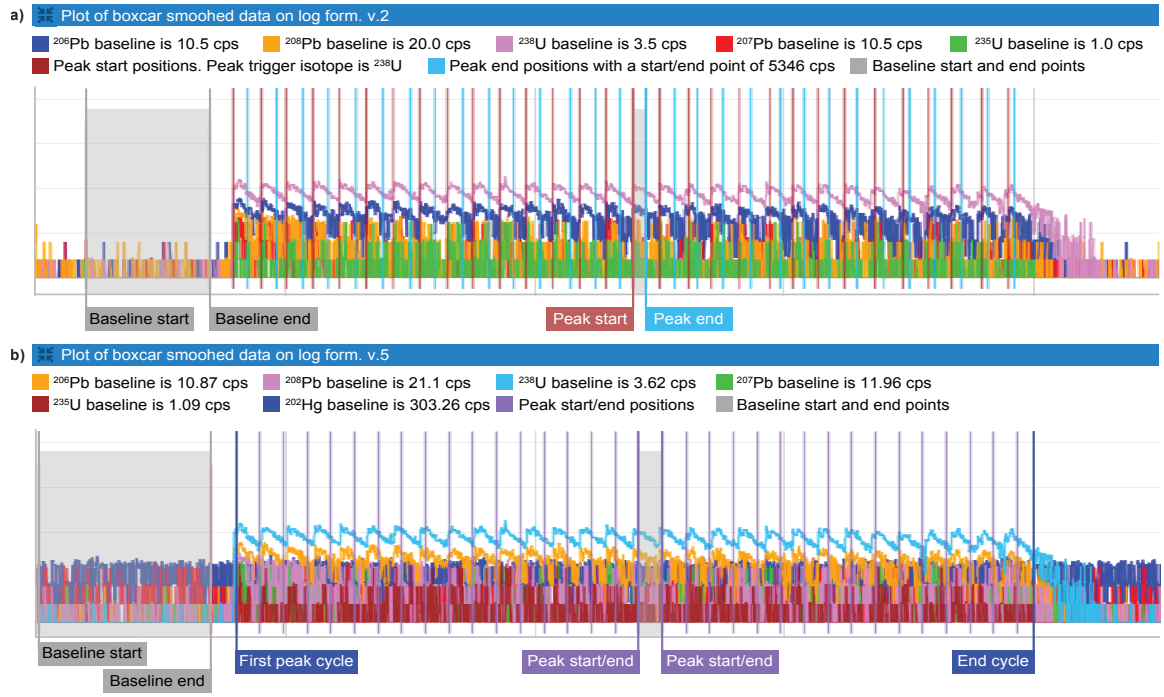


Figure 2.2 Representative TRAs as displayed (with annotation) within the Nu-Quant software of both *NICE script* add-ons for the same 91500 zircon analysis. (a) Version 2 (v.2) was used for data reduction of 30 shot analyses in this contribution, with the exception of Fish Canyon Tuff (U). This version operates by integrating peaks above a threshold 'peak trigger' based on ^{238}U ion signal intensity for a fixed channel width as defined by the user. This effectively operates to crop peak-tops only, ignoring cycles not satisfying user defined thresholds. (b) Version 5 (v.5) was used to integrate analyses of 10 shots and Fish Canyon Tuff (U), where there are fewer cumulative counts to integrate for each isotope. No ion signal intensity dependent peak search function operates in v.5, instead the user defines the first cycle pertaining to the onset of signal pulses and the last. The software then divides the intervening cycles into equal channel widths for integration. The alignment of these fixed width integrations is made difficult with within-run variation in washout efficiency.

2.3.5. Linear drift and mass bias correction

Data processing including correction of instrumental drift and mass bias, as well as uncertainty propagation were carried out using an 'in-house' Microsoft Excel© spreadsheet developed after Simonetti et al. (2005). Mean normalisation factors were calculated for each of the three standard brackets, sensu Fisher et al. (2010). These normalisation factors were multiplied into each integrated ratio for the sample data by fractional degrees, weighted according to their '*within-run*' position relative to the standard brackets to correct for instrumental drift and mass bias during the course of an analytical session.

2.3.6. Uncertainty propagation and data rejection

All potential sources of uncertainty were propagated into individual ratio determinations, including those related to the external reproducibility of the primary reference material. No common Pb or LIEF

corrections were applied to data reported here. In all cases $^{207}Pb/^{235}U$ ratios were calculated using the $^{238}U/^{235}U$ constant of 137.88 (Steiger and Jäger, 1977) and all ages were calculated using the decay constants of Jaffey et al. (1971). Prior to plotting, any acquired data that produced Rho error correlations > 1 were rejected. For those samples overlapping the Concordia curve, an additional rejection was applied based upon percent discordance, whereby data exceeding user defined thresholds are excluded (usually data ≥20% discordance are rejected). For those data plotting as discordant arrays, the rejection of data was conducted on a visual basis by the user. All Concordia plots were constructed using IsoplotR (Vermeesch, 2018) and uncertainties therein are reported at the 2σ level.

2.4. RESULTS

2.4.1. External precision

Both 91500 (1065.4 ± 0.6 Ma; Wiedenbeck et al., 1995) and Plešovice (337.13 ± 0.37 Ma; Sláma et al., 2008) were used as primary reference zircon standards during the course of this study. The reproducibility (2 SD%) of both external reference standards regardless of the pre-treatment they received is < 7.5% and < 5.5% for $^{207}Pb/^{206}Pb$ and $^{206}Pb/^{238}U$, respectively for 30 shot ablations. For analyses employing 10 shots, the reproducibility (2 SD%) of both external reference standards is < 22.5% and < 5% $^{207}Pb/^{206}Pb$ and $^{206}Pb/^{238}U$, respectively. These ratio value determinations were made over the course of several analytical sessions, which were conducted over the course of several days, as summarised in Table 2.3.

External Reference Standard	n	$^{207}Pb/^{206}Pb$ (2SD%)	$^{206}Pb/^{238}U$ (2SD%)
30 shot analyses			
91500 (U)	n=80	6.0	4.8
91500 (850/48)	n=79	6.1	4.9
91500 (1100/96)	n=49	7.4	4.0
Plešovice (U)	n=35	6.1	3.9
Plešovice (850/48)	n=35	7.2	5.4
Plešovice (1100/96)	n=15	5.7	1.9
10 shot analyses			
91500 (U)	n=55	22.2	4.9
Plešovice (U)	n=46	16.1	4.2

Table 2.3. External reproducibility (2SD%) of baseline subtracted raw ratios achieved for all primary reference standards used within this study.

2.4.2. Internal precision

The internal precision of all measured samples within a given analytical session is summarised in Table 2.4. The 'within-run' reproducibility (2 SD%) of all samples receiving 30 shots, regardless of the pre-treatment they received is < 2.4% and < 1.6% for $^{207}Pb/^{206}Pb$ and $^{206}Pb/^{238}U$ respectively, with the exception of Fish Canyon Tuff zircon (U). The relatively low abundance of radiogenic Pb in Fish Canyon Tuff zircon (28.37 ± 0.05 Ma; Bachmann et al., 2007) reduces the precision achievable for a 30 shot analysis (see Table 2.4), regardless of the *NICE script* used to generate integrations. For analyses of 10 shots, the reproducibility (2 SD%) of untreated samples measured is < 3.9% and < 1.4% for $^{207}Pb/^{206}Pb$ and $^{206}Pb/^{238}U$, respectively. These ratio determinations were made during the same analytical sessions for each sample set. Thermal annealing pre-treatment does not improve internal precision.

Sample	$^{207}Pb/^{206}Pb$ (2SD%)	$^{206}Pb/^{238}U$ (2SD%)
91500 (U)	0.64	0.39
91500 (850/48)	0.73	0.35
91500 (1100/96)	0.63	0.49
Plešovice (U)	0.59	0.42
Plešovice (850/48)	0.81	0.51
Plešovice (1100/96)	0.66	0.26
DD81-29 (U)	0.92	1.56
DD81-29 (850/48)	0.34	0.64
DD81-29 (1100/96)	0.31	0.84
DD85-17 (U)	0.68	0.98
DD85-17 (850/48)	0.86	1.15
DD85-17 (1100/96)	0.32	0.93
WRS-1348 (U)	2.35	0.86
Fish Canyon Tuff (U)*	29.41	4.83
91500 (U)*	3.82	0.53
Plešovice (U)*	2.31	0.27
WRS-1348 (U)*	3.00	1.36

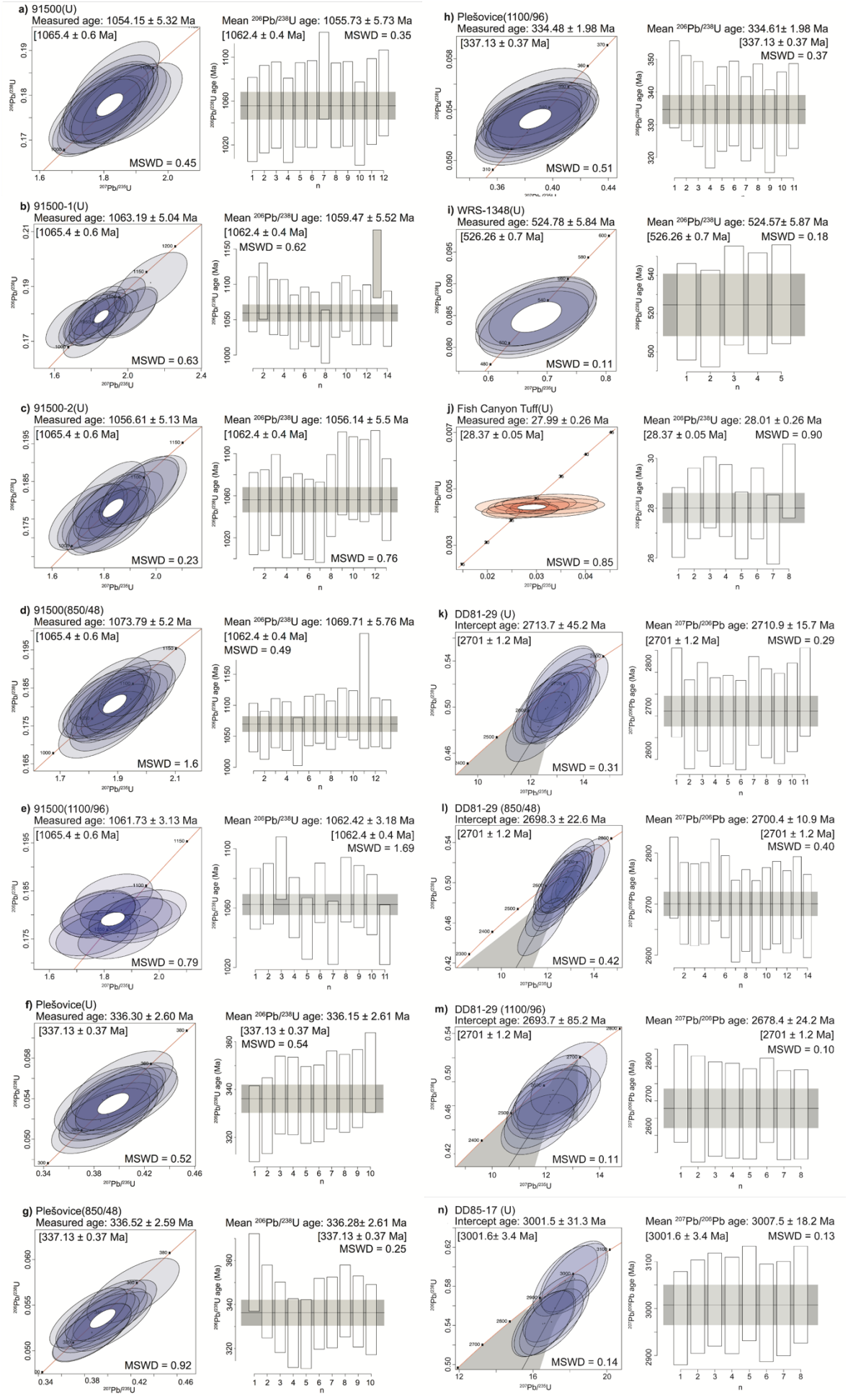
Table 2.4. Internal reproducibility (2 SD%) uncorrected ratios achieved (n = 20) for all samples analysed. Those analyses reduced using NICE script v.5 are highlighted with an asterisk (*).

2.4.3. Age determinations of validation samples

The samples utilized to demonstrate the validity of the multi-shot technique outlined herein all have independently verified ID-TIMS ages. All samples regardless of the pre-treatment they received, have calculated ages consistently reproducible to within ≤1% of their published age, with the exception of Fish Canyon Tuff (1.34%). All are within an acceptable range of MSWD values (Spencer et al., 2016). All age plots are included in Fig. 2.3.

The weighted mean age data (Table 2.5) regardless of heat treatment applied reproduce to within < 1.57% of their published U-Pb ID-TIMS ages for analyses of 30 shots. Moreover, most samples typically reproduce to within << 1% of their published ages. Analyses conducted using 10 shots and reduced using *NICE script version 5* (*v.5*) yield weighted mean ages that are reproducible to within < 0.82% of their accepted ages on samples of untreated 91500, Plešovice, and WRS-1348 zircons. All U-Pb results for samples analysed here are displayed both in Concordia diagrams and in weighted mean

plots (Fig. 2.3) demonstrating both the accuracy and precision achieved by the multi-shot LA-ICP-MS approach adopted here.


a) 91500(U)
Measured age: 1054.15 ± 5.32 Ma
[1065.4 ± 0.6 Ma]
MSWD = 0.45
Mean 206Pb/238U age: 1055.73 ± 5.73 Ma
[1062.4 ± 0.4 Ma]
MSWD = 0.35
b) 91500-1(U)
Measured age: 1063.19 ± 5.04 Ma
[1065.4 ± 0.6 Ma]
MSWD = 0.63
Mean 206Pb/238U age: 1059.47 ± 5.52 Ma
[1062.4 ± 0.4 Ma]
MSWD = 0.62
c) 91500-2(U)
Measured age: 1056.61 ± 5.13 Ma
[1065.4 ± 0.6 Ma]
MSWD = 0.23
Mean 206Pb/238U age: 1056.14 ± 5.5 Ma
[1062.4 ± 0.4 Ma]
MSWD = 0.76
d) 91500(850/48)
Measured age: 1073.79 ± 5.2 Ma
[1065.4 ± 0.6 Ma]
MSWD = 1.6
Mean 206Pb/238U age: 1069.71 ± 5.76 Ma
[1062.4 ± 0.4 Ma]
MSWD = 0.49
e) 91500(1100/96)
Measured age: 1061.73 ± 3.13 Ma
[1065.4 ± 0.6 Ma]
MSWD = 0.79
Mean 206Pb/238U age: 1062.42 ± 3.18 Ma
[1062.4 ± 0.4 Ma]
MSWD = 1.69
f) Plešovice(U)
Measured age: 336.30 ± 2.60 Ma
[337.13 ± 0.37 Ma]
MSWD = 0.52
Mean 206Pb/238U age: 336.15 ± 2.61 Ma
[337.13 ± 0.37 Ma]
MSWD = 0.54
g) Plešovice(850/48)
Measured age: 336.52 ± 2.59 Ma
[337.13 ± 0.37 Ma]
MSWD = 0.92
Mean 206Pb/238U age: 336.28± 2.61 Ma
[337.13 ± 0.37 Ma]
MSWD = 0.25
h) Plešovice(1100/96)
Measured age: 334.48 ± 1.98 Ma
[337.13 ± 0.37 Ma]
MSWD = 0.51
Mean 206Pb/238U age: 334.61± 1.98 Ma
[337.13 ± 0.37 Ma]
MSWD = 0.37
i) WRS-1348(U)
Measured age: 524.78 ± 5.84 Ma
[526.26 ± 0.7 Ma]
MSWD = 0.11
Mean 206Pb/238U age: 524.57± 5.87 Ma
[526.26 ± 0.7 Ma]
MSWD = 0.18
j) Fish Canyon Tuff(U)
Measured age: 27.99 ± 0.26 Ma
[28.37 ± 0.05 Ma]
MSWD = 0.85
Mean 206Pb/238U age: 28.01 ± 0.26 Ma
[28.37 ± 0.05 Ma]
MSWD = 0.90
k) DD81-29 (U)
Intercept age: 2713.7 ± 45.2 Ma
[2701 ± 1.2 Ma]
MSWD = 0.31
Mean 207Pb/206Pb age: 2710.9 ± 15.7 Ma
[2701 ± 1.2 Ma]
MSWD = 0.29
l) DD81-29 (850/48)
Intercept age: 2698.3 ± 22.6 Ma
[2701 ± 1.2 Ma]
MSWD = 0.42
Mean 207Pb/206Pb age: 2700.4 ± 10.9 Ma
[2701 ± 1.2 Ma]
MSWD = 0.40
m) DD81-29 (1100/96)
Intercept age: 2693.7 ± 85.2 Ma
[2701 ± 1.2 Ma]
MSWD = 0.11
Mean 207Pb/206Pb age: 2678.4 ± 24.2 Ma
[2701 ± 1.2 Ma]
MSWD = 0.10
n) DD85-17 (U)
Intercept age: 3001.5 ± 31.3 Ma
[3001.6± 3.4 Ma]
MSWD = 0.14
Mean 207Pb/206Pb age: 3007.5 ± 18.2 Ma
[3001.6 ± 3.4 Ma]
MSWD = 0.13

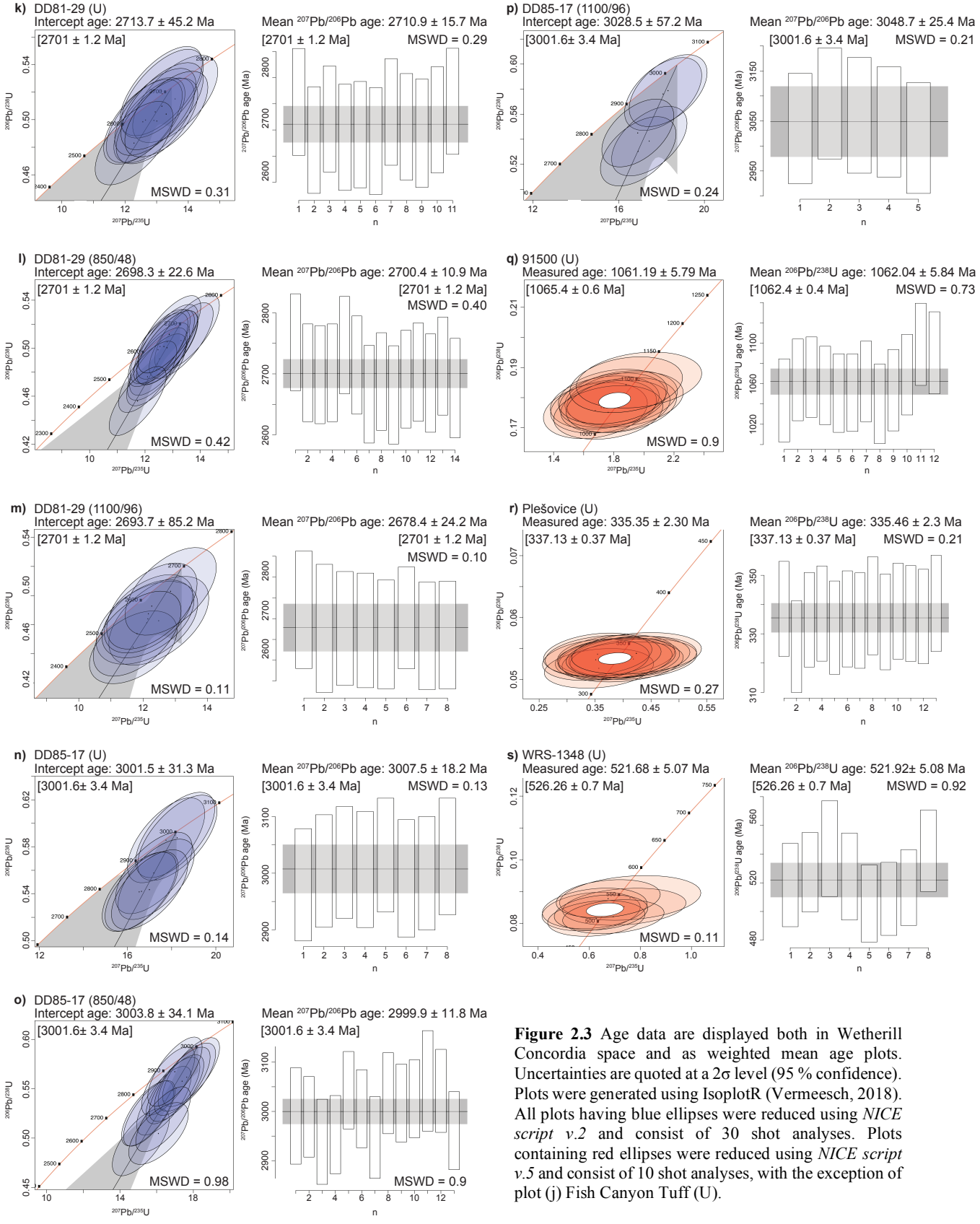


Figure 2.3 Age data are displayed both in Wetherill Concordia space and as weighted mean age plots. Uncertainties are quoted at a 2σ level (95 % confidence). Plots were generated using IsoplotR (Vermeesch, 2018). All plots having blue ellipses were reduced using *NICE script v.2* and consist of 30 shot analyses. Plots containing red ellipses were reduced using *NICE script v.5* and consist of 10 shot analyses, with the exception of plot (j) Fish Canyon Tuff (U).

Sample Name	Concordia Age (Ma)	Reproducibility (%)	MSWD	n	Weighted Mean Age (Ma)	Reproducibility (%)	MSWD	n	*NICE script* version
				30 shot analyses					
91500 *Wiedenbeck et al., 1995*	**1065.4 ± 0.6**				**1062.4 ± 0.4**				
91500 (U)	1054.15 ± 5.32	1.06	0.45	12	1055.73 ± 5.73	0.11	0.35	12/12	v.2
91500-1 (U)	1063.19 ± 5.04	0.21	0.63	14	1059.47 ± 5.52	0.28	0.62	13/14	v.2
91500-2 (U)	1056.61 ± 5.13	0.83	0.23	13	1056.14 ± 5.5	0.59	0.76	13/13	v.2
91500 (850/48)	1073.79 ± 5.2	0.79	1.6	13	1069.71 ± 5.76	0.69	0.49	13/13	v.2
91500 (1100/96)	1061.73 ± 3.13	0.34	0.79	11	1062.42 ± 3.18	0.002	1.69	11/11	v.2
Plešovice *Sláma et al., 2008*	**337.13 ± 0.37**				**337.13 ± 0.37**				
Plešovice (U)	336.30 ± 2.60	0.25	0.52	10	336.15 ± 2.61	0.29	0.54	10/10	v.2
Plešovice (850/48)	336.52 ± 2.59	0.18	0.92	10	336.28 ± 2.61	0.88	0.25	10/10	v.2
Plešovice (1100/96)	334.48 ± 1.98	0.79	0.51	11	334.61 ± 1.98	0.75	0.37	11/11	v.2
DD81-29 *Davis & Edwards, 1986*	**2701 ± 1.2**				**2701 ± 1.2**				
DD81-29 (U)	2713.7 ± 45.2	0.47	0.31	11	2710.9 ± 15.7	0.37	0.29	11/11	v.2
DD81-29 (850/48)	2698.3 ± 22.6	0.10	0.42	14	2700.4 ± 10.9	0.02	0.40	14/14	v.2
DD81-29 (1100/96)	2693.7 ± 85.2	0.27	0.11	8	2678.4 ± 24.2	0.84	0.10	8/8	v.2
DD85-17 *Tomlinson et al., 2003*	**3001.6 ± 3.4**				**3001.6 ± 3.4**				

DD85-17 (U)	3001.5 ± 31.3	0.003	0.14	8	3007.5 ± 18.2	0.20	0.13	8/8	v.2
DD85-17 (850/48)	3003.8 ± 34.1	0.07	0.98	13	2999.9 ± 11.8	0.06	0.90	13/13	v.2
DD85-17 (1100/96)	3028.5 ± 57.2	0.90	0.24	5	3048.7 ± 25.4	1.57	0.21	5/5	v.2
WRS-1348	**526.26 ±**				**526.26**				
Pointon et al., 2012	**0.7**				**± 0.7**				
WRS 1348 (U)	524.78 ± 5.84	0.28	0.11	5	524.57 ± 5.87	0.32	0.18	5/5	v.2
Fish Canyon Tuff	**28.37**				**28.37**				
Bachmann et al., 2007	**± 0.05**				**± 0.05**				
Fish Canyon Tuff (U)	27.99 ± 0.26	1.34	0.85	8	28.01 ± 0.26	1.27	0.90	8/8	v.5
				10 shot analyses					
91500	**1065.4**				**1062.4**				
Wiedenbeck et al., 1995	**± 0.6**				**± 0.4**				
91500 (U)	1061.19 ± 5.79	0.40	0.9	12	1062.04 ± 5.84	0.03	0.73	12/12	v.5
Plešovice	**337.13**				**337.13**				
Sláma et al., 2008	**± 0.37**				**± 0.37**				
Plešovice (U)	335.35 ± 2.30	0.53	0.27	13	335.46 ± 2.3	0.50	0.21	13/13	v.5
WRS-1348	**526.26**				**526.26**				
Pointon et al., 2012	**± 0.7**				**± 0.7**				
WRS-1348 (U)	521.68 ± 5.07	0.87	0.11	8	521.92 ± 5.08	0.82	0.92	8/8	v.5

Table 2.5 Summary of age data illustrated in Fig. 2.3. Accepted ages for each sample are highlighted in bold. 91500 zircon was used as the primary reference standard for all analyses with the exception of those 91500 samples where Plešovice was used instead. Weighted mean ages are based on $^{206}Pb/^{238}U$ ratios for zircons younger than 1100 Ma, otherwise the mean $^{207}Pb/^{206}Pb$ age is adopted for reference.

2.4.4. NICE script comparison

Signal integration by either *NICE* data reduction script will be inhibited when the least abundant isotope measured in a ratio pair (i.e., ^{207}Pb) fails to exceed (or remains close to) the LOQ. Fish Canyon Tuff (U) zircon has a relatively low abundance of radiogenic Pb (i.e. < 5 ppm; Bachmann et al., 2007), and is therefore ideally suited when comparing the efficacy of both *NICE script v.2* and *v.5* for samples and/ or shot counts yielding lower signal intensities.

A 30 shot analysis of Fish Canyon Tuff (U) was processed in the first instance using *NICE script v.2*, which operates to sub-sample integrations (described in detail in *section 2.3.4.1*). This effective 'peak-top' cropping reduces the counts integrated for each laser pulse for each isotope, consequently ^{207}Pb ion signals are for the most part below the LOQ. When plotted in Tera-Wasserberg space (Fig. 2.4a), calculated U/Pb ratios display apparent "Pb gain" effects and/or interferences on mass 204. The ion signal for mass 204 remains below LOQ for both *NICE script* versions however. Consequently, surface contamination by *common* Pb cannot be invoked to explain the apparent "Pb gain" observed when reducing the data using *NICE script v.2*. Instead, this effect is wholly artificial, being an artefact of poor counting statistics on mass 207.

NICE script v.5 by contrast integrates the entirety of a signal pulse. By processing a TRA with the latter script, the resultant counts for a given laser pulse exceed the LOQ for mass 207 and consequently $^{206}Pb/^{238}U$ and $^{207}Pb/^{235}U$ remain unaffected by poor counting statistics (Fig. 2.4b). This highlights the utility of *NICE script v.5* when low ion signals are recorded for either for young zircons, such as Fish Canyon Tuff and/or for analyses of < 30 shots.

Analyses conducted using a shot count of 10 also encountered problems associated with low Pb ion signals where data reduction was conducted in the 'peak-top' cropping fashion of the *NICE script v.2*. Thus, for these analyses *NICE script v.5* was used instead. Analyses of 10 shots reduced in this way reproduce to within < 0.87% of their accepted concordia ages based on analyses of untreated 91500, Plešovice, and WRS-1348. More accurate weighted mean ages result from reducing the entirety of a peak as with *NICE script v.5* for analyses yielding low signal counts; however, external reproducibility suffers as a result (see Table 2.3). *NICE script v.2*. should be utilised preferentially when analysing samples either with a high abundance of Pb or when using a shot count > 10.

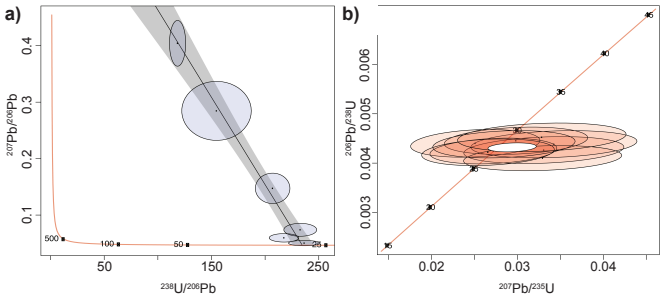


Figure 2.4. A comparison of age data generated for the same 30 shot analysis of Fish Canyon Tuff (U) zircon using (a) NuQuant *NICE script v.2* plotted in Tera-Wasserberg space and (b) *NICE script v.5* plotted in Wetherill Concordia space. Uncertainties are quoted at a 2σ level with a confidence interval of 95%. Plots were generated using IsoplotR (Vermeesch, 2018).

2.4.5. Monitoring time-dependent fractionation

The degree of time-dependent 'downhole' fractionation occurring during a single laser ablation analysis is determined by monitoring the variability of the measured $^{206}Pb/^{238}U$ ratio on a shot-to-shot basis. Where time-dependent fractionation of ^{206}Pb over a relatively more refractory ^{238}U has occurred during ablation, an increasing trend in measured $^{206}Pb/^{238}U$ would be expected on a shot-to-shot basis as the ablation crater deepens. Calculating the degree of time-dependent fractionation over the course of an analysis can be made by dividing the mean $^{206}Pb/^{238}U$ ratio of the first half of an analysis by its corresponding second segment. This calculation constitutes a fractionation index (FI). A FI of near unity suggests a minimal degree of time-dependent fractionation has occurred over the course of an analysis. Fig. 2.5. charts the variability of the $^{206}Pb/^{238}U$ ratio on a shot-to-shot basis over the course of various representative analyses of both 30 and 10 shots (Fig. 2.5. a and b, respectively). No discernible trend of increase exists for $^{206}Pb/^{238}U$ measured between shots over the course of an individual analysis and all have a FI near unity, suggesting minimal time-dependent 'downhole' fractionation has occurred.

2.4.6. Monitoring time-dependent fractionation

The degree of time-dependent 'downhole' fractionation occurring during a single laser ablation analysis is determined by monitoring the variability of the measured $^{206}Pb/^{238}U$ ratio on a shot-to-shot basis. Where time-dependent fractionation of ^{206}Pb over a relatively more refractory ^{238}U has occurred during ablation, an increasing trend in measured $^{206}Pb/^{238}U$ would be expected on a shot-to-shot basis as the ablation crater deepens. Calculating the degree of time-dependent fractionation over the course of an analysis can be made by dividing the mean $^{206}Pb/^{238}U$ ratio of the first half of an analysis by its corresponding second segment. This calculation constitutes a fractionation index (FI). A FI of near unity suggests a minimal degree of time-dependent fractionation has occurred over the course of an analysis. Fig. 2.5. charts the variability of the $^{206}Pb/^{238}U$ ratio on a shot-to-shot basis over the course of various representative analyses of both 30 and 10 shots (Fig. 2.5. a and b, respectively). No discernible trend of increase exists for $^{206}Pb/^{238}U$ measured between shots over the course of an individual analysis and all have a FI near unity, suggesting minimal time-dependent 'downhole' fractionation has occurred.

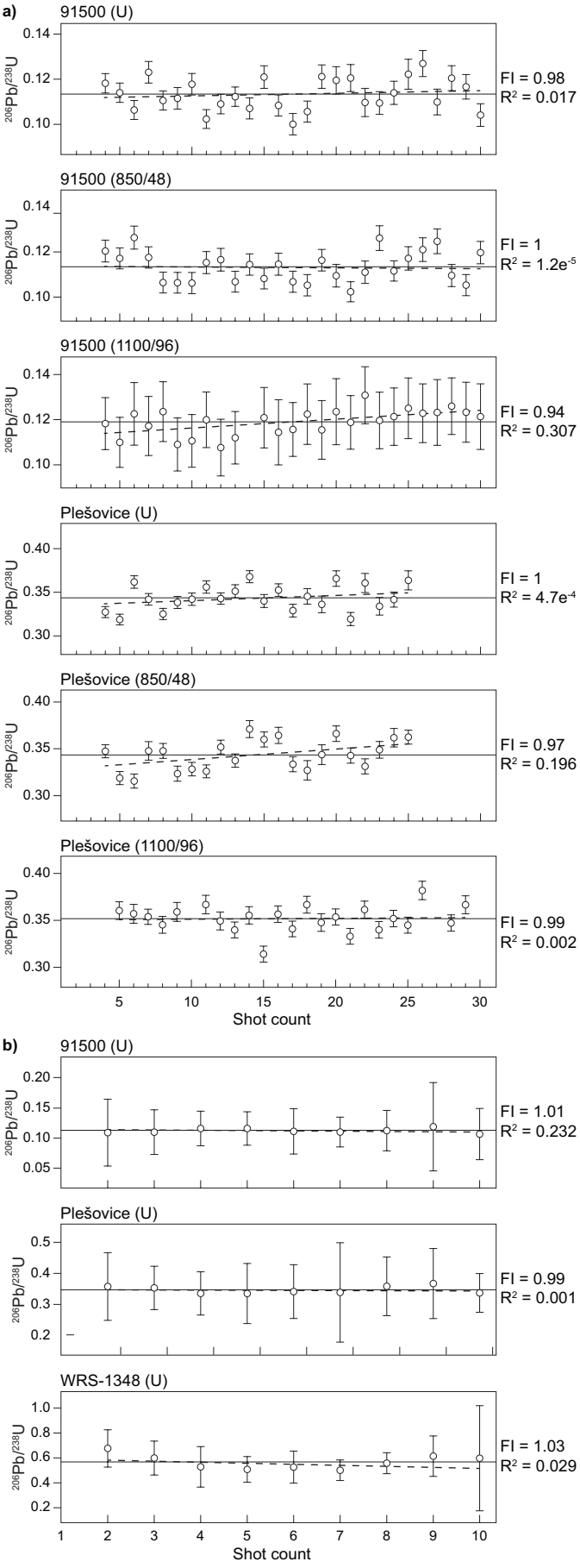


Figure 2.5. $^{206}Pb/^{238}U$ variability charted on a shot-to-shot basis for representative analyses of both; (a) 30 and; (b) 10 shots. Examples of heat-treated samples are also shown. Ratio uncertainties are calculated based upon the minimum ^{206}Pb counts received for each individual shot. Little to no ratio variability in the above analyses results in a FI of near unity for each, suggesting time-dependent 'downhole' fractionation has been significantly reduced for crater aspect ratios << 1.

2.4.7. Sample volume estimates

Individual crater depth measurements and their associated uncertainties are derived from repeated cross-sectional transects (n = 5) of the pit diameter viewed using WLI. Mean crater depth, depth variability and mean ablated volume estimates are summarised in Table 2.6 for each sample set (n = 20). Estimates for the ablated volume assumes a cylindrical crater geometry and 100% transport efficiency of the analyte to the ICP source (i.e., no sample re-deposition or loss within the transfer line to the ICP). The calculated depth achieved per laser pulse is between 47 nm and 70 nm, depending on the target sample.

Fig. 2.6a and b are based a representative WLI analysis of Plešovice (U), with a cross-section comparison of 30 and 10-shot craters. Small-scale inhomogeneous sampling at the crater floor is evidenced in Fig. 2.6a, which is exaggerated in its vertical dimension. The alternate plan view offered by Fig. 2.6b, demonstrates the lateral extent of this sampling inhomogeneity. The effect is less pronounced for 10-shot craters.

A qualitative comparison of laser matter interaction is shown by secondary electron images. Fig. 2.6c and c' illustrates a crater produced by static high frequency ablation (5 Hz, 20 s), with all other parameters being maintained as they are for the multi-shot approach described herein. It has been included as a point of comparison between craters produced by 30 and 10-shots (Fig. 2.6d-d' and e-e', respectively) in the same target matrix (i.e., a single fragment of 91500 (U)). The relative depth, degree of welding and re-deposition is clearly reduced (albeit not eliminated) where fewer shots are applied. The 1:1 scaling of secondary electron imaging also emphasises the much-reduced aspect ratio of craters produced by the multi-shot approach adopted in this study.

Sample Name	Mean Crater Depth (µm)	Crater Aspect Ratio (depth/diameter)	Crater Depth Variability (2SD%)	Approx. Depth per Shot (µm)	Mean Ablated Volume (µm^3)	Approx. Zircon consumption (ng)*	Approx. Pb consumption (pg)**	
30 shot analyses								
91500 (U)	1.41 ± 0.03	0.04	13.2	0.05	1770 ± 120	8.23	0.11-0.13	*(1)*
91500 (850/48)	1.53 ± 0.06	0.04	19.8	0.05	1930 ± 240	8.97	0.12-0.14	
91500 (1100/96)	1.90 ± 0.08	0.05	22.5	0.06	2390 ± 360	11.1	0.14-0.18	
Plešovice (U)	1.67 ± 0.10	0.04	31.2	0.06	2100 ± 420	9.77	0.2-1.54	*(2)*
Plešovice (850/48)	1.82 ± 0.06	0.05	16.8	0.06	2290 ± 270	10.65	0.22-1.68	
Plešovice (1100/96)	1.79 ± 0.07	0.04	20.6	0.06	2250 ± 310	10.46	0.22-1.65	
DD81-29 (U)	2.11 ± 0.09	0.05	18.7	0.07	2650 ± 450	12.32	-	
DD81-29 (850/48)	1.98 ± 0.09	0.05	17.9	0.07	2490 ± 430	11.58	-	
DD81-29 (1100/96)	1.51 ± 0.06	0.04	19.5	0.05	1900 ± 240	8.84	-	
DD85-17 (U)	1.57 ± 0.07	0.04	24.1	0.05	1970 ± 290	9.16	-	
DD85-17 (850/48)	1.67 ± 0.10	0.04	29.3	0.06	2100 ± 410	9.77	-	
DD85-17 (1100/96)	1.62 ± 0.07	0.04	23.7	0.05	2040 ± 300	9.49	-	
WRS-1348 (U)	1.61 ± 0.05	0.04	17.1	0.05	2030 ± 190	9.44	0.06-0.09	*(3)*
Fish Canyon Tuff (U)	1.65 ± 0.08	0.04	24.0	0.06	2080 ± 330	9.67	0.01-0.05	*(4)*
10 shot analyses								
91500 (U)	0.56 ± 0.02	0.01	15.0	0.06	704 ± 23	3.27	0.04-0.05	*(1)*
Plešovice (U)	0.62 ± 0.01	0.02	8.6	0.07	779 ± 17	3.60	0.08-0.57	*(2)*
WRS-1348 (U)	0.70 ± 0.02	0.02	15.5	0.06	880 ± 35	4.09	0.02-0.04	*(3)*

Table 2.6. Data summary of crater morphology and ablation behaviour for several heat treated and untreated zircon matrixes. Mean crater depths (n = 20) as measured by WLI and include analyses of both 30 and 10 shots. *Assuming the speci c gravity of zircon to be 4.65 g cm^{-3} (Deer et al., 1992) **Pb concentrations used for approximation are derived from (1) Wiedenbeck et al., 1995; (2) Sláma et al., 2008; (3) Pointon et al., 2012; (4) Bachmann et al., 2007.

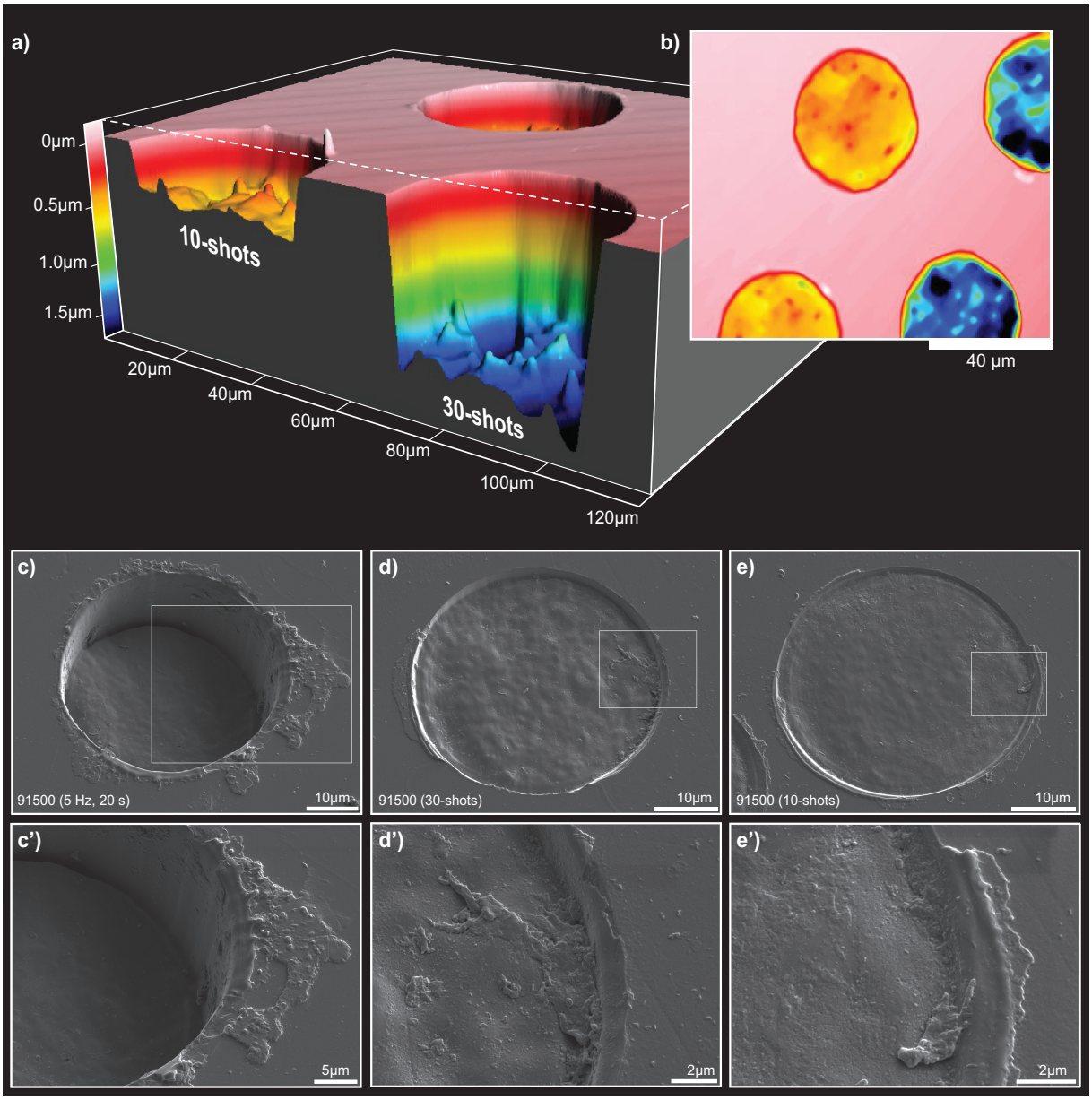


Figure 2.6. (a) A 3-dimensional rendering of the crater morphologies resulting from 30 and 10 shot analyses of Plešovice (U) measured by WLI. It should be noted that the vertical scaling of this graphic is exaggerated. (b) A plan view of the same Plešovice (U) sample surface. This view evidences inhomogeneous sampling at the crater floor. (c-c') Secondary electron SEM images of a static high frequency ablation (5 Hz, 20 s) conducted on 91500 (U), where all other analytical parameters are maintained as employed for multi-shot analysis. Evidence of significant welding and analyte re-deposition is present. The white box in (c) represents the magnified view of the re-deposited material presented in (c'). (d-d') Secondary electron SEM images of a crater generated by 30 consecutive shots on the same fragment of 91500. The crater aspect ratio, as well as the degree of melt generation and re-deposition are significantly reduced relative to that observed in (c) and (c'). (e-e') Secondary electron SEM images of a crater generated by 10 consecutive shots on the same fragment of 91500. The crater aspect ratio, as well as the degree of melt generation and re-deposition are again comparatively reduced to that observed in the high frequency static ablation (c-c').

2.4.8. Thermal annealing

Marillo-Sialer et al. (2016) demonstrated that the rate of ablation of a zircon matrix is at least partially controlled by the crystalline order of its lattice. Thermal annealing was investigated herein as a means by which to exercise some degree of control over ablation rate (depth) of the target matrix and the geometry of the resultant craters. The WLI data (summarised in Table 2.6) demonstrate little utility of thermal annealing as a pre-treatment in limiting resultant crater depths following multi-shot ablation. The variable behaviour of crater excavation was assessed by calculating the standard deviation of the resultant crater depths for a given sample set. The variability (2 SD%) of crater depths for any given sample set is < 31.2%. Thermally annealed sample sets demonstrated no discernible improvement in variability (2 SD%) over their untreated counterparts.

Despite reproducing predominantly to within 1% of their accepted mean ages, the ages calculated for thermally annealed samples often did not overlap (within uncertainty) of their accepted ages. This variability in accuracy would remain difficult to assess for unknowns treated by annealing and analysed by the multi-shot LA-ICP-MS method described here. The most accurate age determinations were made on untreated samples having (for the most part) delivered larger volumes of analyte to the ICP-MS instrument.

2.5. DISCUSSION

2.5.1. Accuracy and precision

The accuracy of the multi-shot LA-ICP-MS analytical method reported here is typically within the 1–2% (2σ) level expected for conventional static LA-ICP-MS analysis (Horstwood et al., 2016). The least abundant isotope measured in a ratio pair (i.e., ^{207}Pb in U-(Th)-Pb geochronology) will remain the limiting factor for determining the accuracy and precision of this technique. Consequently, accuracy and precision are inextricably linked to the volume of analyte produced, and therefore both can only be improved at the expense of depth or lateral resolution.

2.5.2. Thermal annealing as a pre-treatment

Slight variations in optical and thermo-physical properties between zircon matrices due to either radiation damage-induced lattice defects and/or colour will affect the laser–zircon interaction, and thus the amount of material removed by each laser pulse (Kooijman et al., 2012; Marillo-Sialer et al., 2014). Several previous studies have shown that the rate of ablation of a zircon matrix is at least partially controlled by the order of its crystalline lattice (Allen and Campbell, 2012; Crowley et al., 2014; Marillo-Sialer et al., 2016). The magnitude to which zircon crystal lattice recovery by annealing exhibits control over ablation behaviour was examined over 30 shots in this study.

There is only partial support for the hypothesis put forward by Allen and Campbell (2012) that increasing crystal density via annealing reduces the rate ablation rate of the target analyte. In this study,

annealed sample sets almost all demonstrate an increased mean crater depth relative to that of their untreated counterpart, with the notable exception of DD81-29. A reduction in ablation rate therefore, cannot be invoked as a universal behavioural response of annealed zircon matrices. There is also little evidence to suggest that annealing as a pre- treatment unifies/homogenises the ablation response of a sample set to incident laser radiation at the spatial scale investigated here. No discernible improvement in crater depth variability for annealed sample sets is observed, again with the exception of DD81-29. The effect of annealing on both crater geometries and/or resulting ages is difficult to assess between sample sets and is therefore not necessary as a pre-treatment for the protocol described herein.

2.5.3. Applications in geochronology

Where natural minerals are concerned, structural and chemical inhomogeneities are often present yet unresolvable using conventional LA-ICP-MS approaches. By integrating and collating multiple, consecutive single shots it is possible to generate precise ages, which are statistically indistinguishable from dates determined by ID-TIMS. Collating multiple signal pulses in this manner allows for an age determination to be made for as few as 10 shots. Depending on the number of shots applied to the target material, vertical sampling can be conducted from the micron to the sub-micron scale. The ion signals recorded for the least abundant isotope measured (i.e., ^{207}Pb) will remain the limiting factor for vertical resolution of this approach. The laser protocol outlined in this study was designed to be generally applicable to zircon U-Pb work, employing practicable spot sizes and moderate laser fluences. Modifications to this protocol could potentially be employed to maximise ion signals for fewer shots (and hence improve the vertical spatial resolution), alternatively an increased number of shots may be applied to improve the analytical accuracy and precision of the technique described here, so long as a critical aspect ratio of < 1 is maintained in order to minimise LIEF.

2.6. CONCLUSIONS

A multi-shot approach to U-Pb age determinations by LA-ICP-MS allows for precise and often indistinguishable ages compared to those determined by ID-TIMS for the same zircon reference materials and unknowns. The instrumental set-up requires no modification of the standard equipment for both the UP-213 laser ablation system and Attom HR-ICP-MS employed here. Moreover, the standard ablation cell allows for the maintenance of elevated signal intensities when utilised in conjunction with a short washout interval between shots. The shallow ablation depths achieved by multi-shot analysis allow for precise age determinations to be made both on the micron to sub-micron scale whilst negating the need to apply a 'downhole' inter-elemental fractionation correction.

2.7. ACKNOWLEDGMENTS

This work was funded by a Naughton Foundation Fellowship from the University of Notre Dame (USA) to A. Simonetti and Q. Crowley, and a Trinity Award from Trinity College Dublin (Ireland) to E. Corbett. Donald Davis is thanked for providing zircon samples DD81-29 and DD85-17. David Chew is thanked for providing zircon sample WRS-1348 and for providing helpful discussion on the manuscript. Leona O'Connor is thanked for her assistance with the WLI instrument. Paul Guyett is thanked for his assistance in collecting the SEM images. The anonymous reviewers are also thanked for their constructive comments, which helped improve the manuscript.

2.8. REFERENCES

Allen, C.M., Campbell, I.H., 2012. Identification and elimination of a matrix-induced systematic error in LA–ICP–MS $^{206}Pb/^{238}U$ dating of zircon. Chemical Geology, 332-333, 157–165.

Bachmann, O., Oberli, F., Dungan, M.A., Meier, M., Mundil, R., Fischer, H., 2007. $^{40}Ar/^{39}Ar$ and U-Pb dating of the Fish Canyon magmatic system, San Juan Volcanic field, Colorado: evidence for an extended crystallization history. Chemical Geology, 236, 134–166.

Bleiner, D., Günther, D., 2001. Theoretical description and experimental observation of aerosol transport processes in laser ablation inductively coupled plasma mass spectrometry. Journal Analytical Atomic Spectrometry, 16 (5), 449–456.

Chew, D., Drost, K., Petrus, J., 2018. Ultrafast, > 50 Hz LA-ICP-MS spot analysis applied to U–Pb dating of zircon and other U-bearing minerals. Geostandards Geoanalytical Research, 43, 39–60.

Cottle, J.M., Horstwood, M.S.A., Parrish, R.R., 2009. A new approach to single shot laser ablation analysis and its application to in situ Pb/U geochronology. Journal Analytical Atomic Spectrometry, 24, 1355–1363.

Cottle, J.M., Kylander-Clark, A.R., Vrijmoed, J.C., 2012. U–Th/Pb geochronology of detrital zircon and monazite by single shot laser ablation inductively coupled plasma mass spectrometry (SS-LA-ICPMS). Chemical Geology, 332-333, 136–147.

Crowley, Q.G., Heron, K., Riggs, N., Kamber, B.S., Chew, D., McConnell, B., Benn, K., 2014. Chemical abrasion applied to LA-ICP-MS U–Pb zircon geochronology. Minerals, 4, 503–518.

Davis, D.W., Edwards, G.R., 1986. Crustal evolution of Archean rocks in the Kakagi Lake area, Wabigoon subprovince, Ontario, as interpreted from high-precision U-Pb geochronology. Canadian Journal of Earth Sciences, 23, 182–192.

Deer, W.A., Howie, R.A., Zussman, J., 1992. An Introduction to the Rock-Forming Minerals, 2nd ed. Longman, London, UK, 1992.

Eggins, S.M., Kinsley, L.P.J., Shelley, J.M.G., 1998. Deposition and element fractionation processes during atmospheric pressure laser sampling for analysis by ICP-MS. Applied Surface Science, 127-129, 278–286.

Fernández, Beatriz, Claverie, Fanny, Pécheyran, Christophe, Donard, Olivier, 2007. Direct analysis of solid samples by fs-LA-ICP-MS. Trends in Analytical Chemistry, 26 (10), 951–966.

Fisher, C.F., Longerich, H.P., Jackson, S.E., Hanchar, J.M., 2010. Data acquisition and calculation of U–Pb isotopic analyses using laser ablation (single collector) inductively coupled plasma mass spectrometry. Journal of Analytical Atomic Spectrometry, 25 (12), 1905–1920.

Fryer, B.J., Jackson, S.E., Longerich, H.P., 1995. Design, operation and role of the Laser-Ablation Microprobe Coupled with an Inductively-Coupled Plasma Mass Spectrometer (LAM-ICP-MS) in the Earth-Sciences. Canadian Mineralogy, 33 (2), 303–312.

Guillong, M., Günther, D., 2002. Effect of particle size distribution on ICP-induced elemental fractionation in laser ablation-inductively coupled plasma-mass spectrometry. Journal of Analytical Atomic Spectrometry, 17 (8), 831–837.

Günther, D., Heinrich, C.A., 1999. Enhanced sensitivity in laser ablation-ICP mass spectrometry using helium-argon mixtures as aerosol carrier. Journal of Analytical Atomic Spectrometry, 14, 1363–1368.

Hirata, T., Nesbitt, R.W., 1995. U-Pb isotope geochronology and zircon: evaluation of the laser probe-inductively coupled plasma mass spectrometry technique. Geochimica et Cosmochimica Acta, 59, 2491–2500.

Horn, I., Günther, D., 2003. The influence of ablation carrier gasses Ar, He and Ne on the particle size distribution and transport efficiencies of laser ablation-induced aerosols: implications for LA–ICP–MS. Applied Surface Science, 207, 144–157.

Horn, I., Rudnick, R.L., McDonagh, W.F., 2000. Precise elemental and isotope ratio determination by simultaneous solution nebulization and laser ablation-ICP-MS: application to U–Pb geochronology. Chemical Geology, 164 (3–4), 281–301.

Horstwood, M.S.A., 2008. Data reduction strategies, uncertainty assessment and resolution of LA-(MC)-ICP-MS isotope data. In: Sylvester, P. (Ed.), Laser Ablation ICP-MS in the Earth Sciences: Current Practices and Outstanding Issues. Mineralogical Association of Canada, 283–303. (Short course, 40, 40).

Horstwood, M.S.A., Košler, J., Gehrels, G., Jackson, S.E., McLean, N.M., Paton, C., Pearson, N.J., Sircombe, K.N., Sylvester, P., Vermeesch, P., Bowring, J.F., Condon, D.J., Schoene, B., 2016. Community-derived standards for LA-ICP-MS U-(Th-)Pb geochronology – uncertainty propagation, age interpretation and data reporting. Geostandards Geoanalytical Research, 40, 311–332.

Jackson, S.E., Pearson, N.J., Griffin, W.L., Belousova, E., 2004. The application of laser ablation-inductively coupled plasma-mass spectrometry to in situ U–Pb zircon geochronology. Chemical Geology, 211 (1–2), 47–69.

Jaffey, A.H., Flynn, K.F., Glendenin, L.E., Bentley, W.C., Essling, A.M., 1971. Precision measurement of half-lives and specific activities of 235U and 238U. Physical Review Series, C4, 1889–1905.

Koch, J., Feldmann, I., Jakubowski, N., Niemax, K., 2002. Elemental composition of laser ablation aerosol particles deposited in the transport tube to an ICP. Spectrochimica Acta Part B: Atomic Spectroscopy, 57, 975–985.

Kooijman, E., Berndt, J., Mezger, K., 2012. U-Pb dating of zircon by laser ablation ICP-MS: recent improvements and new insights. European Journal of Mineralogy, 24, 5–21.

Košler, J., Wiedenbeck, M., Wirth, R., Hovorka, J., Sylvester, P., Míková, J., 2005. Chemical and phase composition of particles produced by laser ablation of silicate glass and zircon – Implication for elemental fractionation during ICP-MS analysis. Journal of Analytical Atomic Spectrometry, 20 (5), 402–409.

Košler, J., Sláma, J., Belousova, E., Corfu, F., Gehrels, G.E., Gerdes, A., Horstwood, M.S.A., Sircombe, K.N., Sylvester, P., Tiepolo, M., Whitehouse, M.J., Woodhead, J.D., 2013. U-Pb detrital zircon analysis - results of an inter-laboratory comparison. Geostandards Geoanalytical Research, 37, 243–259.

Kroslakova, I., Günther, D., 2007. Elemental fractionation in laser ablation- inductively coupled plasma-mass spectrometry: evidence for mass load induced matrix e ects in the ICP during ablation of a silicate glass. Journal of Analytical Atomic Spectrometry, 22, 51–62.

Kuhn, H.R., Guillong, M., Günther, D., 2004. Size-related vaporisation and ionisation of laser-induced glass particles in the inductively coupled plasma. Analytical and Bioanalytical Chemistry 378 (4), 1069–1074.

Kuhn, B.K., Birbaum, K., Luo, Y., Günther, D., 2009. Fundamental studies on the ablation behaviour of Pb/U in NIST 610 and zircon 91500 using laser ablation inductively coupled plasma mass spectrometry with respect to geochronology. Journal of Analytical Atomic Spectrometry, 25, 21–25.

Liu, H., Borisov, O., Mao, X., Shuttleworth, S., Russo, R., 2000. Pb/U Fractionation during Nd:YAG 213 nm and 266 nm Laser Ablation Sampling with Inductively coupled Plasma Mass Spectrometry. Applied Spectroscopy. 54 (10), 1435–1442.

Longerich, H.P., Jackson, S.E., Günther, D., 1996. Inter-laboratory note. Laser ablation inductively coupled plasma mass spectrometric transient signal data acquisition and analyte concentration calculation. Journal of Analytical Atomic Spectrometry, 11 (9), 899–904.

Mank, A.J.G., Mason, P.R.D., 1999. A critical assessment of laser ablation ICP-MS as an analytical tool for depth analysis in silica-based glass samples. Journal of Analytical Atomic Spectrometry, 14 (8), 1143–1153.

Mank, A.J.G., Mason, P.R.D., 2001. Depth-resolved analysis in multi-layered glass and metal materials using laser ablation inductively coupled plasma mass spectrometry (LA-ICP-MS). Journal of Analytical Atomic Spectrometry, 16, 1381–1388.

Marillo-Sialer, E., Woodhead, J.D., Hergt, J., Grieg, A., Guillong, M., Gleadow, A., Evans, N., Paton, C., 2014. The zircon "matrix effect": evidence for an ablation rate control on the accuracy of U–Pb age determinations by LA-ICP-MS. Journal of Analytical Atomic Spectrometry, 29 (6), 981.

Marillo-Sialer, E., Woodhead, J.D., Hanchar, J.M., Reddy, S.M., Greig, A., Hergt, J., Kohn, B., 2016. An investigation of the laser-induced zircon matrix effect. Chemical Geology, 438, 11–24.

Mattinson, J., 2005. Zircon U–Pb chemical abrasion (bCA-TIMSQ) method: combined annealing and multi-step partial dissolution analysis for improved precision and accuracy of zircon ages. Chemical Geology, 220, 47–66.

Nasdala, L., Kronz, A., Hanchar, J.M., Tichomirowa, M., Davis, D.W., Hofmeister, W., 2006. Effects of natural radiation damage on back-scattered images of single crystals of minerals. American Mineralogist, 91, 1739–1746.

Pointon, M.A., Cli , R.A., Chew, D.M., 2012. The provenance of Western Irish Namurian Basin sedimentary strata inferred using detrital zircon U–Pb LA-ICP-MS geochronology. Geological Journal, 47, 77–98.

Russo, R.E., Mao, X.L., Borisov, O.V., Liu, H., 2000. Influence of wavelength on fractionation in laser ablation ICP-MS. Journal of Analytical Atomic Spectrometry, 15, 1115–1120.

Shaheen, M.E., Gagnon, J.E., Fryer, B.J., 2012. Femtosecond (fs) lasers coupled with modern ICP-MS instruments provide new and improved potential for in situ elemental and isotopic analyses in the geosciences. Chemical Geology, 330-331, 260–273.

Simonetti, A., Heaman, L.M., Hartlaub, R.P., Creaser, R.A., MacHattie, T.G., Böhm, C., 2005. U–Pb zircon dating by laser ablation-MC-ICP-MS using a new multiple ion counting Faraday collector array. Journal of Analytical Atomic Spectrometry, 20, 677–686.

Sláma, J., Košler, J., Condon, D.J., Crowley, J.L., Gerdes, A., Hanchar, J.M., Horstwood, M.S.A., Morris, G.A., Nasdala, L., Norberg, N., Schaltegger, U., Schoene, B., Tubrett, M.N.,Whitehouse, M.J., 2008. Plešovice zircon—a new natural reference material for U-Pb and Hf isotopic microanalysis. Chemical Geology, 249, 1–35.

Spencer, C.J., Kirkland, C.L., Taylor, R.J.M., 2016. Strategies towards statistically robust interpretations of in situ U-Pb zircon geochronology. Geoscience Frontiers, 7, 581–589.

Steiger, R.H., Jäger, E., 1977. Subcommission on geochronology: Convention on the use of decay constants in geo- and cosmochronology. Earth Planetary Science Letters, 36, 359–362.

Tomlinson, K.Y., Davis, D.W., Stone, D., Hart, T.R., 2003. U–Pb Age and Nd Isotopic Evidence for Archean Terrane Development and Crustal Recycling in the South-Central Wabigoon Subprovince, Canada, 144, 684–702.

Vermeesch, P., 2018. IsoplotR: a free and open toolbox for geochronology. Geoscience Frontiers, 9, 1479–1493.

Wiedenbeck, M., Allé, P., Corfu, F., Griffin, W.L., Meier, M., Oberli, F., von Quadt, A., Roddick, J.C., Spiegel, W., 1995. Three natural zircon standards for U-Th-Pb, Lu-Hf, trace element and REE analyses. Geostandards Newsletter, 19, 1–23.

Woodhead, J.D., Hergt, J.M., 2001. Strontium, neodymium and lead isotope analyses of NIST glass certified reference materials: SRM 610, 612, 614. Geostandards Newsletter, 25 (2–3), 261–266.

2.9. SUPPORTING INFORMATION AND SUPPLEMENTARY FIGURES

2.9.1. Annotated copy of the NICE Python script (v.2)

Below is an annotated copy of the python NICE script v.2, which can be found as a python formatted text file in the online version of this article (https://doi.org/10.1016/j.chemgeo.2020.119568). Working copies of the NICE scripts described herein can be acquired from the associated online data repository or by contacting nu.attomservice@ametek.com directly.

```
"""
Definitions of specific variables used in scripts and defined as part of setting up the list of samples:

Name:                       Input or Output variable  Display name
        Hint                                                                    Default value

boxcar_points               In                        Smooth points
        Must be odd number                                                      3
endbl                       In                        Baseline End Cycle
        Last cycle of baseline                                                  50
group                       In                        Sample group
        Group all samples of same type with same integer value, default 0   0
ignore_first_shots          In                        Ignore first X shots
        To avoid surface contamination issues, default is 0 (use all shots)    0
ignore_last_shots           In                        Ignore shot Y and after
        If <= Ignore first shots, not used                                      0
p0                          Out                       Integrated Pb206
p1                          Out                       Integrated Pb207
p2                          Out                       Integrated Pb208
p3                          Out                       Integrated U235
p4                          Out                       Integrated U238
pw                          In                        Peak must be X ch wide
        Width of peak minimum                                                   10
r0                          Out                       207/206Pb
r1                          Out                       208/206Pb
r2                          Out                       208/207Pb
r3                          Out                       Pb206/U238
r4                          Out                       Pb207/U235
stbl                        In                        Baseline Start Cycle
        Start cycle of baseline                                                 1
trig                        In                        Peak Start Trigger
        cps when set at >=1000. Otherwise, no. of SD above baseline             20

"""
import nu # proprietary functions for Nu Instruments
import math # standard Python library
import globals # list of variables for mass, abundance, RSF etc.
import nu_xalglib as xl # Python interface for specialist mathematics library used for calibration curves

store.init() # Store is a specialist Nu function to carry information from scripts between samples

if not 'cyc' in locals(): cyc=0 # cycle counter

if cyc==0:

################################## EDIT
############################################################

  # EDIT: isotopes in batch (remove any that are not to be reported or used in calculations). Required
isotopes in a Python list, isotopes are application variables exposed to the scripts from the data:

  isotopes=[Pb206,Pb207,Pb208,U235,U238]
```

```
   # To display the integrated value, an output parameter needs to be defined for each isotope [p0....pX].
   # To do so click on "variables" button and change the "display name", to add isotopes click on "new" or
"delete selected" needed.
   # Be careful with the order!
   # The order that is chosen in the previous line will define the name in the "variable" window
[p0,p1,...,pX].

   # EDIT: Setup ratios and outputs for batch, each numerator/denominator/lab set in square bracket,
one for each ratio and all within square bracket to make a list
   # I.E : [[numerator1, demoninator1, "label ratio1"],,,,,[numeratorN, demoninatorN, "label ratioN"]]


ratios=[[Pb207,Pb206,"207/206Pb"],[Pb208,Pb206,"208/206Pb"],[Pb208,Pb207,"208/207Pb"],[Pb206,
U238,"Pb206/U238"],[Pb207,U235,"Pb207/U235"]]

   # To display the value of each ratio, an output parameter needs to be defined for each ratio r0.....rX
   # To do so click on the "variables" button and change the "display name", to add isotopes click on "new"
or "delete selected" needed.
   # Be careful with the order!
   # The order that is chosen in the previous line will define the name in the "variable" window
[r0,r1,...,rX]

   # EDIT: Define the master isotope to be used to search for peaks.

   master = U238

############################## NOTHING NEEDS EDITING PAST THIS POINT
#########################################

   # Set up stores to carry data over between samples
   if not store.exists("sample_num_list"):
      store.sample_num=0
      store.sample_num_list={}
      store.sample_list_means={}
      store.sample_list_se2y={}
      store.sample_list_se2x={}

   if str(int(group)) not in store.sample_list_means.keys():
      store.sample_num_list[str(int(group))] = []
      store.sample_list_means[str(int(group))] = [[] for _ in xrange(len(ratios))]
      store.sample_list_se2y[str(int(group))] = [[] for _ in xrange(len(ratios))]
      store.sample_list_se2x[str(int(group))] = [[] for _ in xrange(len(ratios))]

   # Setup variables to be used within the sample
   if not 'iso_sum_current_peak' in locals():
      iso_sum_current_peak=[]
      peak_start_x = []
      peak_start_y = []
      peak_end_x = []
      peak_end_y = []
      iso_peak_avg_background=[]
      iso_list_background_cps=[]
      peak_integral_list_for_ratios=[]
      peak_integral_list_for_ratios_inc=[]
      peak_integral_list_for_ratios_exc=[]
      peak_integral_list_ratios_weighting=[]
      list_shots=[]
      ratio_of_peak_integrals=[]
      list_shots_inc=[]
      ratio_of_peak_integrals_inc=[]
      list_shots_exc=[]
      ratio_of_peak_integrals_exc=[]
      list_shots_sd=[]
      ratio_of_peak_integrals_sd=[]
      rollx=[]
      rollsd=[]
      box0=0
```

```
    box1=0
    shot=0
    peak_width=0
    cycle_counts_4ratios=[]
    cycle_counts_4ratios_rise=[]
    cycle_counts_4ratios_fall=[]
    log_cycle_count=[]
    log_cycle_cps=[]
    ratio_cycles_weighting=[]
    ratio_cycles_list=[]
    iso_means=[]
    peak_integrals=[]
    temp_ratios=[]
    for a in xrange(len(isotopes)):
      log_cycle_cps.append([])
      iso_sum_current_peak.append(0)
      iso_peak_avg_background.append(0)
      iso_list_background_cps.append([])
      peak_integrals.append(0)
    for _ in xrange(len(ratios)):
      ratio_of_peak_integrals.append([])
      peak_integral_list_ratios_weighting.append([])
      list_shots_inc.append([])
      ratio_of_peak_integrals_inc.append([])
      list_shots_exc.append([])
      ratio_of_peak_integrals_exc.append([])
      list_shots_sd.append([])
      ratio_of_peak_integrals_sd.append([])
      ratio_cycles_weighting.append([])
      ratio_cycles_list.append([])
      temp_ratios.append(0)
      cycle_counts_4ratios.append([[],[]])
      cycle_counts_4ratios_rise.append([[],[]])
      cycle_counts_4ratios_fall.append([[],[]])
      peak_integral_list_for_ratios.append([[],[]])
      peak_integral_list_for_ratios_inc.append([[],[]])
      peak_integral_list_for_ratios_exc.append([[],[]])

# Count the cycles
cyc=cyc+1

# By default generate "null" values for each calculation for each cycle. The actual values for each laser
shot will be calculated and displayed in the last cycle of each shot:
if cyc==1:
  for c in range(len(isotopes)):
    exec('p%d = nu.null'%c)
  for c in range(len(ratios)):
    exec('r%d = nu.null'%c)

# Setup rolling 3pt average of master isotope cps
for p in xrange(len(isotopes)):
  if label[master]==label[isotopes[p]] : master_isotope_id=p

avg=(box0 + box1 + cps[master])/3
box0=box1
box1=cps[master]

# Add raw data to list for plotting as log of cps
log_cycle_count.append(cyc)

for j in xrange(len(isotopes)):
  if cps[isotopes[j]]<=0:
    log_cycle_cps[j].append(nu.null)
  else:
    log_cycle_cps[j].append(math.log(cps[isotopes[j]],10))

print 'shot number '+str(shot)
```

```
# If current cycle is not the baseline start, clear out lists for baseline test - start cycle defined in sample
list
if cyc<=int(stbl):
   for k in xrange(len(iso_list_background_cps)):
      iso_list_background_cps[k]=[]

# If baseline region has started but not ended, add found values to lists - end cycle defined in sample list
else:
   if cyc<int(endbl):
      for k in xrange(len(iso_list_background_cps)):
         iso_list_background_cps[k].append(cps[isotopes[k]])

   # If baseline has ended, add current values to list of baselines for subtraction from shot integrations:
   elif cyc==int(endbl):
      for k in xrange(len(iso_list_background_cps)):
         iso_list_background_cps[k].append(cps[isotopes[k]])
         iso_peak_avg_background[k]=nu.mean(iso_list_background_cps[k])

      # If trig value set in sample list is >=1000 use cps otherwise set trigger to determine a peak starting
as some multiple of the baseline SD over the baseline average CPS:
      if trig >=1000:
         peak_find_trigger = trig
      else:
         sd_master_isotope=nu.stddev(iso_list_background_cps[master_isotope_id])
         peak_find_trigger = iso_peak_avg_background[master_isotope_id] + (trig * sd_master_isotope)

      # Default if baseline found to be zero so SD is zero also, set trigger to default 1000:
      if peak_find_trigger==0: peak_find_trigger=1000

   # If baseline ended, clear out baseline lists of variables
   elif cyc>int(endbl):
      if not math.isnan(p0):
         # Report output values as null if previous cycles value was a number
         for c in range(len(isotopes)):
            exec('p%d = nu.null'%c)
         for c in range(len(ratios)):
            exec('r%d = nu.null'%c)

      for n in xrange(len(iso_list_background_cps)):
         iso_list_background_cps[n]=[]

      # Check if current measurement has dropped below trigger
      if avg<peak_find_trigger:

         # Check if peak wide enough to be a true peak - expected peak width in cycles defined in sample
list
         if peak_width<pw:
            for r in xrange(len(iso_sum_current_peak)): iso_sum_current_peak[r]=0
            peak_width=0
            # Remove peak markers used in charts as they will not be needed (check that list is not empty
first)
            if not len(peak_start_x)==len(peak_end_x) and len(peak_start_x)>=3:
               del peak_start_x[-3:]
               del peak_start_y[-3:]


         # Report peak
         else:
            print 'Peak ends'
            shot = shot + 1 #increment number of shots
            list_shots.append(shot)
            print '1st shot number '+str(list_shots[0])
            print 'last shot number '+str(list_shots[-1])
            # Add markers for peak end to lists of values for charts
            peak_end_x.extend([cyc,cyc, cyc])
            peak_end_y.extend([-0.5,8.5, nu.null])
```

```
            last_shots = 0

            # When ignoring the first few shots, increment counter, reset peak width but don't process data
            if shot<=ignore_first_shots:
               peak_width=0

            # When ignoring the last few shots, increment counter, reset peak width but don't process data
                                        elif ignore_last_shots > ignore_first_shots and shot >=
ignore_last_shots:
               peak_width=0
               last_shots = len(list_shots) - ignore_last_shots

            else:
               for a in xrange(len(iso_sum_current_peak)):

                  # Sum channels and remove baseline counts for all cycles accross peak
                  integration = iso_sum_current_peak[a] - (peak_width * iso_peak_avg_background[a])
                  peak_integrals[a]=integration
                  for n in xrange(len(ratios)):
                     if label[ratios[n][0]]==label[isotopes[a]] :
peak_integral_list_for_ratios[n][0].append(integration)
                     if label[ratios[n][1]]==label[isotopes[a]] :
peak_integral_list_for_ratios[n][1].append(integration)

               # Report intergated values
               for c in range(len(isotopes)):
                  exec('p%d = peak_integrals[c]'%c)

               # Report ratios
               for e in xrange(len(ratios)):
                  if peak_integral_list_for_ratios[e][1][-1]<=0:
                     temp_ratios = nu.null
                  else:
                     temp_ratios = peak_integral_list_for_ratios[e][0][-
1]/peak_integral_list_for_ratios[e][1][-1]
                  exec('r%d = temp_ratios'%e)
                  if not math.isnan(temp_ratios): ratio_of_peak_integrals[e].append(float(temp_ratios))

               # Reset peak integration for next peak
               for f in xrange(len(iso_sum_current_peak)):
                  iso_sum_current_peak[f]=0
               peak_width=0

      else:
      # Add markers for charts for peak start
         if peak_width ==0:
            peak_start_x.extend([cyc,cyc, cyc])
            peak_start_y.extend([-0.5,8.5, nu.null])

         # Increment peak width counter and add current values to peak integration
         print 'Peak found'
         peak_width = peak_width + 1
         for h in xrange(len(iso_sum_current_peak)): iso_sum_current_peak[h] =
iso_sum_current_peak[h] + cps[isotopes[h]]

# Check if master cps is high enough to ratio this individual cycle
if cps[master]<=10000:
   pass

else:
   # Check that signal is rising by looking at the cps being more than the average of last 3 readings, add
data to rising signal list
   if len(cycle_counts_4ratios[0][0])<=3 or cps[master]>=avg:

      for l in xrange(len(ratios)):
      # Check for divide by zero and calculate ratio if not
         if not cps[ratios[l][1]]==0:
```

```
            ratio_cycles_list[l].append(cps[ratios[l][0]]/cps[ratios[l][1]])
          else:
            ratio_cycles_list[l].append(nu.null)

          # Add weightings for later calculation
          ratio_cycles_weighting[l].append(0.1)

          # Add cycle cps to all data and rising data lists
          for m in xrange(2):
            cycle_counts_4ratios[l][m].append(cps[ratios[l][m]])
            cycle_counts_4ratios_rise[l][m].append(cps[ratios[l][m]])

    # Add data to falling signal list
    else:
      for l in xrange(len(ratios)):
        # Check for divide by zero and calculate ratio if not
        if not cps[ratios[l][1]]==0:
          ratio_cycles_list[l].append(cps[ratios[l][0]]/cps[ratios[l][1]])
        else:
          ratio_cycles_list[l].append(nu.null)

        # Add weightings for later calculation
        ratio_cycles_weighting[l].append(0.1)

        # Add cycle cps to all data and falling data lists
        for m in xrange(2):
          cycle_counts_4ratios[l][m].append(cps[ratios[l][m]])
          cycle_counts_4ratios_fall[l][m].append(cps[ratios[l][m]])

# When all data has been acquired for this sample, clear out all the stores
if cyc==total_cycles:

    # Setup raw ratios list
    raw_ratios = [[] for b in xrange(len(ratios))]

    # Increment sample number
    store.sample_num=store.sample_num + 1
    store.sample_num_list[str(int(group))].append(store.sample_num)

    # Chart log plot of raw data (boxcar smoothed and nulls replaced with 0 values)
    for w in range(len(log_cycle_count)):
      for v in xrange(len(isotopes)):
        if math.isnan(log_cycle_cps[v][w]): log_cycle_cps[v][w]=0
    chart.SetLabels(0,"Plot of boxcar smoothed data in log form.", "Cycle", "Log of counts per second")

    # Boxcar smooth the data
    for z in xrange(len(isotopes)):
      # Check is boxcar is even and correct
      if not (boxcar_points/2)-int(boxcar_points/2)>0: boxcar_points = boxcar_points + 1

      log_cycle_cps[z]=nu.box(log_cycle_cps[z],int(boxcar_points),1)
      chart.AddSeries(0,label[isotopes[z]]+" baseline is "+str(round(iso_peak_avg_background[z],2))+"
cps", 1, log_cycle_count, log_cycle_cps[z])

    # Plot peak markers
    chart.AddSeries(0,"Peak start positions. Peak trigger isotope is "+str(label[master]), 1, peak_start_x,
peak_start_y)
    chart.AddSeries(0,"Peak end positions with a start/end point of "+str(int(peak_find_trigger))+" cps", 1,
peak_end_x, peak_end_y)
    chart.AddSeries(0,"Baseline start and end points",1,[stbl,stbl,stbl,endbl,endbl],[-0.5,7,nu.null,-0.5,7])


    # Calculate inclusions and exclusions for shot by shot display of ratios
    for n in xrange(len(ratios)):
      mean_ratio_of_peak_integrals = nu.mean(ratio_of_peak_integrals[n])
      if not mean_ratio_of_peak_integrals==0 and not len(ratio_of_peak_integrals[n])==0:
        sd_ratio_of_peak_integrals=nu.stddev(ratio_of_peak_integrals[n])
```

```
    else:
      sd_ratio_of_peak_integrals=1

    for a in range(len(ratio_of_peak_integrals[n])):

      if abs(ratio_of_peak_integrals[n][a]-
mean_ratio_of_peak_integrals)<2*sd_ratio_of_peak_integrals:
        list_shots_inc[n].append(list_shots[int(ignore_first_shots) + a])
        ratio_of_peak_integrals_inc[n].append(ratio_of_peak_integrals[n][a])
        peak_integral_list_for_ratios_inc[n][0].append(peak_integral_list_for_ratios[n][0][a])
        peak_integral_list_for_ratios_inc[n][1].append(peak_integral_list_for_ratios[n][1][a])
      else:
        list_shots_exc[n].append(list_shots[int(ignore_first_shots) + a])
        ratio_of_peak_integrals_exc[n].append(ratio_of_peak_integrals[n][a])
        peak_integral_list_for_ratios_exc[n][0].append(peak_integral_list_for_ratios[n][0][a])
        peak_integral_list_for_ratios_exc[n][1].append(peak_integral_list_for_ratios[n][1][a])

      # Add zeros and weightings with strong weighting for zero to lists
      peak_integral_list_ratios_weighting[n]=[0.1 for _ in
xrange(len(peak_integral_list_for_ratios_inc[n][0]))]
      peak_integral_list_for_ratios_inc[n][0].append(0.0)
      peak_integral_list_for_ratios_inc[n][1].append(0.0)
      peak_integral_list_ratios_weighting[n].append(100)

    # Create +ve and -ve 2SD lines for the chart
    list_shots_sd[n].extend([1,len(list_shots),len(list_shots),1,len(list_shots)])

ratio_of_peak_integrals_sd[n].extend([mean_ratio_of_peak_integrals+(2*sd_ratio_of_peak_integrals),m
ean_ratio_of_peak_integrals+(2*sd_ratio_of_peak_integrals),nu.null,mean_ratio_of_peak_integrals-
(2*sd_ratio_of_peak_integrals),mean_ratio_of_peak_integrals-(2*sd_ratio_of_peak_integrals)])

    chart.SetLabels((1000 + n),"Shot by shot integrated peak display of "+str(ratios[n][2])+" isotope
ratio", "Shots", "Isotope Ratio")
    chart.AddSeries((1000 + n),"Corr. "+str(ratios[n][2])+"
"+str(round(nu.mean(ratio_of_peak_integrals_inc[n]),6))+" +/-
"+str(round(nu.stddev(ratio_of_peak_integrals_inc[n]),6))+" (1SD of included data)", 2,
list_shots_inc[n], ratio_of_peak_integrals_inc[n])
    chart.AddSeries((1000 + n),"Corr. "+str(ratios[n][2])+" (first "+str(int(ignore_first_shots))+", final
"+str(int(last_shots))+" and marked shots excluded)", 2, list_shots_exc[n],
ratio_of_peak_integrals_exc[n])
    chart.AddSeries((1000 + n),"2SD limit used for excluding points", 1, list_shots_sd[n],
ratio_of_peak_integrals_sd[n])

    # Add this samples ratios and standard errors to store for all samples in batch
    store.sample_list_means[str(int(group))][n].append(nu.mean(ratio_of_peak_integrals_inc[n]))

store.sample_list_se2x[str(int(group))][n].extend([store.sample_num,store.sample_num,store.sample_
num])
    store.sample_list_se2y[str(int(group))][n].extend([nu.mean(ratio_of_peak_integrals_inc[n]) + (2 *
(nu.stddev(ratio_of_peak_integrals_inc[n])/math.sqrt(len(ratio_of_peak_integrals_inc[n])))),nu.mean(
ratio_of_peak_integrals_inc[n]) - (2 *
(nu.stddev(ratio_of_peak_integrals_inc[n])/math.sqrt(len(ratio_of_peak_integrals_inc[n])))),nu.null])

    # Create rolling sample chart for first ratio
    chart.SetLabels((2000 + n),"Sample by sample display of integrated peak"+ratios[n][2]+"isotope
ratio", "Samples", "Isotope Ratio")
    chart.AddSeries((2000 + n),"Corr. "+str(ratios[n][2]), 2,
store.sample_num_list[str(int(int(group)))], store.sample_list_means[str(int(group))][n])
    chart.AddSeries((2000 + n),"2SE error per sample", 1, store.sample_list_se2x[str(int(group))][n],
store.sample_list_se2y[str(int(group))][n])

    # After first sample, start creating standard deviation limits for all samples and plotting them for
first ratio
    if len(store.sample_list_means[str(int(group))][n])>1:
      lo = store.sample_num_list[str(int(group))][0]
      hi = store.sample_num_list[str(int(group))][-1]
      rollx.extend([lo,hi,nu.null,lo,hi])
```

```
        sd1hi=nu.mean(store.sample_list_means[str(int(group))][n]) + (2 *
nu.stddev(store.sample_list_means[str(int(group))][n]))
        sd1lo=nu.mean(store.sample_list_means[str(int(group))][n]) - (2 *
nu.stddev(store.sample_list_means[str(int(group))][n]))
        rollsd.extend([sd1hi,sd1hi,sd1hi,sd1lo,sd1lo])
        chart.AddSeries((2000 + n),"Combined samples
"+str(round(nu.mean(store.sample_list_means[str(int(group))][n]),7))+" +/- "+str(round((2 *
nu.stddev(store.sample_list_means[str(int(group))][n])),7))+" (2SD limits)", 1, rollx, rollsd)
        rollx=[]
        rollsd=[]
        # Show combained charts for all samples, split into their groups
        print 'length of key list '+str(len(store.sample_list_means.keys()))
        if len(store.sample_list_means.keys())>1:
          chart.SetLabels((3000 + n),"Sample by sample display of integrated peak for all sample groups
for "+ratios[n][2]+" isotope ratio", "Samples", "Isotope Ratio")
          for x in sorted(store.sample_list_means.keys()):
            # Create rolling sample chart for different sample types
            if len(store.sample_list_means[str(x)][n])>1:
              chart.AddSeries((3000 + n),"Corr. "+str(ratios[n][2])+" for group "+str(x)+".", 2,
store.sample_num_list[x], store.sample_list_means[x][n])
              chart.AddSeries((3000 + n),"2SE error per sample, group "+str(x)+".", 1,
store.sample_list_se2x[x][n], store.sample_list_se2y[x][n])
              lo = store.sample_num_list[x][0]
              hi = store.sample_num_list[x][-1]
              rollx.extend([lo,hi,nu.null,lo,hi])
              sd1hi=nu.mean(store.sample_list_means[x][n]) + (2 *
nu.stddev(store.sample_list_means[x][n]))
              sd1lo=nu.mean(store.sample_list_means[x][n]) - (2 *
nu.stddev(store.sample_list_means[x][n]))
              rollsd.extend([sd1hi,sd1hi,sd1hi,sd1lo,sd1lo])
              chart.AddSeries((3000 + n),"Group "+str(x)+" mean =
"+str(round(nu.mean(store.sample_list_means[x][n]),7))+" +/- "+str(round((2 *
nu.stddev(store.sample_list_means[x][n])),7))+" (2SD)", 1, rollx, rollsd)
              rollx=[]
              rollsd=[]

    # Plot raw cps signals for rising and falling signals sepsartely to visualise any trend and calculate
slope as ratio from all data
    chart.SetLabels((4000 + n),"Plot of raw signals for "+str(label[ratios[n][0]])+" vs.
"+str(label[ratios[n][1]])+" on a cycle by cycle basis.",str(label[ratios[n][1]])+"
cps",str(label[ratios[n][0]])+" cps")
    chart.AddSeries((4000 + n),"Raw data for rising peak (all data
shown)",2,cycle_counts_4ratios_rise[n][1],cycle_counts_4ratios_rise[n][0])
    chart.AddSeries((4000 + n),"Raw data for falling peak (all data
shown)",2,cycle_counts_4ratios_fall[n][1],cycle_counts_4ratios_fall[n][0])

    # Do initial test for zero values which would skew calculations and remove data from all cycle lists
    for y in xrange(len(cycle_counts_4ratios[n][1])):
      if cycle_counts_4ratios[n][0][y] == 0:
        raw_ratios[n].append("fail")
      elif cycle_counts_4ratios[n][1][y] == 0:
        raw_ratios[n].append("fail")
      else:
        raw_ratios[n].append(cycle_counts_4ratios[n][0][y]/cycle_counts_4ratios[n][1][y])

    # Calculate mean and SD ratio from raw cycle data
    for g in xrange(len(raw_ratios[n])):
      if raw_ratios[n][g] == "fail":
        cycle_counts_4ratios[n][1][g] = "fail"
        cycle_counts_4ratios[n][0][g] = "fail"
    raw_ratios[n][:] = [h for h in raw_ratios[n] if not h=="fail"]
    cycle_counts_4ratios[n][1][:] = [a for a in cycle_counts_4ratios[n][1] if not a=="fail"]
    cycle_counts_4ratios[n][0][:] = [a for a in cycle_counts_4ratios[n][0] if not a=="fail"]

    # Remove data that is obviously the wrong ratio (based on mean ratio of peak integrals earlier +/-
2SD)
    for a in xrange(len(cycle_counts_4ratios[n][1])):
```

```
        if abs(raw_ratios[n][a] - nu.mean(ratio_of_peak_integrals_inc[n])) > (2 *
nu.stddev(ratio_of_peak_integrals_inc[n])):
            cycle_counts_4ratios[n][1][a] = "fail"
            cycle_counts_4ratios[n][0][a] = "fail"
      cycle_counts_4ratios[n][1][:] = [a for a in cycle_counts_4ratios[n][1] if not a=="fail"]
      cycle_counts_4ratios[n][0][:] = [a for a in cycle_counts_4ratios[n][0] if not a=="fail"]

      # Calculate ratio on remaining raw cycle data
      slope = nu.slope(cycle_counts_4ratios[n][1],cycle_counts_4ratios[n][0])
      intercept = nu.int(cycle_counts_4ratios[n][1],cycle_counts_4ratios[n][0])
      try:
        correln = nu.cc(cycle_counts_4ratios[n][1],cycle_counts_4ratios[n][0])
      except:
        correln = 0.0

      chart.AddSeries((4000 + n),"After 2SD exclusions, the ratio is the slope "+str(round(slope,6))+" with
correlation coefficient
"+str(round(correln,4)),1,[0,max(cycle_counts_4ratios[n][1])],[intercept,(intercept +
(max(cycle_counts_4ratios[n][1]) * slope))])

      # Plot integrated cps for isotopes of each ratio and calculate slope which will be the ratio
      chart.SetLabels((5000 + n),"Ratio of integrated peak "+str(label[ratios[n][0]])+" and
"+str(label[ratios[n][1]]),"Integrated "+str(label[ratios[n][1]])+" peaks","Integrated
"+str(label[ratios[n][0]])+" peaks")
      chart.AddSeries((5000 + n),str(ratios[n][2])+" inclcuded
points",2,peak_integral_list_for_ratios_inc[n][1],peak_integral_list_for_ratios_inc[n][0])
      chart.AddSeries((5000 + n),str(ratios[n][2])+" excluded points from 2SD
test",2,peak_integral_list_for_ratios_exc[n][1],peak_integral_list_for_ratios_exc[n][0])

      i, fit, info =
xl.polynomialfitwc(peak_integral_list_for_ratios_inc[n][1],peak_integral_list_for_ratios_inc[n][0],peak
_integral_list_ratios_weighting[n],[0],[0],[0],2)
      calfit=xl.polynomialbar2pow(fit)
      slope=calfit[1]
      intercept=calfit[0]
      correln=nu.cc(peak_integral_list_for_ratios_inc[n][0],peak_integral_list_for_ratios_inc[n][1])

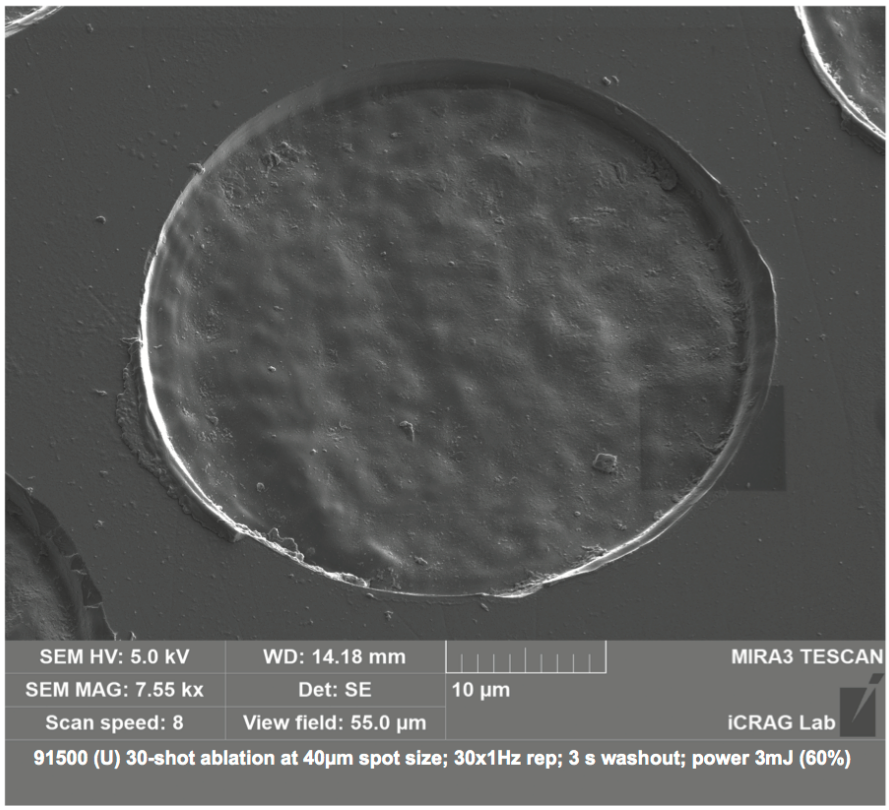
      chart.AddSeries((5000 + n),"Ratio is slope "+str(round(slope,6))+" with correlation coefficient
"+str(round(correln,4)),1,[0,max(peak_integral_list_for_ratios_inc[n][1])],[intercept,intercept +
(max(peak_integral_list_for_ratios_inc[n][1]) * slope)])

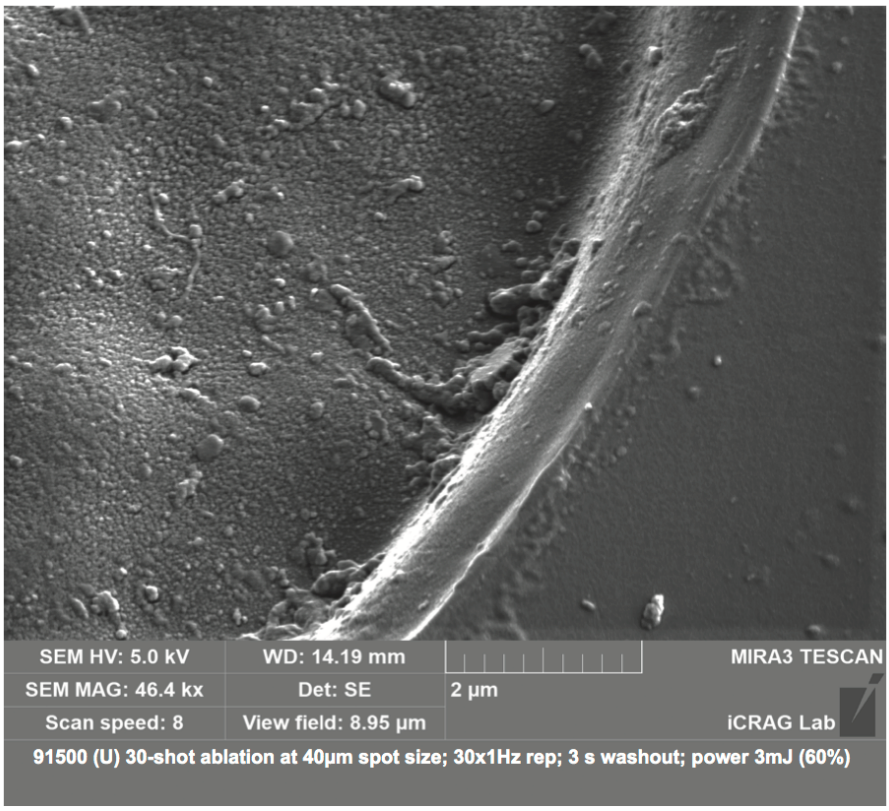
    # Reset all sample variables to starting points
    iso_sum_current_peak=[]
    peak_start_x = []
    peak_start_y = []
    peak_end_x = []
    peak_end_y = []
    iso_peak_avg_background=[]
    iso_list_background_cps=[]
    peak_integral_list_for_ratios=[]
    peak_integral_list_for_ratios_inc=[]
    peak_integral_list_for_ratios_exc=[]
    peak_integral_list_ratios_weighting=[]
    list_shots=[]
    ratio_of_peak_integrals=[]
    list_shots_inc=[]
    ratio_of_peak_integrals_inc=[]
    list_shots_exc=[]
    ratio_of_peak_integrals_exc=[]
    list_shots_sd=[]
    ratio_of_peak_integrals_sd=[]
    rollx=[]
    rollsd=[]
    box0=0
    box1=0
    cyc=0
    shot=0
```

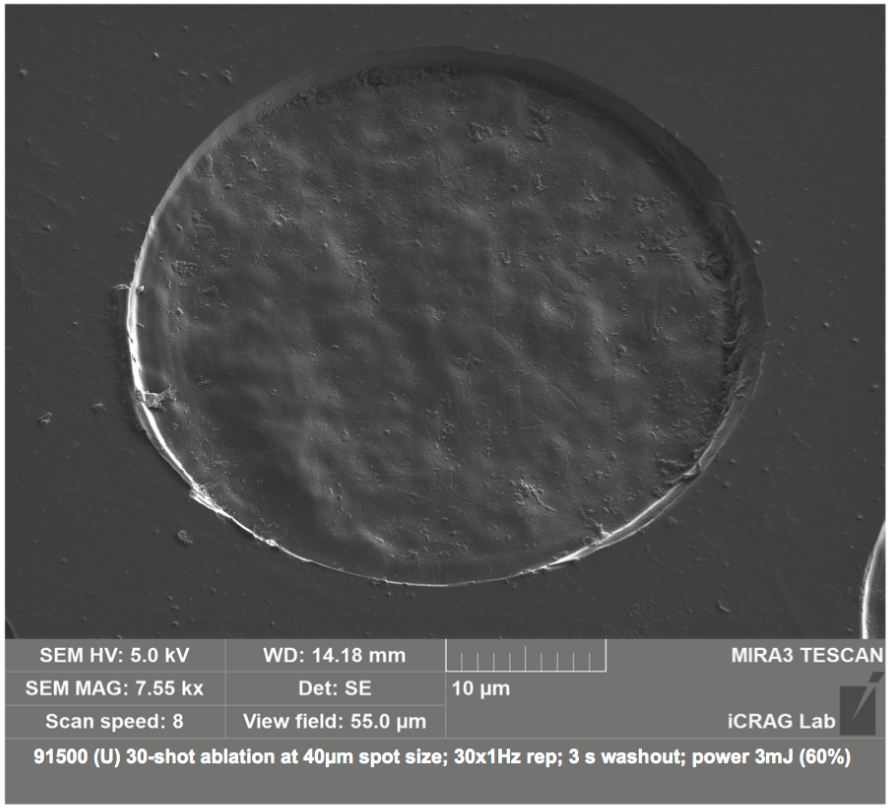
```
peak_width=0
cycle_counts_4ratios=[]
cycle_counts_4ratios_rise=[]
cycle_counts_4ratios_fall=[]
log_cycle_count=[]
log_cycle_cps=[]
ratio_cycles_weighting=[]
ratio_cycles_list=[]
iso_means=[]
peak_integrals=[]
temp_ratios=[]
for a in xrange(len(isotopes)):
   log_cycle_cps.append([])
   iso_sum_current_peak.append(0)
   iso_peak_avg_background.append(0)
   iso_list_background_cps.append([])
   peak_integrals.append(0)
for _ in xrange(len(ratios)):
   ratio_of_peak_integrals.append([])
   peak_integral_list_ratios_weighting.append([])
   list_shots_inc.append([])
   ratio_of_peak_integrals_inc.append([])
   list_shots_exc.append([])
   ratio_of_peak_integrals_exc.append([])
   list_shots_sd.append([])
   ratio_of_peak_integrals_sd.append([])
   ratio_cycles_weighting.append([])
   ratio_cycles_list.append([])
   temp_ratios.append(0)
   cycle_counts_4ratios.append([[],[]])
   cycle_counts_4ratios_rise.append([[],[]])
   cycle_counts_4ratios_fall.append([[],[]])
   peak_integral_list_for_ratios.append([[],[]])
   peak_integral_list_for_ratios_inc.append([[],[]])
   peak_integral_list_for_ratios_exc.append([[],[]])
```

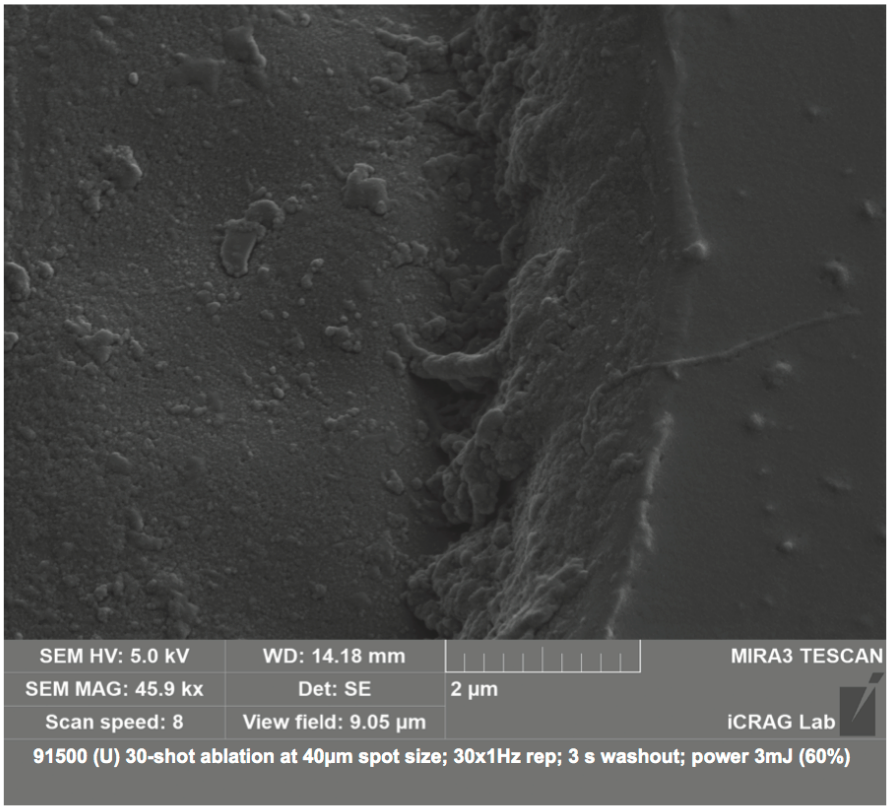
2.9.2. Supplementary SE-SEM images of crater geometries

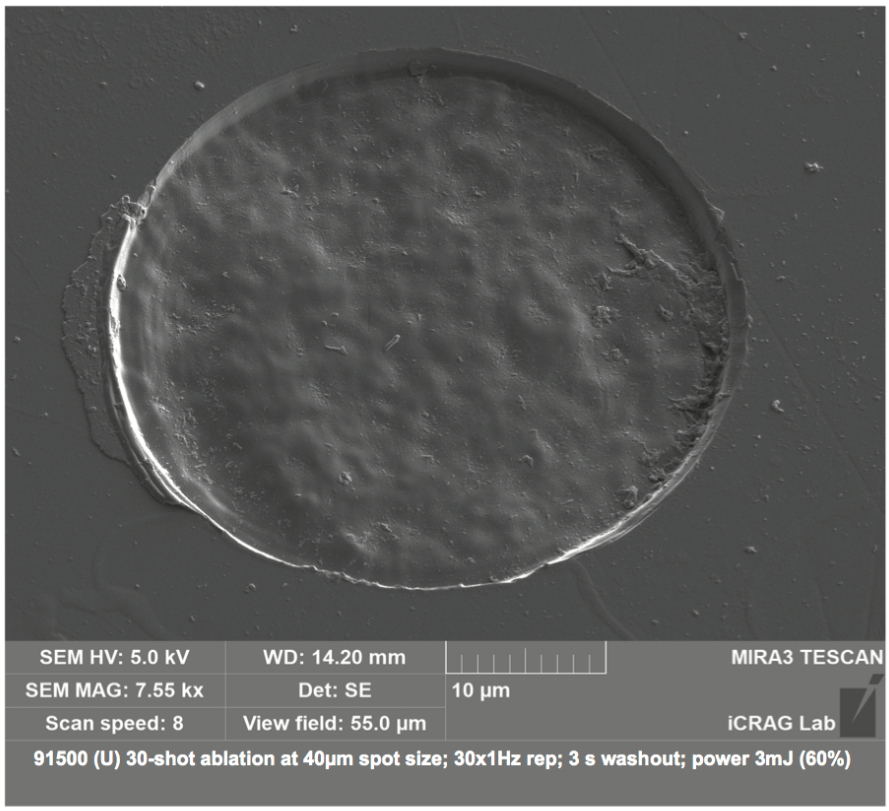
Below are several further secondary electron SEM images of both 'conventional' static high frequency ablation conducted on 91500 (U), Evidence of welding and analyte re-deposition is present. SE-SEM images of a crater generated by both 30- and 10-shot analyses on same fragment of 91500(U) and of Plešovice(U) are also included.

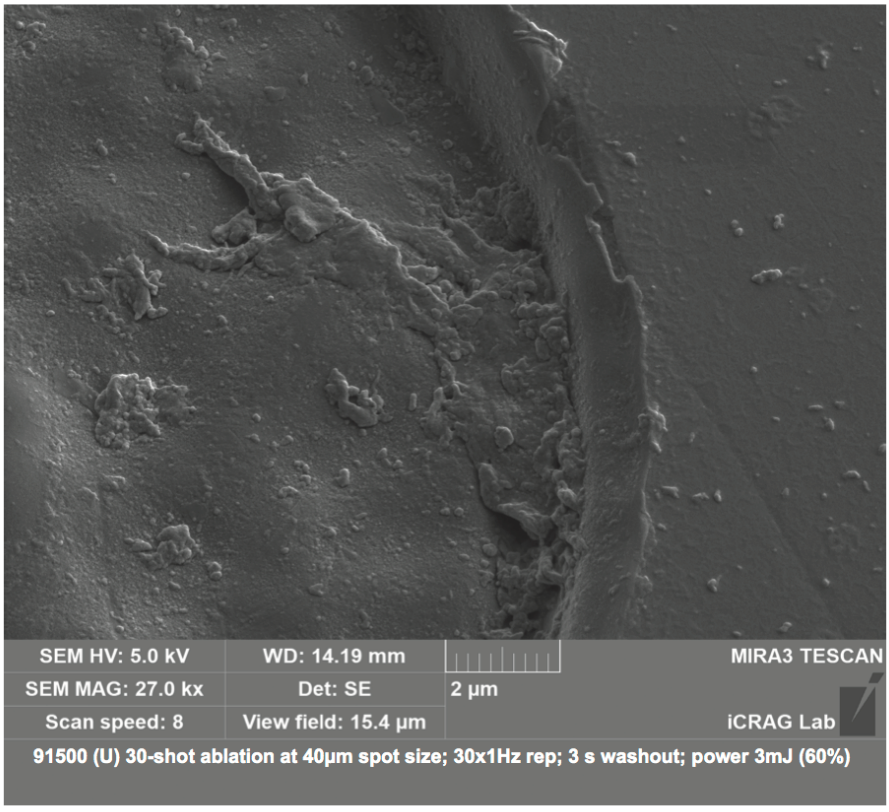

SEM HV: 5.0 kV
WD: 14.18 mm
MIRA3 TESCAN
SEM MAG: 7.55 kx
Det: SE
10 µm
Scan speed: 8
View field: 55.0 µm
iCRAG Lab
91500 (U) 30-shot ablation at 40µm spot size; 30x1Hz rep; 3 s washout; power 3mJ (60%)

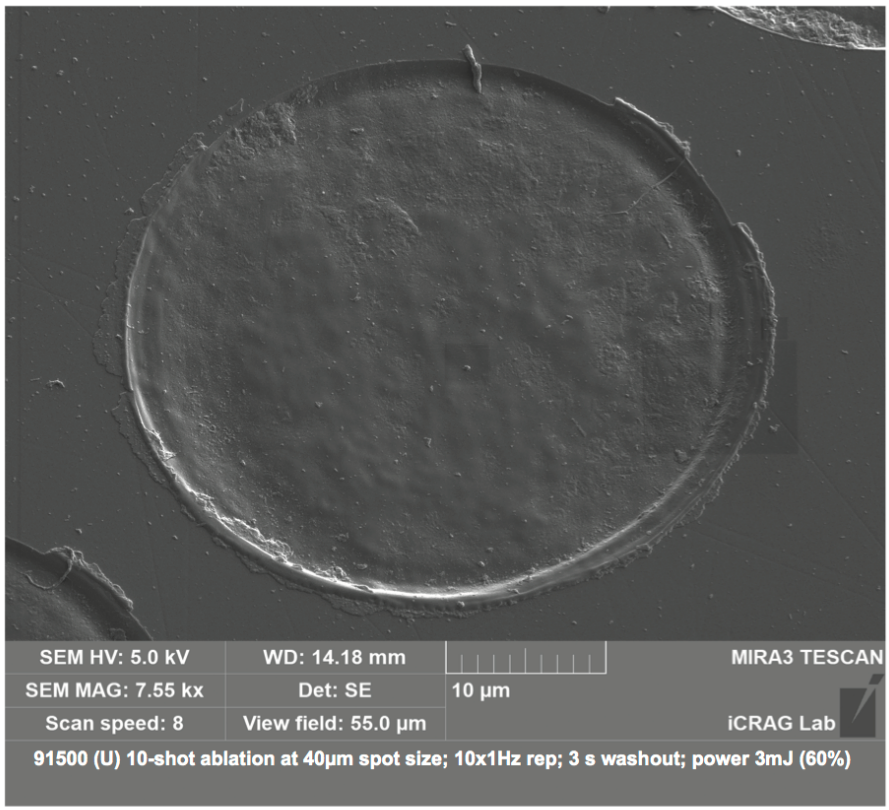

SEM HV: 5.0 kV
WD: 14.19 mm
MIRA3 TESCAN
SEM MAG: 46.4 kx
Det: SE
2 µm
Scan speed: 8
View field: 8.95 µm
iCRAG Lab
91500 (U) 30-shot ablation at 40µm spot size; 30x1Hz rep; 3 s washout; power 3mJ (60%)

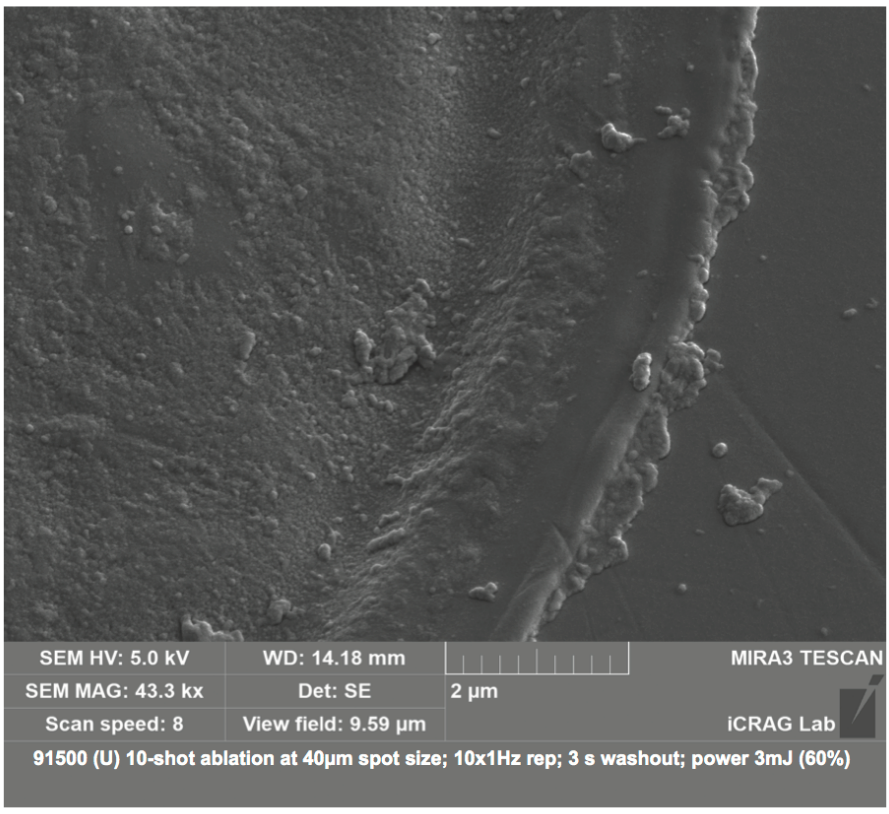

SEM HV: 5.0 kV
WD: 14.18 mm
MIRA3 TESCAN
SEM MAG: 7.55 kx
Det: SE
10 µm
Scan speed: 8
View field: 55.0 µm
iCRAG Lab
91500 (U) 30-shot ablation at 40µm spot size; 30x1Hz rep; 3 s washout; power 3mJ (60%)

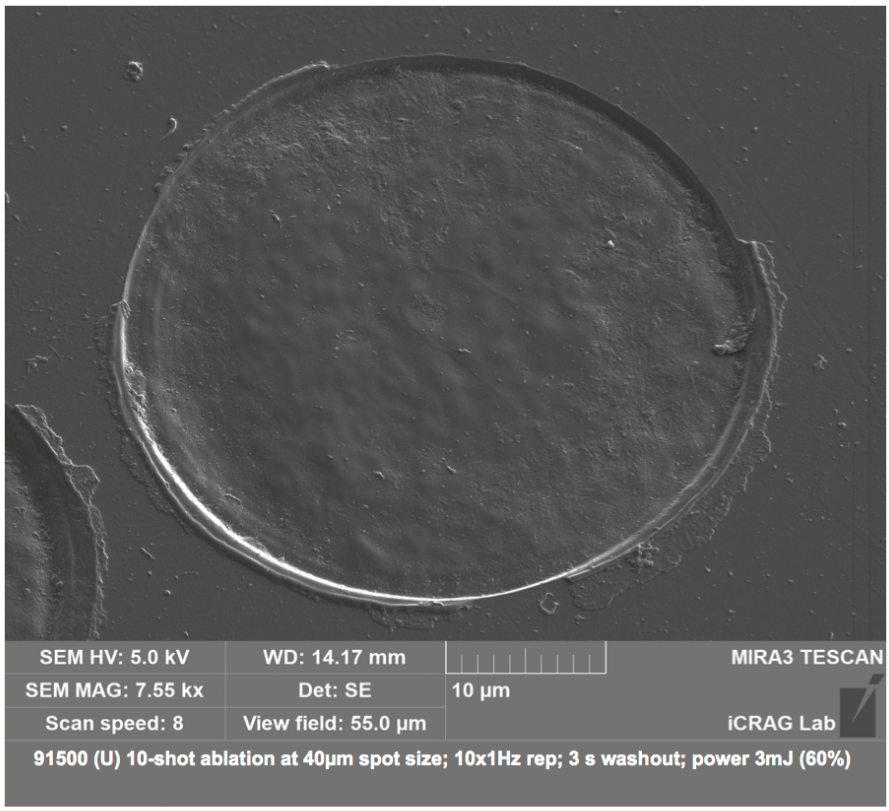

SEM HV: 5.0 kV
WD: 14.18 mm
MIRA3 TESCAN
SEM MAG: 45.9 kx
Det: SE
2 µm
Scan speed: 8
View field: 9.05 µm
iCRAG Lab
91500 (U) 30-shot ablation at 40µm spot size; 30x1Hz rep; 3 s washout; power 3mJ (60%)

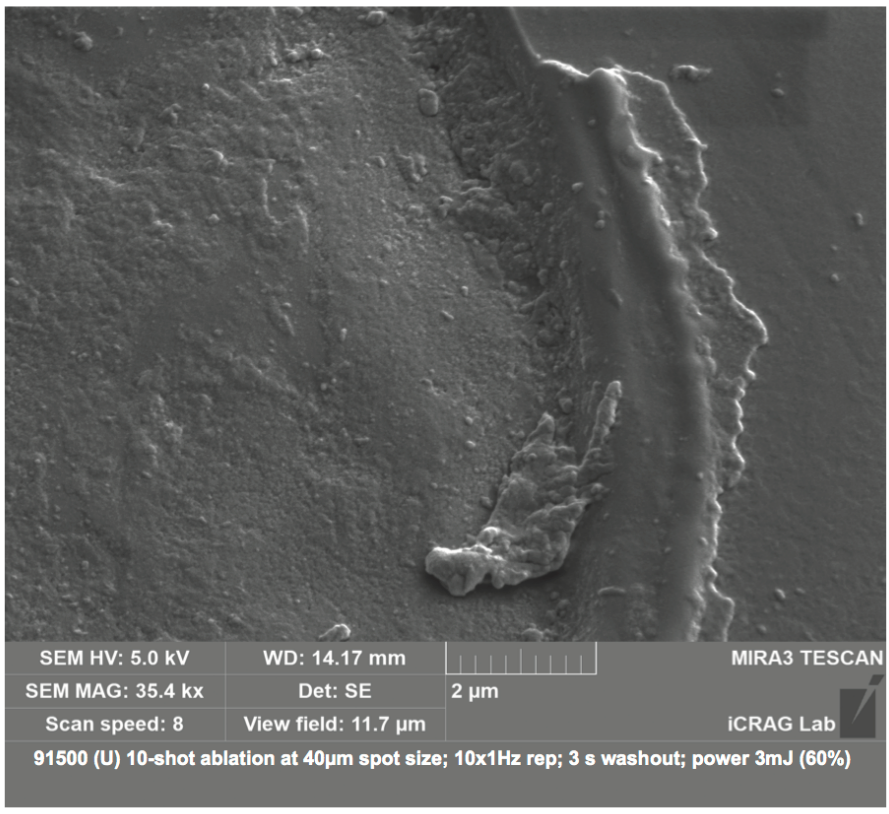

SEM HV: 5.0 kV
WD: 14.20 mm
MIRA3 TESCAN
SEM MAG: 7.55 kx
Det: SE
10 µm
Scan speed: 8
View field: 55.0 µm
iCRAG Lab
91500 (U) 30-shot ablation at 40µm spot size; 30x1Hz rep; 3 s washout; power 3mJ (60%)

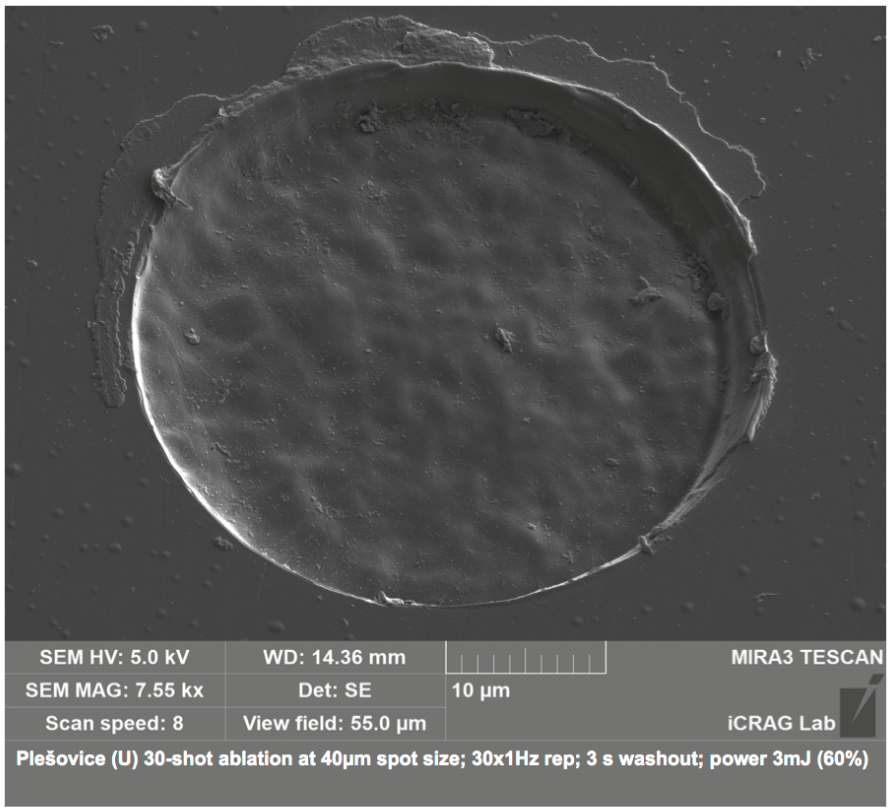

SEM HV: 5.0 kV
WD: 14.19 mm
MIRA3 TESCAN
SEM MAG: 27.0 kx
Det: SE
2 µm
Scan speed: 8
View field: 15.4 µm
iCRAG Lab
91500 (U) 30-shot ablation at 40µm spot size; 30x1Hz rep; 3 s washout; power 3mJ (60%)

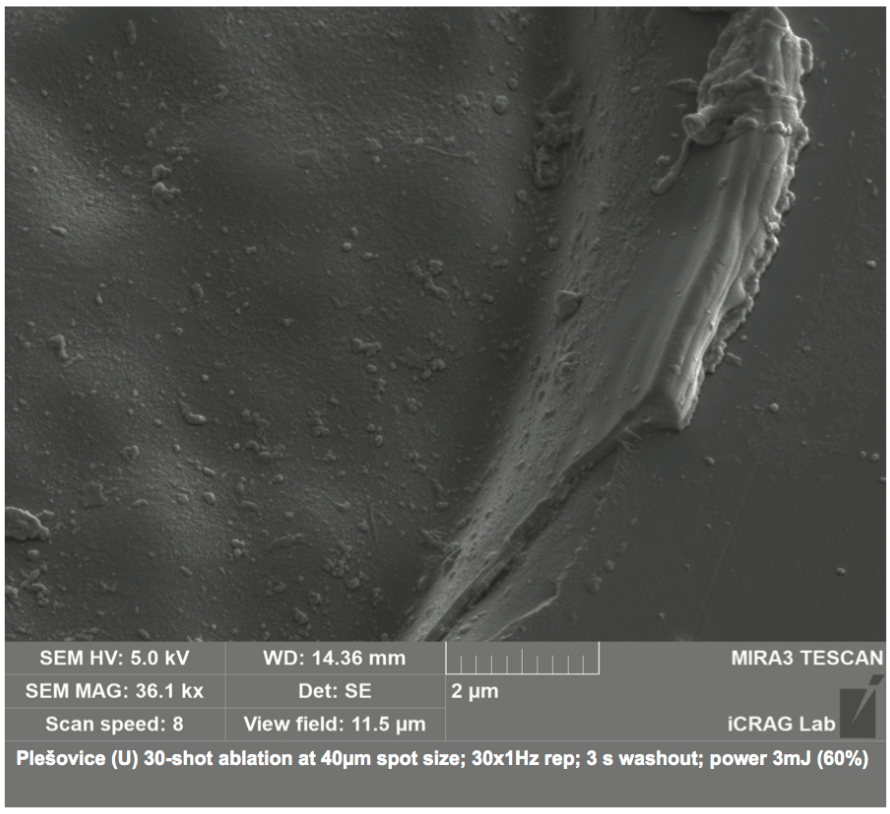

SEM HV: 5.0 kV
WD: 14.18 mm
MIRA3 TESCAN
SEM MAG: 7.55 kx
Det: SE
10 µm
Scan speed: 8
View field: 55.0 µm
iCRAG Lab
91500 (U) 10-shot ablation at 40µm spot size; 10x1Hz rep; 3 s washout; power 3mJ (60%)

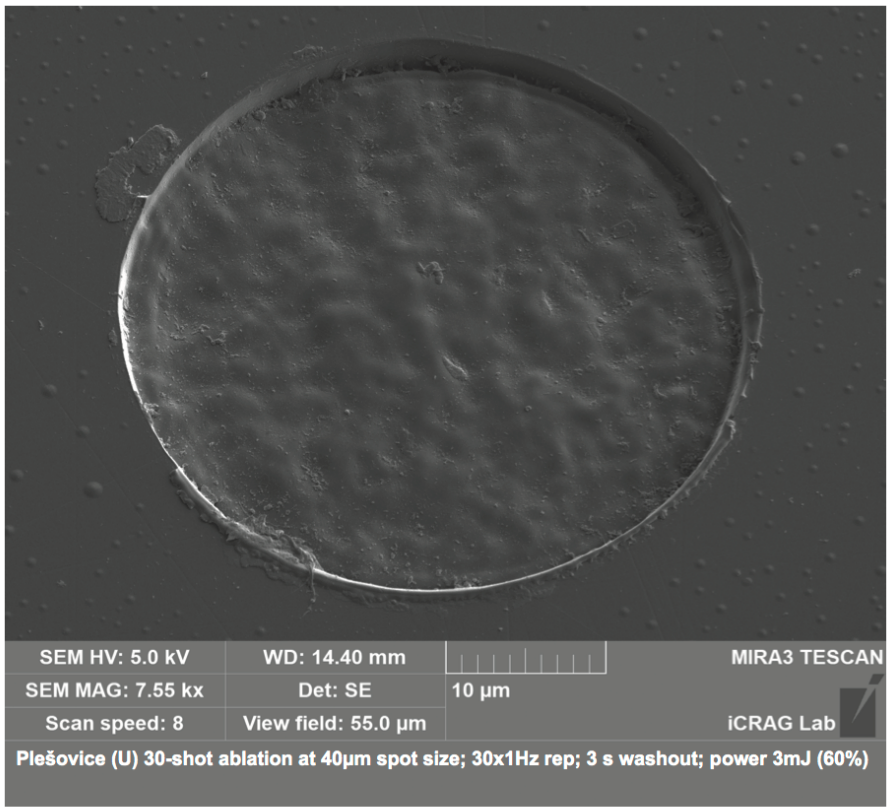

SEM HV: 5.0 kV
WD: 14.18 mm
MIRA3 TESCAN
SEM MAG: 43.3 kx
Det: SE
2 µm
Scan speed: 8
View field: 9.59 µm
iCRAG Lab
91500 (U) 10-shot ablation at 40µm spot size; 10x1Hz rep; 3 s washout; power 3mJ (60%)

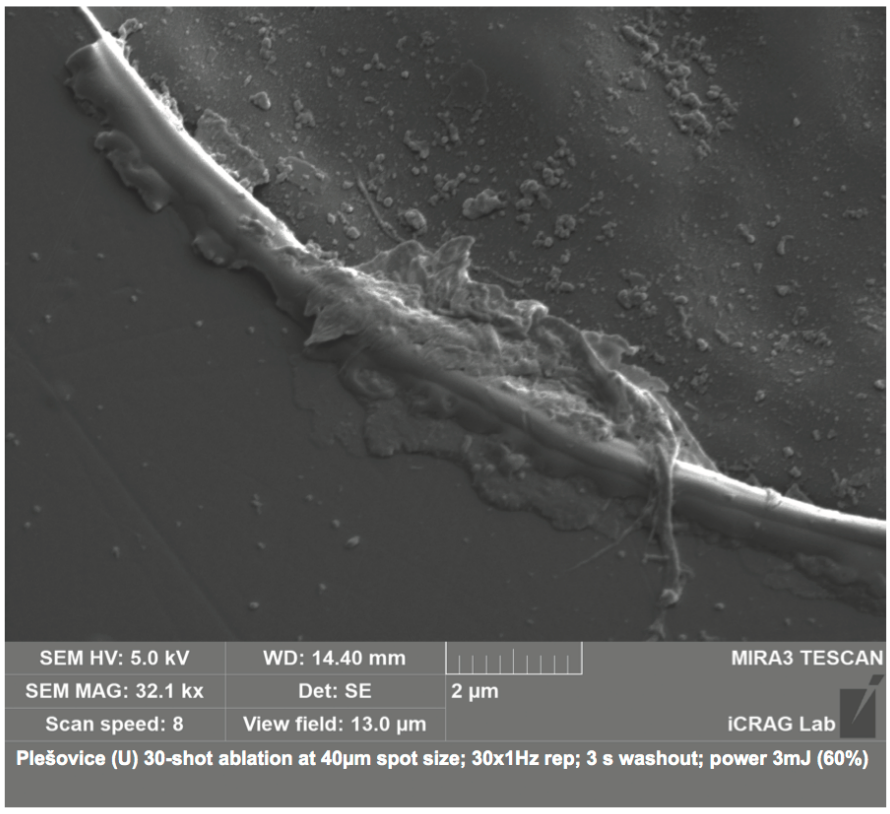

SEM HV: 5.0 kV
WD: 14.17 mm
MIRA3 TESCAN
SEM MAG: 7.55 kx
Det: SE
10 µm
Scan speed: 8
View field: 55.0 µm
iCRAG Lab
91500 (U) 10-shot ablation at 40µm spot size; 10x1Hz rep; 3 s washout; power 3mJ (60%)

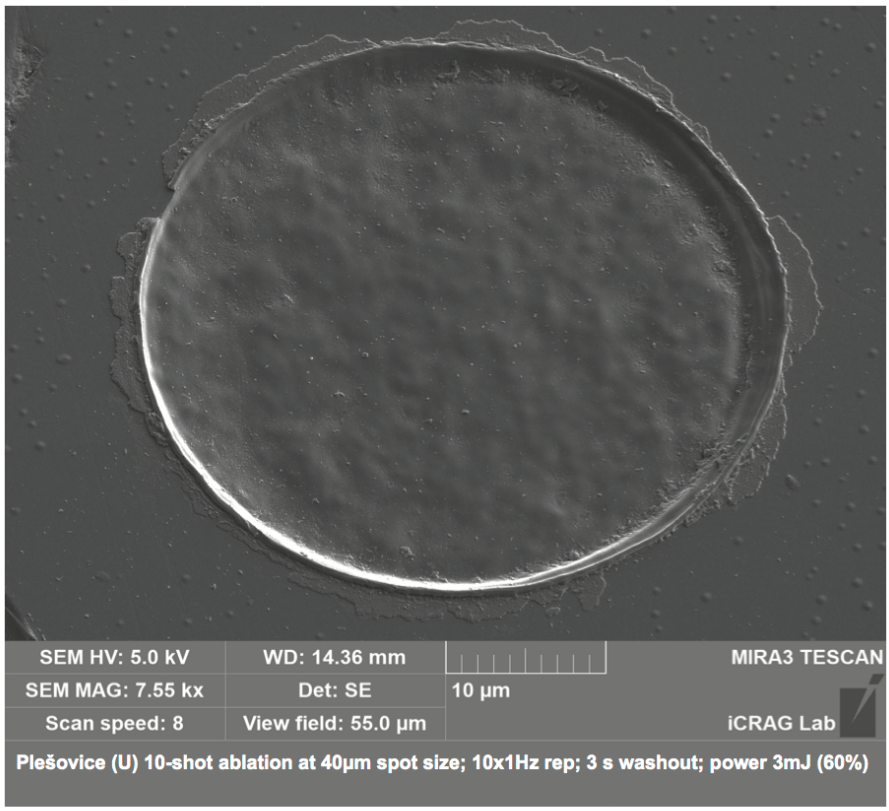

SEM HV: 5.0 kV
WD: 14.17 mm
MIRA3 TESCAN
SEM MAG: 35.4 kx
Det: SE
2 µm
Scan speed: 8
View field: 11.7 µm
iCRAG Lab
91500 (U) 10-shot ablation at 40µm spot size; 10x1Hz rep; 3 s washout; power 3mJ (60%)

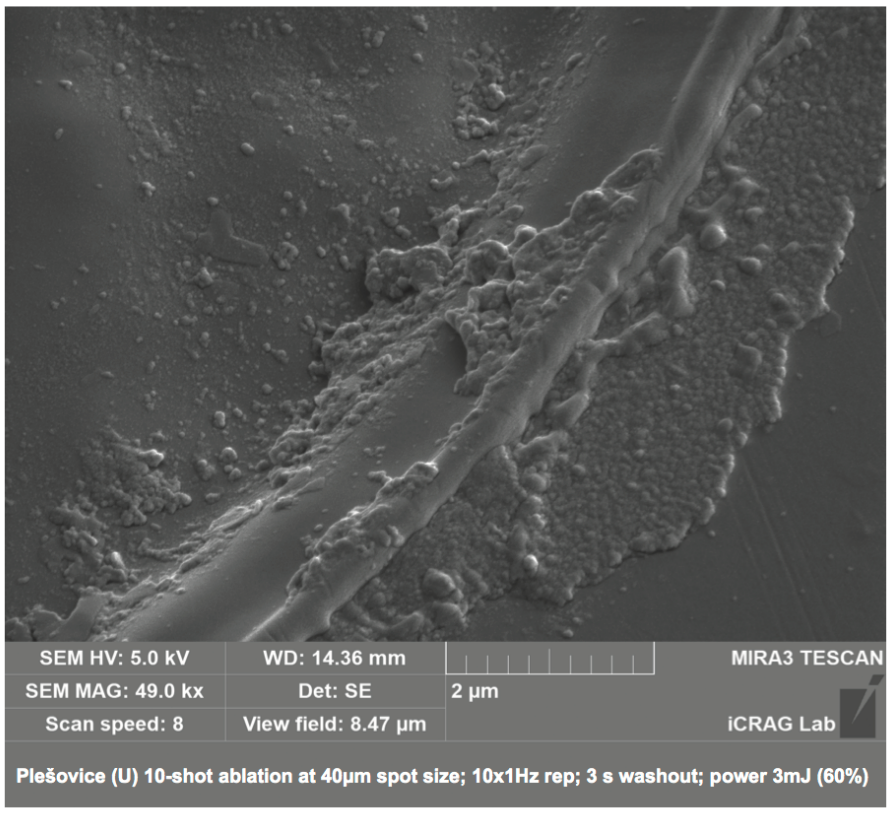

SEM HV: 5.0 kV
WD: 14.36 mm
MIRA3 TESCAN
SEM MAG: 7.55 kx
Det: SE
10 µm
Scan speed: 8
View field: 55.0 µm
iCRAG Lab
Plešovice (U) 30-shot ablation at 40µm spot size; 30x1Hz rep; 3 s washout; power 3mJ (60%)

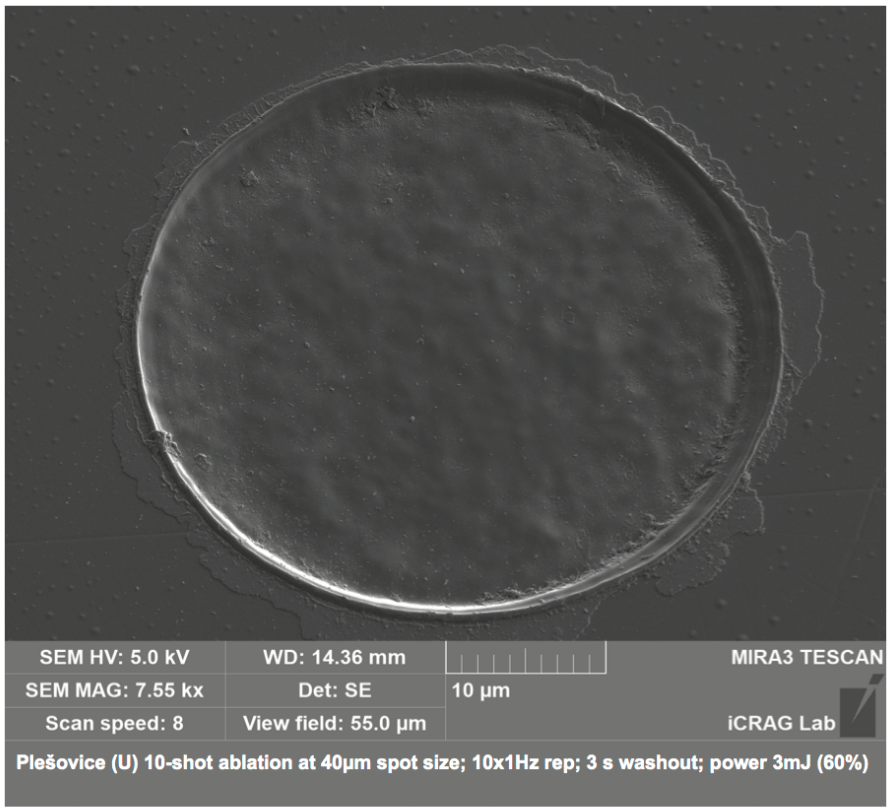

SEM HV: 5.0 kV
WD: 14.36 mm
MIRA3 TESCAN
SEM MAG: 36.1 kx
Det: SE
2 µm
Scan speed: 8
View field: 11.5 µm
iCRAG Lab
Plešovice (U) 30-shot ablation at 40µm spot size; 30x1Hz rep; 3 s washout; power 3mJ (60%)

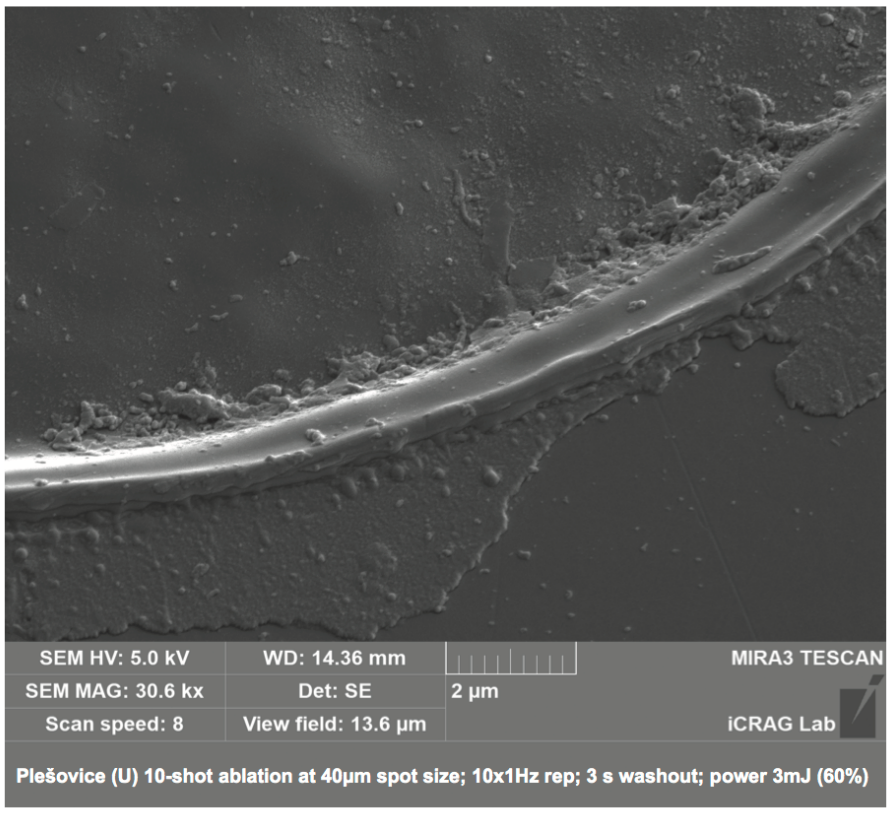

SEM HV: 5.0 kV
WD: 14.40 mm
MIRA3 TESCAN
SEM MAG: 7.55 kx
Det: SE
10 µm
Scan speed: 8
View field: 55.0 µm
iCRAG Lab
Plešovice (U) 30-shot ablation at 40µm spot size; 30x1Hz rep; 3 s washout; power 3mJ (60%)

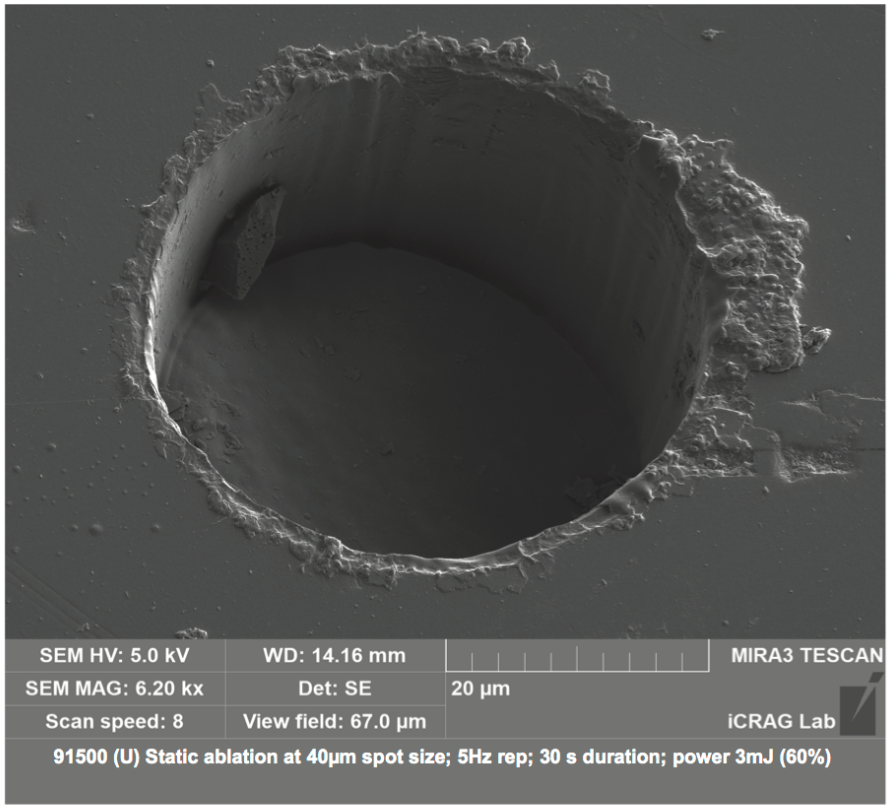

SEM HV: 5.0 kV
WD: 14.40 mm
MIRA3 TESCAN
SEM MAG: 32.1 kx
Det: SE
2 µm
Scan speed: 8
View field: 13.0 µm
iCRAG Lab
Plešovice (U) 30-shot ablation at 40µm spot size; 30x1Hz rep; 3 s washout; power 3mJ (60%)

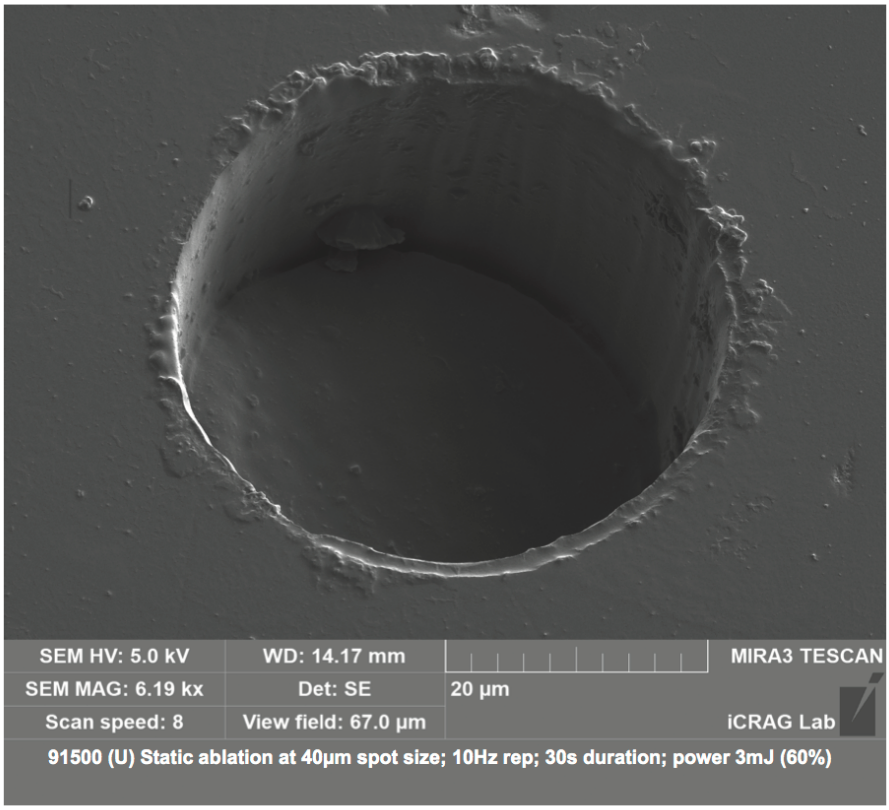

SEM HV: 5.0 kV
WD: 14.36 mm
MIRA3 TESCAN
SEM MAG: 7.55 kx
Det: SE
10 µm
Scan speed: 8
View field: 55.0 µm
iCRAG Lab
Plešovice (U) 10-shot ablation at 40µm spot size; 10x1Hz rep; 3 s washout; power 3mJ (60%)

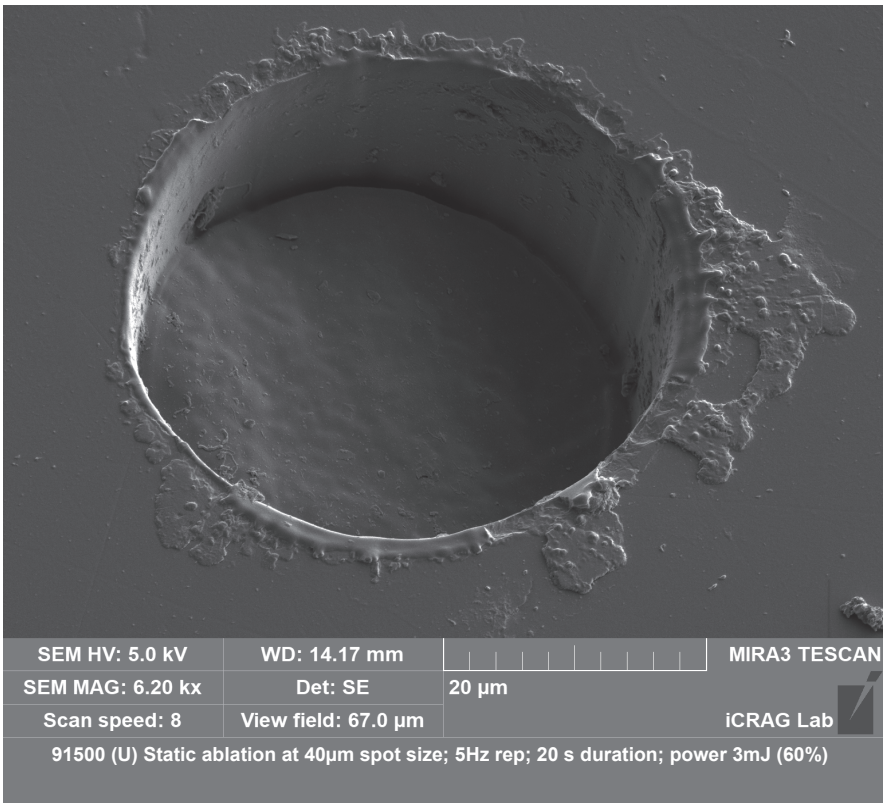

SEM HV: 5.0 kV
WD: 14.36 mm
MIRA3 TESCAN
SEM MAG: 49.0 kx
Det: SE
2 µm
Scan speed: 8
View field: 8.47 µm
iCRAG Lab
Plešovice (U) 10-shot ablation at 40µm spot size; 10x1Hz rep; 3 s washout; power 3mJ (60%)

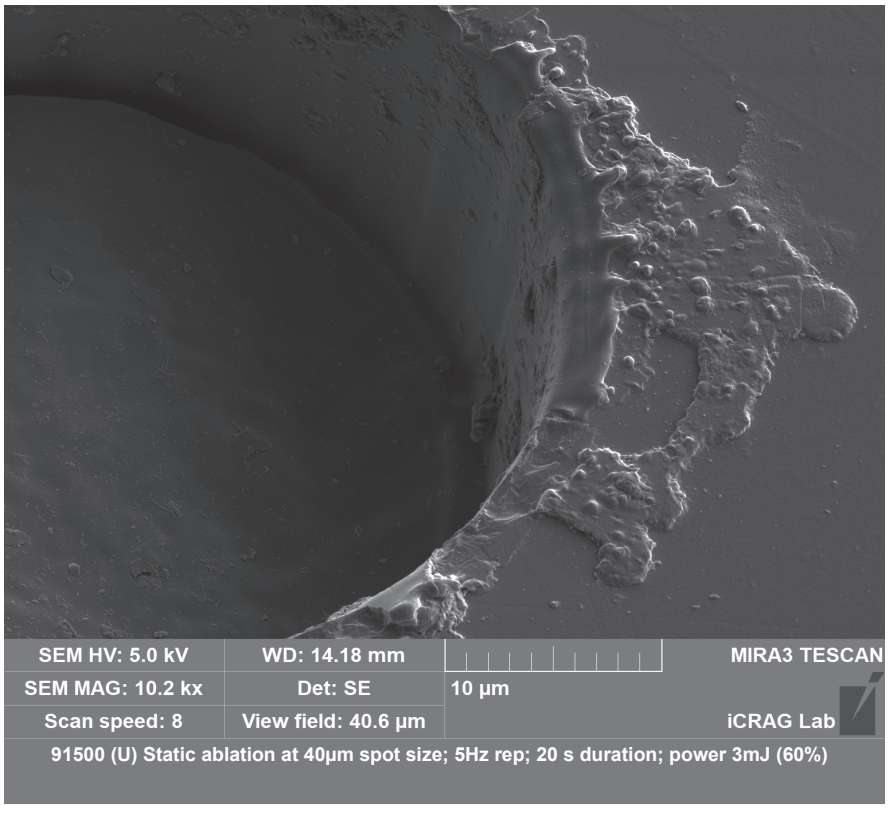

SEM HV: 5.0 kV
WD: 14.36 mm
MIRA3 TESCAN
SEM MAG: 7.55 kx
Det: SE
10 µm
Scan speed: 8
View field: 55.0 µm
iCRAG Lab
Plešovice (U) 10-shot ablation at 40µm spot size; 10x1Hz rep; 3 s washout; power 3mJ (60%)

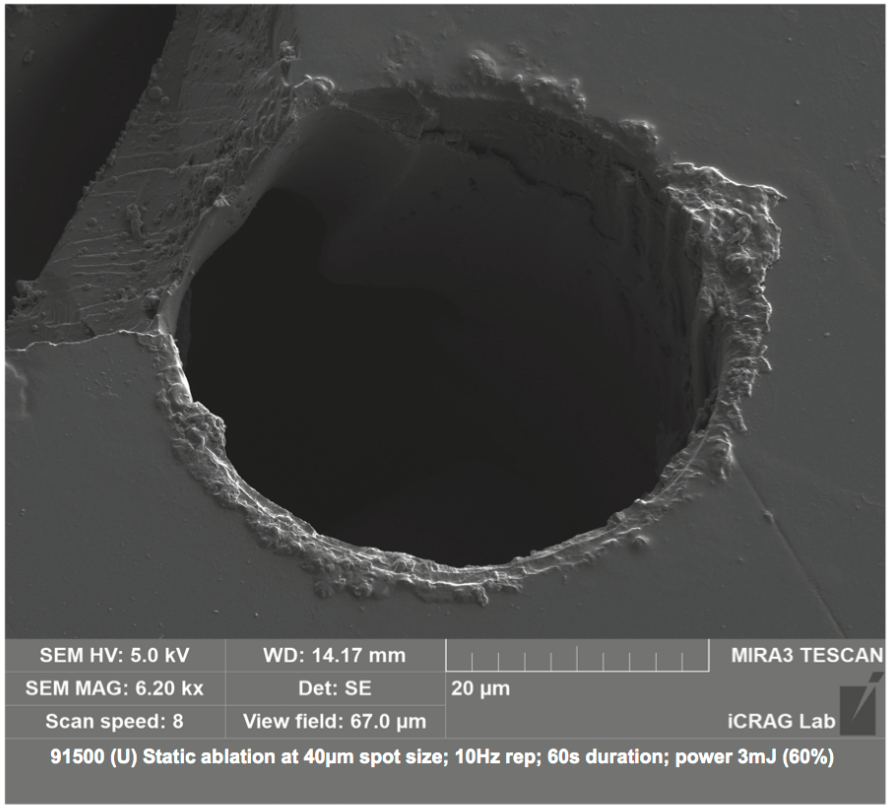

SEM HV: 5.0 kV
WD: 14.36 mm
MIRA3 TESCAN
SEM MAG: 30.6 kx
Det: SE
2 µm
Scan speed: 8
View field: 13.6 µm
iCRAG Lab
Plešovice (U) 10-shot ablation at 40µm spot size; 10x1Hz rep; 3 s washout; power 3mJ (60%)


SEM HV: 5.0 kV
WD: 14.16 mm
MIRA3 TESCAN
SEM MAG: 6.20 kx
Det: SE
20 µm
Scan speed: 8
View field: 67.0 µm
iCRAG Lab
91500 (U) Static ablation at 40µm spot size; 5Hz rep; 30 s duration; power 3mJ (60%)


SEM HV: 5.0 kV
WD: 14.17 mm
MIRA3 TESCAN
SEM MAG: 6.19 kx
Det: SE
20 µm
Scan speed: 8
View field: 67.0 µm
iCRAG Lab
91500 (U) Static ablation at 40µm spot size; 10Hz rep; 30s duration; power 3mJ (60%)


SEM HV: 5.0 kV
WD: 14.17 mm
MIRA3 TESCAN
SEM MAG: 6.20 kx
Det: SE
20 µm
Scan speed: 8
View field: 67.0 µm
iCRAG Lab
91500 (U) Static ablation at 40µm spot size; 5Hz rep; 20 s duration; power 3mJ (60%)


SEM HV: 5.0 kV
WD: 14.18 mm
MIRA3 TESCAN
SEM MAG: 10.2 kx
Det: SE
10 µm
Scan speed: 8
View field: 40.6 µm
iCRAG Lab
91500 (U) Static ablation at 40µm spot size; 5Hz rep; 20 s duration; power 3mJ (60%)


SEM HV: 5.0 kV
WD: 14.17 mm
MIRA3 TESCAN
SEM MAG: 6.20 kx
Det: SE
20 µm
Scan speed: 8
View field: 67.0 µm
iCRAG Lab
91500 (U) Static ablation at 40µm spot size; 10Hz rep; 60s duration; power 3mJ (60%)

CHAPTER 3

Effective optical opacity and radiation damage in zircon; matrix dependent controls on U-Pb LA-ICP-MS

Prepared for submission to the *Journal of Analytical Atomic Spectrometry (JAAS)*.

Co-authors: [1]Christoph Lenz, [2]Brendan C. Hoare, [2]Foteini Drakou and [2]Quentin G. Crowley

[1.] Macquarie University, Australia
[2.] Trinity College Dublin, Ireland

3.1. ABSTRACT

The actinide concentration, thermal, and alteration history experienced by zircon governs its present day expression of radiation damage. The degree of radiation damage influences physical, thermo-physical and optical properties of zircon and consequently contributes to the coupling efficiency of laser-zircon during laser ablation inductively coupled plasma mass spectrometric (LA-ICP-MS) analysis. In this study, a single Plešovice zircon crystal was cut and prepared as two mirrored halves, with one half subjected to an artificial annealing process at ~1100˚C for 96 h. Comparison of chemically analogous ablated locations between annealed and untreated crystal halves reveals differential ablation behaviour and non-stoichiometric U-Pb sampling, resulting in a systematic apparent younging of the damage free annealed half from the accepted age by ~22 Ma (i.e. 6.7%). The mean particle size fraction of ablated material increases in the annealed sample matrix, which is devoid of radiation damage defects. As a result, it is proposed that a greater density of structural defects accrued as a result of self-irradiation in zircon act as colour/absorption centres, aiding laser coupling. We posit that mean particle size of ablated material, and crater geometry are principally governed by the effective optical opacity and thermo-physical properties for a given laser wavelength. Optical opacity and thermal conductivity of a given matrix may be intrinsic factors for laser sampling, which contribute towards the U-Pb age biases observed between LA-ICP-MS and benchmark thermal ionisation mass spectrometric (TIMS) techniques.

3.2. INTRODUCTION

Laser ablation ICP-MS is a commonly used analytical technique for age determination applied to geosciences (Cocherie and Robert, 2008 and references therein). Laser sampling of crystalline material should ideally generate a constant volume of analyte material during the course of ablation, sampling a reproducible number of free atoms available for excitation within the plasma source with each pulse (Mank and Mason, 1999). However, in reality, slight variations in optical and thermo-physical properties within and between zircons, may exert a large degree of control over the amount of material removed by each laser pulse, as well as the particulate composition of the emission products of ablation. These variations are thought to lead to phenomena broadly termed 'matrix effects' which can significantly impact the accuracy of U-Pb dating (Marillo-Sialer et al., 2014; Allen and Campbell, 2012; Klötzli et al., 2009; Black et al., 2004). Various authors have suggested that high accumulated radiation damage is correlated with an improvement in ablation efficiency and an apparent systematic increase in U-Pb age when compared to annealed examples (Wiemer et al., 2017; Marillo-Sialer et al. 2014; Steely et al., 2014; Allen and Campbell, 2012). Contrastingly a detailed comparison of U-Pb age determinations made by laser ablation inductively coupled plasma mass-spectrometry (LA-ICP-MS) from Lenz et al. (2020) observed contradictory behaviour between several samples (of different geological origin) in respect of the relationship between $^{206}Pb/^{238}U$ age and the quantity of radiation damage present. Lenz et al. (2020) carried out a comparison of U-Pb age determinations on damage-free annealed halves, in which some samples revealed a systematic bias in age determinations towards older apparent ages made relative to their untreated counterpart halves (i.e. Sri Lankan sample; SL1-U). Such contradictory behaviour suggests that the interaction of incident laser radiation is strongly influenced by the radical physical, mechanical and optical transformation of a target zircon substrate following artificial heat treatment.

Laser-matter interactions with natural substrates are inherently complex. The degree of lattice disorder as a result of accrued radiation damage may vary considerably in natural samples owing to differing initial actinide concentrations, age, thermal and/or alteration histories (Allen and Campbell, 2012). U-Pb age determinations made using LA-ICP-MS has, throughout its history of use, been systematically at variance to the 'benchmark' isotope-dilution thermal ionisation mass spectrometry (ID-TIMS) method in terms of accuracy (by about 2%) (Horstwood et al. 2016) owing to the fundamentally different mechanism of ion generation inherent to each technique. LA-ICP-MS commonly employs the use of an external reference material (of known, independently verified age) incorporated at intervals throughout an analytical session so as to monitor and correct for mass bias and instrumental drift and can also be utilised for downhole fractionation correction where necessary (Horstwood et al., 2016; Marillo-Sialer et al., 2014). Unknowns and standards are assumed for this purpose to behave analogously with respect to incident laser radiation (i.e. to be matrix matched). In practice, laser-matter interactions are largely unpredictable especially when targeting uncharacterised and often internally complex natural zircon, with potentially very different formational, thermal and alteration histories. The variable manner with which both unknown samples and external standard zircon targets respond during laser sampling is thought to constitute a significant contribution towards the systematic bias observed between LA-ICP-MS and ID-TIMS techniques (Marillo-Sialer et al. 2014; Allen & Campbell 2012; Klötzli et al. 2009).

By studying equivalent locations across structurally modified halves of the same sample, it is possible to assess the cause(s) of the observed systematic biases in U-Pb age determination, independently of variables

including formation, composition and/or differing geological histories in so far as possible. A comparison of structural order between the untreated and annealed matrixes is made by way of photoluminescence (PL), cathodoluminescence (CL) and back-scattered electron (BSE) imaging. Relative differences in ablation behaviour are assessed both by a direct characterisation of crater geometry by optical white light interferometry (WLI) imaging and indirectly by virtue of elemental fractionation behaviour. Observations made herein are also applicable to natural samples having variable structural order and further our understanding of the age bias due to laser sampling.

3.3. EXPERIMENTAL

3.3.1. Sample Preparation

Plešovice (Sláma et al., 2008) is a widely used zircon natural reference material for matrix-matched calibration of LA-ICP-MS analysis, relatedly therefore it is also well-characterised in respect of age (e.g. Chew et al., 2019, 2017; Crowley et al., 2014; Marillo-Sialer et al., 2014; Nasdala et al., 2008). It is typified by concordant U-Pb ages, with a weighted mean $^{206}Pb/^{238}U$ age of 337.13 ± 0.37 Ma which is homogenous at scale appropriate to U-Pb LA-ICP-MS, despite trace element variation across primary growth zones (Sláma et al., 2008). A proportion of grains are also known to contain actinide-rich domains with correspondingly high levels of metamictisation (see Fig. 3.1d). Two principal morphological types are identified for Plešovice; a prevailing equant morphology and a less common prismatic form (Sláma et al., 2008). The sample analysed herein belongs to the latter morphological type being a dark brown-orange (see Fig. 3.1c), euhedral crystal of roughly 5 mm in length. It was cut in half perpendicular to its c-axis dimension in a manner similar to that described in both Nasdala et al. (2006) and Lenz et al. (2020), using a diamond impregnated stainless-steel wire saw (WELL Precision Vertical Diamond Saw 3242). Material lost to the cutting process were minimised by utilising a thin diameter wire (with an effective kerf width of 230 μm). One half underwent heat treatment in air at ~1100°C for 96 h whilst its counterpart remained untreated. A subset of 91500 zircon was also subjected to an identical annealing procedure for use as a primary reference material during analysis.

Both halves of the Plešovice crystal were subjected to several rounds of sonication and rinsing prior to being dried and mounted in close proximity in a two-part epoxy resin mount. Glass beads of a known diameter (1 ± 0.02 mm) were included alongside both halves to monitor the depth of polishing necessary to expose the crystal interiors. Approximately 300 μm of material was removed uniformly from the surface of the mount using a Struers LaboPol 21 automated polisher using 6 μm and then 1 μm diamond suspension fluids. Grain halves prepared in this manner are intended to reflect broadly analogous internal texture and chemical compositions, but contrast significantly with respect to their relative structural order.

3.3.2. Instrumentation

The mount containing both the annealed and untreated halves of the Plešovice zircon was cleaned and dried before receiving a ~12 nm-thick layer of carbon coating prior to back-scattered electron (BSE) and cathodoluminescence (CL) imaging using a TESCAN TIGER MIRA3 variable pressure field-emission scanning electron microscope (FE-SEM) at the iCRAG lab, Trinity College Dublin. An accelerating voltage of 15 kV and 10 kV were used for

BSE and CL, respectively. The carbon coat was removed prior to LA-ICP-MS using ethanol and a lint-free wipe.

A confocal, dispersive LabRam Evolution HR800 spectrometer was used for Raman and laser-induced steady-state photoluminescence (PL) spectroscopic measurements, following Lenz et al. (2020). The method is non-destructive and involves the excitation of rare-earth elements (REE) by use of a blue laser (λ = 473 nm), typically resulting in the emission spectral bands identified for a multitude of trace REEs substituted in the crystal structure, the bands associated with Dy^{3+} and Sm^{3+} in the green-yellow spectral range being the most intense. Any given band in a well-ordered zircon structure is constituted of distinctive, narrow crystal-field split sub-level bands whose emission may be easily identified especially for Dy^{3+}. As radiation damage accumulates, these narrow bands become progressively broader and diminish in intensity. A high accumulation of amorphous domains results in the superposition of PL emissions from an elevated number of Dy^{3+} ions in structurally altered sites with respect to ions in unaffected remnant crystalline domains. Deconvolution of the spectral component of the amorphous domains allows for a reasonable estimate of the amorphous fraction (AF%) to be mapped over the zircon polished sample surface at high-resolution. Note, that the deconvolution procedure used here follows a classic least square (CLS) fitting by using reference components/loadings (see details in Lenz et al. 2020).

LA-ICP-MS analyses were performed using a Photon Machines Analyte Excite 193 nm ArF excimer laser-ablation system with a Helex 2-volume ablation cell coupled to an Agilent 7900 ICP-MS via an aerosol rapid introduction system (ARIS) at the Department of Geology, Trinity College Dublin. Prior to sample analysis, the ICP-MS was tuned using NIST612 standard glass to yield Th/U ratios of unity and Th oxide production rates of << 1% (see Table 3.1 for further details). Ablations took place in a 100% He atmosphere of the 2-volume cell design, wherein a 0.25 l min^{-1} He sweep gas flow was maintained at the site of ablation within the small volume sampling 'cup' and at 0.15 l min^{-1} within the sample chamber. Combined with the high washout efficiency of the sample cell design, a washout interval of 10 s allowed for a complete restoration of baseline level signals between analyses.

The He sweep gas was combined with a minor constituent of N_2 (11 ml min^{-1}) via a 'T-piece' within the ARIS adapter before entering an in-house signal smoothing device, where it is mixed with an auxiliary gas flow comprising Ar (0.65 l min^{-1}) prior to entering the plasma torch. Further details of this introduction procedure is outlined by Chew et al., (2019). The addition of N_2 enhances signal sensitivity and reduces oxide formation (Chew et al., 2019, 2017). Ten isotopes (^{31}P, ^{49}Ti, ^{57}Fe, ^{91}Zr, ^{204}Pb, ^{206}Pb, ^{207}Pb, ^{208}Pb, ^{232}Th, ^{238}U) were analysed with a total duty cycle of 932 ms. Isotopes and elements beyond those necessary for age determinations were also measured, to monitor for inclusions and/or contamination hosted in secondary structures (i.e. fractures etc.) not readily detectable on the sample surface. LA-ICP-MS analytical set-up and operating parameters are summarised in Table 3.1.

Analytical spots were arranged in a 'grid-of-spots' pattern totalling 63 spots, with the location of each spot mapped in space directly across from its counterpart so as to produce a mirror image. An area which demonstrated a high degree of variation with respect to radiation damage (as observed in the PL maps) on the untreated half, was used to locate the sampling grid. An effort was made to locate analytical spots in direct equivalency across both halves, which required the removal of the sample chamber and a subtle realignment of the sample mount within the sample chamber before the commencement of further analyses in a second

experimental session. A line raster on NIST612 standard glass was run to provide and internal check on plasma conditions to ensure similar sensitivity and oxide production were maintained between both analytical sessions. In addition, the reproducibility of $^{206}Pb/^{238}U$ age results were monitored by way of an untreated in-house secondary standard WRS-1348, to ascertain whether any drift in plasma performance occurred between the two sessions.

An intentional effort was made to amplify the effects of downhole elemental fractionation where they might occur between annealed and untreated samples. As such, a narrower circular spot of a 24 μm diameter was combined with an elevated laser pulse repetition rate of 17 Hz in respect of the in-house protocols usually employed for static spot ablations, to yield ablation crater geometries exceeding the critical aspect ratio of 1 (Kuhn et al., 2009).

Crater depth determinations and imaging were made using a Pro film3D WLI at the iCRAG lab, Trinity College Dublin following the same procedure as Corbett et al. (2020). The WLI is a non destructive technique, which allows for a quantitative measurement of ablation crater depth to a vertical resolution of 0.176 μm. The representative depth of an individual crater is given by the mean of separate cross-sectional measurements made in differing orientation, with each intersecting the central region of the crater (n = 5) and its associated uncertainty is derived from the range in measured values.

Both grain halves were subsequently imaged under plane polarised light (PPL) at identical conditions (e.g. brightness, contrast and white balance) using a using a Nikon DS-Ri2 (iCRAG lab, Trinity College Dublin). The vertical thickness of both halves from the polished surface is almost identical.

Laboratory and Sample Mount Preparation

Laboratory name(s)	iCRAG lab, Trinity College Dublin, Ireland.
Sample type/mineral	Polished zircon

Laser ablation system

Make, Model and type	Teledyne Photon Machines Analyte Excite, ArF excimer
Wavelength (λ)	193 nm
Pulse width	<5 ns
Fluence	~2.25 J cm^{-2}
Repetition rate	17 Hz
Spot size	24 μm
Sampling mode/pattern	grid-of-spots (n=63), static spot ablation
Washout interval	10 s

Transport regime and sweep gas flow

Cell atmosphere and transport gas composition	100% He in cell, N_2 combined via 'T'-style connection within the ARIS adapter and then mixed with Ar make-up gas in a signal smoothing device, before entry into the ICP source

Sweep gas flow	0.4 l min^{-1} (He) split between the sampling "cup" and chamber
Auxiliary gas flow	11 ml min^{-1} (N_2) and 0.65 l min^{-1} (Ar)

ICP-MS Instrument

Make, Model and type	Agilent 7900 Q-ICP-MS
Forward RF power	1550 W
Reflected power	≤ 5 W
Measured masses with dwell times [ms] listed.	^{31}P[7], ^{49}Ti[5], ^{57}Fe[7], ^{91}Zr[7], ^{204}Pb[18], ^{206}Pb[45], ^{207}Pb[90], ^{208}Pb[18], ^{232}Th[18], ^{238}U[100]
Duty Cycle	932 ms
Th/U	Pr1(U) 0.99; Pr1(A) 0.98
ThO[%]	Pr1(U) 0.16; Pr1(A) 0.13

Data Processing

Calibration strategy	2 consecutive analyses of 91500 either side of 'unknown' samples (n=21) for a total of 8 analyses per session, constituted the primary calibration standard. Two variations of 91500 primary reference were included as part of every standard bracket; annealed (91500A) and untreated (91500U). Both variations could be applied during data reduction, as explained in *section 3.3.3* of the text. An untreated WRS-1348 was chosen as a secondary standard. It too occupies the standard bracket, receiving 2 consecutive analyses.
Data processing and plotting package(s)	Agilent MassHunter 3.3 for time resolved analysis; Iolite v3.5 for U-Pb data processing (Paton et al., 2011); IsoplotR online for age calculation and plotting (Vermeesch, 2018)
Common-Pb correction	No common-Pb correction applied
Down-hole fractionation correction	Linear
Normalization and drift correction	Drift correction, reference material normalization and uncertainty propagation were achieved by way of the VizualAge DRS procedure, outlined in detail within Petrus and Kamber (2012), using a median spline fit.

Table 3.1 LA-ICP-MS set-up and operational parameters

3.3.3. U-Pb data reduction

The Plešovice standard reference material, despite being a well-characterised, is in this instance treated as an 'unknown' sample. Batches of 21 analyses of these unknowns are bracketed before-and-after, by primary calibration standard and secondary 'quality control' analyses, until a total of 63 analyses are obtained. The 91500 zircon (1065.4 ± 0.6 Ma; Wiedenbeck et al., 1995) was used as the primary U–Pb calibration standard and was present throughout the session in its heat-treated (~1100°C for 96 h) and untreated form as part of each sample-standard bracket. It is usually advised that when analysing a heat-treated sample, a primary calibration standard having received the same treatment is used as an external standard to minimise biases associated with a mismatching of sample matrixes (e.g. Crowley et al., 2014). The degree to which age bias can be induced by a purposeful mismatching of primary reference and unknown, was assessed by conducting two data reduction experiments identical in every respect except in the choice of heat-treatment (or lack-thereof) of the 91500 primary reference material. An untreated example of WRS-1348 (526.26 ± 0.7 Ma; Pointon et al., 2012) was chosen as a secondary standard to monitor plasma stability during sessions, due to its broadly homogenous chemical composition and reliable behaviour under laser radiation.

Data processing was conducted using Iolite (v3.5) a commonly used software package developed for mass spectrometric data reduction and visualisation (Paton et al., 2011). The 'VizualAge' data reduction scheme (DRS) of Petrus and Kamber (2012) was used to process the mass spectrometric data recorded by the Agilent 7900 ICP-MS. The on-peak signals were defined by cropping 1.5 s from the initial rise and 0.5 s subsequent fall of the incoming ablation signal. A baseline signal is defined between ablations and is used to calculate session-wide baseline-corrected values for each isotope. Sample-standard bracketing was used to correct for mass bias by normalizing all isotopic ratios to those that of 91500 zircon reference material, whilst also correcting for instrumental drift during a given session. Two consecutive analyses for each of; 91500 (untreated), 91500 (annealed) and WRS-1348 (untreated) zircon were made within each standard bracket throughout a session. A median spline was fit through the interspersion of primary reference materials, to model the instrument associated drift. Furthermore, a linear downhole correction model was chosen for ease of comparison between analyses on annealed and non-annealed grain halves (see Fig 3.3e-e'). All Concordia plots and derived U-Pb concordia ages were generated using IsoplotR (Vermeesch, 2018) and uncertainties therein are reported at the 2σ (95% confidence) level. A total of 31 (of 63) analyses were plotted and used to determine ages, following a rejection procedure in which analyses were rejected if they intersected fractures and/or inclusions either visible (by BSE or CL) at the sample surface. Ablations which intersected sub-surface inclusions (identified by a suite of monitor elements; see Table 3.1) were also rejected. Additionally, because the comparison of chemically analogous counterparts was of primary interest, any analyses which did not overlap within uncertainty of U concentration were rejected. Every sample analysis remaining after the rejection procedure, we argue is directly comparable with its mirrored counterpart analysis in the opposing sample half.

The 'CellSpace' module within iolite was used to generate a spatially coordinated visualisation of the VizualAge DRS outputs for each analysis with respect to imaging undertaken by CL, BSE and PL

mapping (Paul et al., 2012). LA-ICP-MS outputs (e.g. U ppm, Th ppm, Pb ppm, α-dose and/or age) can therefore be contextualised alongside features imaged at the grain surface such as; growth zonation, alteration texture and quantity of radiation damage. By utilising a grid sampling pattern, variation in age or other outputs, can be charted not only against a secondary underlay-image, but also relative to one another. The grid-of-spots processed within the CellSpace module effectively generate a very low-resolution "map", which correlate well with the imaging undertaken by various other methods (Fig. 3.2).

3.4. RESULTS AND DISCUSSION

3.4.1. Textural and structural comparison

Numerous imaging and 2D mapping methods were employed to characterise the internal surface features of the variably treated Plešovice grain halves, presented in Figure 3.1 as mirror images for the purposes of comparison. A depth of material approximately 830 µm was lost during the preparation stage, despite this however both halves share internal textural features as observed most evidently by CL (see Fig. 3.1a). Primary growth zonation in both halves is bounded for the most part by crystal faces, with many zones being discontinuous over sharply delineated crystal facet junctions. There also exist relatively CL-bright secondary alteration features stemming from inclusions and/or fractures, which extend outwards as blade-shaped penetrations parallel to the growth zones.

The comparative CL images demonstrate a conspicuous suppression of CL intensity of the untreated, radiation damaged half relative to its annealed counterpart. It should be noted however, that a comparison of intensity in the CL response of both halves cannot be made directly because gain and contrast were adjusted (albeit to a minor extent) for each half, to make internal textures recognizable. Factors controlling CL are numerous and complex however, the contrasting CL responses observed herein between chemically analogous zircon surfaces suggests that a restoration of crystalline order has occurred to some degree in the annealed half and more generally, that structural order is at least partially responsible for CL intensities (Wiemer et al., 2017; Nasdala et al., 2002).

Nasdala et al., (2006) demonstrated that annealing of radiation damage resulted not only in a dramatic increase of CL emission, but also in a decrease in BSE intensity relative to counterpart grain halves which remained untreated. Nasdala et al., (2006) note that relative lessening of BSE intensity is particularly noticeable in zircons which have been strongly affected by radiation damage. There is a negligible relative difference in BSE response between the sample halves investigated herein (Fig. 3.1b), suggesting that there was a minimal degree of initial structural disorder due self-irradiation (as corroborated by PL mapping). The BSE images highlight the presence of surface inclusions and fractures most clearly and were used as an aid to sample spot rejection prior to the calculation and plotting of age data. An identification of inclusion phases, aided by energy dispersive x-ray analysis (EDS) is included as supplementary material to this publication. These data informed the choice of isotopes used to monitor and avoid sampling sub-surface inclusions.

Dy^{3+} photoluminescence hyperspectral maps accurately chart structural disorder as a result of self-irradiation in-situ (Figure 3.1d). The percentage amorphous fraction (AF%), is a measure of structural disorder which can be made at high-spatial resolution. The untreated sample half evidences a minimal to moderate degree of radiation damage accumulation containing an amorphous component < 50%. Within the untreated half, relatively high AF% are especially notable in actinide-rich prismatic faces and conspicuously lower in domains affected by secondary alteration, as observed in CL (Fig. 3.1a). In-situ measurement of PL in the annealed half by contrast, demonstrate a marked reduction in AF% values (within 5% uncertainty limit of the PL technique; cf. Lenz et al., 2020) when compared to its counterpart half, suggesting a near complete restoration of crystallinity has occurred during annealing. A restoration of crystalline order, is accompanied by a recovery of physical attributes such as; density, elastic moduli, hardness (Pidgeon, 2014). It is also accompanied by an increase in crystal transparency (Kooijman *et al.* 2012) which can adversely affect the efficiency of laser energy absorption for a given wavelength (Guillong et al., 2003; Russo et al., 2000; Mank and Mason, 1999).

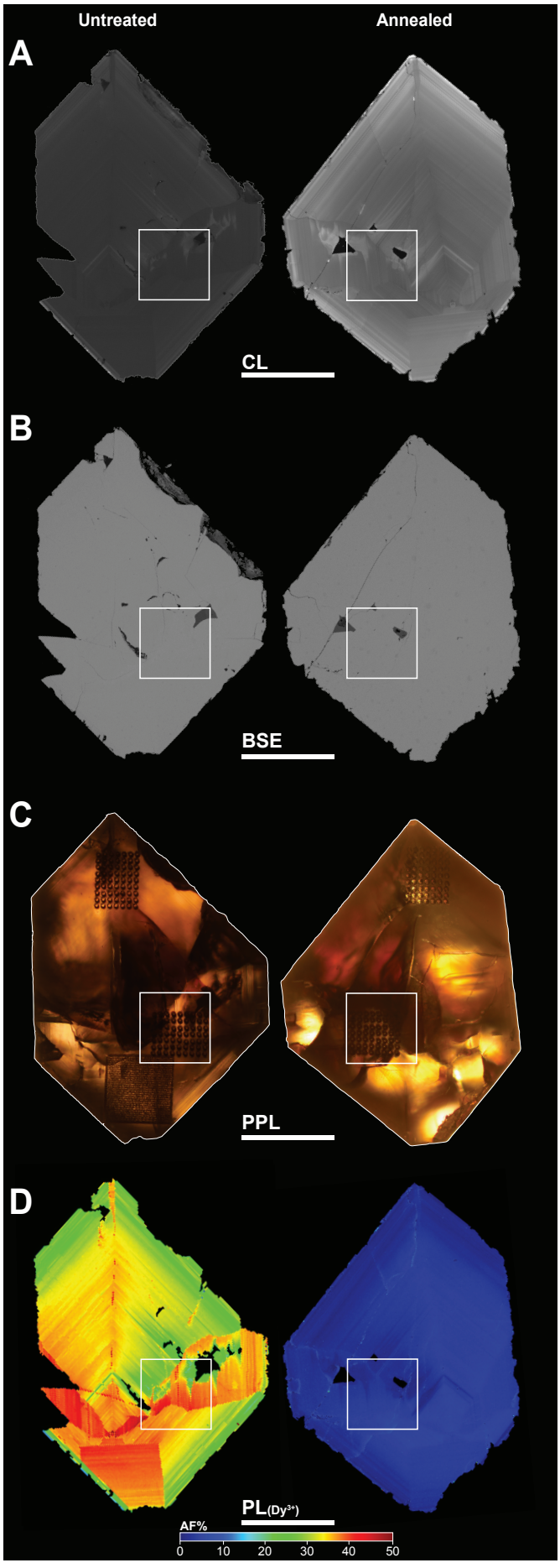


Figure 3.1 A) Comparison CL images of untreated and annealed surfaces of the same Plešovice grain, which was halved perpendicular to its c-axis dimension and are presented as mirror images. **B)** BSE images acquired for the same sample surfaces each demonstrate a uniform intensity (with the exception of inclusions and fracture features), suggesting zircon substrate in each case has experienced only minor structural disruption/alteration (see discussion in Nasdala et al. 2006). **C)** A PPL transmitted light photograph of the sample surface highlighting the opacity and colour change invoked by annealing (in the visible spectrum). **D)** PL hyperspectral maps chart in-situ accumulation of structural disorder expressed as a percentage amorphous fraction (AF%). The untreated sample half evidences a minimal-moderate degree of radiation damage containing an amorphous component < 50%. The annealed counterpart half demonstrates a marked increase in structural order. The white squares highlight the region analysed by LA-ICP-MS as seen in Fig. 3.3. Scale bar is 0.5 mm in length.

3.4.2. Radionuclide composition

The U, Th and Pb concentrations (Fig. 3.2a-c) are for the most part, shared between counterpart spots, and are within uncertainty of one another. This indicates that most spots are chemically analogous in terms of their U, Th and Pb concentration, despite a notable difference in structural state (as indicated by the PL underlay image). The shared chemistry in this regard, intimates that the grid-pattern is accurately aligned in 2-D space between grain halves. Some discrepancies in chemical concentration do exist however (e.g. spots; E3, E4, E5), which cannot be attributed to any visible surface features. Such discrepancies may be due to the fact that some intervening material has been lost to preparation processes (sawing and polishing) and domains having differing chemical compositions have been exposed. The most obvious demonstration of this vertical inhomogeneity is observed between spots which sample inclusions or fractures which are not mirrored in the corresponding half, and thus demonstrate the largest relative offset in concentration (e.g. spots; A1, A2). The grid-pattern approach allows laser outputs to be traced out in 2D at low-resolution. Indeed, it is notable that regions of high elevated AF% as estimated by PL (i.e. higher relative damage) in the untreated half correlate with higher relative concentrations of parent actinides and their related daughter products. This spatial distribution is also mirrored directly in the annealed counterpart, suggesting that the artificial (dry) annealing process has little-to-no effect on element mobility nor does it effect determinations of concentration made by LA-ICP-MS.

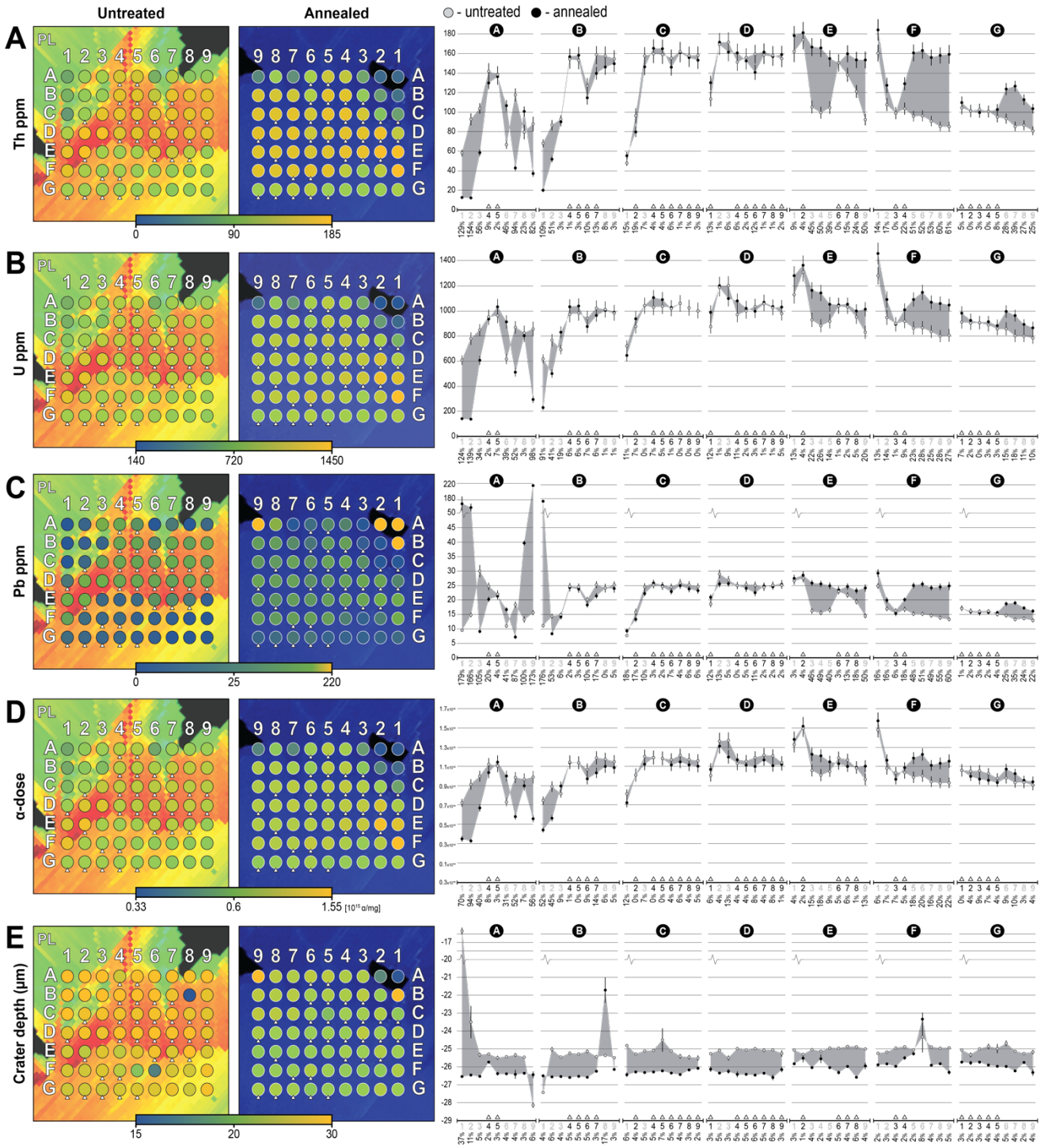


Figure 3.2 A comparison of untreated and annealed LA-ICP-MS counterpart grid-of-spots overlaid on the PL hyperspectral map and accompanying x-y scatter plot for each of **A)** Th ppm, **B)** U ppm, **C)** Pb ppm, **D)** α-dose and **E)** crater depth (µm). Counterpart spots are labelled using an alpha-numerical coordinate grid. The scatter plots right of the grid-of-spots, again chart data by way of direct comparison between individual untreated (black markers) and annealed (grey markers) counterpart spots. These data are displayed in order of row (A-G) as depicted in the coordinated grid-of-spots, with each spot (1-9) in a given row being labelled on the x-axis. A percentage difference in measured values between counterpart spots is also displayed beneath each x-axis label. Counterpart locations used for age determinations were carefully selected to avoid inclusions and/or fractures and share U ppm within uncertainty of one another, are marked with a white triangular marker (see *section 3.3.3* in text for rejection parameters).

3.4.3. Age determination

All age data are drawn from the grid-pattern sampling protocol for both untreated and annealed sample halves which, for the purposes of sample alignment, were divided into two individual analytical sessions namely Pr1U and Pr1A respectively. Biases associated with plasma stability and sensitivity between sessions were monitored using an untreated WRS-1348 secondary standard (526.26 ± 0.7 Ma; Pointon et al., 2012) calibrated against untreated 91500 primary reference standard, deriving ages of 528.45 ± 1.13 Ma [MSWD = 1.4] and 520.69 ± 0.95 Ma [MSWD = 0.76] for the Pr1U and Pr1A session accordingly and which deviate by 0.34 % and 1.13 % from the accepted age respectively (see supplementary material for age plots). These data are within or near accepted reproducibility limit of 1 %, therefore the contribution of plasma instability towards the observed age bias is minimal. The external reproducibility of primary and secondary reference materials used for both sessions are included in Table 3.2. Variability for most ratio determinations, is near 2 % (2SD) with the exception of the 91500(A) bracket within the Pr1A session, which has a $^{207}Pb/^{206}Pb$ of 3.09 % (2SD).

	Untreated Sample Half ("Pr1U" session)						Annealed Sample Half ("Pr1A" session)					
	91500 (U)		91500 (A)		WRS (U)		91500 (U)		91500 (A)		WRS (U)	
Sample No.	$^{206}Pb/^{238}U$	$^{207}Pb/^{206}Pb$	$^{206}Pb/^{238}U$	$^{207}Pb/^{206}Pb$	$^{206}Pb/^{238}U$	$^{207}Pb/^{206}Pb$	$^{206}Pb/^{238}U$	$^{207}Pb/^{206}Pb$	$^{206}Pb/^{238}U$	$^{207}Pb/^{206}Pb$	$^{206}Pb/^{238}U$	$^{207}Pb/^{206}Pb$
1	0.179	0.075	0.183	0.076	0.086	0.058	0.180	0.073	0.177	0.076	0.081	0.057
2	0.180	0.074	0.182	0.077	0.086	0.058	0.179	0.076	0.181	0.073	0.081	0.057
3	0.181	0.075	0.183	0.075	0.085	0.057	0.177	0.076	0.181	0.074	0.080	0.057
4	0.178	0.076	0.182	0.075	0.085	0.058	0.181	0.074	0.181	0.076	0.081	0.057
5	0.179	0.074	0.183	0.076	0.086	0.058	0.179	0.075	0.178	0.077	0.081	0.057
6	0.176	0.076	0.180	0.077	0.086	0.058	0.181	0.075	0.178	0.074	0.080	0.059
7	0.180	0.075	0.184	0.076	0.087	0.057	0.179	0.075	0.178	0.075	0.079	0.058
8	0.181	0.075	0.184	0.076	0.085	0.059	0.179	0.075	0.179	0.075	0.079	0.058
mean	0.179	0.075	0.183	0.076	0.086	0.058	0.179	0.075	0.179	0.075	0.080	0.057
2SD%	1.56	1.87	1.56	2.19	1.58	2.23	1.65	2.21	1.92	3.09	1.88	2.05

Table 3.2 Baseline subtracted raw ratios measured for primary and secondary reference standards bracketing sessions which include both untreated and annealed sample halves. Reproducibility (2SD %) of external calibration standards and mean values for each ratio pair are included beneath each listing.

Ellipses plotted in Figure 3.3, corresponds to a total of 31 sampling locations from across the grid of spots coordinated in their lateral dimension over both untreated (U) and annealed (A) Plešovice sample halves. These analyses are spatially and chemically analogous in-so-far as possible allowing for a near direct comparison of age data between sample halves, whereupon the structural, optical and thermo-physical changes caused by annealing are the primary variables. All plots generated using IsoplotR (Vermeesch, 2018) and uncertainties are quoted at a 2σ level (95 % confidence) in each case. The MSWD value presented incorporates both x-y equivalence and the MSWD of concordance. MSWD values higher than 1 indicate an underestimation of uncertainty, which is likely a reflection of the simplified data processing regime employed herein, details of which are provided in *section 3.3*.3. The Wetherill concordia age derived for the untreated sample half (displayed in Fig. 3.2a) reproduces to 0.07 % of the accepted age. By comparison laser sampling of chemically analogous counterpart locations in the annealed half produces a concordia age which is apparently younger than its counterpart by 6 % (~20 Ma).

A systematic trend towards younger apparent $^{206}Pb/^{238}U$ ages for annealed counterpart analyses is in evidence most clearly in a plot of weighted mean $^{206}Pb/^{238}U$ ages for both halves (Fig. 3.3b). The offset in age is evident between individual spots which are chemically analogous in terms of U, Th and Pb concentration (See Fig. 3.2a, b and c). Interestingly the trend of $^{206}Pb/^{238}U$ age variation on a spot-to-spot basis, is loosely mirrored between untreated and annealed samples notwithstanding the observable apparent offset in age. This suggests that intracrystalline variation in $^{206}Pb/^{238}U$ is primarily controlled by the μm scale compositional variability which is shared across both halves.

Age data presented in Figure 3.3 is divided between those data calibrated using an untreated 91500 primary reference zircon (A-C) and those calibrated using a fragment of 91500 which underwent the same dry annealing process as the annealed sample half (A'-C'). Plots A'-C' are plotted at the same scale in each case and are included for the purpose of comparison. Several studies (e.g. Crowley et al., 2014; Marillo-Sialer et al., 2014; Allen and Campbell, 2012) suggest that primary calibration standards which have undergone the same pre-treatment could help reduce the effects of matrix-related age bias. Both an untreated (91500U) and annealed (91500A) variant of 91500 was used during data reduction to assess their relative influence on the calculated ages. A negligible increase of 0.08 % is observed in the weighted mean $^{206}Pb/^{238}U$ age determined between the same analyses of the annealed sample half (A) when 91500A is used during calibration. Conversely however, there is a 2.26 % underestimation in weighted mean $^{206}Pb/^{238}U$ age determined for the same analyses of the the untreated sample half (U), when 91500A is applied during data reduction relative to the same analyses calibrated using 91500U. The underestimation of weighted mean $^{206}Pb/^{238}U$ age of ~ 2.5 % (relative to the accepted age), observed for analyses of the untreated matrix, is consistent with the magnitude of matrix-related biases determined by Marillo-Sialer et al. (2014). In this study, authors attributed the observed offset in age to differential laser ablation depths between sample and calibrants, whereby a greater rate of ablation of the calibration standard relative to the sample results in an underestimation of the calculated $^{206}Pb/^{238}U$ age. Matrix 'mis-matching' observably influences the age

determinations made on analyses of the untreated matrix, however the observed ~ 6 % apparent younging observed in analyses of the annealed sample half (relative to untreated counterpart analyses), cannot adequately explained by a non-equivalent pre-treatment of the primary reference alone.

The weighted mean $^{207}Pb/^{206}Pb$ ages (Fig. 3.3c-c') almost overlap within uncertainty, with most individual analyses sharing a significant overlap in $^{207}Pb/^{206}Pb$ age. This indicates that intra-elemental (Pb-Pb) mass fractionation is not expected during laser sampling as isotopes of Pb behave almost identically during ablation. $^{207}Pb/^{206}Pb$ ages are thereby independent of any micro-structural and optical controls on laser-matter interaction and its associated effects.

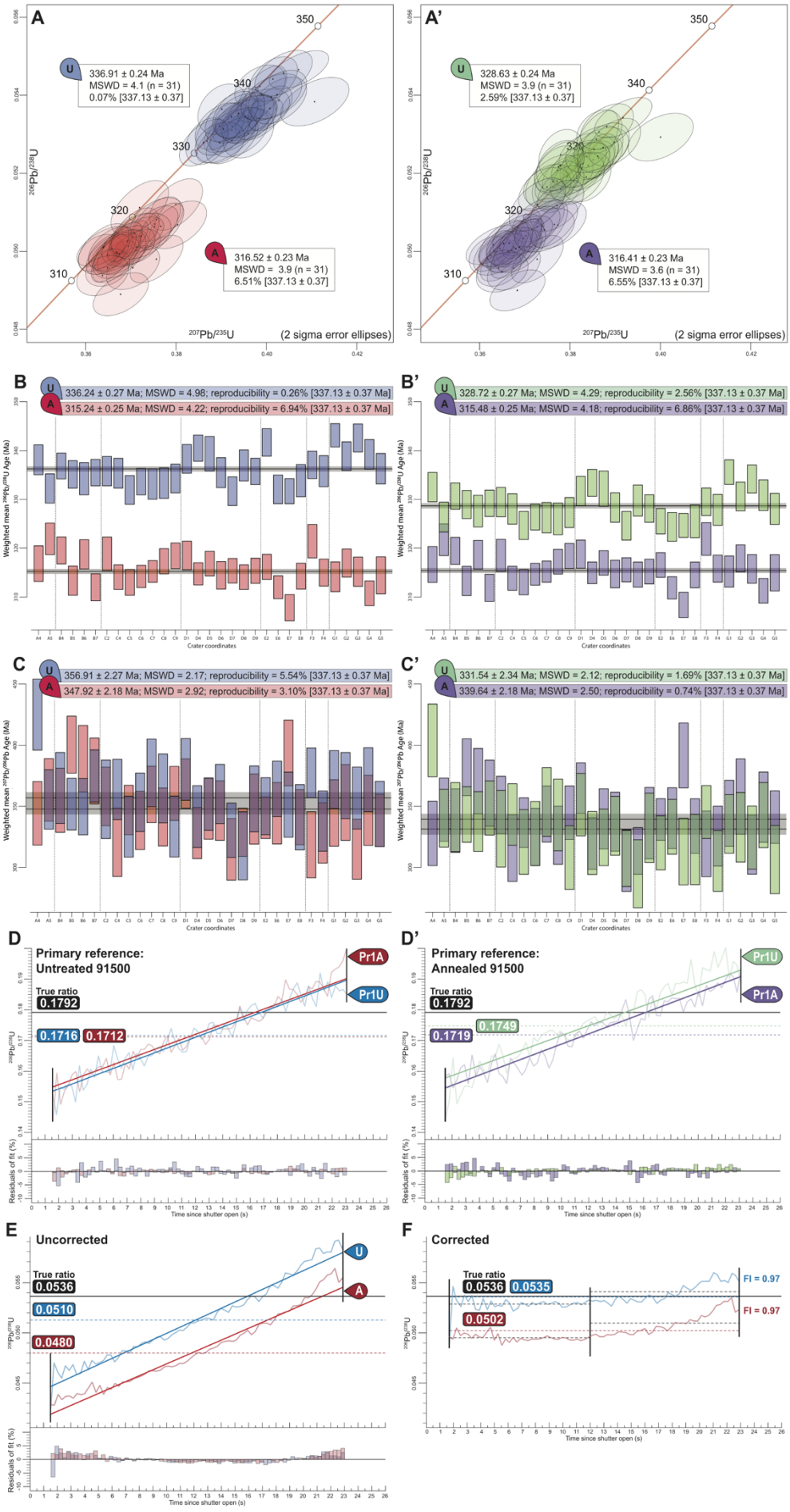

A
U
336.91 ± 0.24 Ma
MSWD = 4.1 (n = 31)
0.07% [337.13 ± 0.37]
A
316.52 ± 0.23 Ma
MSWD = 3.9 (n = 31)
6.51% [337.13 ± 0.37]
$^{206}Pb/^{238}U$
$^{207}Pb/^{235}U$
(2 sigma error ellipses)
A'
U
328.63 ± 0.24 Ma
MSWD = 3.9 (n = 31)
2.59% [337.13 ± 0.37]
A
316.41 ± 0.23 Ma
MSWD = 3.6 (n = 31)
6.55% [337.13 ± 0.37]
B
336.24 ± 0.27 Ma; MSWD = 4.98; reproducibility = 0.26% [337.13 ± 0.37 Ma]
315.24 ± 0.25 Ma; MSWD = 4.22; reproducibility = 6.94% [337.13 ± 0.37 Ma]
Weighted mean $^{206}Pb/^{238}U$ Age (Ma)
Crater coordinates
B'
328.72 ± 0.27 Ma; MSWD = 4.29; reproducibility = 2.56% [337.13 ± 0.37 Ma]
315.48 ± 0.25 Ma; MSWD = 4.18; reproducibility = 6.86% [337.13 ± 0.37 Ma]
C
356.91 ± 2.27 Ma; MSWD = 2.17; reproducibility = 5.54% [337.13 ± 0.37 Ma]
347.92 ± 2.18 Ma; MSWD = 2.92; reproducibility = 3.10% [337.13 ± 0.37 Ma]
Weighted mean $^{207}Pb/^{206}Pb$ Age (Ma)
C'
331.54 ± 2.34 Ma; MSWD = 2.12; reproducibility = 1.69% [337.13 ± 0.37 Ma]
339.64 ± 2.18 Ma; MSWD = 2.50; reproducibility = 0.74% [337.13 ± 0.37 Ma]
D
Primary reference:
Untreated 91500
True ratio
0.1792
0.1716
0.1712
Pr1A
Pr1U
Residuals of fit (%)
Time since shutter open (s)
D'
Primary reference:
Annealed 91500
True ratio
0.1792
0.1719
0.1749
Pr1U
Pr1A
E
Uncorrected
True ratio
0.0536
0.0510
0.0480
U
A
F
Corrected
True ratio
0.0536
0.0535
0.0502
FI = 0.97
FI = 0.97

Figure 3.3. (A-C) and **(A'-C')** contain a graphical comparison of LA-ICP-MS age data for untreated (U) and annealed (A) counterpart analyses (n = 31), whereby age data presented in plots **A-C** were calibrated using untreated 91500 and those data plotted in **A'-C'** were calibrated using an annealed 91500. All plots generated using IsoplotR (Vermeesch, 2018) and uncertainties are quoted at a 2σ level (95% confidence) in each case. The MSWD value presented incorporates both x-y equivalence and the MSWD of concordance. See text for further details. **(D-D')** present mean $^{206}Pb/^{238}U$ signal ratios determined for a time resolved integrations (n=8) of 91500 variants used as calibration reference standards in analytical sessions Pr1U and Pr1A, each containing analyses of both untreated and annealed matrixes respectively. Downhole fractionation was modelled in by a best fit linear regression. The adequacy of this model is charted below each plot as a distribution of residuals about the line, expressed in percentage. The annealed 91500 in D', both exhibit noisier relative signal ratios, hence a larger residual values. **E)** A comparison of the uncorrected mean $^{206}Pb/^{238}U$ values for all individual integrations of both untreated and annealed matrixes used in age determination (n = 31). Both traces demonstrate an offset in mean $^{206}Pb/^{238}U$ towards values lower than the true ratio, whereby the annealed analyses demonstrate a greater relative offset. Downhole fractionation is also in evidence, whereby $^{206}Pb/^{238}U$ gradually increases as ablation continues, the rate of which is approximated by the slope of the linear regression fit through the data. **F)** The corrected approximation of mean ratio values exhibit an offset from the true value of 0.19 % and 6.55 % for the untreated and annealed analyses respectively. Despite a systematic offset in $^{206}Pb/^{238}U$ ratio determination, analyses of both matrixes exhibit the same trend and magnitude of downhole fractionation. Relatedly the black markers, demarcate the beginning, middle and end of the signal integration used in FI calculation (further details in *section 3.4.4*).

3.4.4. Downhole fractionation correction:

Inter-elemental fraction associated with LA-ICP-MS can originate during ablation, aerosol transport, or during subsequent process of vaporization, atomization, and ionization which take place within the ICP. Laser induced elemental fractionation (LIEF) phenomena are attributed to processes occurring at the site of ablation and are considered to be the most likely source of elemental fractionation (Eggins et al., 1998). Zircon specifically demonstrates a preferential retention of U (and Hf) within and around a deepening crater due to a laser induced phase separation into SiO_2 and ZrO_2, due to their high affinity with Zr (Kuhn et al., 2009). Both Si and Pb show no such affinity and freely are mobilised out of ablation craters as vapour condensate independently of their diameter (Košler et al., 2005, Kuhn et al., 2009). This zircon specific form of fractionation was shown by Kuhn et al. (2009) to highly dependent crater aspect ratio, where craters exceeding a "critical" depth/diameter ratio of 1 exhibit a fractionated $^{206}Pb/^{238}U$ signal. The evolution of $^{206}Pb/^{238}U$ over the course of an ablation is plotted for all variants of the 91500 primary calibration standard (Fig. 3.3d and d') as well as being compared between untreated and annealed halves of the Pr1 sample (Fig. 3.3e). Where depth-dependent fractionation of ^{206}Pb over a relatively more refractory ^{238}U has occurred during ablation an increasing trend in measured $^{206}Pb/^{238}U$ would be expected as the ablation crater deepens (i.e. in seconds since the laser shutter opens).

Downhole fractionation can be modelled in the calibration standard and used to approximate and correct for fractionation effects in the sample material. Downhole correction (DHC) models assume sample and calibration standards are well matched in terms of their matrix behaviour under incident laser radiation. A linear DHC was chosen to model the evolution of $^{206}Pb/^{238}U$ in both sample halves and is charted in Figure 3.3d and d', as a best fit line through the mean of all $^{206}Pb/^{238}U$ 91500 calibrant traces used in data reduction

(n=8). The closeness of fit for each linear regression to the measured $^{206}Pb/^{238}U$ be visualised in terms of percentage residual fit, where a positive excursion denotes an underestimation of fractionation and vice versa. A linear regression is fit through the uncorrected $^{206}Pb/^{238}U$ for both sample halves as a point of comparison in Figure 3.3e, where fractionation is underestimated by ~3-5 % in the initial 5.5s and final 3s of the integration (as seen in the 'residuals of fit' plot).

A measure of inter-elemental fractionation is made by dividing the mean $^{206}Pb/^{238}U$ value of the first half of an analysis (demarcated by black vertical lines; Fig. 3.3f) by the mean value determined for the latter half of the integration (Fryer et al. 1995). This calculation constitutes a fractionation index (FI). A FI of near unity (i.e. 1) suggests a minimal degree of time-dependent fractionation has occurred over the course of an analysis. Figure 3.3f describes the evolution of the mean corrected $^{206}Pb/^{238}U$ trace which is derived from all individual integrations (n = 31) used in age calculation. Both mean $^{206}Pb/^{238}U$ traces demonstrate similar trending increases in $^{206}Pb/^{238}U$ as ablation continues and both fractionate to the same extent, which each departing from unity only slightly (i.e. FI = 0.97). Combined, these observations suggest that the offset towards younger apparent ages for analyses of the annealed sample half cannot be attributed to the down-hole fractionation effects typically associated with zircon. Moreover, had the depth-dependent preferential retention of U occurred during the laser induced phase separation of zircon, the annealed half would demonstrate an increase in apparent age (Kuhn et al., 2009).

3.4.5. Radiation damage

A calculation of α-dose (D_α) approximates the number of α-decay events per mg, and is commonly used as a proxy for accrued radiation damage. An estimation α-dose (D_α) was made using the equation 1, expressed below (Nasdala et al., 2001; Murakami et al., 1991).

$$D = 8 \cdot \frac{C_U \cdot N_A \cdot 0.9928}{M_{238} \cdot 10^6} \cdot \left[exp^{(\lambda 238 * t)} - 1\right] + 7 \cdot \frac{C_U \cdot N_A \cdot 0.0072}{M_{235} \cdot 10^6} \cdot \left[exp^{(\lambda 235 * t)} - 1\right] + 6 \cdot \frac{C_U \cdot N_A}{M_{232} \cdot 10^6}$$

whereby; C_U and C_{Th} correspond to present actinide concentrations in ppm; N_A is Avogadro's number; M_{238}, M_{235}, and M_{232} are the molecular weights of suffixed isotopes; decay constants for each of ^{238}U, ^{235}U and ^{232}Th are denoted by $\lambda 238$, $\lambda 235$ and $\lambda 232$ respectively (Firestone and Shirley, 1996); and *t* was represented in this case by the accepted age Plešovice in Ma (i.e. 337.13 ± 0.37 Ma; Sláma et al., 2008). This equation assumes a present natural abundance of 99.28 % and 0.72 %, for ^{238}U and ^{235}U respectively.

Estimates of α-dose (D_α), for analyses used in age calculations (discussed later) range from 0.75-1.49 [10^{15} α mg^{-1}], all of which lie within the first stage of damage accumulation as described by Murakami

et al. (1991). In this framework of damage accumulation; Stage 1 (i.e. up to $D_\alpha = 3$ [10^{15} α mg^{-1}]) is dominated by the accumulation of point defects, resulting in unit cell expansion and accounts for most of the decrease in density associated with self-irradiation in zircon (Pidgeon, 2014). Determinations of α-dose constitute a proxy for present day structural order within zircon. The process of structural restoration by annealing either by by geological or artificial means are not accounted for within a calculation of α-dose, hence the similarity between the calculated α-dose between untreated and annealed halves.

Instead an in-situ measurement of radiation damage by PL is made for each sampling location across the two halves. A circular mask, approximating crater diameter is used to quantify the mean AF% for each sampling location used in age determination (see Table 3.3). The AF% determinations for the annealed half fall within or near the uncertainty limit of the model's calculation (± 5 %), hence little can be interpreted from these data, except to conclude that a complete restoration of crystalline order following annealing has occurred. The untreated sample half evidences a minimal-moderate degree of radiation damage containing an amorphous component < 43%. Regions highest AF% are correlated with regions of higher actinide concentration (Fig. 3.4a and b). A very weak inverse correlation exists between AF% and $^{206}Pb/^{238}U$ age (Fig. 3.4c), whereby higher damage domains often produce younger ages, this may reflect some minor contributing influence of radiation damage towards the age variation observed between some individual analyses of untreated sample half. The range of radiation damage expressed within the untreated sample half cannot be correlated with any corresponding change in crater depth (Fig. 3.4d), because the most highly damaged location differs by only 0.87 μm when compared with the least damaged location measured. The principle control over ablated volume, must therefore be only loosely correlated to zircon structural state.

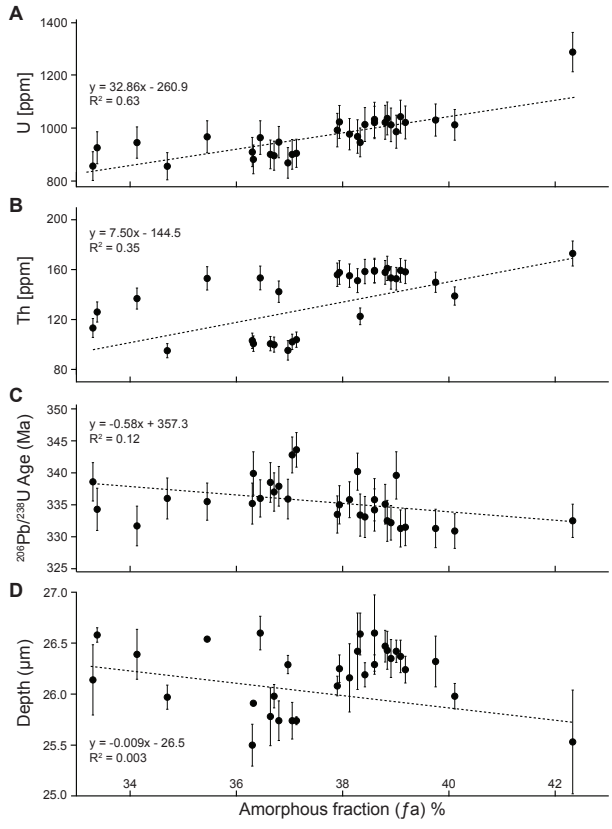


Figure 3.4. The relationship between various measured parameters and radiation damage (AF%) within the untreated sample half, for all sample locations used to generate age plots. **A)** U ppm **B)** Th ppm **C)** $^{206}Pb/^{238}U$ Age (Ma) and **D)** crater depth.

3.4.6. Crater geometry:

A comparison of crater geometry between sample locations (Fig. 3.5a) models their differential ablation behaviour by proxy. The craters generated for each sample half were broadly internally consistent with regards to their overall geometry (Fig. 3.5a), however a comparison of geometries between counterpart halves suggests that two distinct modes of ablation were operative. For a given laser system, the ablative character as well as the temperature evolution within the system are governed by; the effective laser fluence per pulse, mass-density, thermal conductivity and specific heat capacity of the target matrix (Markopoulos et al, 2016). The significant structural and associated optical differences between otherwise analogous zircon matrixes may lead to contrasting results as observed between crater geometries within counterpart halves, as all other variables are held constant insofar as possible (e.g. laser operational parameters, matrix composition, crystal anisotropy etc.).

Ablation at nano-second pulse-durations, is ideally dominated photothermal processes characterised by a near-complete absorbance laser energy by the target substrate (high effective fluence). Ideally the energy is absorbed within a finite volume of material at/near the sample surface, wherein initial electron excitation is transformed into heat energy within a fraction of the pulse-duration. The surface emission of various particles (i.e. electrons, ions, neutral atoms, or molecules) occurs once a threshold temperature is reached within the interacting volume, whose increase can be defined by the following equation (2);

$$\Delta T = \frac{\alpha \cdot F}{\rho \cdot C_P} e^{-az}$$

where; ΔT is the temperature increase, α is the substrate absorption coefficient, F is the energy density of the laser, ρ is the mass-density of the material, C_p is the heat capacity per unit volume, and z is the optical penetration depth (Markopoulos et al, 2016). A lower effective threshold fluence of ablation is exhibited by craters within the untreated matrix relative to their annealed counterparts under the same laser operational parameters, as exemplified by a more reproducible and voluminous removal of analyte material (Russo et al., 2000). A relative change in effective heat capacity and/or optical absorption could explain the contrasting crater geometries as well as the fractionation behaviour (discussed later).

'Ablation rate' is a metric often used to characterise ablation behaviour and is defined as the ratio between the resultant crater depth and the number of laser shots applied (e.g. Marillo-Sialer et al. 2016), however critically it assumes measured craters have a well-defined geometry. An assessment of crater geometries (including a measurement of depth) as applied herein, form a more informative proxy for ablation behaviour. Contrasting cross-sectional crater geometries at location 'B5' are representative of the ablative character (e.g. depth, volume and quality) demonstrated by other counterpart pairs in this study (Fig. 3.5b), in which the untreated crater has near-parallel sidewalls as well as a more consistent exposure of interconnected crater floor at any given depth, lacking the patchy lateral distribution of partially-ablated substrate (topographic highs) as observed within the confines of the annealed counterpart craters (Fig. 3.5b). Craters within the untreated matrix also demonstrate a greater approximation of the circular area defined by

the laser-spot mask at the sample surface. At location 'B5' the surface expression of the 24 µm laser-spot is reproduced to within 97 % accuracy, whereas the annealed counterpart crater exhibits an area of ablation extending beyond the confines of the laser-spot mask, being 118 % (Fig. 3.5c).

As noted previously, there is little to no correlation between ablative depth and the structural order as measured by PL (Fig. 3.4d). Indeed, Kooijman et al., (2012) observed a stronger correlation between ablation properties and the matrix colour (at 193 nm) expressed by a set of zircon standards, then was observed for relative differences in their structural order. Noting also that zircon colour, is only indirectly correlated with crystallinity. Annealing is accompanied herein with a notable colour change within the visible spectrum of light (Fig..3.1c), which may be concomitant with an increase in the optical penetration of laser energy in the UV. Consequently, the differences in ablation processes as evidence by contrasting crater geometries may be principally governed by a change in matrix opacity (with respect to the incoming 193 nm laser light), possibly due in part to the presence or absence of radiation damage defects in the untreated or annealed matrixes respectively. Lattice defects as a result of self-irradiation may act as 'colour/absorption centres', aiding an increased absorption efficiency in a manner similar to laser-induced lattice defects as described by Becker and Tenzler, (2001).

The high absorption efficiency within the untreated matrix is further exemplified by the deeply incised sub-domains surrounding the central portion of the crater (Fig. 3.5a). These sub-domains likely experience an enhanced rate of ablation because in addition to absorbing direct incident laser pulses, they also absorb indirect internally reflected laser radiation. The development of these domains is potentially initiated by inefficient absorption of laser energy by the near-vertical walls of the crater itself, which are steeply inclined relative to the incidence of the laser beam. This would explain their proximal association with the crater margins. As a result, a proportion of the energy is thought to be reflected inwardly until it strikes matrix material at a suitable angle for absorption (often at depth), thus causing an enhanced deepening of such sub-domains (Eggins et al., 1998). A sidewall adjacent to deepening of a crater's profile is likely a universal indication of efficient laser-matrix coupling.

By contrast, the annealed craters lack many of the same attributes as their untreated counterparts, exhibiting instead features associated with lower effective absorption at the sample surface, for the same laser parameters. Annealed crater geometries evidence a poor approximation of circular area defined by the laser-spot mask, often ablating material beyond the confines of the spot diameter (Fig. 3.5c). The quality of ablation exhibited within the ablated area is often laterally inconsistent, whereby material is often only partially sampled (Fig. 3.5c). In cross-section (Fig. 3.5b) the annealed crater exhibits a relatively shallower depth of ablation, steeper crater walls, as well as 'topographic' high points, again indicating that some regions remain largely un-ablated. Annealed craters also lack the deeply incised sub-domains as expressed by their untreated counterparts, suggesting that laser energy reflected from sidewall interactions was poorly absorbed by the annealed matrix. Instead, annealed craters are characterised by a broadly conical geometry, wherein the central portion of the crater is most deeply sampled.

The quantity of laser energy imparted to the sample surface and the depth to which it is absorbed, is governed by effective opacity of target matrix at a given wavelength. However, the intrinsic thermal properties of the substrate matrix dominate the processes occurring in the wake of a laser pulse (i.e. conduction, melting, vaporisation and expulsion) (Hager, 1989). Both the temperature and the rate of heating within the matrix are governed by its heat capacity and thermal conductivity (Vasantgadcar et al., 2010). The intrinsic heat capacity of zircon is unlikely to vary considerably between counterpart matrices, however an improvement in thermal conductivity is probable following annealing, due a reduction in lattice defect density. Consequently, heat energy within the interaction volume of the annealed sample would be dissipated more quickly away from the site of absorption and would potentially explain the emission of surface products outside the confines of the laser-spot mask (Fig. 3.5c). The lower effective opacity combined with an improved thermal conductivity potentially enacted by annealing may serve to effect a change in ablation process.

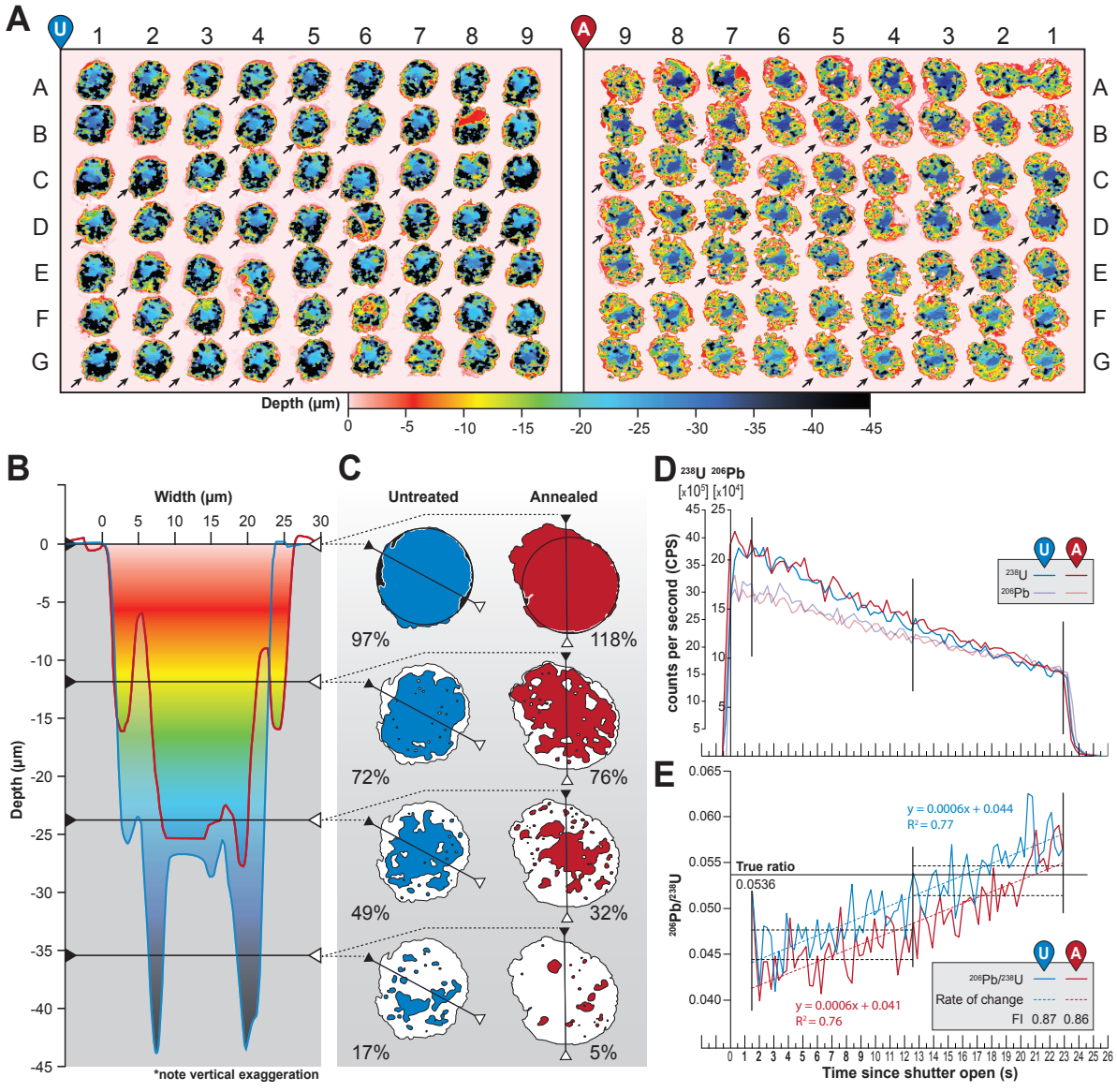


Figure 3.5. A) A comparison of representative untreated (U) and annealed (A) crater geometries in Plešovice as determined

by WLI, which models their differential ablation behaviour by proxy. Craters used in age determination are marked with a black arrow **B)** A representative 2D cross-sectional comparison of crater geometry, charting the ablation characteristics of both untreated (U) and annealed (A) halves at location 'B5'. **C)** The expression of crater floor exposure with depth as a percentage proportion of the area defined by the 24 µm laser spot mask applied at the sample surface. The orientation of the cross-section (as in B) is indicated by line markers. **D)** A comparison of baseline-subtracted CPS, for masses 238 and 206 during a time resolved analysis (TRA) of the same sample location 'B5' (as in B and C) in variably treated halves. The black markers, highlight the beginning, middle and end of the signal integration. **E)** A comparison of uncorrected $^{206}Pb/^{238}U$ determinations made on the same signal integration as highlighted in (D), where a best fit polynomial regression is fitted through the ratio traces of both untreated and annealed TRAs (R^2 displayed), which highlight the rate of change of $^{206}Pb/^{238}U$ as ablation continues. Additionally, a mean $^{206}Pb/^{238}U$ is calculated for the first and second half of an integration in each case and is represented by a dashed black line. The FI highlights the degree of inter-elemental fractionation occurring in each case.

3.4.7. Downhole fractionation and crater geometry

Craters for which ages were derived demonstrate a universally shallower depth in the annealed sample half by ~1 µm (4 %) relative to counterpart craters in the untreated sample half. On the basis of depth measurements alone (Table 3.3), annealed sample halves would be expected to have correspondingly less $^{206}Pb/^{238}U$ fractionation than their deeper counterparts in the untreated sample half, owing to an improved (depth/diameter) aspect ratio. Despite the systematic offset of $^{206}Pb/^{238}U$ in analyses of the annealed half towards relatively lower values, both treated and untreated analyses exhibit a similar trend in uncorrected $^{206}Pb/^{238}U$ signal evolution during the course of an ablation (Fig. 3.3e). Furthermore, the mean traces of all analyses used in age calculation (Fig. 3.3f), exhibit an equivalent magnitude inter-elemental fractionation (FI = 0.97) over the duration of ablation between downhole corrected counterpart analyses. Such similarities are maintained despite fundamentally different ablation characteristics for both matrixes, as evidenced by their differing crater geometries (Fig. 3.5a).

A comparison of untreated and annealed crater geometries at location 'B5' is plotted in Figure 3.5b-c. Very different modes of ablation are expressed by their respective crater geometries, wherein the annealed matrix demonstrates reduced ^{206}Pb and elevated ^{238}U signal intensities over the duration of analysis relative to its untreated counterpart (Fig. 3.5d). These systematic disparities in transient signal detection between counterpart matrixes, are also manifested by an offset in $^{206}Pb/^{238}U$ ratios, but which maintain a similar rate (slope) and fractionation index (Fig. 3.5e).

A proportion of $^{206}Pb/^{238}U$ fractionation observed in each case, can be attributed to conventional aspect ratio dependent retention of refractory ^{238}U. The onset and magnitude of this effect however, is entirely dependent on crater geometry development. All analyses used in the determination of ages within the untreated matrix, exhibit craters which have deeply incised sub-domains in close association with the crater walls. The development of these sub-domains during the initial stages of ablation, may actually aid in the stoichiometric sampling of the bulk proportion of analyte volume sampled from the central, more elevated portion of the crater, by maintaining near-parallel crater walls and an aspect ratio of < 1. As ablation continues however these domains expand laterally within the confines of the 24 µm mask and in so doing,

they contribute an ever larger volumetric proportion of the measured signal. An inflection point is reached, after which any potentially stoichiometric sampling of analyte from the central region of the crater, is proportionately surpassed by the highly fractionated analyte volume sampled from the deeply incised domains as they expand. These more deeply excavated domains are also present in the annealed sample, but are volumetrically much more discreet and largely disconnected from the central portion of the crater, thus are not likely to influence $^{206}Pb/^{238}U$ fractionation to the same extent (see Fig. 3.5a). Moreover, downhole fractionation where it exists in the annealed sample, is a likely consequence of an ever-increasing aspect ratio, as a result of progressively narrowing, broadly conical crater geometry (Fig. 3.5b).

It is also clear that similar trends in downhole $^{206}Pb/^{238}U$ fractionation (notwithstanding the systematic offset in value) are observed for very different modes of ablation, as expressed by contrasting resultant crater geometries. However, conventional downhole phenomena associated with laser-induced zircon phase separation and the retention of U cannot be invoked to explain the apparent younging of annealed analyses as it would have the opposite effect. The observed age bias must be a depth-independent process causing an apparent relative increase in U and/or a decrease in Pb measured for analyses of the annealed sample half.

Treatment	U	A	U	A	U	A	U	A	U	A	U	A	U	A	U	A
Sample Location	***206Pb/238U Age** (Ma)	***206Pb/238U Age** (Ma)	***Pb^{207}/Pb^{206} Age** (Ma)	***Pb^{207}/Pb^{206} Age** (Ma)	***U** [ppm]	***U** [ppm]	***Th** [ppm]	***Th** [ppm]	***Pb** [ppm]	***Pb** [ppm]	****Dose** [$_x10^{15}$ α/mg]	****Dose** [$_x10^{15}$ α/mg]	†AF (%)	†AF (%)	‡**Depth** (μm)	‡**Depth** (μm)
A4	337.9 ± 3.1	316.2 ± 3.8	420 ± 29	340 ± 25	947 ± 59	939 ± 51	142.3 ± 8.6	131.1 ± 6.7	24.4 ± 1.2	20.25 ± 0.9	1.12	1.09	36.80	~5	25.7 ± 1.4	25.3 ± 1.4
A5	331.7 ± 3.1	321.6 ± 3.1	353 ± 26	366 ± 24	945 ± 59	1035 ± 66	136.8 ± 8.5	137.3 ± 8.6	21.8 ± 1.2	21.4 ± 1.1	1.10	1.20	34.13	~5	26.4 ± 1.2	25.5 ± 1.2
B4	336.0 ± 2.9	319.3 ± 2.8	374 ± 28	342 ± 27	964 ± 63	1021 ± 61	153.4 ± 9.5	156.5 ± 8.9	24.6 ± 1.2	24.0 ± 1.2	1.13	1.21	36.45	~5	26.6 ± 0.7	25.2 ± 0.7
B5	335.5 ± 2.9	313.6 ± 2.9	359 ± 21	370 ± 23	967 ± 60	1035 ± 60	153.0 ± 9.4	159.4 ± 9.2	24.5 ± 1.2	23.7 ± 1.2	1.13	1.21	35.45	~5	26.5 ± 1.3	25.3 ± 1.3
B6	334.3 ± 3.3	319.1 ± 2.9	367 ± 24	376 ± 27	926 ± 60	874 ± 53	126.0 ± 8.1	115.1 ± 7.1	19.9 ± 1.1	18.22 ± 0.8	1.06	1.02	33.38	~5	26.6 ± 1.3	25.1 ± 1.3
B7	335.0 ± 3.0	312.9 ± 2.8	361 ± 25	364 ± 25	1023 ± 62	961 ± 49	157.7 ± 9.5	139.1 ± 6.4	25.1 ± 1.1	21.4 ± 0.9	1.19	1.12	37.94	~5	26.3 ± 1.2	25.4 ± 1.2
C2	335.9 ± 3.1	318.3 ± 3.2	355 ± 31	362 ± 22	869 ± 58	916 ± 61	95.3 ± 7.8	79.9 ± 5.3	15.3 ± 1.1	13.2 ± 0.9	0.99	1.08	36.97	~5	26.3 ± 1.2	25.3 ± 1.2
C4	334.2 ± 3.3	314.2 ± 2.5	363 ± 24	319 ± 27	1031 ± 66	1097 ± 62	159.4 ± 9.7	164.4 ± 9.3	25.4 ± 1.2	25.9 ± 1.1	1.19	1.29	38.60	~5	26.3 ± 1.3	25.1 ± 1.3
C5	331.5 ± 2.9	313.7 ± 2.7	335 ± 26	337 ± 19	1021 ± 62	1075 ± 61	158.2 ± 9.4	165.7 ± 9.4	24.7 ± 1.2	25.2 ± 1.0	1.18	1.27	39.18	~5	26.2 ± 1.2	25.1 ± 1.2
C6	332.2 ± 2.7	315.0 ± 2.2	357 ± 24	317 ± 25	1012 ± 63	1033 ± 61	153.4 ± 9.0	147.6 ± 8.7	24.3 ± 1.2	23.1 ± 1.0	1.17	1.20	38.91	~5	26.4 ± 1.2	24.5 ± 1.2
C7	332.5 ± 3.2	315.7 ± 2.2	366 ± 24	344 ± 24	1036 ± 62	1052 ± 62	161.1 ± 9.7	159.8 ± 9.3	25.5 ± 1.3	24.9 ± 1.1	1.22	1.24	38.84	~5	26.4 ± 1.2	25.1 ± 1.2
C8	333.1 ± 3.2	317.4 ± 2.5	352 ± 33	337 ± 23	1013 ± 64	1022 ± 61	158.5 ± 9.7	156.2 ± 9.5	25.1 ± 1.3	23.8 ± 1.1	1.16	1.19	38.42	~5	26.2 ± 1.4	25.4 ± 1.4
C9	333.5 ± 2.9	319.5 ± 2.6	338 ± 25	349 ± 22	992 ± 63	1000 ± 59	155.9 ± 9.4	152.1 ± 8.7	24.4 ± 1.2	23.4 ± 1.0	1.16	1.17	37.90	~5	26.1 ± 1.4	25.5 ± 1.4
D1	338.6 ± 3.0	318.6 ± 2.8	372 ± 26	384 ± 21	857 ± 54	979 ± 60	113.2 ± 7.6	130.6 ± 7.7	18.3 ± 1.1	21.0 ± 1.0	1.00	1.15	33.30	~5	26.1 ± 1.3	25.3 ± 1.3
D4	340.2 ± 2.9	314.7 ± 2.2	346 ± 25	335 ± 22	968 ± 63	1071 ± 62	151.2 ± 9.6	158.2 ± 9.2	24.9 ± 1.3	24.8 ± 1.1	1.14	1.27	38.28	~5	26.4 ± 1.2	25.0 ± 1.2
D5	339.6 ± 3.7	317.0 ± 2.4	365 ± 22	349 ± 24	986 ± 62	990 ± 58	152.7 ± 9.1	152.3 ± 9.0	25.0 ± 1.2	23.7 ± 1.1	1.16	1.19	39.01	~5	26.4 ± 1.3	25.1 ± 1.3
D6	335.1 ± 3.1	315.1 ± 2.8	353 ± 25	345 ± 24	1022 ± 64	1002 ± 58	157.9 ± 9.5	142.4 ± 7.9	25.2 ± 1.2	22.5 ± 1.0	1.19	1.16	38.80	~5	26.5 ± 1.3	25.0 ± 1.3
D7	331.3 ± 2.9	315.9 ± 2.7	328 ± 24	309 ± 24	1043 ± 62	1077 ± 60	159.4 ± 9.5	162.7 ± 9.1	24.2 ± 1.2	24.8 ± 1.0	1.21	1.25	39.09	~5	26.4 ± 1.3	25.1 ± 1.3
D8	335.8 ± 3.3	315.0 ± 2.6	313 ± 27	326 ± 21	1021 ± 61	1018 ± 58	158.8 ± 9.5	156.2 ± 8.8	25.0 ± 1.3	24.9 ± 1.1	1.20	1.20	38.60	~5	26.6 ± 1.3	25.1 ± 1.3
D9	335.8 ± 2.8	315.9 ± 2.7	351 ± 26	344 ± 30	977 ± 59	1023 ± 60	155.2 ± 9.3	156.0 ± 8.8	25.1 ± 1.2	24.9 ± 1.2	1.15	1.20	38.13	~5	26.2 ± 1.3	25.3 ± 1.3
E2	332.5 ± 2.6	315.8 ± 2.5	354 ± 23	338 ± 18	1122 ± 72	1364 ± 77	163.0 ± 11.0	180.0 ± 10	26.6 ± 1.4	28.4 ± 1.4	1.34	1.58	42.33	~5	25.5 ± 1.2	25.3 ± 1.2

E6	331.3 ± 3.0	312.0 ± 2.3	367 ± 26	343 ± 25	1030 ± 61	1057 ± 57	149.9 ± 8.1	148.8 ± 8.3	23.1 ± 1.0	23.3 ± 1.0	1.19	1.22	39.75	~5	26.3 ± 1.3	25.0 ± 1.3
E7	330.9 ± 2.7	307.9 ± 2.4	345 ± 27	388 ± 28	1012 ± 58	1046 ± 53	138.9 ± 7.3	157.4 ± 8.3	21.8 ± 1.0	24.8 ± 0.9	1.18	1.23	40.11	~5	26.0 ± 0.9	24.9 ± 0.9
E8	333.4 ± 3.3	314.9 ± 2.7	360 ± 28	326 ± 24	946 ± 54	999 ± 53	122.6 ± 6.7	155.5 ± 8.5	19.4 ± 0.9	23.3 ± 0.7	1.07	1.17	38.33	~5	26.6 ± 0.8	24.9 ± 0.8
F3	337.0 ± 3.0	321.0 ± 3.6	377 ± 22	329 ± 28	896 ± 55	877 ± 52	99.9 ± 6.0	98.1 ± 5.7	16.3 ± 0.8	15.3 ± 0.8	1.04	1.03	36.71	~5	26.0 ± 0.9	24.9 ± 0.9
F4	335.2 ± 3.2	316.3 ± 2.7	337 ± 24	331 ± 27	910 ± 55	1005 ± 54	102.9 ± 6.1	129.6 ± 6.6	16.9 ± 0.9	20.3 ± 0.8	1.05	1.17	36.30	~5	25.5 ± 1.0	24.9 ± 1.0
G1	343.6 ± 2.7	314.1 ± 3.1	356 ± 24	334 ± 29	905 ± 53	987 ± 57	103.8 ± 6.2	110.3 ± 6.5	17.2 ± 1.0	17.1 ± 0.9	1.08	1.13	37.13	~5	25.7 ± 1.0	25.1 ± 1.0
G2	338.5 ± 3.1	316.9 ± 2.6	362 ± 26	356 ± 32	901 ± 54	928 ± 56	100.7 ± 5.8	100.4 ± 5.8	16.3 ± 0.8	16.1 ± 0.9	1.06	1.07	36.64	~5	25.8 ± 0.9	25.3 ± 0.9
G3	342.8 ± 2.8	315.2 ± 3.0	350 ± 23	323 ± 24	901 ± 56	894 ± 51	102.1 ± 6.2	98.9 ± 5.6	15.9 ± 0.8	15.5 ± 0.8	1.05	1.05	37.05	~5	25.7 ± 0.8	25.0 ± 0.8
G4	339.9 ± 3.4	311.6 ± 2.7	351 ± 29	351 ± 28	882 ± 54	914 ± 47	100.6 ± 6.1	100.3 ± 5.1	16.0 ± 0.8	15.7 ± 0.8	1.03	1.06	36.32	~5	25.9 ± 0.8	24.9 ± 0.8
G5	336.0 ± 3.2	314.7 ± 3.9	338 ± 25	341 ± 23	856 ± 51	885 ± 49	95.0 ± 5.6	101.0 ± 5.6	14.9 ± 0.7	15.8 ± 0.8	0.98	1.02	34.70	~5	26.0 ± 0.8	25.0 ± 0.8

Table 3.3. Data pertaining to Age, U, Th and Pb concentration, calculated α-dose, amorphous fraction (AF%) and crater depth collected for counterpart locations between untreated (U) and annealed (A) Plešovice sample halves. *Uncertainties quoted for both age and concentration values are at the 2se level. **Uncertainties for α-dose were many orders of magnitude smaller than the calculated amount and were therefore not included for clarity. †The uncertainty associated with the AF%, require uncertainties of at least ± 5% accounting for scatter among multiple analyses and deviations due to different model loadings. Hence why absolute AF % values are not quoted for the annealed sample half, as the modelled values fall within this uncertainty limit. ‡ The representative depth of an individual crater is given by the mean of separate cross-sectional measurements made in differing orientation, with each intersecting the central region of the crater (n = 5) and its associated uncertainty is derived from the range in measured values.

3.4.8. Matrix dependent ablation behaviour

An examination of differential transient signal behaviour through time suggests a matrix dependent control over ablative process, enacting the systematic changes observed in measured $^{206}Pb/^{238}U$, without any contribution from ^{204}Pb. Transient signal behaviour can also be correlated to changes in particle size distribution by proxy with $^{238}U/^{232}Th$ fractionation (Fig. 3.6a).

3.4.8.1 *Seconds 0 – 1.5;*

An incomplete conversion of larger particulate matter into ions within the ICP, is thought to fractionate $^{238}U/^{232}Th$ towards high relative values (Guillong et al., 2003). Both matrixes demonstrate an energetic initial interaction with incident laser radiation, evidenced by a sharp rise in mean $^{238}U/^{232}Th$ at the onset of ablation (Fig. 3.6a). Initial laser-matter interactions for both matrixes therefore likely promoted the surface emission of larger particles relative to those produced subsequently.

The untreated matrix is interpreted to generate smaller mean particle sizes during its initial interaction with incident laser radiation than those of its annealed counterpart, as evidenced by a less dramatic increase in $^{238}U/^{232}Th$ at the onset of ablation. As laser coupling is established for each matrix, $^{238}U/^{232}Th$ decreases towards a stable lower value, reflecting a change in the particle size distribution within the emission products of ablation towards a distribution dominated by a smaller mean size fraction.

The shape of transient mean signal intensity traces within the first 1.5 s of analysis may also be indicative of difference in laser coupling efficiencies for both matrixes (Fig. 3.6b). The mean ^{206}Pb signal intensity trace pertaining to analyses of the untreated matrix diminish sharply from a peak value, whereas traces of the annealed analyses gradually reach peak intensity during this time interval before decaying. The mean ^{238}U signal intensity traces for both untreated and annealed samples similarly demonstrate a gradual rise towards and fall from a peak value, thus exhibiting a more "rounded" trace appearance (Fig. 3.6b).

3.4.8.2 *Seconds 1.5 – 5.5;*

The untreated matrix undergoes a decrease of mean $^{238}U/^{232}Th$ over the first 5.5 s of ablation from a peak value, eventually stabilising at a lower signal ratio value relative to its annealed counterpart (Fig. 3.6a). Furthermore, poor ionisation efficiency between 1.5 - 5.5 s for each matrix is also corroborated by a noisy $^{206}Pb/^{238}U$ signal ratio relative to the signal trace which follows thereafter (Fig. 3.6c-d).

The transient signal intensities derived from all analyses of annealed samples used in age determination (n = 31), when expressed as a mean trace demonstrate a universal increase in ^{238}U signal intensity by 5.46 % relative to their annealed counterparts, whilst also maintaining a similar rate of signal intensity decay (most notable from 1.5 s onward; Fig 3.6b). Despite the mean ^{206}Pb signal intensity trace being broadly similar between untreated and annealed halves (i.e. 0.93 %), the rate of ^{206}Pb signal intensity decay is slightly elevated in the untreated half (Fig. 3.6b).

3.4.8.3 *Seconds ~13;*

13 s marks a point of inflection in ^{206}Pb behaviour within the annealed mean trace, whereby before this point the mean ^{206}Pb signal intensity of the annealed sample analyses is 2.38 % lower relative to its untreated counterpart and where after it's 1.44 % higher. The behaviour of Pb during ablation of zircon is independent of crater-geometric control, therefore the difference in ^{206}Pb signal intensity and the change in the rate of its decay may point towards a matrix-dependent control on its measurement. On peak contributions from common ^{204}Pb contamination, cannot be invoked as a cause for this difference in signal response as the ^{204}Pb measured for both traces is well below the limit of detection (LOD), determined to be 3σ of 30 s baseline continuum signal. Surface contamination by common ^{204}Pb is also made unlikely by virtue of the fact that both crystal halves are mounted in close proximity within the same epoxy mount and were subject to the same polishing and cleaning protocols. Additionally, no significant change to mean $^{238}U/^{232}Th$ signal ratio is observed between the two analytical sessions in analyses of either untreated 91500 or WRS-1348 shown as inset plots within Figure 3.6d, suggesting that the change in particle size distribution is matrix dependent and not a result of fluctuating plasma conditions.

3.4.8.4 *Seconds 13 – 19;*

The bias in $^{206}Pb/^{238}U$ towards lower values observed within analyses of the annealed matrix, can be attributed to the systematic influence of reduced laser coupling efficiency with the annealed matrix. A relative decrease in mineral opacity following annealing (Fig. 3.1c) as well an increase in thermal conductivity and mass-density as a result of structural restoration in the wake of radiation damage related defects elicits a change in ablation emission products, relative to those produced in the untreated matrix. The change in ablation style as corroborated by observations of crater geometry, is correlated with a shift in particle size distribution towards large mean particle sizes which ionised less efficiently within the ICP, resulting in fractionation of $^{206}Pb/^{238}U$ signal ratios. The increase in mean ^{238}U measured signal intensity as observed within the annealed sample analyses is not reflected by a commensurate increase in measured ^{206}Pb signal intensity indicating a change in $^{206}Pb/^{238}U$ away from stoichiometric values is present from the onset of ablation and therefore cannot be attributed to depth-dependent fractionation.

The generation of larger relative particle distribution within the annealed samples is evidenced by proxy by means of a higher value $^{238}U/^{232}Th$ signal ratio relative to those displayed in the untreated sample. A similar matrix dependency upon mean particle size is noted by Guillong et al. (2003), wherein decreasing target opacity resulted in a greater optical penetration depth for wavelengths >193 nm. During the 5.5 – 19 s period of the time resolved analysis, there is a gradual increase in $^{206}Pb/^{238}U$ resulting from a depth-dependent retention of refractory ^{238}U during the laser-induced breakdown of zircon. The increasing rate of ^{238}U signal diminishment within the untreated matrix is subtle and likely due to a protracted development of what eventually become deeply incised sub-domains. The effect of downhole ^{238}U retention occurring at depth within in the annealed matrix however, demonstrates an earlier onset and greater rate of downhole fractionation due to the much higher rate of overall aspect-ratio increase (see Fig. 3.6d).

3.4.8.5 *Seconds 19-23 (23.5 s = laser-off);*

There is a marked increase $^{206}Pb/^{238}U$ after ~ 19 s evident in analyses of both matrixes. This increase is concomitant with a slight decrease in U^{238}/Th^{232} (Fig. 3.6a). A fractionation of U^{238}/Th^{232} towards yet lower values (Fig. 3.6a) may be indicative of a change in ablative mechanism occurring at depth, in which the emission products of ablation towards increasingly smaller mean particle sizes (Guillong et al., 2003). The observed decrease in U^{238}/Th^{232} may be attributed to a change in ablation processes away from a photothermal dominated mode of ablation potentially contributing towards an enhanced expression of downhole fractionation. Laser-induced plasma sampling (Eggins et al., 1998) and/or low-irradiance sampling (Liu et al., 2000) may become the dominant sampling processes within the confines of a deep, steeply sided crater. Both mechanisms have been shown to increase $^{206}Pb/^{238}U$ at depth. After 23.5 s there is a dramatic instability in U^{238}/Th^{232} following the cessation of the laser.

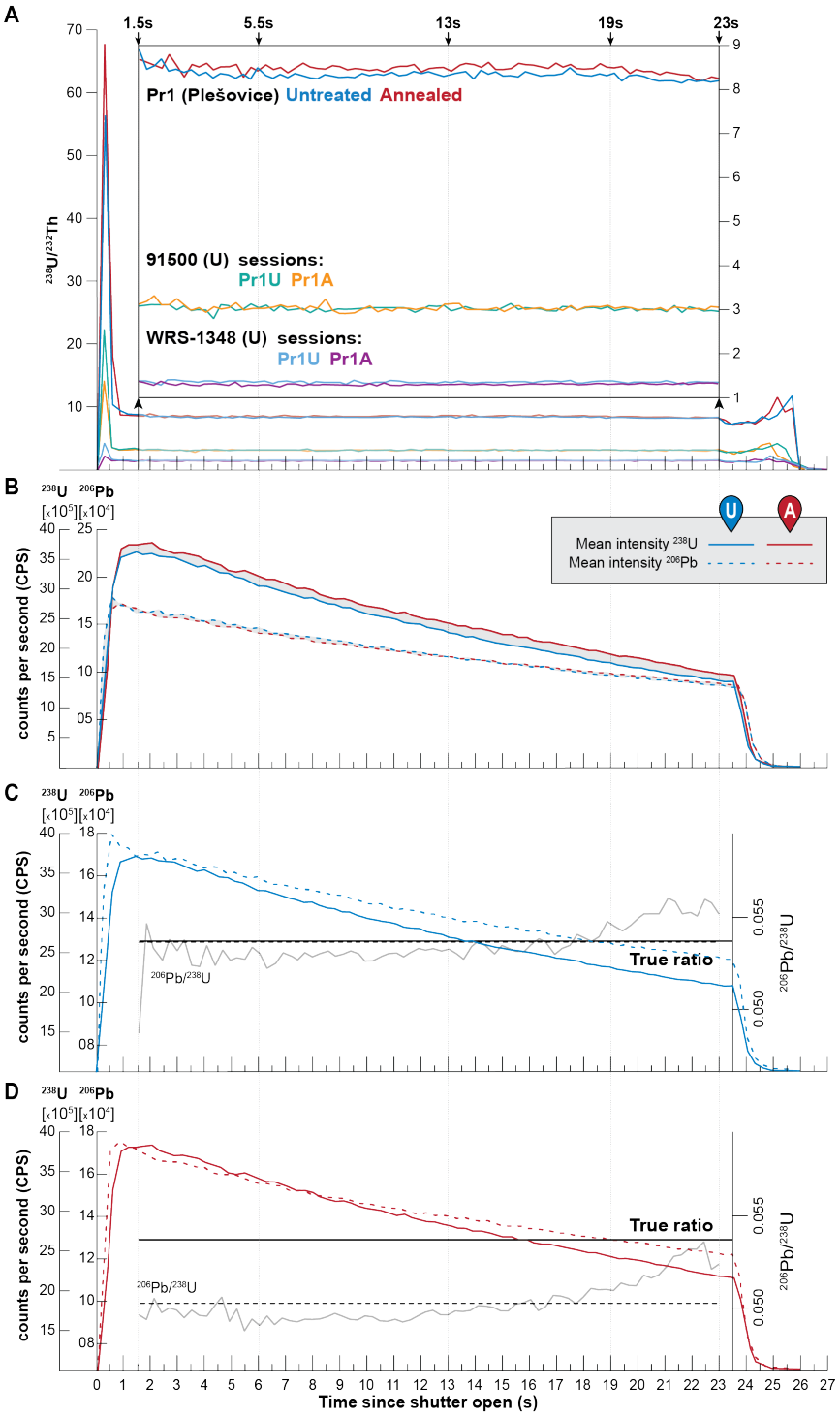


Figure 3.6 A) The mean of all uncorrected $^{238}U/^{232}Th$ determined over the course of ablation, evidences a relative difference in particle size distribution between the matrixes by proxy. The inset figure charts $^{238}U/^{232}Th$ for the integration period (between 1.5 and 23 s) at an expanded y-scale, annealed and untreated halves of the Pr1 sample demonstrate a significant offset in $^{238}U/^{232}Th$ value throughout the integration period. No such significant offset in $^{238}U/^{232}Th$ between analytical sessions Pr1U and Pr1A is observed for untreated analyses of both 91500 and WRS-1348. **B)** A comparison of the mean of all transient signal intensity traces used in age determination (n = 31) for both untreated and annealed analyses. **C)** The mean ^{206}Pb and ^{238}U intensity measured within an integration period for analyses of the untreated matrix. The scale of the ^{206}Pb [CPS] axis has

been adjusted for clarity. Also displayed is the corrected mean $^{206}Pb/^{238}U$ and its relationship to the accepted ratio value of Plešovice. **D)** charts the same parameters as B, but for analyses of the annealed matrix.

3.5. CONCLUSION

A comparative examination of Plešovice zircon crater geometry and elemental fractionation (i.e. U-Pb and U-Th) indicate ablation processes are matrix dependent. Differences in ablation emission products may be related to a disparity in optical and thermo-physical properties between otherwise analogous annealed and untreated matrixes. Inefficient coupling between the excimer 193 nm laser and a defect-free annealed matrix demonstrates a bias towards younger apparent weighted mean $^{206}Pb/^{238}U$ ages of (~ 7 % in this instance). Efficient laser-matter coupling is characterised by a shallow optical penetration depth coupled with low thermal conductivity for a given matrix, promoting substrate excitation and heating within a small interaction volume at or near the sample surface.

A maintenance of an efficient photothermal interaction is broadly exhibited by the untreated matrix by way of contrast with the defect-free annealed matrix herein. We suggest the presence of defects as a result of self-irradiation likely act as absorption centres, inhibiting excessive depths of optical absorption and dissipation of heat energy beyond a small volume of interaction. Analyses of the untreated matrix are characterised by craters which, in contrast to those of the annealed matrix, accurately approximate the area outlined by the laser-spot mask at the sample surface (97 %), degrading relatively slowly at depth (i.e. near-parallel side-walls).

Furthermore, there is little significant correlation between structural order (as assessed by PL) and ages determined within analyses of the untreated matrix, suggesting that effective mineral opacity (and relatedly colour) at 193 nm are only indirectly correlated with crystallinity. This is further corroborated, as a qualitative assessment of opacity and colour change occurring in the visible spectrum of light, does not render the annealed Plešovice matrix colourless or optically transparent despite a full restoration of crystalline order. What is more, the primary reference standard 91500 (although not shown) undergoes a dramatic loss of colour and opacity, becoming transparent in the visible spectrum following the same annealing treatment. High-temperature annealing as a pre-treatment, therefore should not be considered to homogenise a matrix sampling response under laser radiation, as the chemical composition remains unchanged. Instead the underlying element and trace element composition of a zircon primarily govern its behaviour during ablation, whereas its structural state acts only as the secondary control over ablation characteristics.

The fractionation of $^{238}U/^{232}Th$ is significant in this regard, as not only does it corroborate the differential ablation behaviour as observed in the differing crater geometries, but it also identifies by proxy, a relative difference in the mean particle sizes which reach the ICP source. The emission products of ablation within the annealed matrix are characterised by a distribution of particle sizes around a larger mean size relative to counterpart analyses in the untreated matrix. Apparent particle size distributions centred around

a larger mean size fraction are less efficiently ionised by the ICP source, thus enacting non-stoichiometric sampling from the onset of ablation.

The effective optical opacity of a target zircon matrix is an intrinsic contributing factor in the accuracy and precision of the determined U-Pb ages, owing to its control over particle-size distributions within the analyte volume. Similar optical absorption phenomena have been well documented for various wavelengths of laser (Guillong et al., 2003; Horn et al., 2001; Russo et al., 2000), however this study presents evidence that the effective optical opacity and thermo-physical properties of zircon govern the character and emission products of ablation even at deep UV wavelengths (193 nm). Improved ablation efficiency is correlated with a more accurate determination of $^{206}Pb/^{238}U$ age, as evidenced by the untreated zircon matrix, which retains a higher relative density of lattice defects.

The untreated Plešovice sample used herein expressed moderate radiation damage and it is likely that further improvements to ablative character would be expressed at yet higher levels of metamictisation, however other ablative processes may take effect for highly metamict zircons which may be dominantly or wholly amorphous, making a universal assessment of ablation behaviour difficult. Inducing crystal lattice defects by way exposure to an external source of ionising radiation may help to improve laser coupling by generating colour/absorption centres in matrixes which otherwise lack radiation damage. Sample pre-irradiation in this manner may therefore allow a more precise U-Pb dating of young (< 100 Ma) and/or defect free zircon matrixes by LA-ICP-MS.

3.6. ACKNOWLEDGEMENTS

C.L. acknowledge the use of instrumentation funded through an honorary-associate agreement with the ARC CCFS/Gemoc at Macquarie University Sydney. The analytical data were obtained using instrumentation funded by DEST Systemic Infrastructure Grants, ARC LIEF, NCRIS/AuScope, industry partners and Macquarie University. This is a contribution from the ARC Centre of Excellence for Core to Crust Fluid Systems (http://www.ccfs.mq.edu.au) and from the GEMOC Key Centre (http://www.gemoc.mq.edu.au). Financial support of C.L. and funding for publishing open access was provided by the Austrian Science Fund (FWF), through project J3662-N19 granted to C.L. J. Sláma is thanked for the supply of the Plešovice samples.

3.7. REFERENCES:

Allen C. M. and Campbell I. H., 2012. Identification and elimination of a matrix-induced systematic error in LA-ICP-MS $^{206}Pb/^{238}U$ dating of zircon. Chemical Geology, 323-333, 157-165.

Becker J. S. and Tenzler D., 2001. Studies of LA-ICP-MS on quartz glasses at different wavelengths of a Nd:YAG laser. Fresenius Journal of Analytical Chemistry, 370, 637-640.

Black L.P., Kamo S.L., Allen C.M., Davies D.W., Aleinikoff J.N., Valley J.W., Mundil R., Campbell I.H., Korsch R.J., Williams I.S. and Foudoulis C., 2004. Improved $^{206}Pb/^{238}U$ microprobe geochronology by the monitoring of trace element related effects; SHRIMP, ID-TIMS, ELA-ICP-MS and oxygen isotope documentation for a series of zircon standards. Chemical Geology, 205, 115-140.

Chew D. M., Petrus J. A., Kenny G. G. and McEvoy N., 2017. Rapid high-resolution U–Pb LA-Q-ICPMS age mapping of zircon. Journal of Analytical Atomic Spectrometry, 32, 262-276.

Chew D. M., Drost K., and Petrus J. A., 2019. Ultrafast, > 50 Hz LA-ICP-MS Spot Analysis Applied to U–Pb Dating of Zircon and other U-Bearing Minerals. Geostandards and Geoanalytical Research, 14, 39-60.

Cocherie A. and Robert M., 2008. Laser ablation coupled with ICP-MS applied to U-Pb zircon geochronology: A review of recent advances. Gondwana Research, 14, 597–608.

Corbett E. P., Simonetti A., Shaw P., Corcoran L., Crowley Q. G. and Hoare B. C., 2020. Shallow sampling by multi-shot laser ablation and its application within U-Pb zircon geochronology. Chemical Geology, 544, article 119568.

Crowley Q. G., Heron K., Riggs N., Kamber B., Chew D. M., McConnell B. and Benn K., 2014 Chemical Abrasion Applied to LA-ICP-MS U-Pb Zircon Geochronology, Minerals, 4, 503-518.

Eggins S. M., Kinsley L. P. J. and Shelley J. M. G., 1998. Deposition and element fractionation processes during atmospheric pressure laser sampling for analysis by ICP-MS, Applied Surface Science, 127-129, 278-286.

Fryer B. J., Jackson S. E. and Longerich, H. P., 1995. The design, operation and role of the laser-ablation microprobe coupled with an inductively coupled plasma-mass spectrometer (LAM- ICP-MS) in the Earth sciences. Canadian Mineralogist, 33(2), 303-312.

Firestone R. B., Shirley V. S., 1996. Table of isotopes. Wiley, New York, 3168.

Guillong M., Horn I. and Günther D., 2003. A comparison of 266 nm, 213 nm and 193 nm produced from a single solid state Nd:YAG laser for laser ablation ICP-MS. Journal of Analytical Atomic Spectrometry, 18, 1224-1230.

Hager J. W., 1989. Relative Elemental Responses for Laser Ablation-Inductively Coupled Plasma Mass Spectrometry. Analytical Chemistry, 61, 1243-1248.

Horstwood M. S. A., Košler J., Gehrels G., Jackson S. E., McLean N. M., Paton C., Pearson N. J., Sircombe K. N., Sylvester P., Vermeesch P., Bowring J. F., Condon D. J. and Schoene B., 2016. Community-derived standards for LA-ICP-MS U-(Th-)Pb geochronology – uncertainty propagation, age interpretation and data reporting. Geostandards and Geoanalytical Research, 40, 311-332.

Horn I., Guilling M. and Günther D., 2001. Wavelength dependant ablation rates for metals and silicate glasses using homogenized laser beam profiles – implications for LA-ICP-MS. Applied Surface Science, 182, 91-102.

Klötzli U., Klötzli E., Günes Z., and Koštler J., 2009. Accuracy of laser ablation U–Pb zircon dating: results from a test using five different reference zircons. Geostandards and Geoanalytical Research, 33 (3), 5-15.

Kooijman E., Berndt J., and Mezger K., 2012. U-Pb dating of zircon by laser ablation ICP-MS: recent improvements and new insights. European Journal of Mineralogy, 24, 5–21.

Košler J., Wiedenbeck M., Wirth R., Hovorka J., Sylvester P. and Míková J., 2005. Chemical and phase composition of particles produced by laser ablation of silicate glass and zircon – Implication for elemental fractionation during ICP-MS analysis. Journal of Analytical Atomic Spectrometry, 20 (5), 402-409.

Kuhn B. K., Birbaum K., Luo Y., Günther, D., 2009. Fundamental studies on the ablation behaviour of Pb/U in NIST 610 and zircon 91500 using laser ablation inductively coupled plasma mass spectrometry with respect to geochronology. Journal of Analytical Atomic Spectrometry, 25, 21-25.

Lenz C., Belousova E. and Lumpkin G. R., 2020. The In-Situ Quantification of Structural Radiation Damage in Zircon Using Laser-Induced Confocal Photoluminescence Spectroscopy. Minerals, 10, 83.

Liu H., Borisov O. V., Mao X. L., Shuttleworth S. and Russo R. E., 2000. Pb/U Fractionation during Nd:YAG 213 nm and 266 nm Laser Ablation Sampling with Inductively Coupled Plasma Mass Spectrometry. Applied Spectroscopy, 54 (10), 1435-1442.

Markopoulos A. P., Koralli P., Kyriakakis G., Kompitsas M., and Manolako D. E., 2016. Molecular dynamics simulation of material removal with the use of laser beam. In: Davim J. P. (ed), Materials Forming and Machining: Research and Development. Woodhead Publishing (Cambridge), 117-153.

Mank A. J. G. and Mason P. R. D., 1999.. A critical assessment of laser ablation ICP-MS as an analytical tool for depth analysis in silica-based glass samples Journal of Analytical Atomic Spectrometry, 14 (8), 1143–1153.

Marillo-Sialer E., Woodhead J. D., Hergt J., Grieg A., Guillong M., Gleadow A., Evans N., and Paton C., 2014. The zircon "matrix effect": evidence for an ablation rate control on the accuracy of U–Pb age determinations by LA-ICP-MS. Journal of Analytical Atomic Spectrometry, 29 (6), 981.

Marillo-Sialer, E., Woodhead, J.D., Hanchar, J.M., Reddy, S.M., Greig, A., Hergt, J., Kohn, B., 2016. An investigation of the laser-induced zircon matrix effect. Chemical Geology, 438, 11–24.

Murakami T., Chakoumakos B. C., Ewing R. C., Lumpkin G. R., Weber W. J., 1991. Alpha-decay event damage in zircon. American Mineralogist, 76, 1510-1532.

Nasdala L., Wenzel M., Vavra G., Irmer G., Wenzel T. and Kober B., 2001. Metamictisation of natural zircon: Accumulation versus thermal annealing of radioactivity-induced damage. Contributions to Mineralogy and Petrology, 141, 125-144.

Nasdala L., Lengauer C. L., Hanchar J. M., Kronz A., Wirth R., Blanc P., Kennedy A. K., and Seydoux-Guillaume A. M., 2002. Annealing radiation damage and the recovery of cathodoluminescence. Chemical Geology, 191, 119–138.

Nasdala L., Kronz A., Hanchar J. M., Tichomirowa M., Davis D. W. and Hofmeister W., 2006. Effects of natural radiation damage on back-scattered electron images of single crystals of minerals. American Mineralogist, 91, 1739-1746.

Nasdala L., Hofmeister W., Norberg N., Mattinson J. M., Corfu F., Dörr W., Kamo S. L., Kennedy A. K., Kronz A., Reiners P. W., Frei D., Kosler J., Wan Y., Götze J., Häger T., Kröner A. and Valley J., 2008. Zircon M257 - a homogeneous natural reference material for the ion microprobe U-Pb analysis of zircon. Geostandards and Geoanalytical Research, 32(3), 247-265.

Petrus J. A. and Kamber B. S., 2012. VizualAge: A novel approach to laser ablation ICP-MS U– Pb geochronology data reduction. Geostandards and Geoanalytical Research, 36, 247–270.

Pointon M. A., Cliff R. A. and Chew D. M., 2012. The provenance of Western Irish Namurian Basin sedimentary strata inferred using detrital zircon U–Pb LA-ICP-MS geochronology. Geological Journal, 47, 77–98.

Paton C., Hellstrom J., Paul B., Woodhead J. and Hergt J., 2011. Iolite: Freeware for the visualisation and processing of mass spectrometric data. Journal of Analytical Atomic Spectrometry, 26, 2508–2518.

Paul B., Paton C., Norris A., Woodhead J., Hellstrom J., Hergt J. and Grieg A., 2012. CellSpace: A module for creating spatially registered laser ablation images within the Iolite freeware environment.Journal of Analytical Atomic Spectrometry, 27, 700-706.

Pidgeon R. T., 2014. Zircon radiation damage ages. Chemical Geology, 367, 13-22.

Russo R. E., Mao X. L., Borisov O. V. and Liu H., 2000. Influence of wavelength on fractionation in laser ablation ICP-MS. Journal of Analytical Atomic Spectrometry, 15 1115-1120.

Steely A. N., Hourigan J. K., and Juel E., 2014. Discrete multi-pulse laser ablation depth profiling with a single-collector ICP-MS: Sub-micron U-Pb geochronology of zircon and the effect of radiation damage on depth-dependent fractionation. Chemical Geology, 372, 92-108.

Sláma J., Kosler J., Condon D. J., Crowley J. L., Gerdes A., Hanchar J. M., Horstwood M. S. A., Morris G. A., Nasdala L., Norberg N., Schaltegger U., Schoene B., Tubrett M. N., Whitehouse,M. J., 2008. Plešovice zircon – A new natural reference material for U-Pb and Hf isotopic microanalysis. Chemical Geology, 249, 1–35.

Vasantgadkar N. A., Bhandarkar U. V., and Joshi S. S., 2010. A finite element model to predict the ablation depth in pulsed laser ablation. Thin Solid Films, *519*(4), 1421–1430.

Vermeesch P., 2018. IsoplotR: a free and open toolbox for geochronology. Geoscience Frontiers, 9, 1479–1493.

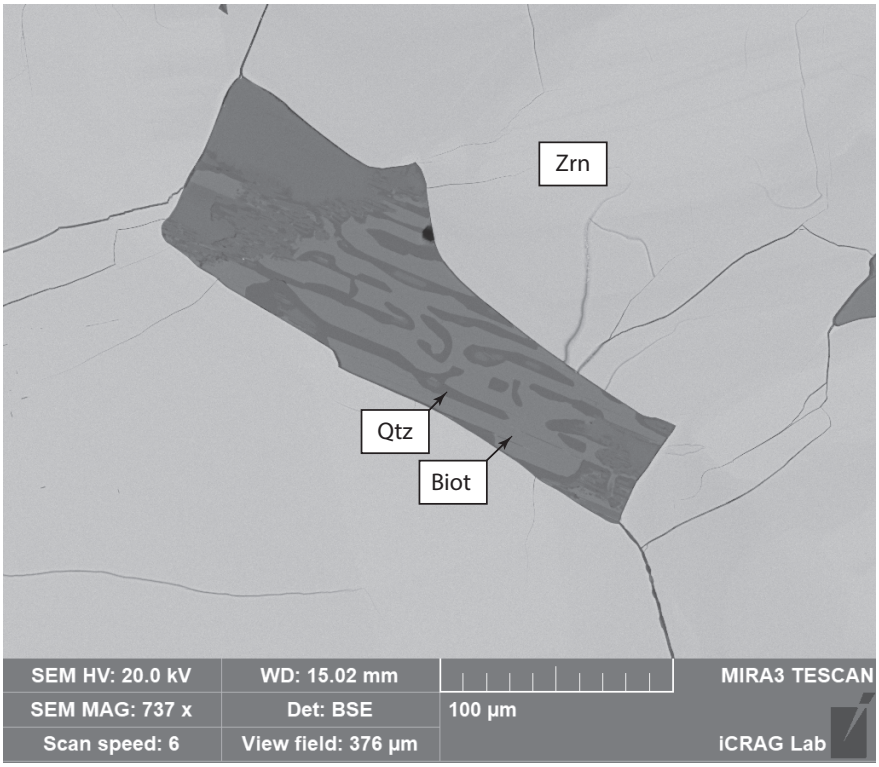
Wiedenbeck M., Alle P., Corfu F., Griffin W. L., Meier M., Oberli F., von Quadt A., Roddick J. C. and Spiegel W., 1995. Three natural zircon standards for U-Th-Pb, Lu-Hf, trace element and REE analyses. Geostandards Newsletter, 19, 1–23.

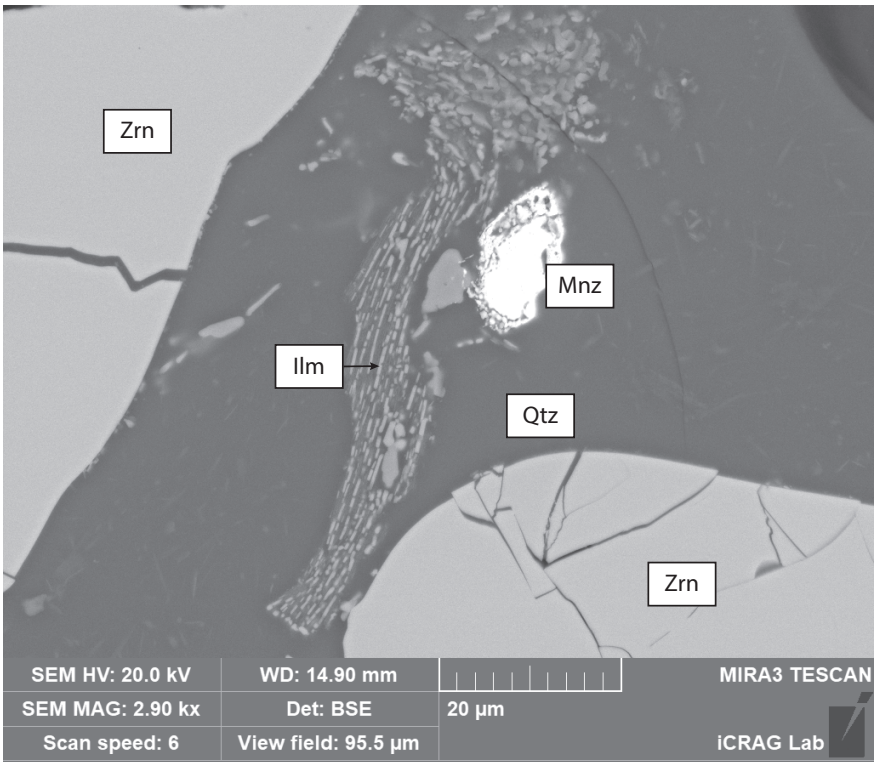
Wiemer, D., Allen C. M., Murphy D. T. and Kinaev I., 2017. Effects of thermal annealing and chemical abrasion on ca. 3.5 Ga metamict zircon and evidence for natural reverse discordance: Insights for U-Pb LA-ICP-MS dating. Chemical Geology, 466, 285-302.

3.8. SUPPORTING INFORMATION AND SUPPLEMENTARY FIGURES

3.8.1. Identification of inclusions present within Plešovice zircon

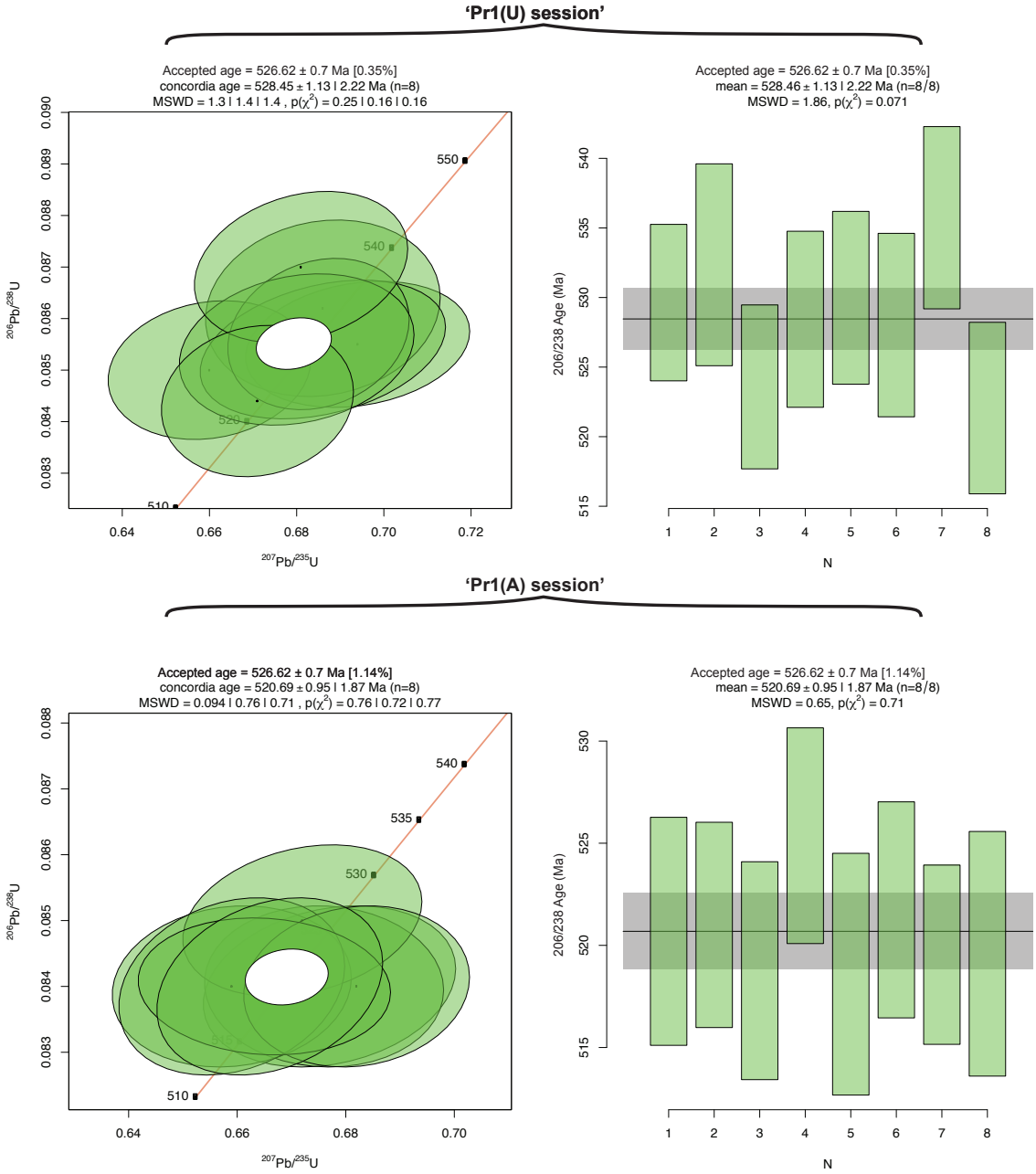
An identification of surface inclusions was made aided by an EDS probe, and are shown herein on annotated BSE images. An identification of these inclusions guided the choice of monitor elements used to identify occurrences of sub-surface inclusions where they might be encountered during LA-ICP-MS.





3.8.2. WRS-1348 Age plots

Concordia and weighted mean $^{206}Pb/^{238}U$ plots corresponding to secondary validation standard analyses of WRS-1348 zircon, conducted within Pr1(U) and Pr1(A) sessions as part of a sample-standard bracket. WRS-1348 bracketed analyses of untreated and annealed Plešovice, which was treated as an 'unknown' in separate sessions, Pr1(U) and Pr1(A) respectively.



CHAPTER 4

Anomalous age distribution, isochron evolution and trace element mobilisation in crystalline zircons as evidence for fluid mediated structural re-equilibration.

Prepared for submission to Chemical Geology

Co-authors: [1]Martin J. Whitehouse, [2]Brendan C. Hoare, [3]John M. MacDonald, [4]Elisabetta Mariani, [2]Niall McEvoy, [5]Antonio Simonetti, [2]Quentin G. Crowley

[1.] Naturhisoriska Riksmuseet, Sweden
[2.] Trinity College Dublin, Ireland
[3.] University of Glasgow, UK
[4.] University of Liverpool, UK
[5.] University of Notre Dame, USA

4.1. ABSTRACT

Zircon grains from shear zone adjacent granulite-facies banded gneisses of the Lewisian Gneiss Complex in Northwest Scotland demonstrate a distribution of apparent ages which are anomalous both in respect of their intra-crystalline textural context and wider geological context. Detailed textural, micro-structural, and isotopic observations evidence a fluid-catalysed recrystallisation of pre-existing radiation-damaged zircon material by a fluid-mediated recrystallisation reaction process, which operates to partially reset zircon U-Pb systematics. A recognition of its characteristic features allows for reacted and un-reacted domains to be distinguished and for meaningful ages pertaining to discrete intra-crystalline domains to be determined from zircons, which might otherwise be disregarded in an analysis of such rocks. Upper-intercept ages from unreacted domains, potentially record protolith ages, whereas reacted and/or partially reacted domains may provide temporal constraints on the timing of the recrystallisation reaction. Isolated age determinations made in the absence of textural context and without a recognition of alteration features may result in a misinterpretation of timing of tectonothermal events within complex rocks such as these.

4.2. INTRODUCTION

Zircon ($ZrSiO_4$) is a widely used U-Pb mineral chronometer due its, ability to incorporate U and Th in trace concentrations (i.e. up to thousands of ppm), its primary exclusion of incompatible ^{204}Pb during crystallisation, its robust mechanical properties, its low solubility in both fluids and melts, its chemical stability over a wide temperature range and its diverse lithological occurrence (Peterman et al., 2016; Kusiak et al., 2015; Seydoux-Guillaume et al., 2015; Kogawa et al. 2012; Cherniak et al., 2010; Reddy et al., 2006; Watson et al., 1997). Zircon also has a tendency to incorporate trace elements (e.g. REE, Hf, Y, Ti) useful as geochemical tracers (Kogawa et al, 2012; Cherniak et al., 2010). Combined, these traits enable zircon to preserve several generations worth of textural, chemical and age information at a fine-scale internally.

Spectacular internal zoning is a common feature of zircon observed by back-scattered electron or cathodoluminescence imaging. The "sluggish" rate by which the diffusion of most cations proceeds in crystalline zircon lattice, accounts for the preservation of such sharply contrasting domains even at the most extreme thermal conditions (Cherniak et al., 2010; Cherniak et al., 1997). Empirically-derived diffusion coefficients for tetravalent cations of U, Th and Hf substituting on the Zr site are extremely slow in the temperature ranges between 1400-1650 ºC and essentially immobile below *c*. 900 °C (Meis and Gale, 1998; Cherniak et al., 1997). Divalent cations of Pb have a diffusion coefficient 4 orders of magnitude greater than that of U and Th at 1100 °C (Lee et al., 1997), and possibly as high as 6 orders of magnitude (Cherniak and Watson, 2000). It should be made clear, however, that these diffusion estimates apply strictly to crystalline zircon. Diffusion may be significantly enhanced in zircon whose structure has been altered either by metamictisation or plastic deformation (e.g., MacDonald, et al., 2015; Reddy et al., 2006, 2007; Cherniak and Watson, 2000; Cherniak et al., 1991).

There is ample evidence to suggest however that elements, even those bound at primary tetravalent sites within the zircon lattice, can be mobilised at temperature conditions lower than those predicted by empirical diffusion studies (e.g. Timms et al., 2006; Geisler et al., 2003; Geisler et al., 2002; Pidgeon and Compston 1992; Gebauer and Grünenfelder 1976). The seemingly inconsistent retention of elements at low temperatures has been variously observed, however little consensus has been reached on any causative mechanism(s) (as discussed by Kramers et al., 2009). An isotopic disturbance of the system which results in a loss of intermediate or end-member products from the U-Pb decay chains, helpfully manifests as a non-corroboration of $^{206}Pb/^{238}U$ and $^{207}Pb/^{235}U$ ages (i.e. *normal* discordancy). Much of the attention on element mobility has focussed on the phenomenon of episodic Pb loss (Mezger and Krogstadt, 1997; Mattinson et al. 1996; Silver and Deutsch, 1963). Relatedly therefore, the valency and specific locus of radiogenic Pb accommodation within the lattice structure are all topics of attention and debate (e.g. Villa and Hanchar, 2017; Kogawa et al., 2012; Kramers et al., 2009; Utsunomiya et al., 2004; Cherniak and Watson, 2003; Cherniak and Watson, 2000; Cherniak et al., 1997; Kober 1987). In addition to being locally lost, Pb can be gained (e.g. McFarlane et al. 2005), or redistributed at an intracrystalline level (e.g. Regis et al. 2017; Peterman et al. 2016; Valley et al. 2014; Whitehouse et al. 2014; Kusiak et al. 2013). The loss or gain of U

(e.g. Seydoux-Guillaume et al., 2015; Romer, 2003; Geisler et al. 2002) and intermediate daughter products (i.e. Rn), have also seen increasing attention as potential causes of discordancy (e.g. Eakin et al., 2016; Suzuki, 1987).

It is broadly agreed, that the retention of elements and isotopes in zircon is governed to some degree by the maintenance of a sound crystal structure, ergo any physical modification of the lattice structure could result in the loss or redistribution of component elements and isotopes (Wiemer et al. 2017; Kogawa et al., 2012). The zircon lattice provides stoichiometric sites that can accommodate 5^+ ions (e.g. P, on the 4-fold coordinated Si site), 4^+ ions (Hf, U, Th and Ti replacing the Zr site in 6-fold coordination), and 3^+ ions (REE, also replacing the Zr site) (Crowley et al., 2014; Schaltegger et al., 2014; Finch and Hanchar 2003). The suitability for primary substitution by cations is governed by both their ionic radius and charge. Substitutions which incur minimal strain across either or both Si^{4+} and Zr^{4+} sites will be favoured (Harley and Kelly, 2007). The large ionic radius of Pb^{2+} (1.29 Å) is prohibitive for direct substitution into either 4-fold coordinated site (Kogawa et al., 2012; Shannon, 1976). Large quantities of Pb^{2+} (including ^{204}Pb) cannot therefore be accommodated within the cation sites of zircon during initial crystallisation (Watson, 1997).

Metamictisation by self-irradiation is often proffered as an explanation for the observed distribution (and accommodation) of incompatible elements (e.g. Pb, Ca and Al) in zircon (Geisler et al. 2007; Rayner et al. 2005; Ewing et al. 2003; Nasdala et al. 2001). During an α-decay event, a high-energy light α-particle (Helium nucleus) is ejected from the nucleus, losing most of its energy through electronic interactions along the length of its trajectory (Nasdala et al. 2001). At the termination of this 'track' the α-particle dissipates its remaining energy in the form of elastic collision with surrounding lattice atoms, whereby hundreds of atoms may be displaced (Geisler et al., 2003; Nasdala et al. 2001). Isolated atoms are displaced (forming mainly Frenkel defects), along this relatively long-order α-particle trajectory of 16-22 μm (Geisler et al. 2007; Utsunomiya et al., 2004). Momentum is conserved during the ejection of the α-particle, by the low-energy α-recoil of the relatively heavier daughter nucleus. This dissipates a large proportion of its energy over a very short-order range through elastic collision with surrounding atoms. A collision cascade involving approximately 4000 atoms radiates from the point of recoil until all of the energy is dissipated, resulting in a disordered (amorphous) domain of up to 5 nm in diameter (Geisler et al. 2003, 2007; Ewing et al., 2003, 2000; Farnan and Salje, 2001;). Atomic displacements as a result of α-recoil therefore account for the primary source of radiation damage (Geisler et al., 2001). Isolated amorphous domains may continue to accumulate over geological time to form an interconnected network of overlapping amorphous domains (i.e. the so-called "first percolation transition"; Salje et al., 1999), until such a point as crystalline domains cease to remain interconnected (i.e. the "second percolation transition"; Salje et al., 1999). Self-irradiation (metamictisation) is also a contributing factor in intracrystalline elemental mobility and/or redistribution. Incompatible elements partition into crystal point-defects, fractures and/or amorphous domains in preference to pristine lattice material (Wiemer et al, 2017). Metamictisation in many cases facilitates the enhanced diffusion of U, Th and Pb even at low temperatures through the associated development of so-called fast-

diffusion pathways (FDPs) (Peterman et al., 2016; Piazolo et al., 2016; Kusiak et al., 2015). Metamictisation may also catalyse mineral-fluid interaction (Geisler et al., 2007) and potentially reduce Pb^{4+} to Pb^{2+} (Seydoux-Guillaume et al., 2015).

Metamictisation may facilitate element redistribution however it does not always appear to be a requirement (Whitehouse et al., 2014). Microstructures (e.g., dislocations, low-angle orientation boundaries, and sub-grains) generated as a result of plastic deformation of the crystal structure can also aid in the diffusion of elements (MacDonald et al., 2013; Reddy et al., 2007, 2006; Timms et al., 2006). Plastic deformation occurs when stress is accommodated within a grain by the formation and migration of dislocations through a crystal lattice (MacDonald et al., 2013; Reddy et al., 2006). Crystals may also grow with such defects and therefore contain deformation-related microstructures from the time of their initial formation (MacDonald et al., 2013). Mechanisms by which crystalline order is restored during the 'amorphous-to-crystalline transition', play a critical role in the migration and retention of elements. Crystallinity can be restored either via a process of annealing or recrystallisation.

The direct mechanism by which annealing proceeds remains debated (Gesiler et al. 2001; Nasdala et al., 2001). It has been suggested that annealing of entirely metamict zircon is a two stage process, which occurs under both "dry" and "wet" conditions alike (Pidgeon et al., 2017; Gesiler et al. 2001; Capitani et al., 2000, Zhang et al., 2000). The recovery kinetics of annealing is temperature dependent involving an initial phase of low temperature diffusion of structural defects, resulting in strain relaxation (e.g., Colombo and Crosch, 1998). This initial recovery phase is followed at higher temperature conditions by a phase of epitaxial recrystallisation (e.g., Capitani et al. 2000). The transitory appearance of a possible intermediate phase between 800 and 1400 K (e.g., Zhang et al., 2000) as well as the formation of a ZrO_2 phase (e.g., Pidgeon et al., 2017) have also been suggested to aid in the 'amorphous-to-crystalline transition'. Geisler et al. (2004) highlighted the profound influence of water in lowering the activation energy for nucleation and zirconia formation. As well as temperature and the presence (or absence) of fluids, it has been suggested that the initial structural state of the zircon crystals may also dictate the specific mechanism by which annealing proceeds (Zhang et al., 2000). The establishment of nucleation and subsequent epitaxial recrystallisation is slower in fully metamict zircon (Capitani et al., 2000). The migration and concentration of elements (especially radiogenic Pb), have been variously reported following partial or wholesale structural recovery of the zircon crystal lattice by annealing (e.g. Kusiak et al., 2018; Whitehouse et al., 2017; Valley et al., 2015; Utsunomiya et al., 2004).

Recrystallisation is arbitrarily defined, however it is used herein to refer to a process of structural and chemical re-equilibration or "re-growth" of zircon at the expense of amorphous components. Complex secondary internal textures imaged by means of backscatter electron (BSE) or cathodoluminescence (CL) microscopy can be indicative of zircon which has reacted with a fluid or melt. Such textures may be characterised by inward-penetrating, irregularly curved and/or 'cauliflower-like' alteration zones, which

commonly cross cut primary growth structures and often display a close association with fractures, inclusions and porous domains (Geisler et al. 2007). Geisler et al. (2007) proposed two distinct mechanisms by which such complex secondary internal textures and element transport may arise; coupled dissolution-reprecipitation (CDR) and diffusion-reaction. Both mechanisms have significant implications for the chemical stability of both metamict and crystalline zircon and each leave an indicative post-re-equilibration chemical and structural signature, outlined in greater detail within Geisler et al. (2007).

Zircon studied herein provide evidence of a decoupling of textural, chemical and age information on an intra-crystalline scale. This study combines observations variously obtained at micrometer to sub-micrometer scales, by cathodoluminescence (CL), back-scatter electron (BSE) microscopy, raman spectroscopy, and scanning ion imaging (SII) by way of secondary ion mass spectrometry (SIMS). We provide nanoscale evidence for trace element mobility during a fluid-mediated re-equilibration of zircon by CDR. This observation has important consequences for the understanding of phenomena of U–Pb discordance, reverse discordance and anomalous (reverse) age zonation of natural zircon.

4.3. GEOLOGICAL SETTING AND SAMPLES

4.3.1. Regional Geology

The four zircon samples used in this study belong to the JM09/DP01 sample set of MacDonald et al. (2015) which were collected near Duartmore Point (UK grid reference NC178359) belonging to the central region of the Archaean-Palaeoproterozoic Lewisian Gneiss Complex (LGC) of NW Scotland, and a detailed interpretation of their temperature-time history is included therein. The rocks of the LGC contains examples of some of the oldest rocks in Europe with protolith ages of up to ~3 Ga (Kinny et al. 2005; Whitehouse 1989; Friend and Kinny 1995), however the distinctions made between metamorphic episodes has been made difficult by complex polyphase intra-crystalline textural relationships coupled with pervasive alteration and Pb-loss overprinting (e.g. Whitehouse and Kemp, 2010). The difficulty in determining the absolute timing of tectonothermal events has been made manifest in the literature by numerous conflicting interpretations of their relative timing (see discussion in Crowley et al., 2015).

4.3.1.1 *Protolith (c. 3.0 – 2.8 Ga):*

The lithologies of the LGC, are largely composed of tonalite-trondhjemite-granodiorite (TTG) orthogneisses (Rollinson and Windley, 1980), with minor components of mafic, ultramafic and metasedimentary rocks. The rocks of the central region of the LGC have experienced a protracted and complex history of deformation, metamorphism and intrusion spanning over 1 Ga (Johnson and White, 2011). Of the complicated post-crystallisation tectonothermal-history recorded by the LGC, lithologies of central region preserves structures metamorphic assemblages and field-relationships associated with a sequence of three distinct events, namely the; Badcallian, Inverian and Laxfordian.

The complex post-crystallisation history is often manifested within internally complex polyphase zircon as a distribution of U-Pb ages along the concordia curve. Profound and variable Pb-loss severely complicates the interpretation of the magmatic crystallisation age of protolith, as well as earlier metamorphic events (see discussion in Whitehouse and Kemp, 2010), what is more there is little consensus on whether ages derived from core domains represent inherited xenocrystic or primary magmatic growth components (Crowley et al., 2015). The oldest estimates of the TTG protolith age were proposed by Friend and Kinny (1995) to be in the range c. 3030 - 2960 Ma. A similar estimate of c. 2960 Ma, was made by MacDonald et al. (2015). Younger age estimates of c. 2950 - 2850 and c. 2843 Ma were made by Whitehouse and Kemp (2010) and Goodenough et al. (2013) respectively.

4.3.1.2 *Badcallian (at c. 2.76 Ga):*

During the earliest granulite-facies Badcallian event, the TTG magmatic protoliths underwent gneissification and partial melting (Rollinson, 2012; Johnson and White, 2011) and are thought by some to have experienced protracted ultra-high temperature (UHT) granulite-facies metamorphism at 2490 - 2480 Ma (Love et al., 2010), however there is also evidence of an earlier 2760 Ma metamorphic event (Zhu et al., 1997; Corfu et al., 1994; Cohen et al., 1991).

Peak temperatures (T) are interpreted to have reached either c. 769 - 841 °C (Zircon Ti-thermometry; MacDonald et al., 2015) or 875 - 975 °C (mineral equilibria modelling; Johnson and White, 2011) and pressures (P) at c. 8.5 - 11.5 Kbar. Rollinson (2012) demonstrated that the protolith to the TTG granulite gneisses probably contained a mafic hydrous phase (most probably hornblende) and underwent fluid-absent partial melting, whereby the un-melted fraction evidences an ultra-depleted basaltic pre-cursor source, with very low concentrations of Rb, Th, U and Ta. The onset of granulite-facies metamorphism, is concomitant with extreme instances of Pb-loss in accessory zircons at c. 2.5 Ga (Whitehouse and Kemp, 2010).

4.3.1.3 *Inverian (c. 2.49 – 2.48 Ga)*

The rocks from which the zircons in this study were isolated, retain Badcallian gneissic layering despite having experienced subsequent static retrogression to an amphibolite-facies mineralogy in the presence of shear-zone related fluids, during the Inverian event (Evans, 1965; Attfield, 1987; Jensen, 1984). The timing of the Inverian event has been constrained to between 2490 - 2480 Ma by some authors (e.g. Goodenough et al., 2013; Whitehouse and Kemp, 2010; Corfu et al., 1994), although some attribute these dates to Badcallian Granulite-facies events (e.g. Love et al., 2012, Kinny et al., 2005). An episode of mafic dyke intrusion in the central region constitutes an important field-based chronological marker largely designating the end of the Inverian event. The main intrusion of the so-called Scourie Dyke Swarm was dated by Davies and Heaman (2014) between c. 2418 - 2375 Ma. Any subsequent deformation of the dykes separates pre- and post-dyke tectonothermal events, namely ‘Scourian’ and ‘Laxfordian’ events respectively (MacDonald, et al. 2015; Sutton & Watson 1951).

4.3.1.4 *Laxfordian (c. 1.79 Ga, c. 1.75 Ga; 1.69 – 1.67 Ga)*

The term Laxfordian, has been commonly used to describe 'post-dyke' deformation and is associated with an amphibolite-facies event which demonstrates widespread static overprinting earlier assemblages and structures (Sutton and Watson, 1951). However, in addition to evidence of widespread deformational processes, evidence of several temporally and spatially discrete events have also been recorded, including magmatic emplacement and hydrothermal episodes (Goodenough et al., 2013). U-Pb analysis of titanite and monazite from the central region determine an age of c. 1750 Ma for Laxfordian metamorphism, which is followed by significant hydrothermal events at between c. 1690 – 1670 Ma, with widespread expression throughout the LGC (Kinny and Friend, 1997; Corfu et al., 1994). The timing constraints for partial melting and metamorphism within the Laxfordian have since been extended as far back as c. 1790 Ma (Goodenough et al., 2013).

4.4. SAMPLE DETAILS

The zircons studied herein were collected from lithologies which retain Badcallian associated granulite-facies gneissic layering, despite having experienced subsequent static retrogression to an amphibolite-facies mineralogy within the margins of a ~15 m wide Laxfordian shear zone. The adjacent Laxfordian shear zone has moderate to strong planar and linear fabrics and an amphibolite-facies hornblende + plagioclase + quartz assemblage. The shear zone locally cross-cuts both the Badcallian gneissic fabric as well as a nearby metadoleritic intrusion of the Scourie Dyke Swarm (for details see MacDonald, et al. 2015).

4.5. ANALYTICAL METHODS

Samples GMDP01Z2, GMDP01Z6, DP01Z10 and DP01Z4 have all been previously analysed by MacDonald, et al. (2015) recording their U-Pb age and trace element (REE and Ti) composition by ion-microprobe, details of which can be found therein. Samples GMDP01Z2 and GMDP01Z6 contain individual zircon crystals isolated from the host rock by conventional separation techniques. Samples DP01Z10 and DP01Z4 however, are zircons hosted within rock fragments and retain their lithological context. All samples were mounted in 25mm diameter epoxy rounds, which have since been re-polished to reveal a new internal surface. Material was removed uniformly from the surface of the mount using a Struers LaboPol 21 automated polisher using successively finer diamond suspension fluids, until a 0.25 µm was achieved. Then chemical polishing using a colloidal silica suspension, to remove the surface layer damage. Sample mounts were thoroughly sonicated in both ethanol and purified water, before being dried with compressed air prior to receiving a ~ 12 nm-thick layer of carbon coating.

Electron backscatter diffraction (EBSD) imaging was conducted using a CamScan X500 CrystalProbe thermionic field-emission scanning electron microscope (FE-SEM) at the University of Liverpool. Analytical procedures broadly follow that of Mariani et al., (2009). Electron backscatter diffraction patterns (EBSPs) were obtained using a 20 kV acceleration voltage, 35 nA beam current and 25

mm working distance. These data were indexed within the Flamenco module of HKL CHANNEL5 software and misorientation maps were processed in the Tango module and are composites of both band contrast (BC) and texture component (TC) maps. Grid spacing between 0.3 and 0.5 µm was used over areas between 200 x 175 µm and 330 x 350 µm respectively. The orientation differences (disorientation or misorientation) are made relative to a single point reference. The uncertainty on measurements of orientation is ± 0.5 °.

Cathodoluminescence (CL), back-scattered electron (BSE) and energy-dispersive X-ray spectroscopy (EDS) imaging were conducted using a TESCAN TIGER MIRA3 variable pressure field-emission scanning electron microscope (FE-SEM) at the iCRAG lab, Trinity College Dublin. An accelerating voltage of 10 kV and 5 kV was used for grain-scale CL and BSE imaging respectively, both using a 5nA beam current. Inset images of DP01Z10 for both BSE and EDS were obtained using 15kV accelerating voltage, maintaining a 5nA beam current.

Raman spectroscopic mapping was performed at the Centre for Research on Adaptive Nanostructures and Nanodevices (CRANN), Trinity College Dublin, using a WITec Alpha 300R in an identical fashion to methods employed by Chew et al. (2017). Excitation was achieved using a 532 nm (green) wavelength laser operating at 5mW power. A 20x objective lens (0.4 numerical aperture) and a spectral grating of 1800 lines/mm were used allowing the resolution of spectral features and bands within a spectral window of ~1cm^{1}. A single pixel on the Raman maps is equivalent to 1 µm^2 (i.e. each 100 x 100 µm area consists of 10000 individual spectra).

Scanning Ion Imaging (SII) was performed using a CAMECA IMS-1280 large-geometry ion microprobe located at the NordSIMS facility, Swedish Museum of Natural History. The analytical method herein follows closely those described by Bellucci et al. (2016) and Whitehouse et al. (2014) and is only briefly described here. Prior to SIMS analysis, the carbon coat was removed with a lint-free wipe and the mounts were subjected to repeated sonication in both ethanol and high-purity water before being dried and gold-coated. Before each SII acquisition, an area of 80 x 80 µm undergoes a pre-sputtering by an O_2^- primary beam for 10 min using a 200 µm projected aperture (~20 µm effective spot diameter) at a beam current of ~10 nA. This effectively removes surface gold coating and any residual surface contamination. The uniform implantation of oxygen across the upper surface of the intended 70 x 70 µm target grid also enhances secondary ion yield (Bellucci et al., 2016). For SII acquisition over this same area, the primary beam formed in the projected aperture (Köhler) mode generates and effective ~2 µm spot diameter (projected 20 µm aperture, nominal beam current of ~ 100 pA), which is translated through a raster grid pattern of 70 x 70 µm. The synchronous secondary ion beam was deflected using the dynamic transfer optical system (DTOS) onto the ion optic axis of the instrument, thereby allowing high mass-resolution (i.e. M/ΔM 4,860), whilst the image acquisition software reconstructs the sample image based on the primary beam position at a specific time. Simultaneous detection of ^{204}Pb, ^{206}Pb, ^{207}Pb, and ^{208}Pb was achieved using four ion-counting electron multipliers in the multi-collector array, while ions of ^{180}Hf^{16}O, ^{238}U and ^{238}U^{16}O2 were measured in subsequent peak hops.

Images were processed using the CAMECA WinImage2 software package, which integrated all cycles and calculated isotope ratios from user defined 'regions of interest' (ROIs) selected over the imaged area. The selection of ROIs was guided principally by zonation and features as observed in CL, as well as the identification of ^{206}Pb 'hot spots'. The same ROIs selections are applied to grids analyses of the M257 zircon reference material (Nasdala et al., 2008) under the same analytical conditions as a control. Isotope ratios of $^{204}Pb/^{206}Pb$, $^{207}Pb/^{206}Pb$, $^{208}Pb/^{206}Pb$, $^{206}Pb/^{238}U^{16}O_2$, $^{238}U^{16}O_2/^{180}Hf^{16}O_2$ were calculated in WinImage2 and exported to in-house Microsoft Excel© spreadsheet where ion gain and U/Pb elemental fraction corrections were applied (for details see; Whitehouse et al., 2014). No common Pb correction was applied.

4.6. RESULTS AND DISCUSSION

4.6.1. Isotopic disturbance and textural decoupling

A detailed description of textural features is made in *section 4.6.2*, for representative sample DP01Z10, however all panchromatic CL images as shown in Figure 4.1, demonstrate a textural complexity typical of zircons from high-grade metamorphic rocks (e.g. Ge et al., 2019; MacDonald et al., 2015). Most samples contain a homogenous CL-dark core indicative either of primary magmatic or inherited origin, mantled by moderately intense CL-grey domains, which may to varying degrees cross-cut and/or embay the pre-existing CL-dark material. The CL-grey domains may either feature oscillatory zonation (as in DP01Z10), or sector zonation (as in GMDP01Z2 and GMDP01Z6). CL-bright domains comprise the largest proportion of these zircons and may feature truncated zonation as well as some internal structure, characterised by replacement-style variably chaotic, streaked and/or mottled CL patterns, which in most cases are also spatially associated with a thin CL-grey outer rim. Sample DP01Z4 lacks any CL-dark component, suggesting either that the core component was not revealed during polishing or more likely still (given its relative size), that the core domain has been entirely replaced by a recrystallisation reaction which has gone to completion. All grains have a sub-rounded morphology in cross-section.

A comparison of panchromatic CL images and data derived from SII in Figure 4.1, demonstrates a seemingly spurious distribution of apparent $^{207}Pb/^{206}Pb$ ages, which are spatially decoupled from what would be the expected textural succession within a zoned zircon grain. It must be assumed that the CL-dark domains where they are observed, represent the oldest textural domain within these four samples and domains surrounding the CL-dark core, represent later intervals of zircon growth or recrystallisation, which should become progressively younger towards the exterior of the grain. Despite this however, domains outboard of the core exhibit comparatively older apparent isotopic ages and indicate that these grains have experienced intra-crystalline element redistribution.

The inset boxes represent each SII sampling grid (70 x 70 µm), with each being numbered according to their order of appearance in Figure 4.1. Representative $^{207}Pb/^{206}Pb$ ages are denoted for each region defined by the dashed lines. The distribution of ages as observed cannot be reconciled with the textural

succession of domains outboard of the CL-dark core and are geologically meaningless when observed in isolation, with some examples having and apparent age older than the Earth without any spatial association with potential sources of common Pb contamination, such as fractures (e.g. 4715 Ma; Fig. 4.1; DP01Z10(3)). Isotopic redistribution can lead to differences in apparent age of up to ~ 2.2 Ga within an area less than 70 x 70 μm.

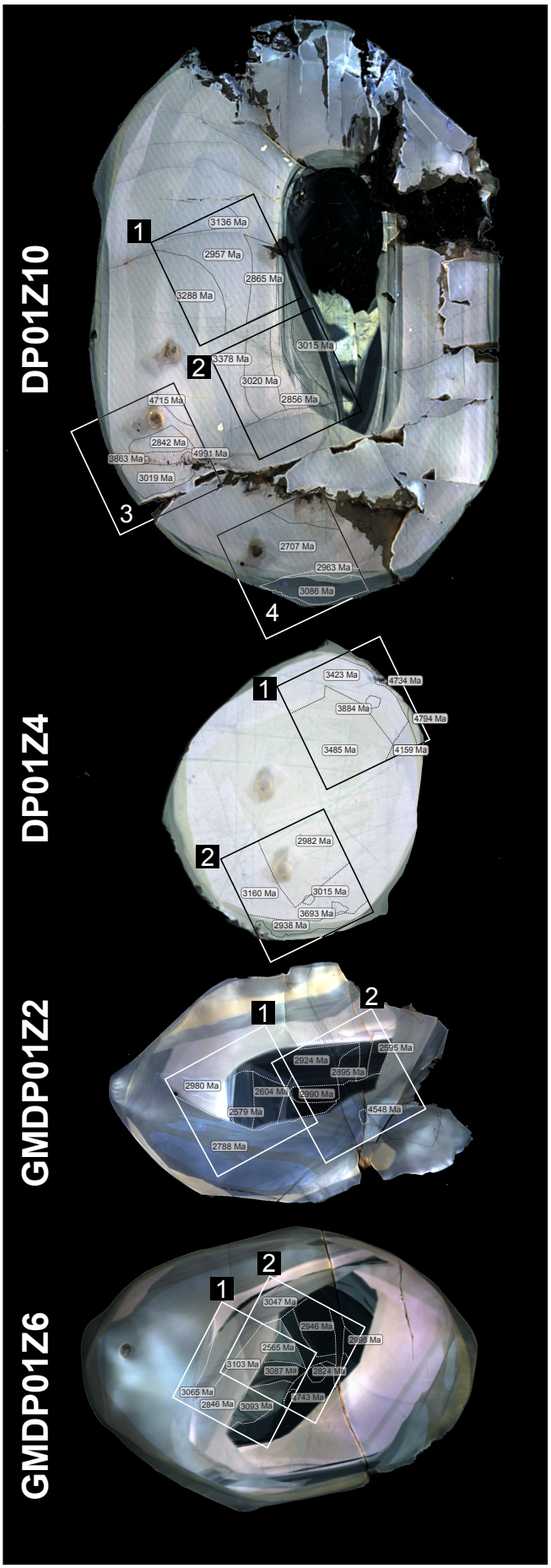


Figure 4.1 Panchromatic CL images for each of the four grains within this study. Boxes delineate the location of SII sampling grids of 70 x 70 µm, within which representative regions demonstrating an anomalous distribution of apparent $^{207}Pb/^{206}Pb$ ages are superimposed.

4.7. TEXTURAL OBSERVATIONS

For brevity and clarity, observations made on sample DP01Z10 (Fig. 4.2) are assumed largely representative of metamorphic processes shared between all samples within this study, however detailed textural observations were made on all samples, which collectively inform the subsequent interpretation of isotopic age data. The numbered squares represent the sampling location of subsequent SII grids, each of which is 70 x 70 μm. The dashed rectangle represents the sampling location of further imaging by BSE and EDS as seen in Fig. 4.3. Furthermore, both raman and EBSD are both techniques which are sensitive to small changes in surface topography therefore both failed to adequately sample regions below the surface, notably; the innermost core domain, fractures, old SIMS spot analyses and most the uppermost portion of the grain (Figures 4.2c and d respectively). Textural features cited within each section of the text below are labelled with roman numerals which are also displayed in Fig 4.2.

4.7.1. CL imaging

The innermost textural domains of sample DP01Z10 contain both a CL-dark core [i] in close association with a contrastingly bright, yellow-blue CL domain [ii] (Fig. 4.2a). These contrasting domains interface along a sharply defined and jagged junction [iii], perhaps consistent with the CL-dark core domain having experienced late- to post-magmatic recrystallisation as it cooled, however a metamorphic origin cannot be discounted (Corfu et al., 2003). It is likely that the innermost domain is xenocrystic in origin, as remnant zonation evident in the CL-bright domain is oriented at right angles to subsequent cross-cutting zonation. The innermost domain is mantled by CL-grey material expressing fine-scale oscillatory zonation [iv], which truncates pre-existing domains along an inwardly-penetrating and sharply defined, curved boundary [v]. These CL-grey domains have previously been interpreted to reflect zones which have grown either by solid-state recrystallisation of the existing core, or through an episode of growth during the partial melting and resorption occurring during the Badcallian tectonothermal event. (MacDonald et al., 2015; Johnson et al., 2013, 2012; Rollinson, 2012; Rollinson and Gravestock, 2012).

The CL-grey domain has potentially experienced a subsequent episode of fluid-catalysed recrystallisation, as evidenced by the disruption of its zonation by a CL-bright domain [vi]. Altered domains are characterised by a more intense CL response interpreted by Geisler et al. (2003a) to indicate structural recovery after radiation damage. The presence of hydrothermal fluids (> 200 ºC) greatly enhances the reaction kinetics of nucleation and regrowth (hereafter termed recrystallisation) after amorphous zircon (Geisler et al., 2003b). The interface between the CL-grey material and the surrounding CL-bright material is delineated again by a further sharp compositional boundary, which is rounded in outline [vii]. The CL-bright domain constitutes the largest single CL component by area, however it demonstrates heterogeneous luminescence being characterised by a streaky appearance. Zircon CL expression is governed by compositional and structural state. The heterogeneity expressed within the CL-bright domain therefore likely represents an underlying variability with regard to chemical composition (e.g. REEs and actinide concentration) as well as an incomplete recovery of zircon lattice order during recrystallisation (Geisler et

al., 2003b; Nasdala, et al., 2002). The outermost rim domain [viii] is similar in CL intensity to that of the CL-grey mantle surrounding the core domain. It also is observed to penetrate pre-existing CL-domains along curved boundaries.

CL imaging also reveals a multitude of faint fractures which traverse the interior of the grain cross-cutting all CL domains, but which are mainly concentrated outboard of the CL-grey domain outboard of the innermost core. Most of these faint fractures are absent from BSE images (Fig. 4.2b), suggesting that they were likely to have been 'healed' either during one (or several) of the fluid-mediated structural recrystallisation events and/or by annealing during protracted high temperatures. These fractures may have facilitated an inward progression fluid as well as acting as pathways for chemical exchange between the reaction front and percolating fluids during previous recrystallisation reaction processes. CL imaging potentially evidences several temporally distinct episodes of fluid-mediated zircon reaction may be in evidence for sample DP01Z10 whose relative timing can be determined by virtue of cross-cutting relationships along inwardly curved embayments or by the truncation of zonation. However, the presence of inwardly-curved embayments of previously existing textural domains, as well as the presence of patchy heterogeneous CL expression alone cannot adequately distinguish between the processes of CDR or diffusion-reaction, as these features are common to both.

4.7.2. BSE imaging

Sample GMDP01Z10 as imaged under BSE (Fig. 4.2b), highlights most noticeably a radial pattern of fractures propagating from the boundary of the CL-dark core cross-cutting each successive CL domains [i]. This pattern of brittle fracturing within the zircon material surrounding the core likely results from the macroscopic volume expansion of amorphous the xenocrystic cores as a result of accrued radiation damage (Wiemer et al., 2017; Seydoux-Guillaume et al., 2015). The establishment of fractures following radiation damage is an important initial step in the fluid-mediated recrystallisation process, as it provides a preferential pathway from fluid ingress and elemental exchange. Previously healed fractures are not represented in BSE imagery, potentially having been chemically equilibrated during successive recrystallisation events. A change in BSE intensity towards brighter responses can be observed in close association with most of the major fractures contained within this sample [ii], corroborating the notion that fluid-interface exchange was facilitated by a network of fractures within the grain (Wiemer et al., 2017; Seydoux-Guillaume et al., 2015; Geisler et al 2003b).

4.7.3. Structural order and lattice orientation

If it is assumed that the U-Pb isotopic system has remained relatively undisturbed within the CL-dark core domain, a maximum α-dose of ~ 3.7 x 10^{15} α mg^{-1} is predicted from preliminary LA-ICP-MS analysis of GMDP01Z2 (see supplementary material). Guiding an interpretation of a pre-cursor zircon, which had accrued α-recoil damage within Stage II damage accumulation beyond which, an intra-crystalline network of overlapping amorphous domains is established (Pidgeon, 2014; Salje et al., 1999; Murakami et al., 1991).

This is corroborated by textural evidence of volume swelling as a result of self-irradiation of the core domain (i.e. radial fracturing of the surrounding CL-bright mantle). It is recognised that the α-recoil damage predicted within the surrounding reacted domain of ~ 3 x10^{14} α mg^{-1} is inaccurate due to isotopic disturbance of the ages used in their calculation, and no textural evidence exists in support of this prediction.

Raman crystallinity maps evidence a lattice which is generally well-ordered, yielding no significant raman spectral shifts or broadening of the $\nu_3(SiO_4)$ stretching band at the ~1005.5 nm spectral peak (Fig. 4.2c). The full width half-maximum (FWHM) values of this band from the sample surface are < 5 cm^{-1} and thus considered *'well-crystallised'* (Nasdala et a., 2001, 1996, 1995). Domains which may have experienced significant radiation damage, have since had their crystalline order largely restored by a combination of the recrystallisation process in the reacted domains and considerable wholesale annealing. The innermost core domain retains a higher FWHM relative to the surrounding domains, which supports the assumption that it has remained largely unaffected by subsequent fluid alteration reactions, however its present day expression of radiation damage as charted by raman FWHM mapping, is lower than that predicted by α-dose calculations. This suggests that it has experienced natural annealing during its thermal history.

Domains interpreted to have experienced recrystallisation demonstrate a subtle, lateral variation in measured structural order, which are correlative with the streaky appearance of CL intensity response within the same domain. Despite the a somewhat variable expression of structural order within the recrystallised domain levels of structural order are higher relative to those of domains interpreted to have remained unreacted (e.g. CL-dark core) which retain radiation damage associated structural disorder. Sharply defined boundaries as viewed in CL between textural domains, are mirrored in many cases by a sharp interface between domains of high structural order and those of lower relative structural order, best expressed at the boundaries of both the core and outermost rim features [i]. A sharply defined interface between reacted and un-reacted domains by way of structural order is expected following a CDR reaction, whereas a gradual restoration of structural order over broader length scales is expected during diffusion-reaction (Geisler et al., 2007).

The outermost rim also demonstrates an elevated degree of radiation damage relative to the reacted domain, which is concomitant with the moderate CL-grey intensities as observed in Figure 4.2a [viii]. Enhanced radiation damage in this domain is consistent with its elevated concentration of U as observed by SII (e.g. Fig. 4.4; DP01Z4(4)). This outermost domain may represent an overgrowth crystallisation of a new phase from a more U-enriched source, however this domain is cross-cut by both old 'healed' and more recent fractures, suggesting that it existed prior to their creation. A more likely explanation is that this CL-grey, U-rich, radiation damaged domain represents a repository for incompatible elements removed from reconstituted zircon at the trailing edge of the reaction.

A measure of lattice misorientation by EBSD is charted in Figure 4.2d. EBSD mapping reveals no significant lattice misorientation within the reacted domain. The proportion domains offset from the reference point (marked by a red dot) is denoted by the scale-bar adjacent histogram, whereby the majority of point measurements across the sample surface demonstrate a relative offset of < 2º. Despite lacking misorientation data from the topographically depressed core, the establishment of preferential pathways of trace element re-distribution (including Pb^{*}) within the reacted domain by the proliferation of low-angle boundary formation and/or dislocation creep during crystal-plastic deformation (e.g. Kovaleva et al., 2017; Piazolo et al., 2016; MacDonald et al., 2013; Reddy et al., 2006) is not supported by lattice orientation measurements made herein.

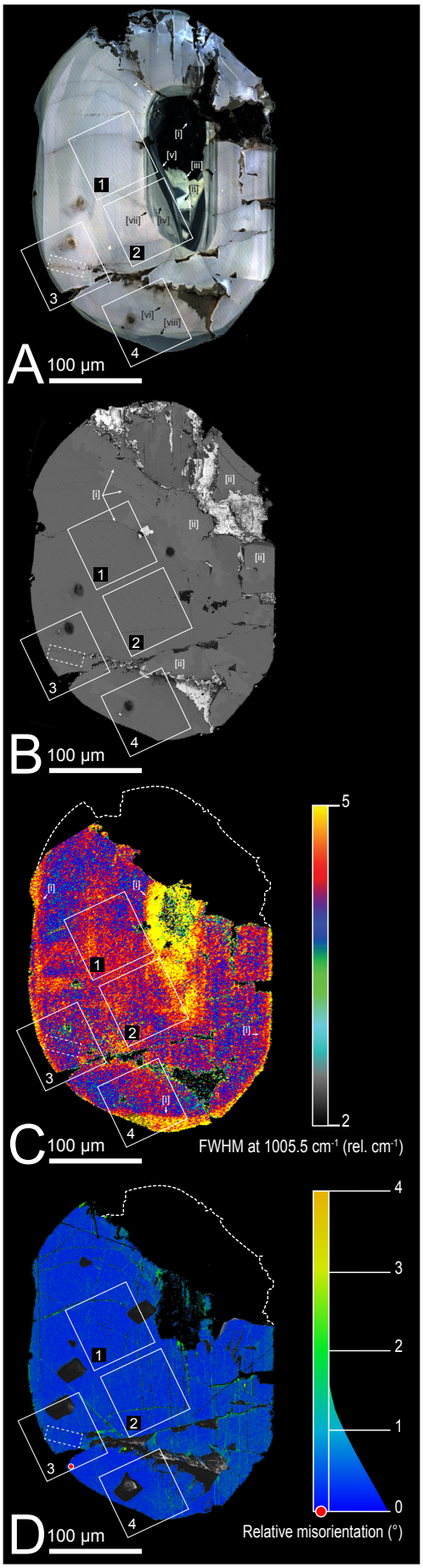


Figure 4.2 A) Panchromatic CL imaging of sample DP01Z10 exhibits a succession of distinctive domains mantling a CL-dark remnant core. The surrounding CL-bright zircon is interpreted to represent a recrystallised domain characterised by inwardly curved embayments of the core, and a chaotic, streaked appearance. Features marked by roman numerals are described in detail in the text. **B)** BSE imaging reveals sets of conchoidal fractures radiating from the central most domain, indicative of volume expansion of a radiation damaged core domain. Chemical alteration is also in evidence in close association with larger fracture zones. **C)** Raman micro-structural mapping reveals a recrystallised matrix which is well-ordered with respect to broadening of the $\nu_3(SiO_4)$ spectral peak at 1005.5 nm (expressed as FWHM). The streaked appearance exhibited in CL of the recrystallised domain, is mirrored to some extent by the structural order exhibited by raman mapping. Both the core and rim domains exhibit the greatest degree of structural disorder, wherein the core is interpreted to represent an unreacted remnant of pre-existing zircon. A stark contrast in structural order is exhibited within boundary domains of both the core and rim where they meet the recrystallised domain, is indicative of structural re-equilibration by CDR (see Geisler et al., 2003b). **D)** EBSD misorientation mapping reveals a zircon lattice which broadly contains < 2º relative orientation difference to the reference point marked in red. Also indicated are the SII imagining grid locations (boxes) and the region containing inclusions as seen in Fig. 4.3 (dashed rectangle).

4.7.4. The occurrence of non-formula elements

Fluid mediated alteration in zircon has been variously reported be accompanied by the influx of zircon non-formula elements U, Th, Y, P and in particular Ca occurrences of which are associated with an anti-correlation with primary Zr (e.g. Wiemer et al., 2017; Seydoux-Guillaume et al., 2015; Untsunomiya et al., 2004; Geisler et al., 2003a, 2003b). Samples GMDP01Z2 and DP01Z10, exhibit micrometer-scale sub-circular to elongate features containing non-formula elements which display an anti-correlation with Zr, an example of which can be seen in Fig. 4.3. These features usually exhibit a sub-circular surface expression and are distributed in alignment as a trail, often associated with fracture zones. Some exhibit an elongate habit, which are themselves aligned perpendicular to the direction of spread within the trail and resemble pores and channel structures associated with reaction front domains (e.g. Figure 1 in Geisler et al., 2003b). Other nano-scale features exhibiting a similar distribution are also present (highlighted in Fig. 4.3 by white arrows), however their composition cannot be determined due to their small size.

The features may be interpreted in one of two ways; they may represent remnant pores which facilitated the kinetic progression of a fluid catalysed reaction and an exchange of elements between the dissolution-reprecipitation front and the external fluids. Their micrometer scale dimension and anti-correlation with Zr would indicate they were formed during a CDR reaction (as opposed to a diffusion-reaction), acting as active pathways for elemental flux which operated in close association with fracture domains. During a CDR reaction, the 'parent' zircon is completely dissolved and any incompatible elements hosted therein are actively rejected from the newly forming zircon, therefore the enrichment of newly formed zircon with non-formula elements is highly unlikely. An enrichment of non-formula elements within the recrystallised zircon is usually an unambiguous indicator of a diffusion-reaction process, however the occurrence of non-formula is limited in this instance to some isolated pores in close association with fracture domains. It is conceivable that the non-formula elements observed occupying these pore-like features represent an outgoing flux of incompatible elements which were trapped as the reaction was halted.

The alternative interpretation is that these features may once have been part of a fracture network involved in fluid percolation and element redistribution. Inclusions enriched in non-formula elements become spatially isolated from the fracture as it 'heals' either during recrystallisation or by annealing. Such a process may trap non-formula elements (including incompatible Pb^{2+}) as inclusions within a recrystallized zircon matrix which is otherwise U, Th, Pb, Fe, Mg and Ca poor. Such inclusions often occur below spatial scales resolvable by SII (~ 2 μm). The process of inclusion formation is akin to the process of metallic Pb entrapment within nano-spheres as described by Kusiak et al., 2013. It must be also considered however, that the juxtaposition of these features with fractures may be an artefact of the polishing process, which exposes small cross-sectional regions of a larger sub-surface fracture enriched in non-formula elements. Some micrometer-scale and all nano-scale trails exist however, in spatial isolation from any visible fractures, however they retain the trail-like alignment with one another.

An interpretation of closure of these features be they pores or fracture zones by annealing is supported by the observation that the relative concentration of non-formula elements increases in concentric bands towards the interior-most regions of the inclusion, whilst the opposite trend is observed in Zr intensity. The hazy outline exhibited by some of these features imaged by BSE microscopy is correlated with a recovery of Zr intensity and a complete lack of non-formula enrichment. This may indicate that zircon structural recovery after fracturing may be hampered by the presence of residual incompatible element enriched domains.

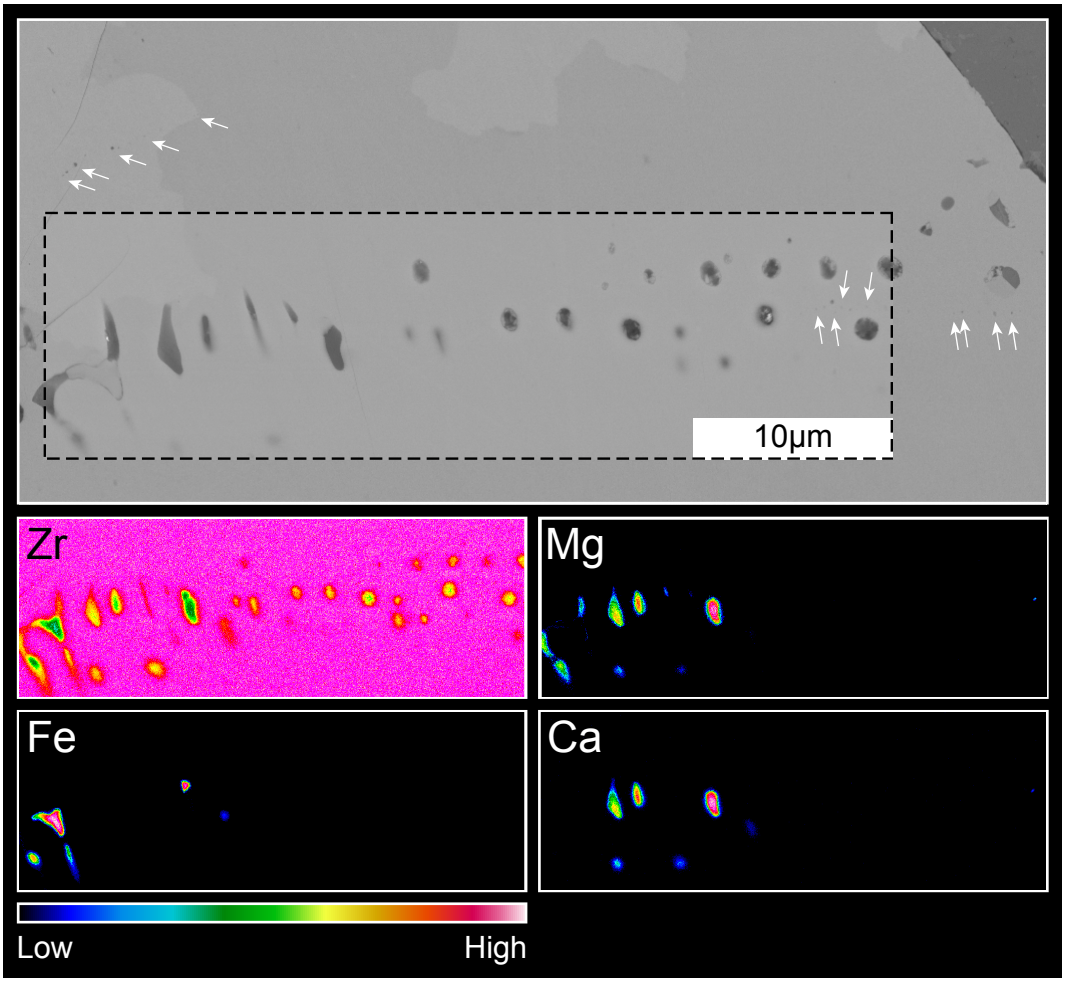


Figure 4.3 A BSE image of micrometer-sized circular to elongated inclusions in DP01Z10, which are variously observed within almost all samples. They exist either as trails stemming from visible fracture zones at a micrometer scale, or as nanometer features isolated from obviously fracture domains (marked as arrows). The composition of the nanometer features is unknown due to their size, however the micrometer sized features exhibit an enrichment in non-formula elements (i.e. Mg, Ca, Fe) with respect to their surroundings. EDS mapping of the sub-region marked by the dashed rectangle, reveals the relative intensities of these elements, which often increases in a concentric pattern towards the interior of the features, and exhibit an anti-correlation with Zr.

4.8. ANOMALOUS AGE ZONATION REVEALED BY SCANNING ION IMAGING

4.8.1. General observations

A SII image was produced across an analytical grid of 70 x70 μm was conducted for each of; ^{180}Hf, ^{238}U, common (Pb_c) and all radiogenic (Pb^*) Pb isotopes (Fig. 4.4). An inset figure of correlated CL expression accompanies each, however for a macroscopic spatial context readers are directed to Figure 4.1. SII herein do not display any obvious signs of trace element redistribution in the form of obvious "hotspots", as are often reported by age zoned zircons from other metamorphic zircons (e.g. Whitehouse et al., 2014; Kusiak et al., 2013), moreover these zircons are notably lacking in terms of U and Pb counts outboard of core domains where analysed.

Isotopic ratio determinations were made for user-defined regions of interest (ROIs) and are delineated by solid or dashed lines in each case and all ratio and age determinations for ROIs displayed in Figure 4.4 are summarised in Table 4.1. ROIs delineated by dashed lines in Figure 4.4 enclose domains which are enriched with respect to one or other of the measured isotopes and are not necessarily guided by domains as observed in CL. These regions are usually small in area and exhibit poor counting statistics, having $^{207}Pb/^{206}Pb$ and $^{206}Pb/^{238}U$ measurement uncertainties in excess of 10 %. Nonetheless they have their $^{207}Pb/^{206}Pb$ ages displayed (which often vary dramatically) as they inform an observation of elemental redistribution into localised intra-crystalline domains. It is recognised that some of these ROIs outline features which reside within or very near fracture domains and are relatively enriched in Pb_c (e.g. Figure 4; GMDP01Z2(2); 4548 Ga). Others however display spurious ages and an enrichment in isotopes (including Pb_c) in spatial isolation from surface expressions of fracturing (Fig. 4.4; DP01Z10(3); 4715 Ma). ROIs approximately enclosing the inclusion features as observed in Figure 4.3, exhibit an enrichment in Pb^* isotopes and generate apparent ages of 4116 Ma, 3361 Ma, and 5016 Ma (Fig. 4.4; DP01Z10(3))

Some other occurrences of faint sub-circular enrichments are also variously observed in most if not all other sampling grids, giving Pb^* isotope (especially ^{206}Pb) maps a faint mottled appearance. Some are highlighted within dashed ROIs existing as enrichments of unsupported Pb^* isotopes only (i.e. in the absence of ^{238}U and Pb_c) and are in spatial isolation of any visible features in CL (e.g. Fig. 4.4; DP01Z10(1, 2); DP01Z4(1, 2)). This may point towards a matrix enrichment in Pb^* within inclusions after healed fracture domains, which are unsupported by a similar enrichment in ^{238}U. The large rounded enrichments in ^{180}Hf are due to enhanced secondary ion yield from within pre-existing SIMS spots which survived the polishing process.

ROIs which are enclosed by solid lines and which are labelled numerically represent analyses which are included within concordia diagrams (Figs. 4.5 and 4.7). Each sample is labelled in numerical sequence in order of increasing $^{207}Pb/^{206}Pb$ age and the colour coded circle makes reference to the textural domain to which each ROI pertains. This colour coding is applied to all figures containing data derived from these ROIs wherein; *red* coded domains represent the innermost CL-domain interpreted to have remained

unaltered during the CDR reaction; *purple* being domains demonstrating oscillatory and/or sector zonation potentially representing an episode of zircon growth during the partial melting and resorption occurring during the Badcallian tectonothermal event (CL-grey domain (I)); *blue* belongs to the same sequence of zircon generation, but is variably affected by alteration and is isotopically distinct (CL-grey domain (II)); *green* regions represent domains which have been recrystallised by CDR and; *pink* analyses, represent the outermost reaction product incorporating non-formula elements including a component of Pb_c.

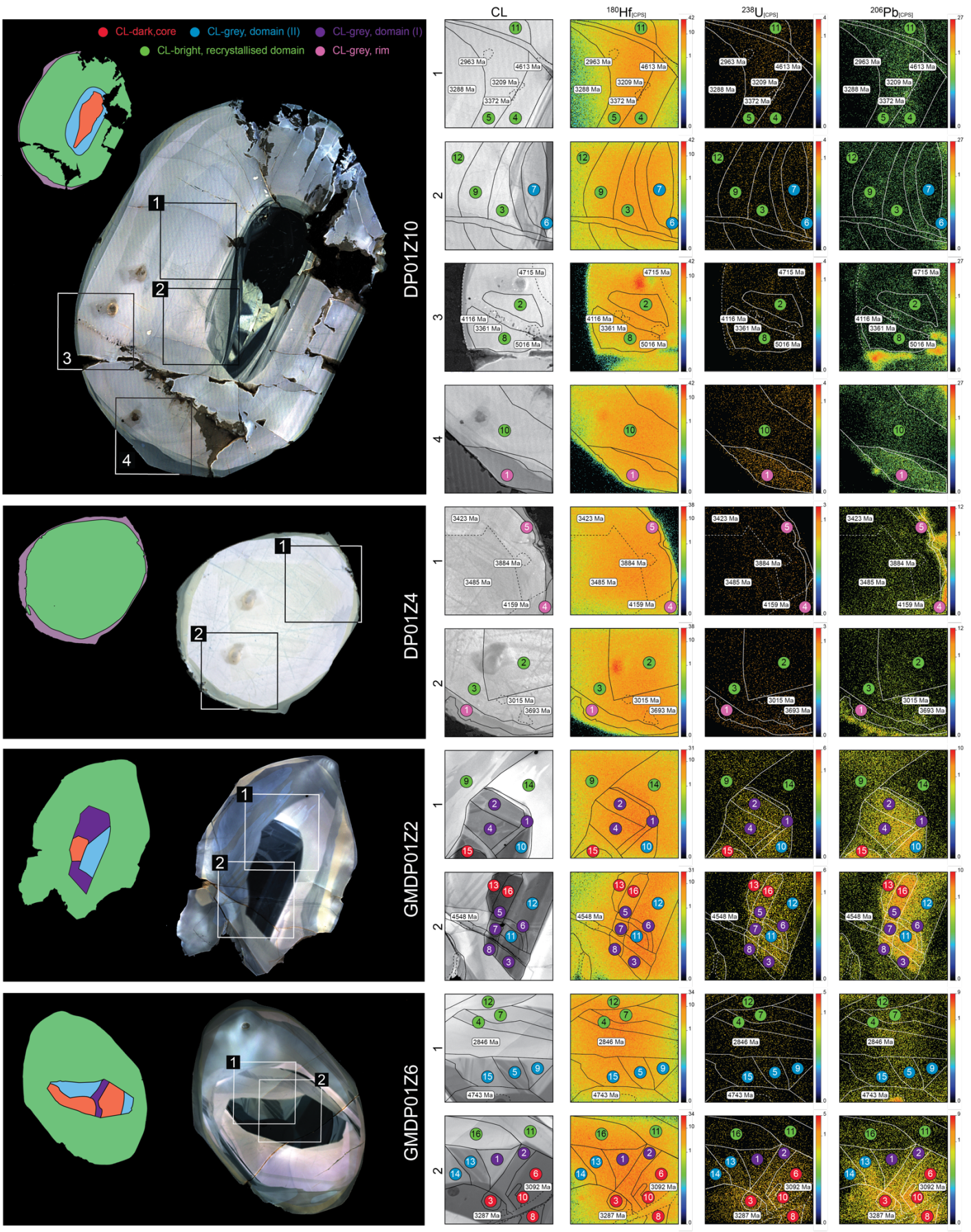

CL-dark,core
CL-grey, domain (II)
CL-grey, domain (I)
CL-bright, recrystallised domain
CL-grey, rim
DP01Z10
DP01Z4
GMDP01Z2
GMDP01Z6
CL
180Hf[CPS]
238U[CPS]
206Pb[CPS]

Figure 4.4. A set of SII grids pertaining to samples; DP01Z10, DP01Z4, GMDP01Z2 and GMDP01Z6 is shown for isotopes ^{180}Hf, ^{238}U, ^{206}Pb. Highlighted in each case is the CL image which guided the selection of ROIs. ROIs are delineated by solid lines enclosing sub-domains in order of increasing $^{207}Pb/^{206}Pb$ age within the domain categorisation to which they belong, which is referenced by colour coding of the labels, henceforth used in all subsequent figures. The instance of anomalous ages corresponding to "hotspots", suspected fractures and/or domains variably affected by ^{204}Pb are enclosed by ROIs having dashed lines and have their apparent $^{207}Pb/^{206}Pb$ age (Ma) denoted nearby. A accompanying figure displaying isotopes ^{204}Pb, ^{207}Pb and ^{208}Pb is provided in the supplementary material.

	Sample Grid	ROI	$^{238}U/^{206}Pb$	1 se (Ma)	$^{207}Pb/^{206}Pb$	1 se (Ma)	$^{206}Pb/^{238}U$ Age (Ma)	1 se (Ma)	$^{207}Pb/^{206}Pb$ Age (Ma)	1 se (Ma)	Concordia Age (Ma)	1 se (Ma)	Discordance (%)	U (ppm)
CL-dark, core; *red*	GMDP01Z2 (1)	15	2.5955	4.3	0.2202	4.6	2100.9	77.1	2981.4	74.2	2369.7	99.5	40	176.3
	GMDP01Z2 (2)	16	1.9836	2.9	0.2214	2.2	2631.5	63.0	2990.2	36.0	2905.0	32	13	164.3
	GMDP01Z2 (2)	13	2.5022	4.0	0.2156	3.4	2167.4	74.0	2947.4	55.2	2647.5	58.6	30	149.7
	GMDP01Z6 (2)	3	2.5190	5.7	0.1998	4.2	2155.0	105.0	2823.8	68.6	2632.0	64.3	27	121.2
	GMDP01Z6 (2)	6	2.5248	2.4	0.2154	2.2	2150.9	43.5	2945.9	36.0	2561.0	41.6	31	114.6
	GMDP01Z6 (2)	8	2.4719	3.9	0.2226	3.7	2189.9	72.8	2998.9	59.0	2620.7	68	32	116.6
	GMDP01Z6 (2)	10	2.3262	6.8	0.2272	4.6	2305.0	131.0	3031.7	73.9	2877.6	65.9	29	118.9
CL-grey, domain (I); *purple*	GMDP01Z2 (1)	1	2.8029	5.5	0.1715	5.0	1966.9	93.4	2571.6	84.2	2260.5	84.2	25	68.8
	GMDP01Z2 (1)	2	2.4733	4.6	0.1723	4.0	2188.9	86.0	2579.4	67.5	2425.7	59.7	15	73.8
	GMDP01Z2 (2)	3	2.6955	5.2	0.1739	3.8	2034.1	90.9	2594.8	63.0	2417.2	58.4	23	106.0
	GMDP01Z2 (1)	4	2.5863	3.9	0.1749	2.6	2107.3	69.9	2604.3	43.3	2475.8	38.7	21	86.1
	GMDP01Z2 (2)	5	2.6205	8.1	0.1750	8.2	2084.0	144.0	2605.0	136.0	2324.0	126	21	166.0
	GMDP01Z2 (2)	6	2.8128	5.6	0.1805	5.8	1960.9	95.3	2656.7	96.3	2209.0	103	30	126.2
	GMDP01Z2 (2)	7	2.5912	6.2	0.1824	5.0	2104.0	112.0	2674.1	82.8	2468.1	78.3	23	158.9
	GMDP01Z2 (2)	8	2.4622	6.3	0.1908	6.1	2197.0	117.0	2748.0	100.0	2488.3	95.5	22	141.3
	GMDP01Z6(2)	1	2.7640	5.3	0.1709	5.1	1990.7	90.4	2565.7	84.8	2254.6	82.4	23	38.1
	GMDP01Z6 (2)	2	2.8800	3.9	0.1774	3.3	1921.3	65.3	2628.0	54.5	2299.8	58.8	29	82.2
CL-grey, domain (II); *blue*	DP01Z10 (3)	6	2.4629	6.0	0.2211	5.6	2197.0	112.0	2988.0	89.9	2628.0	101	31	60.8
	DP01Z10 (3)	7	2.3876	4.6	0.2248	4.7	2255.2	86.9	3014.7	75.9	2610.3	85.4	30	22.5
	GMDP01Z2 (1)	10	2.5137	3.5	0.2051	3.1	2159.0	63.4	2866.5	50.7	2558.4	53.2	28	97.2
	GMDP01Z2 (2)	11	2.3408	4.8	0.2088	3.7	2293.1	92.7	2895.5	60.0	2723.5	55.6	23	130.6
	GMDP01Z2 (2)	12	2.3970	3.5	0.2126	2.4	2247.7	67.3	2924.7	38.2	2779.5	33.9	27	92.4
	GMDP01Z6 (1)	5	1.6831	7.9	0.2085	6.1	3006.0	190.0	2893.2	98.8	2917.6	87.5	-4	25.0
	GMDP01Z6 (1)	9	2.2069	8.6	0.2235	9.1	2409.0	173.0	3005.0	146.0	2725.0	143	23	25.0

continued overleaf

	Sample Grid	ROI	$^{238}U/^{206}Pb$	1 se (Ma)	$^{207}Pb/^{206}Pb$	1 se (Ma)	$^{206}Pb/^{238}U$ Age (Ma)	1 se (Ma)	$^{207}Pb/^{206}Pb$ Age (Ma)	1 se (Ma)	Concordia Age (Ma)	1 se (Ma)	Discordance (%)	U (ppm)
	GMDP01Z6 (2)	13	1.7101	4.6	0.2337	3.4	2968.0	109.0	3076.8	54.50	3055.6	48.7	3.9	49.2
	GMDP01Z6 (2)	14	1.9724	6.1	0.2352	5.5	2644.0	132.0	3087.1	88.40	2948.2	80	16	69.1
	GMDP01Z6 (1)	15	2.2024	5.1	0.2361	5.3	2413.0	102.0	3093.2	84.50	2774.7	87.1	26	21.8
CL-bright, recrystallised domain; *green*	DP01Z10 (1)	2	2.3209	6.3	0.2020	6.4	2310.0	123.0	2842.0	105.0	2592.1	98.7	21	12.7
	DP01Z10 (3)	3	2.2917	5.3	0.2038	5.2	2334.0	103.0	2856.1	85.0	2627.3	79.4	20	12.8
	DP01Z10 (4)	4	2.3328	4.8	0.2039	5.1	2299.7	92.5	2856.9	83.2	2573.2	79	22	15.6
	DP01Z10 (4)	5	2.4260	3.9	0.2169	3.1	2225.0	73.5	2957.1	49.7	2730.5	48.4	28	19.8
	DP01Z10 (1)	8	2.3383	5.7	0.2254	5.1	2295.0	110.0	3018.9	82.2	2739.2	84.4	27	17.7
	DP01Z10 (3)	9	2.2287	4.3	0.2255	4.1	2389.4	86.7	3019.7	66.0	2770.5	64.8	24	20.7
	DP01Z10 (2)	10	2.1168	3.0	0.2350	2.7	2494.1	61.1	3085.7	42.3	2889.6	40	22	18.1
	DP01Z10 (4)	11	2.2167	6.2	0.2425	6.0	2400.0	124.0	3135.7	95.0	2832.4	99.5	28	21.7
	DP01Z10 (3)	12	2.0100	6.5	0.2829	6.1	2603.0	140.0	3378.3	94.4	3126.1	94.8	28	17.6
	GMDP01Z6 (1)	4	2.3582	6.5	0.2012	6.3	2279.0	125.0	2835.0	102.0	2593.6	97.3	21	12.8
	GMDP01Z6 (1)	7	2.2429	5.2	0.2179	5.5	2377.0	103.0	2964.5	89.0	2677.2	86.3	23	17.4
	GMDP01Z2 (1)	9	2.6003	2.6	0.1954	2.8	2097.6	46.1	2787.4	45.9	2355.2	48.1	29	45.4
	GMDP01Z6 (2)	11	2.4096	5.5	0.2294	5.6	2238.0	104.0	3047.1	89.8	2615.0	107	32	22.5
	GMDP01Z6 (1)	12	2.4517	6.0	0.2319	6.2	2205.0	112.0	3064.5	99.6	2555.0	128	36	14.8
	GMDP01Z2 (1)	14	2.6387	3.6	0.2200	3.8	2071.5	63.2	2980.0	61.0	2325.9	86.1	42	20.9
	GMDP01Z6 (2)	16	2.3370	4.5	0.2375	4.5	2296.2	87.9	3102.6	72.4	2709.6	83.5	31	16.8
	DP01Z4 (2)	2	2.4071	4.0	0.2203	4.0	2239.7	75.1	2982.2	64.2	2605.8	70.8	29	4.3
	DP01Z4 (2)	3	2.1046	3.6	0.2462	3.2	2506.1	74.4	3159.8	50.3	2951.8	48.2	24	4.9
CL-grey, rim; *pink*	DP01Z10 (2)	1	2.7088	3.3	0.1861	3.0	2025.5	56.8	2707.3	48.7	2374.4	51.5	27	48.8
	DP01Z4 (2)	1	2.7719	4.8	0.2144	5.2	1985.8	81.8	2938.4	84.5	2146.0	118	48	12.0
	DP01Z4 (1)	4	0.3861	9.1	0.7319	3.0	8240.0	425.0	4794.0	42.4	4867.7	86.2	-83	28.5
	DP01Z4 (1)	5	0.3820	9.6	0.7023	3.4	8289.0	447.0	4734.8	49.3	4827.2	99.5	-86	22.7

continued overleaf

"Hotspots", anomalies and fractures	DP01Z10 (4)	3.2499	6.2	0.2670	7.3	1729.4	94.8	3288.0	114.0	1469.0	109.0	110	17.2
	DP01Z10 (4)	1.9512	24.1	0.2177	24.0	2667.0	526.0	2963.0	388.0	2856.0	335.0	11	17.0
	DP01Z10 (4)	1.8850	20.2	0.2817	18.3	2744.0	452.0	3372.0	286.0	3193.0	269.0	22	21.3
	DP01Z10 (4)	2.4823	23.2	0.2539	24.4	2182.0	430.0	3209.0	386.0	2455.0	696.0	48	23.6
	DP01Z10 (4)	0.8508	19.5	0.6455	11.0	5010.0	678.0	4613.0	159.0	4636.0	166.0	-11	17.3
	DP01Z10 (1)	1.9819	23.8	0.4598	18.4	2633.0	515.0	4116.0	273.0	3863.0	243.0	52	19.4
	DP01Z10 (1)	1.2049	28.9	0.2798	21.7	3895.0	846.0	3361.0	339.0	3442.0	326.0	-17	13.2
	DP01Z10 (1)	1.0107	16.4	0.8555	8.6	4434.0	526.0	5016.0	122.0	4991.0	105.0	17	20.3
	DP01Z10 (1)	0.5406	9.5	0.6927	3.6	6751.0	399.0	4715.1	51.3	4769.7	78.7	-53	12.4
	DP01Z4 (1)	2.0779	3.4	0.2911	2.9	2532.8	70.8	3422.9	44.6	3175.2	44.4	32	14.0
	DP01Z4 (1)	1.9022	3.9	0.3031	2.8	2723.3	86.4	3485.4	43.3	3353.0	38.0	27	12.1
	DP01Z4 (1)	1.2460	18.5	0.3935	12.7	3798.0	531.0	3884.0	191.0	3874.0	178.0	2.7	10.6
	DP01Z4 (1)	1.1000	7.9	0.4732	4.8	4168.0	243.0	4159.1	70.5	4159.8	67.8	-0.28	16.9
	DP01Z4 (2)	2.1330	20.9	0.2248	21.3	2478.0	429.0	3015.0	341.0	2789.0	321.0	20	5.0
	DP01Z4 (2)	1.2083	14.2	0.3469	9.4	3887.0	414.0	3693.0	143.0	3715.0	139.0	-6.2	7.2
	GMPD01Z2 (2)	1.0385	19.6	0.6169	11.0	4348.0	619.0	4548.0	159.0	4536.0	149.0	5.9	42.6
	GMDP01Z6 (1)	0.2629	15.3	0.7061	4.5	10117.0	779.0	4742.5	64.9	4851.0	185.0	-120	41.4
	GMDP01Z6 (1)	2.2631	3.9	0.2025	3.7	2359.0	77.2	2845.4	60.0	2652.2	55.1	18	19.4

Table 4.1. Ratio, age and U ppm determinations made for each ROI within CL categorised domain groupings plotted within concordia diagrams in Fig. 4.5. (1 se <10 %). Included also are some representative ROIs enclosing "hotspots", fractures and other anomalous domains, as observed in Fig. 4.4.

4.9. AGE DETERMINATIONS

The process of ROI selection has been outlined previously in *section 4.5*, data have been plotted in Terra-Wasserburg concordia space (Fig. 4.5.) and have been divided into separate panels (i.e. a,b and c) which have been identically scaled for clarity. Uncertainty ellipses represent ratio determinations of $^{207}Pb/^{206}Pb$ and $^{206}Pb/^{238}U$ made from ROI selections as delineated in Fig. 4.4. and tabulated in Table 4.1, which have uncertainties of < 10% (1 se %). Ellipses have been colour coded to reflect the CL-domains from which they were selected. Fig. 4.5a, presents isochron ages for domains interpreted to represent unreacted domains within the interior-most CL-dark and CL-grey domains, and are colour coded *red* and *purple* respectively. ROIs selected from CL-dark domains (*red*), define an upper-intercept age of 3036.4 ± 64.6 Ma [MSWD = 0.97], which overlaps with older estimates of U-Pb protolith ages previously determined for zircons of the Lewisian (Friend and Kinny, 1995). The upper-intercept age of 2644 ± 124 Ma [MSWD = 0.42] defined by ROIs from within the variously zone CL-grey domains pre-date Badcallian and/or Inverian metamorphic episodes by a small margin. A direct interpretation that they represent zircon formed during during partial melting and resorption occurring during the Badcallian tectonothermal event is difficult to determine confidently but may still be valid. The lower-intercept values for both populations plotted, overlap with 0 Ma, suggesting both have experienced recent bulk Pb loss, perhaps during low temperature alteration (see shaded inset figure in c).

The *blue* ellipses shown in Fig. 4.5b were selected from CL-grey sub-domains immediately outboard of the innermost core (*red* ellipses). The *blue* isochron intercepts concordia at 3086.5 ± 62.5 Ma [MSWD = 1] which cannot be reconciled within the observed textural succession in CL, having an older apparent age than those determined for the CL-dark un-reacted core (*red* ellipses). These sub-domains also exist in spatial juxtaposition to those ROIs which define a younger intercept age (*purple* ellipses) and yet texturally, they are indistinguishable. This suggests that the mechanism(s) operating to redistribute elements operated at discrete in spatial scales, potentially altering domains of high accumulated radiation damage (i.e. higher actinide concentration) preferentially. The lower-intercept intersection at near-origin values of age, again suggest that domains experienced the same recent Pb-loss as those analyses depicted in Fig. 4.5a. The intersection of the isochron defined by the *green* ellipses (Fig. 4.5b) defines an apparent upper intercept age of 3605 ± 139 [MSWD = 1.1] Ma which does not overlap with any known geological events for the region and is similarly decoupled from a meaningful intra-crystalline spatial context as expressed in CL. The isochron demonstrates an evolution towards increased $^{207}Pb/^{206}Pb$, evidencing a departure in Pb^{*} isotopic composition away from those expressed by domains contained with the interior-most CL domains. The lower-intercept age of 1605 ± 129 Ma defined herein, overlaps with hydrothermal events which have widespread expression throughout the LGC dated between c. 1690 - 1670 Ma (Kinny and Friend, 1997; Corfu et al., 1994). This date may constraint the timing of isotopic disturbance and supports a hydrothermal fluid-catalysed origin for the formation of the CL-bright zone.

The regions selected from the outermost CL-grey rim domains, display the oldest apparent upper-intercept ages (4462.4 ± 40.8 Ma [MSWD = 1]) and a lower-intercept age (1796.8 ± 52.9 Ma) which is again consistent with Laxfordian overprinting at ~1790 - 1750 Ma (Goodenough et al., 2013; Kinny and

Friend, 1997; Corfu et al., 1994). Although the isochron defined by these 4 analyses, are derived from ROIs pertaining to rim domains, two ROIs (namely those of DP01Z4(1) labelled 4 and 5) demonstrate a greater enrichment in Pb_c relative to other rim selections, which only demonstrate enrichments in U and Pb^*. Interpretation of the derived isochron ages are therefore considered with caution.

The elevated $^{207}Pb/^{206}Pb$ composition is due to the influence of a Pb_c component. The origin of this Pb_c within ROIs labelled 4 and 5 within DP01Z4(1) (Fig. 4.4) may be due to their close spatial juxtaposition with surrounding interstitial phases and the associated potential for external contamination. Efforts were made however to make all ROI selections, inboard of the outermost crystal bounds insofar as possible, guided by the intensity of the zircon matrix proxy (i.e. ^{180}Hf cps). Despite this, the two regions containing Pb_c (as well as Pb^*) enrichment and demonstrate an anti-correlation with ^{180}Hf, which may suggest that these rim domains represent the trailing edge of the reaction domain.

The other rim domains lacking an observable Pb_c enrichment (i.e. ROIs labelled 1 within each of DP01Z10(4) and DP01Z4(1); Fig. 4.4) demonstrate a relative enrichment in U and Pb^* counts and are thus the youngest domains with respect to their apparent $^{207}Pb/^{206}Pb$ ages. This points to one of two interpretations; the CL-grey rims represent a metamorphic overgrowth domain formed from a relatively enriched U source composition at ~ 2.7 Ga and ~ 2.9 Ga, for samples DP01Z10 and DP01Z4 respectively, if the $^{207}Pb/^{206}Pb$ ages are assumed to be accurate (in spite of evident recent Pb-loss) alternatively; these rim domains may represent a reaction repository for zircon incompatible elements (including Pb^* and U) rejected at the trailing edge of an inwardly progressing reaction front. These non-formula elements may be hosted within secondary sites whose presence is intimated by the relative diminishment in structural order within rim domains (see Fig. 4.2c).

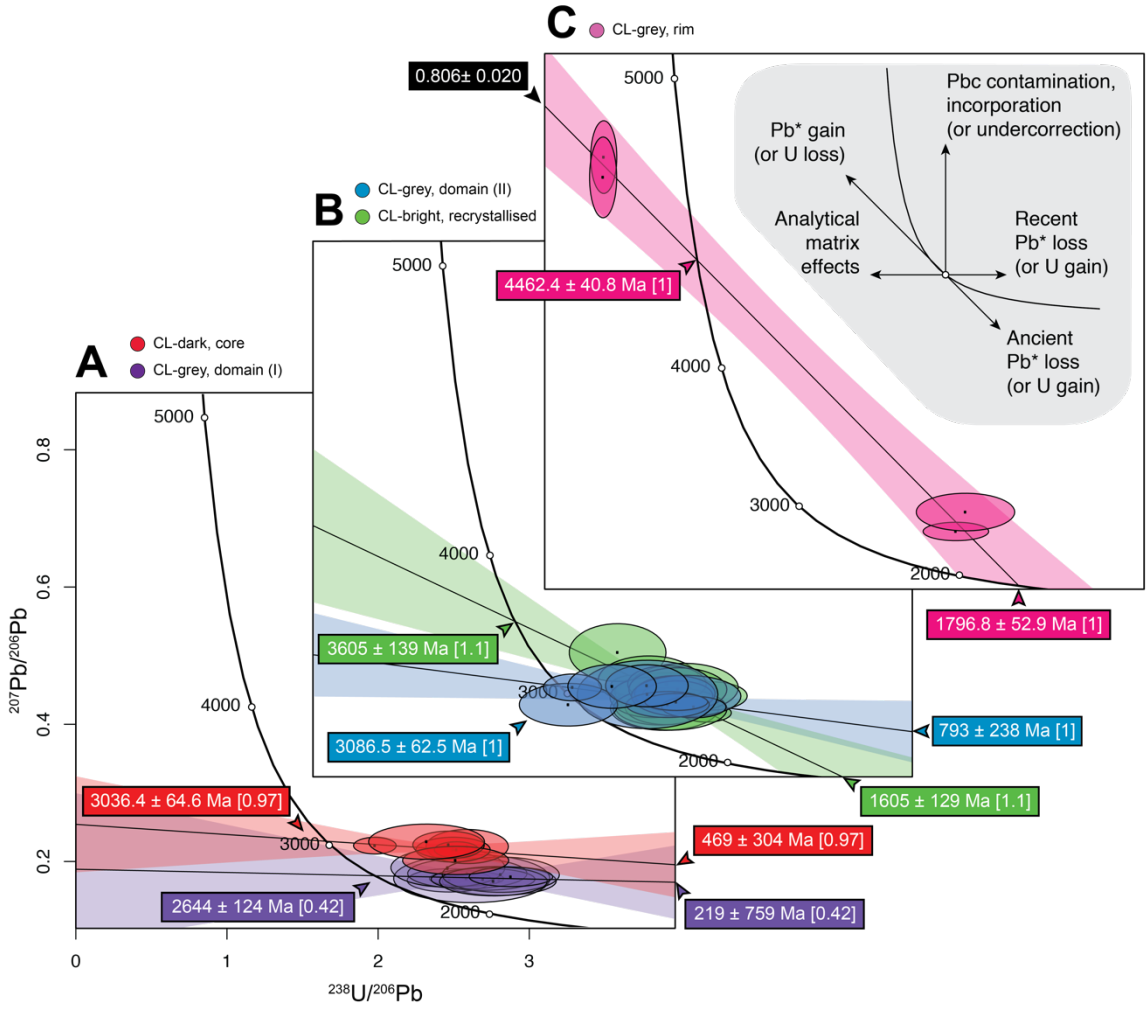


Figure 4.5 Terra-Wasserburg plots containing age determinations made from ROIs highlighted in Figure 4.4. Uncertainty ellipses are < 10% in each case and are quoted at a 1 se % level. All plots are scaled to the same extent for ease of comparison and the colour coding reflects the domain distinctions made on the basis of SII and CL imagery (see *section 4.3.2* for description). The upper and lower intercept values are displayed in each case and MSWD is shown in brackets. Shown too in the shaded portion of plot C, are hypothetical arrays highlighting the potential effect of element mobility on age determinations.

4.10. ELEMENT REDISTRIBUTION DURING FLUID-MEDIATED RECRYSTALLISATION

4.10.1. Evidence in support of CDR mechanism.

Both diffusion-reaction and CDR re-equilibration processes share some similarities in terms of their textural expression and can be hard to distinguish. This task is made especially difficult if the thorite, coffinite and xenotime inclusion phases common to CDR reacted zircon are absent and/or the pores which form during the reaction process have closed either by Oswald ripening or by wholesale re-equilibration (Geisler et al., 2007). The curved embayments into previously existing 'parent' zircon material, as seen under CL are indicative of fluid and/or melt-mediated recrystallisation processes however they cannot be used to distinguish between diffusion-reaction and CDR, as it is a textural feature common to both processes.

The reacted zircon is lacking both in trace-element components (i.e. U) as well as non-formula elements (i.e. Ca, Fe and Pb), which is usually an unambiguous indicator of a CDR process of recrystallisation (Geisler et al., 2007). Non-formula elements are however concentrated in some micrometer-sized sub-circular features, which may represent incompatible elements which were trapped within porosity on a pathway of outgoing flux into external fluids during CDR. To the same end, the outermost reaction rim is characterised not only by its relative enrichment in incompatible and non-formula elements (e.g. U and Pb_c), but also by a diminished intensity of the matrix proxy, Hf as well as a low structural order relative to its neighbouring recrystallised domain. All of which may point towards its existence as a repository of incompatible components at the fluid-zircon interface.

$^{207}Pb/^{206}Pb$ isotopic composition of the innermost core domains (*red* ellipses), is shared within uncertainty by domains constituting the CL-grey textural domain, namely domain I (*purple* ellipses) and domain II (*blue* ellipses) (see Fig 4.5a and b). The development of these texturally successive CL-grey sub-domains therefore retain a degree of isotopic memory of the CL-dark innermost core domains (*red* ellipses), which cannot be attributed to a CDR process and is instead likely represents an episode of zircon growth during the partial melting and resorption occurring during the Badcallian tectonothermal event. The process by which the CL-bright recrystallised domain (*green* ellipses) contrastingly shares no isotopic memory with previously existing 'parental' domains, indicative of re-equilibration of the isotope system by CDR (Geisler et al., 2007). The lower-intercept age of 1605 ± 129 Ma defined by the ellipses of the recrystallised domain, overlaps with known hydrothermal events at c. 1690 - 1670 Ma (Kinny and Friend, 1997; Corfu et al., 1994). This date may constraint the timing of isotopic disturbance and further supports a CDR process of formation of the recrystallised domain.

4.10.2. U concentration and secondary ion signal stability

Textural domains are plotted with respect to their U concentration (ppm) and apparent $^{207}Pb/^{206}Pb$ age in Fig. 4.6a. In general, LGC zircons are notable for their relatively low U concentrations (Whitehouse, et al., 2010) and these zircons are no exception. ROIs selected from within the CL-dark core constitute domains with the highest U ppm values (maximum measured U = 176 ppm). The concentration of U demonstrates no anti-correlation with increasing age, as might be expected and similar observations are made by Whitehouse, et al. (2010). Indeed, the oldest apparent ages are associated with domains of lowest U ppm (in *green*) selected from within the recrystallised domain, with the exception of the Pb_c affected ROIs (not shown). Recrystallised domains demonstrate the narrowest constraint with respect to U concentration (between ~ 4 - 45 ppm) for all ROIs analysed and also exhibit the greatest spread in their calculated apparent $^{207}Pb/^{206}Pb$ ages (~ 590 Ma). ROIs isolated from within the CL-grey domains surrounding the core (*blue* and *purple*), demonstrate a division with respect to their $^{207}Pb/^{206}Pb$ age, but a large degree of overlap of their U concentration.

Analytical uncertainties (1 se %) in excess of those predicted by Poisson counting statistics alone for determinations of both $^{207}Pb/^{206}Pb$ and $^{206}Pb/^{238}U$, are usually a reliable indication of unsupported quantities of Pb^{*} within the analytical volume, resulting from an excess instability in the secondary Pb ion signal when compared with matrix HfO and UO_2 signal intensities (Whitehouse et al., 2014; Kusiak et al., 2013). Analytical uncertainties determined for $^{207}Pb/^{206}Pb$ for all domains broadly describe a 1:1 relationship (see Fig. 4.6b), with the greatest offset being only 1.75 times the expected uncertainty. Analytical uncertainties determined for $^{206}Pb/^{238}U$ however demonstrate a greater variability by as much as 3.2 times the expected Poisson uncertainty estimation. ROIs demonstrating an excess in analytical uncertainty, are all within domains outboard of the CL-dark core (*red*). Interpretation of these data is made cautiously, as the determinations of Poisson uncertainty calculated on the basis or ROIs are much less precise than those made on conventional SIMS analyses. The data present greater offset from predicted uncertainty within determinations of $^{206}Pb/^{238}U$ relative to those predicted for $^{207}Pb/^{206}Pb$, (which are in good agreement with the expected values (i.e. 1:1)), which may suggest the Pb outboard of the CL-dark core domain was 'supported' by a quantity of U retained during wholesale elemental redistribution by CDR, but which has since largely decayed.

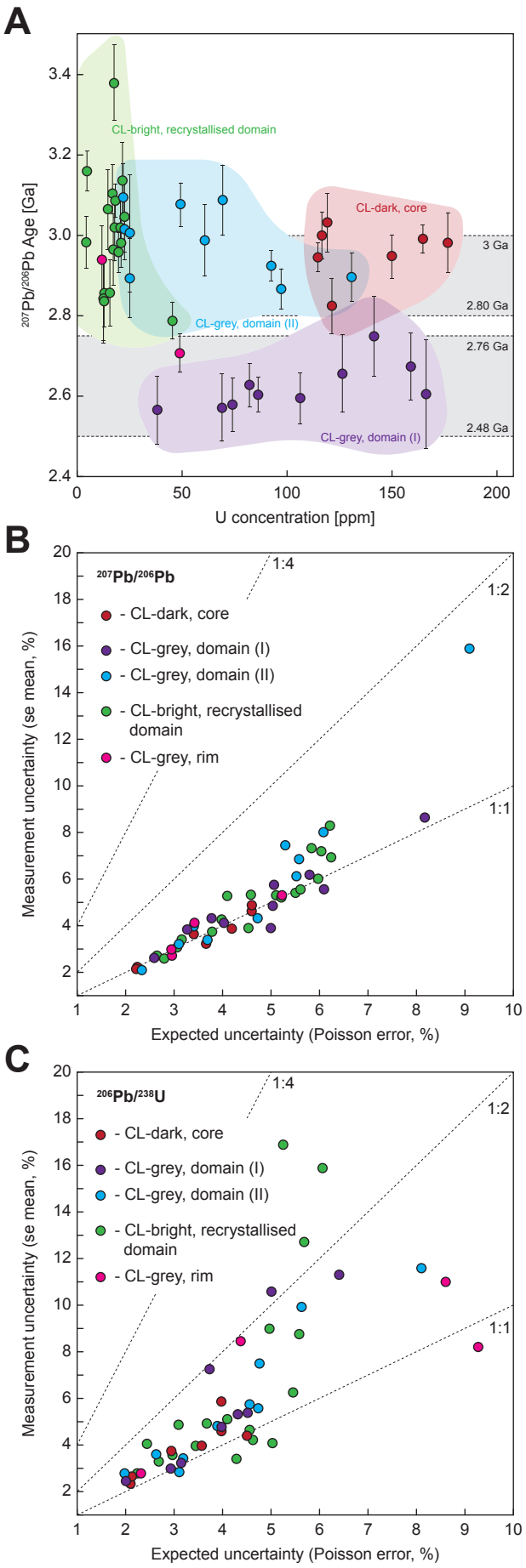


Figure 4.6 A) Groupings of textural domains as determined from CL imagery, reflecting the variability in apparent $^{207}Pb/^{206}Pb$ age with U concentration (ppm). Known timing constraints are marked as shaded regions. **B)** Correlative agreement of $^{207}Pb/^{206}Pb$ uncertainty determinations made on the basis of within-run measurement uncertainty (1 se %) and Poisson counting statistics (%). **C)** A non-correlation is expressed between measured and predicted uncertainties determined for $^{206}Pb/^{238}U$.

4.11. CONCEPTUAL MECHANISM RESULTING ANOMALOUS AGE DISTRIBUTIONS

Various causative mechanisms for element redistribution (either by Pb- and/or U- remobilisation) at micrometer or nanometer scales, resulting in occurrences of anomalous intra-crystalline ages have previously been proposed for similarly complex rocks, many having experienced several metamorphic episodes often at UHT conditions (e.g. Ge et al., 2019; Laurent et al., 2018; Seydoux Guillaume et al., 2015; Whitehouse et al., 2014; Kusiak et al., 2013). The precise mechanism by which element redistribution occurs is often unique to the metamorphic conditions to which zircon samples were exposed.

A model for the development of the observed anomalous age distributions as a result of elemental redistribution is conceptualised in Fig. 4.7, wherein panels labelled a, b, and c illustrate the development of texture at the grain-scale (bottom-most illustration), the rectangular box highlights a magnified depiction of operative processes (middle section) and the consequent effect each successive process has on the apparent age evolution is illustrated in the top-most plot. Fig. 4.7a charts initial zircon crystallisation (i.e. red circle; T_0 = ~ 3 Ga). This initial zircon may represent a primary in-situ growth as magmatic zircon or exist as inherited component derived of separate magmatic origin, regardless, it is interpreted to have been preserved more-or less unchanged (with the exception of recent bulk Pb-loss) through successive processes, having a present day expression as a sub-domain within the zircon grain as a whole (location marked with a *red* dot).

Fig. 4.7b conceptualises the subsequent occurrence of sector, fir-tree and/or oscillatory zonation outboard of the core at ~ 2.5 Ga, potentially representing an episode of zircon growth during the partial melting and resorption occurring during the Badcallian tectonothermal event. This interpretation is supported by evidence of curved inward embayments of the pre-existing CL-dark zircon as well as by upper-intercept ages overlapping with known events at ~ 2.5 Ga. Both the homogenous CL-dark core and some of the zoned CL-grey domains also overlap within uncertainty of their upper-intercept age and $^{207}Pb/^{206}Pb$ isotopic composition to differing extents (Fig. 4.5a and b; *purple* and *blue* respectively), which might indicate some degree of compositional recycling during the resorption process indicated by a gradient arrow between *red* and *blue* domains (Fig. 4.7c). Domains marked in *purple* (i.e. CL-grey, domain (II)), represent domains potentially exhibiting a distinct compositional origin from that of their neighbouring CL-grey domains (i.e. CL-grey, domain (I)), having younger upper-intercept ages (as in Fig. 4.5a; *purple*), but both overlap in respect of their $^{207}Pb/^{206}Pb$ isotopic composition making a conclusive determination of this origin impossible.

Within the conceptual model outlined in Figure 4.7c, the development of radial fractures as a result of volume expansion due to radiation-damage accrued in the intervening ~ 0.8 Ga, act as vectors for inward penetration of hydrothermal fluids. The reaction is triggered by the presence of an external aqueous fluid, when the zircon has a higher solubility in the external aqueous phase than its pure zircon

end member (Altree-Williams et al., 2015). The kinetics of the reaction may become more favourable in radiation damaged zircon (Geisler et al., 2007). The presence of an undersaturated aqueous fluid (with respect to the zircon) catalyses a structural and chemcial re-equilibration of radiation damaged material which is accompanied by the development of porosity within which percolating fluid advance chemical exchange along a inwardly penetrating reaction front (indicated by gradient arrows, whose colours represent a vector of component mixing between texturally distinct domains). An active exchange of elements is likely established initially within (and immediately surrounding) fracture zones. The active reaction front then progresses into unreacted domains along inwardly curved penetrations (now observed as embayments). The material re-equilibrated in the wake of the reaction front is characterised by an almost wholesale and preferential loss of all secondarily sited zircon-incompatible elements (including Pb^{*}) in favour of elements compatible with primary substitution. The CDR process therefore concentrates compatible elements within recrystallising zircon and perhaps therefore U is lost to perhaps to a lesser extent during this process due to its greater compatibility for primary substitution within the newly crystalline lattice. The residence of non-formula elements within micrometer sized inclusions and fracture zones as observed in Figure 4.3, indicates that these non-formula elements were expelled from the newly forming zircon as the reaction proceeded.

The outermost CL-grey rims may represent the trailing edge of the reaction front, which accommodates structural strain as well as acting as a repository for partially compatible and incompatible elements mobilised outward from the recrystallising matrix (i.e. U and Pb_c). This is indicated by the increase in radiation damage between the crystalline reacted domains and rim domains (Fig. 4.2c), as well as an increased U count as observed in SII (Fig. 4.4). The marked increase in apparent age is due to component mixing with a source of Pb_c, either derived from an external source of contamination (i.e. neighbouring phases or interstices) or due to a limited fluid assisted influx of Pb_c into secondary sites within the structurally disordered rim domains. The former being the most likely explanation.

Figure 4.7d, illustrates the present day discordia arrays in Wetherill concordia space, derived from ROI data. The uncertainty envelopes are not shown for clarity. Several discordant arrays emerge evolving along an increasing apparent age trajectory, when a selection of ROIs based on their relative position within a textual succession of CL-domains is made outward from the core. ROIs selected from the domains highlighted in *red* and *blue*, demonstrate a shared isotopic composition evidenced by their closely overlapping upper intercept value, suggesting that *blue* domains have been sourced at least in part from pre-existing core components (*red*), explaining their older apparent ages. *Purple* domains may also exhibit a degree of compositional mixing with pre-existing material, as their upper-intercept value overlap within uncertainty of one another (not shown), however these domains unlike their neighbouring CL-grey domains (CL-grey, domain (II)), demonstrate a geologically meaningful intercept age at 2644 ± 124 Ma, overlapping with known tectonothermal events at ~ 2760 Ma. Isochrons pertaining to each of the core and zoned domains overlap within uncertainty at similar lower-intercept values indicating they experienced recent bulk Pb-loss. The recrystallised domain (*green*) demonstrates an evolved isotopic composition of anomalously high apparent age, which does not share an isotopic memory of any one

domain. It may instead contain a degree of isotopic compositional recycling from all other pre-existing domains, marked by gradient vectors (arrows) of different colours. The most evolved isotopic composition is defined by ROIs selected from the CL-grey outermost rim, which exhibit a component of either Pb_c incorporation or contamination.

It must be considered that all domains experienced the same recent bulk Pb-loss which is exhibited by the CL-dark core (*red*) and CL-grey zoned domains (*blue* and *purple*). If recent Pb-loss has effected all domains uniformly the lower-intercepts as defined by ROIs within the recrystallised and rim domains (*green* and *pink*), may have earlier evidence of disturbance overprinted and may lie within the *green* or *pink* shaded envelopes as represented in Figure 4.7e. Alternatively, the lower intercept values, which are consistent with known Laxfordian hydrothermal events (~1.75 Ga), may reflect a true timing of isotopic disturbance whereby reacted domains don't suffer to the same degree from the recent Pb-loss event, due to their relatively low U concentrations and high crystallinity. Pb-loss from the innermost domains may be facilitated through the presently observed network of fractures.

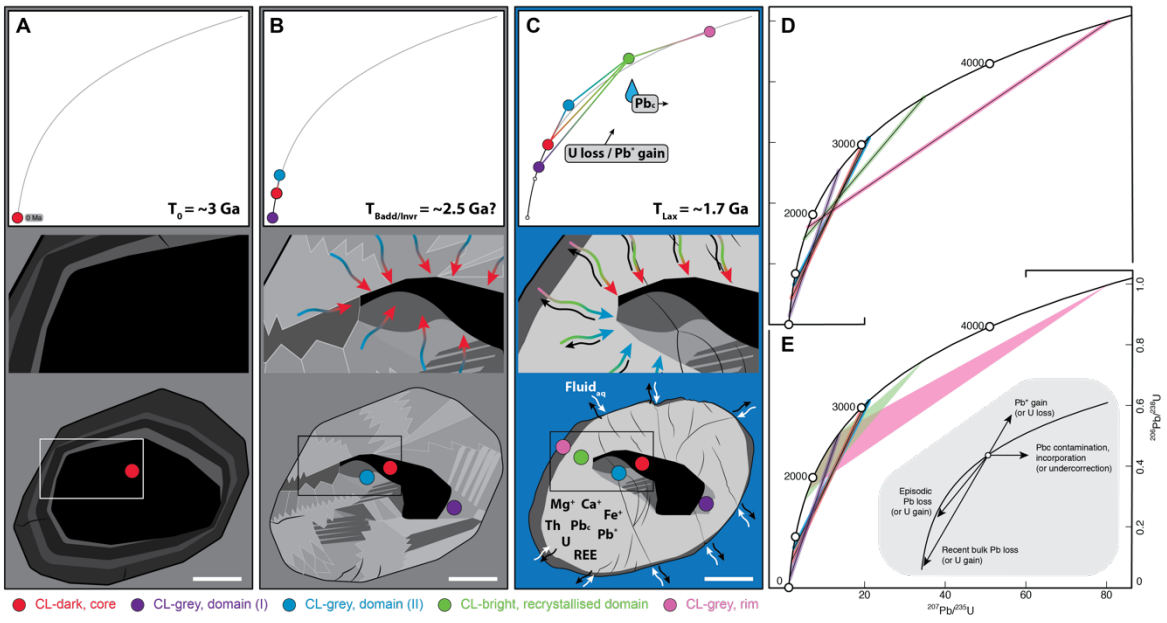


Figure 4.7. A conceptual model for the evolution of isochron ages presently observed (see *section 4.5* for description). Scale bar is 50 µm.

4.12. Conclusion

Four zircon grains from shear zone adjacent granulite-facies banded gneisses of the Lewisian Gneiss Complex in Northwest Scotland previously analysed by conventional SIMS spot analysis (MacDonald et al., 2015) reveal an anomalous intra-crystalline distribution of ages. These grains were subject to numerous imaging techniques, revealing textural and micro-structural evidence of fluid-mediated CDR process, which is invoked to explain the observed distribution of apparent ages.

CL imaging reveals a textural succession of domains, which exist either as un-reacted (or partially reacted) remnants of pre-existing zircon or as domains which have experienced structural re-

equilibration and elemental exchange in the wake of an inwardly penetrating reaction front. In the case of DP01Z4, the reaction has potentially gone to completion (owing to the smaller relative size of this sample), as there is no evidence of pre-existing zircon preserved. Ages derived from the un-reacted interior-most domains are in agreement with known protolith and tectonothermal event ages for Lewisian rocks, whilst regions dated within the alteration affected, recrystallised domains generate anomalous apparent ages which are decoupled from the expected succession of zircon growth (i.e. outward from the centre). Reacted domains are characterised by intense CL responses which have mottled and/or streaked appearance and cross-cut pre-existing domains (where they still exist), with inwardly curved embayments. The reacted domains are largely well ordered in respect of their crystallinity, but exhibit a gradual increase in structural disorder towards both the leading and trailing edges of the reaction zone, highly suggestive of structural control on the reaction progression (Geisler et al., 2003).

The noticeably diminishment of U concentration, coupled with an observation patchy occurrences of Pb^{*} revealed by SII, is suggestive of a reaction process which mobilises incompatible elements into the percolating fluid along pathways of chemical exchange, which are likely to exist within fracture networks. The persistence of isolated occurrences of Pb within the reacted domain may be attributed to the existence of sub-micrometer inclusions, which trap non-formula elements and which formed during the closure of chemical exchange pathways (i.e. pores and/or fracture networks). Evidence in support of such a mechanism of non-formula element entrapment may be in evidence within trails of micrometer scale sub-circular inclusions observed in close association with non-formula element enriched fractures (Fig. 4.3). Nanoscale features are also in evidence (largely isolated from present day fracture features) but their small scale precludes a resolution of their composition.

Instability in the secondary Pb ion signals is observed almost exclusively within measurement of $^{206}Pb/^{238}U$, from within domains interpreted to have undergone reaction alteration (Fig. 4.6c). Reacted domains may therefore display older apparent ages perhaps due to partial retention of more compatible U during what otherwise is a wholesale loss of incompatible elements. The reacted domains potentially exhibit combination of Pb-loss (but also localised entrapment within inclusions) as well as apparent U-gain during recrystallisation (by way of incomplete U-loss).

Decoding complex metamorphic histories may therefore be possible for complexly altered zircons by way of careful textural analysis in combination with high-spatial resolution SII, wherein domains retaining protolith ages may be preserved. Radiation damaged zircons may experience partial resetting of their isotope systematics, by way of a CDR mediated structural and chemical re-equilibration catalysed by the inward percolation of fluids which are initially undersaturated with respect to the 'parent' zircon.

4.13. ACKNOWLEDGMENTS

Both H Jeon and G Kenny is acknowledged for their assistance with SII collection. S Hinton-DeAngelis and M Allen are thanked for their assistance with EBSD analysis and data reduction.

4.14. REFERENCES

Altree-Williams, A., Pring, A., Ngothai, Y., Brugger, J., 2015. Textural and compositional complexities resulting from coupled dissolution–reprecipitation reactions in geomaterials. Earth-Science Reviews, 150, 628-651.

Attfield, P., 1987. "The structural history of the Canisp Shear Zone" In: Park, R.G. and Tarney, J. (eds) Evolution of the Lewisian and Comparable Precambrian High-Grade Terrains. Geological Society, London, Special Publications, 27, 165-173.

Bellucci, J.J., Whitehouse, M.J., Nemchin, A.A., Snape, J.F., Pidgeon, R.T., Grange, M., Reddy, S.M., Timms, N., 2016. A scanning ion imaging investigation into the micron-scale U-Pb systematics in a complex lunar zircon. Chemical Geology, 438, 112-122.

Capitani, G.C., Leroux, H., Doukhan, J.C., Ríos, S., Zhang, M., Salje, E.K.H., 2000. A TEM investigation of natural metamict zircons: structure and recovery of amorphous domains. Physics and Chemistry of Minerals, 27, 545-556.

Cherniak, D.J., 2010. Diffusion in Accessory Minerals: Zircon, Titanite, Apatite, Monazite and Xenotime. Reviews in Mineralogy & Geochemistry, 72, 827-869.

Cherniak, D.J., Watson, E.B., 2003. "Diffusion in zircon" In: Hanchar, J.M., Hoskin, P.W.O. (eds) Zircon. Mineralogical Society of America Reviews in Mineralogy & Geochemistry, 53, 113-143.

Cherniak, D.J., Watson, E.B., 2000. Pb diffusion in zircon. Chemical Geology, 172, 5-24.

Cherniak, D.J., Hanchar, J.M., Watson, E.B., 1997. Diffusion of tetravalent cations in zircon. Contributions to Mineralogy and Petrology, 127, 383-390.

Cherniak D.J., Lanford W.A., Ryerson F.J., 1991. Lead diffusion in apatite and zircon using ion implantation and Rutherford Backscattering techniques. Geochimica et Cosmochimica Acta, 55, 1663-1673.

Chew, D.M., Petrus, J.A., Kenny, G.G., McEvoy, N., 2017. Rapid high-resolution U–Pb LA-Q-ICPMS age mapping of zircon. Journal of Analytical Atomic Spectrometry, 32, 262-276.

Cohen, A. S., O'Nions, R. K.,O'Hara, M. J., 1991. Chronology and mechanism of depletion in Lewisian granulites, Contributions to Mineralogy and Petrology, 106, 142-153.

Colombo, M., Crosch, J., 1998. Annealing of natural metamict zircons: 1 low degree of radiation damage. Radiation Physics and Chemistry, 53, 555–561.

Corfu, F., Hanchar, J.M., Hoskin, P.W.O., Kinny, P., 2003 “Atlas of zircon textures” In: Hanchar, J.M., Hoskin, P.W.O. (eds) Zircon. Mineralogical Society of America Reviews in Mineralogy & Geochemistry, 53, 469-500.

Corfu, F., Heaman, L. M., Rogers, G., 1994. Polymetamorphic evolution of the Lewisian complex, NW Scotland, as recorded by U-Pb isotopic compositions of zircon, titanite and rutile. Contributions to Mineralogy and Petrology, 117, 215-228.

Crowley, Q.G., Key, R., Noble, S.R., High-precision U–Pb dating of complex zircon from the Lewisian Gneiss Complex of Scotland using an incremental CA-ID-TIMS approach. Gondwana Research, 27, 1381-1391.

Crowley, Q.G., Heron, K., Riggs, N., Kamber, B.S., Chew, D., McConnell, B., Benn, K., 2014. Chemical abrasion applied to LA-ICP-MS U–Pb zircon geochronology. Minerals, 4, 503-518.

Davies, J.H.F.L., Heaman, L., 2014. New U-Pb baddeleyite and zircon ages for the Scourie dyke swarm: a long-lived large igneous province with implications for the Paleoproterozoic evolution of NW Scotland. Precambrian Research, 249, 180–198.

Eakin, M., Brownlee, S.J., Baskaran, M., Barbero, L., 2016. Mechanisms of radon loss from zircon: Microstructural controls on emanation and diffusion. Geochimica et Cosmochimica Acta, 184, 212-226.

Ewing R.C., Meldrum A., Wang L.M., Weber W. J., Corrales R.L., 2003. “Radiation Effects in Zircon” In: Hanchar, J.M., Hoskin, P.W.O. (eds) Zircon. Reviews in Mineralogy and Geochemistry 53(1), 387–425.

Ewing R.C., Meldrum A., Wang L.M., Wang S.X., 2000. Radiation-induced amorphization. “Transformation Processes in Minerals” In Redfern S.A.T. and Carpenter M.A. (eds) Reviews in Mineralogy and Geochemistry 39, 319-361.

Evans, C. R., 1965. Geochronology of the Lewisian basement near Lochinver, Sutherland. Nature, 207, 54-56.

Farnan I, Salje E.K.H., 2001. The degree and nature of radiation damage in zircon observed by 29Si nuclear magnetic resonance. Journal of Applied Physics, 89, 2084-2090.

Finch R.J., Hanchar, J.M., 2003. Structure and chemistry of zircon and zircon-group minerals. In: Hanchar J.M., Hoskin P.W.O. (eds) Zircon. Reviews in Mineralogy and Geochemistry 53(1), 1-25.

Friend, C.R.L., Kinny, P.D., 1995. New evidence for protolith ages of Lewisian granulites, northwest Scotland. Geology, 23, 1027-1030.

Ge, R., Wilde, S.A., Nemchin A.A., Whitehouse M.J., Bellucci J.J., Erickson T.M., 2019. Mechanisms and consequences of intra-crystalline enrichment of ancient radiogenic Pb in detrital Hadean zircons from the Jack Hills, Western Australia. Earth and Planetary Science Letters, 517, 38-49.

Gebauer, D. and Grünenfelder, M., 1976. U-Pb zircon and Rb-Sr whole-rock dating of low-grade metasediments example: Montagne Noire (Southern France). Contributions to Mineralogy and Petrology, 59(1), 13-32.

Geisler, T., Schaltegger, U. and Tomaschek, F., 2007. Re-equilibration of zircon in aqueous fluids and melts. Elements, 3(1), 43-50.

Geisler, T, Seydoux-Guillaume, A.M., Wiedenbeck, M., Wirth R., Berndt, J., Zhang, M., Mihailova, B., Putnis, A., Salje, E.K.H., Schlüter, J., 2004. Periodic precipitation pattern formation in hydrothermally treated metamict zircon. American Mineralogist, 89, 1341-1347.

Geisler T, Schleicher H, Pidgeon RT, Kurtz R, van Bronswijk W., 2003a. Experimental hydrothermal alteration of partially metamict zircon. American Mineralogist, 88(10), 1496-1513.

Geisler, T., Zhang, M. and Salje, E.K., 2003b. Recrystallization of almost fully amorphous zircon under hydrothermal conditions: An infrared spectroscopic study. Journal of Nuclear Materials, 320(3), 280-291.

Geisler, T., Pidgeon R.T., van Bronswijk, W., Kurtz R., 2002. Transport of uranium, thorium, and lead in metamict zircon under low-temperature hydrothermal conditions. Chemical Geology, 191, 141–154.

Geisler, T., Pidgeon, R.T., Van Bronswijk, W. and Pleysier, R., 2001. Kinetics of thermal recovery and recrystallization of partially metamict zircon: a Raman spectroscopic study. European Journal of Mineralogy, 13(6), 1163-1176.

Goodenough, K.M., Crowley, Q., Krabbendam, M., Parry, S.F., 2013. New U-Pb age constraints for the Laxford Shear Zone, NW Scotland: evidence for tectono-magmatic processes associated with the formation of a Palaeoproterozoic supercontinent. Precambrian Research, 223, 1–19.

Harley, S.L. and Kelly, N.M., 2007. Zircon tiny but timely. Elements, 3(1), 13-18.

Hoskin P.W.O., 2005. Trace-element composition of hydrothermal zircon and the alteration of Hadean zircon from the Jack Hills, Australia. Geochimica et Cosmochimica Acta, 69, 637-648

Jensen, L.N., 1984. Quartz microfabric of the Laxfordian Canisp shear zone, NW Scotland. Journal of Structural. Geology, 6 (3), 293–302.

Johnson, T.E., Fischer, S., White, R.W., 2013. Field and petrographic evidence for partial melting of TTG gneisses from the central region of the mainland Lewisian complex, NW Scotland. J. Geol. Soc. 170 (2), 319–326.

Johnson, T.E., Fischer, S., White, R.W., Brown, M., Rollinson, H.R., 2012. Archaean intracrustal differentiation from partial melting of Metagabbro-field and geo- chemical evidence from the central region of the Lewisian Complex, NW Scotland. Journal of Petrology, 53 (10), 2115–2138.

Johnson, T.E., White, R.W., 2011. Phase equilibrium constraints on conditions of granulite-facies metamorphism at Scourie, NW Scotland. Journal of the Geological Society, 168 (1), 147–158.
Kinny, P.D., Friend, C.R.L., Love, G.J., 2005. Proposal for a terrane-based nomenclature for the Lewisian Gneiss complex of NW Scotland. Journal of the Geological Society, 162, 175– 186.

Kinny, P.D., Friend, C.R.L., 1997. U-Pb isotopic evidence for the accretion of different crustal blocks to form the Lewisian Complex of northwest Scotland. Contributions to Mineralogy and Petrology, 129, 326–340.

Kober, B., 1987. Single-zircon evaporation combined with Pb+ emitter bedding for 207Pb/206Pb age investigations using thermal ion mass spectrometry, and implications to zirconology. Contributions to Mineralogy and Petrology, 96, 63–71.

Kogawa, M., Watson, B.E., Ewing, R.C., Utsunomiya, S., 2012. Lead in zircon at the atomic scale. American Mineralogist, 97, 1094–1102.

Kovaleva, E., Klötzli, U., Habler, G., Huet, B., Guan, Y., Rhede, D., 2017. The effect of crystal-plastic deformation on isotope and trace element distribution in zir- con: combined BSE, CL, EBSD, FEG-EMPA and NanoSIMS study. Chem. Geol. 450, 183–198.

Kramers, J., Frei, R., Newville, M., Kober, B., Villa, I., 2009. On the valency state of radiogenic lead in zircon and its consequences. Chemical Geology, 261, 4–10.

Kusiak, M.A., Wilde, S.A., Wirth, R., Whitehouse, M.J., Dunkley, D.J., Lyon, I., Reddy, S.M., Berry, A. and de Jonge, M., 2018. Detecting Micro- and Nanoscale Variations in Element Mobility in High-Grade Metamorphic Rocks: Implication for Precise U- Pb Dating of Zircon. Microstructural Geochronology: Planetary Records Down to Atom Scale, 277-291.

Kusiak, M.A., Dunkley D.J., Wirth, R., Whitehouse, M.J., Wilde, S.A., Marquardt, K., 2015. Metallic lead nanospheres discovered in ancient zircons. Proceedings of the National Academy of Sciences of the United States of America, 112(16), 4958–4963.

Kusiak, M.A., Whitehouse, M.J., Wilde, S.A., Nemchin, A.A. and Clark, C., 2013. Mobilization of radiogenic Pb in zircon revealed by ion imaging: Implications for early Earth geochronology. Geology, 41(3), 291-294.

Laurent, A.T., Bingen, B., Duchene, S., Whitehouse, M.J., Seydoux-Guillaume, A.M. and Bosse, V., 2018. Decoding a protracted zircon geochronological record in ultrahigh temperature granulite, and persistence of partial melting in the crust, Rogaland, Norway. Contributions to Mineralogy and Petrology, 173(4), 1-25.

Lee, J.K., Williams, I.S. and Ellis, D.J., 1997. Pb, U and Th diffusion in natural zircon. Nature, 390(6656), 159-162.

Love, G.J., Friend, C.R.L., Kinny, P.D., 2010. Palaeoproterozoic terrane assembly in the Lewisian Gneiss complex on the Scottish mainland, south of Gruinard Bay: SHRIMP U-Pb zircon evidence. Precambrian Res. 183 (1), 89–111.

MacDonald, J.M., Goodenough, K.M., Wheeler, J., Crowley, Q., Harley, S.L., Mariani, E. and Tatham, D., 2015. Temperature–time evolution of the Assynt Terrane of the Lewisian Gneiss Complex of Northwest Scotland from zircon U-Pb dating and Ti thermometry. Precambrian Research, 260, 55-75.

MacDonald, J.M., Wheeler, J., Harley, S.L., Mariani, E., Goodenough, K.M., Crowley, Q. and Tatham, D., 2013. Lattice distortion in a zircon population and its effects on trace element mobility and U–Th–Pb isotope systematics: examples from the Lewisian Gneiss Complex, northwest Scotland. Contributions to Mineralogy and Petrology, 166(1), 21-41.

Mariani, E., Mecklenburgh, J., Wheeler, J., Prior, D.J. and Heidelbach, F., 2009. Microstructure evolution and recrystallization during creep of MgO single crystals. Acta Materialia, 57(6), 1886-1898.

Mattinson, J.M., Graubard, C.M., Parkinson, D.L., McClelland, W.C., 1996. U-Pb reverse discordance in zircons: the role of fine-scale oscillatory zoning and sub-micron transport of Pb. In: Basu, A., Hart, S. (eds.), Earth Processes: Reading the Isotopic Code. Geophysical Monograph. American Geophysical Union, Washington, DC, 355–370.

McFarlane, C.R.M., Connelly, J.N., Carlson, W.D., 2005. Intracrystalline redistribution of Pb in zircon during high-temperature contact metamorphism. Chem. Geol. 217, 1–28.

Meis, C., Gale, J.D., 1998. Computational study of tetravalent uranium and plutonium lattice diffusion in zircon. Material Science and Engineering B, 57, 52-61

Mezger, K., Krogstad, E.J., 1997. Interpretation of discordant U-Pb ages: An evaluation. Journal of Metamorphic Geology, 15, 127-140.

Murakami T, Chakoumakos BC, Ewing RC, Lumpkin GR, Weber WJ (1991) Alpha-decay event damage in zircon. American Mineralogist, 76, 1510-1532.

Nasdala, L., Hofmeister, W., Norberg, N., Martinson, J.M., Corfu, F., Dörr, W., Kamo, S.L., Kennedy, A.K., Kronz, A., Reiners, P.W. and Frei, D., 2008. Zircon M257- a homogeneous natural reference material for the ion microprobe U- Pb analysis of zircon. Geostandards and Geoanalytical Research, 32(3), 247-265.

Nasdala, L., Lengauer, C.L., Hanchar, J.M., Kronz, A., Wirth, R., Blanc, P., Kennedy, A.K., and Seydoux-Guillaume, A.M., 2002. Annealing radiation damage and the recovery of cathodoluminescence. Chemical Geology, 191, 119–138.

Nasdala, L., Wenzel, M., Vavra, G., Irmer, G., Wenzel, T., and Kober, B., 2001. Metamictisation of natural zircon: accumulation versus thermal annealing of radioactivity-induced damage. Contributions to Mineralogy and Petrology, 141, 125–144.

Nasdala, L., Pidgeon, R.T. and Wolf, D., 1996. Heterogeneous metamictization of zircon on a microscale. Geochimica et Cosmochimica Acta, 60(6), pp.1091-1097.

Nasdala L., Irmer G. and Wolf D., 1995., The degree of metamictization in zircons: A Raman spectroscopic study. European Journal of Mineralogy, 7, 471-478.

Peterman, E.M., Reddy, S.M., Saxey, D.W., Snoeyenbos, D.R., Rickard, W.D., Fougerouse, D., and Kylander-Clark, A.R., 2016. Nanogeochronology of discordant zircon measured by atom probe microscopy of Pb-enriched dislocation loops. Science Advances 2., e1601318.

Piazolo, S., La Fontaine, A., Trimby, P., Harley, S., Yang, L., Armstrong, R. and Cairney, J.M., 2016. Deformation-induced trace element redistribution in zircon revealed using atom probe tomography. Nature communications, 7(1), 1-7.

Pidgeon, R.T., Nemchin, A.A., Whitehouse, M.J., 2017. The effect of weathering on U-Th-Pb and oxygen isotope systems of ancient zircons from the Jack Hills, Western Australia. Geochimica et Cosmochimica Acta 197, 142–166.

Pidgeon, R.T., O'Neil, J.R., Silver, R.T., 1995. The interdependence of U-Pb stability, crystallinity and external conditions in natural zircons - an early experimental study. In: Leon T. Silver 70th Birthday Symposium and Celebration, Extended Abstracts: 225-231.

Pidgeon, R.T. and Compston, W., 1992. A SHRIMP ion microprobe study of inherited and magmatic zircons from four Scottish Caledonian granites. Transactions of the Royal Society of Edinburgh: Earth Sciences, 83(1-2), 473-483.

Rayner, N., Stern, R.A., Carr, D., 2005. Grain-scale variations in trace element composition of fluid-altered zircon, Acasta Gneiss Complex, northwestern Canada. Contributions to Mineralogy and Petrology, 148, 721-734.

Reddy, S.M., van Riessen, A., Saxey, D.W., Johnson, T.E., Rickard, W.D., Fougerouse, D., Fischer, S., Prosa, T.J., Rice, K.P., Reinhard, D.A., 2016. Mechanisms of deformation-induced trace element migration in zircon resolved by atom probe and correlative microscopy. Geochimica et Cosmochimica Acta 195, 158–170.

Reddy, S.M., Timms, N.E., Pantleon, W. and Trimby, P., 2007. Quantitative characterization of plastic deformation of zircon and geological implications. Contributions to Mineralogy and Petrology, 153(6), 625-645.

Regis, D., Acosta-Gongora, P., Davis, W.J., Knox, B., Pehrsson, S.J., Martel, E., Hulbert, L., 2017. Evidence for Neoarchean Ni-Cu-bearing mafic intrusions along a major lithospheric structure: a case study from the south Rae craton (Canada). Precambrian Research, 302, 312–339.

Rollinson, H. and Gravestock, P., 2012. The trace element geochemistry of clinopyroxenes from pyroxenites in the Lewisian of NW Scotland: insights into light rare earth element mobility during granulite facies metamorphism. Contributions to Mineralogy and Petrology, 163(2), 319-335.

Rollinson, H.R. and Windley, B.F., 1980. An Archaean granulite-grade tonalite-trondhjemite-granite suite from Scourie, NW Scotland: geochemistry and origin. Contributions to Mineralogy and Petrology, 72(3), 265-281.

Romer, R.L., 2003. Alpha-recoil in U–Pb geochronology: effective sample size matters. Contributions to Mineralogy and Petrology, 145(4), 481-491.

Salje, E.K.H., Chrosch, J. and Ewing, R.C., 1999. Is "metamictization" of zircon a phase transition? American Mineralogist, 84, 1107-1116.

Schaltegger, U., Wotzlaw, J.F., Ovtcharova, M., Chiaradia, M. and Spikings, R., 2014. Mass Spectrometry in Earth Sciences: The Precise and Accurate Measurement of Time. CHIMIA International Journal for Chemistry, 68(3), 124-128.

Schmidt, C., Rickers, K., Wirth, R., Nasdala, L., Hanchar, J.M., 2006. Low-temperature Zr mobility: An in situ synchrotron- radiation XRF study of the effect of radiation damage in zircon on the element release in H2O + HCl ± SiO2 fluids. American Mineralogist, 91, 1211-1215.

Seydoux-Guillaume, A.M., Bingen, B., Paquette, J.L. and Bosse, V., 2015. Nanoscale evidence for uranium mobility in zircon and the discordance of U–Pb chronometers. Earth and Planetary Science Letters, 409, 43-48.

Shannon, R.D., 1976. Revised effective ionic radii and systematic studies of interatomic distances in halides and chalcogenides. Acta Crystallographica, (A)32, 751-767.

Silver, L.T., Deutsch, S., 1963. Uranium–lead isotopic variations in zircons: a case study. Journal of Geology, 71, 721–758.

Sinha, A.K., Wayne, D.M., Hewitt, D.A., 1992. The hydrothermal stability of zircon: Preliminary experimental and isotopic studies. Geochimica et Cosmochimica Acta, 56, 3551-3560.

Sutton, J.,Watson, J. V., 1951. The pre-Torridonian metamorphic history of the Loch Torridon and Scourie areas in the northwest Highlands, and its bearing on the chronological classification of the Lewisian. Quarterly Journal of the Geological Society of London, 106, 241-307.

Suzuki, K., 1987. Discordant distribution of U and Pb in zircon of Naegi granite: A possible indication of Rn migration through radiation damage: Geochemical Journal, 21, 173–182.

Timms, N.E., Kinny, P.D. and Reddy, S.M., 2006. Enhanced diffusion of uranium and thorium linked to crystal plasticity in zircon. Geochemical Transactions, 7(1), 1-16.

Utsunomiya, S., Palenik, C.S., Valley, J.W., Cavosie, A.J., Wilde, S.A., and Ewing, R.C., 2004. Nanoscale occurrence of Pb in an Archean zircon. Geochimica et Cosmochimica Acta, 68, 4679−4686.

Valley, J.W., Cavosie, A.J., Ushikubo, T., Reinhard, D.A., Lawrence, D.F., Larson, D.J., Clifton, P.H., Kelly, T.F., Wilde, S.A., Moser, D.E., and Spicuzza, M.J., 2014. Hadean age for a post-magma ocean zircon confirmed by atom-probe tomography. Nature Geoscience, 7, 219-223.

Villa, I.M. and Hanchar, J.M., 2017. Age discordance and mineralogy. American Mineralogist, 102(12), 2422-2439.

Watson, E.B., Cherniak, D.J., Hanchar, J.M., Harrison, T.M., Wark, D.A., 1997. The incorporation of Pb into zircon. Chemical Geology. 141, 19-31.

Whitehouse, M.J., Kusiak, M.A., Wirth, R. and Kumar, G.R., 2017. Metallic Pb nanospheres in ultra-high temperature metamorphosed zircon from southern India. Mineralogy and Petrology, 111(4), 467-474.

Whitehouse, M.J., Kumar, G.R. and Rimša, A., 2014. Behaviour of radiogenic Pb in zircon during ultrahigh-temperature metamorphism: an ion imaging and ion tomography case study from the Kerala Khondalite Belt, southern India. Contributions to Mineralogy and Petrology, 168(2), 1042.

Whitehouse, M.J. and Kemp, A.I.S., 2010. On the difficulty of assigning crustal residence, magmatic protolith and metamorphic ages to Lewisian granulites: constraints from combined in situ U–Pb and Lu–Hf isotopes. Geological Society, London, Special Publications, 335(1), 81-101.

Whitehouse, M.J., 1989. Sm-Nd evidence for diachronous crustal accretion in the Lewisian Complex of Northwest Scotland. Tectonophysics, 161(3-4), pp.245-256.

Wiemer, D., Allen, C.M., Murphy, D.T. and Kinaev, I., 2017. Effects of thermal annealing and chemical abrasion on ca. 3.5 Ga metamict zircon and evidence for natural reverse discordance: Insights for UPb LA-ICP-MS dating. Chemical Geology, 466, 285-302.

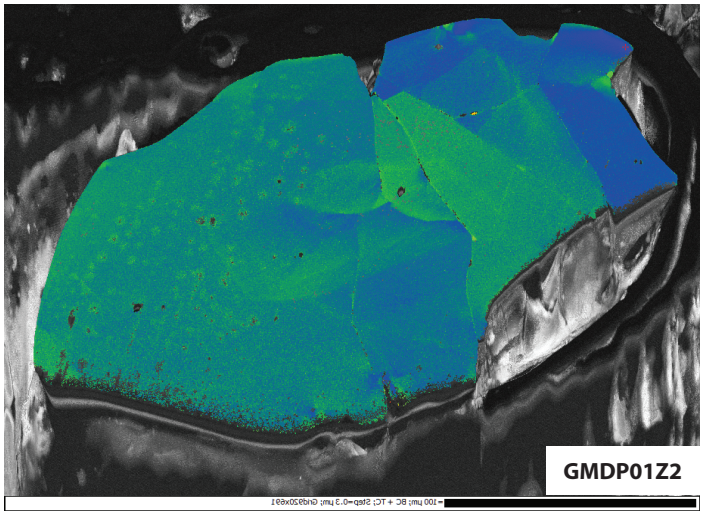
Zhang, M., Salje, E.K., Capitani, G.C., Leroux, H., Clark, A.M., Schlüter, J. and Ewing, R.C., 2000. Annealing of-decay damage in zircon: a Raman spectroscopic study. Journal of Physics: Condensed Matter, 12(13), 3131.

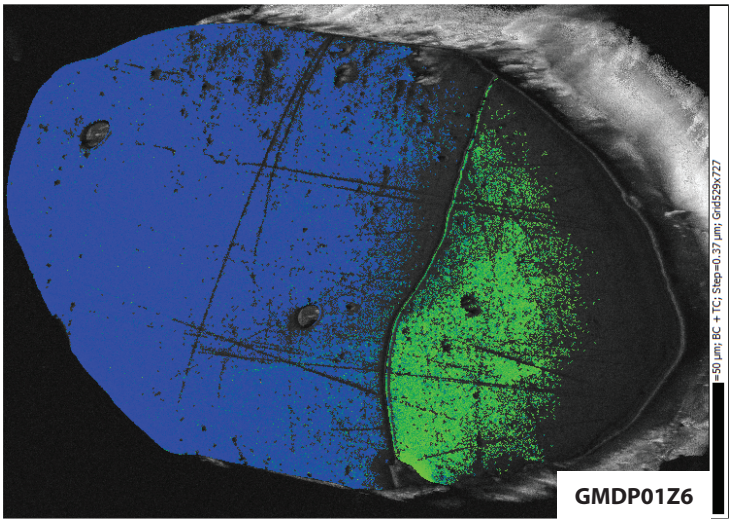
Zhu, X. K., O'Nions, R. K., Belshaw, N. S., and Gibb, A. J., 1997. Lewisian crustal history from in situ SIMS mineral chronometry and related metamorphic textures. Chemical Geology 136, 205-218.

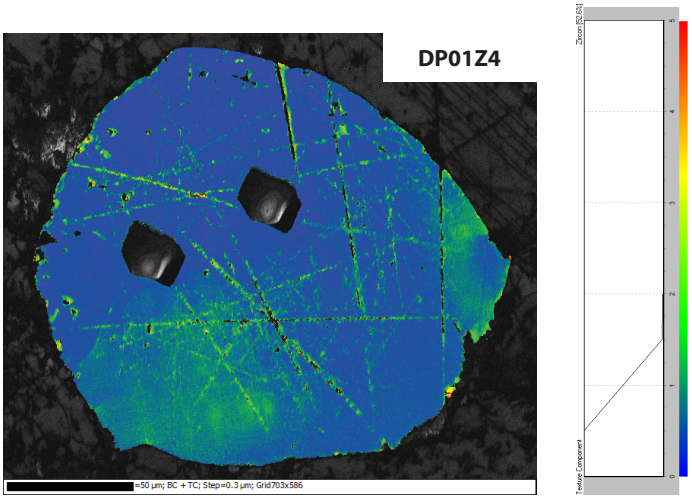
4.15. SUPPORTING INFORMATION AND SUPPLEMENTARY FIGURES

4.15.1. Additional EBSD misorientation maps

Included below are additional EBSD misorientation maps imaged over the surface of samples GMDP01Z2, GMDP01Z6, DP01Z4. All images share the same dimensional and misorientation scales.

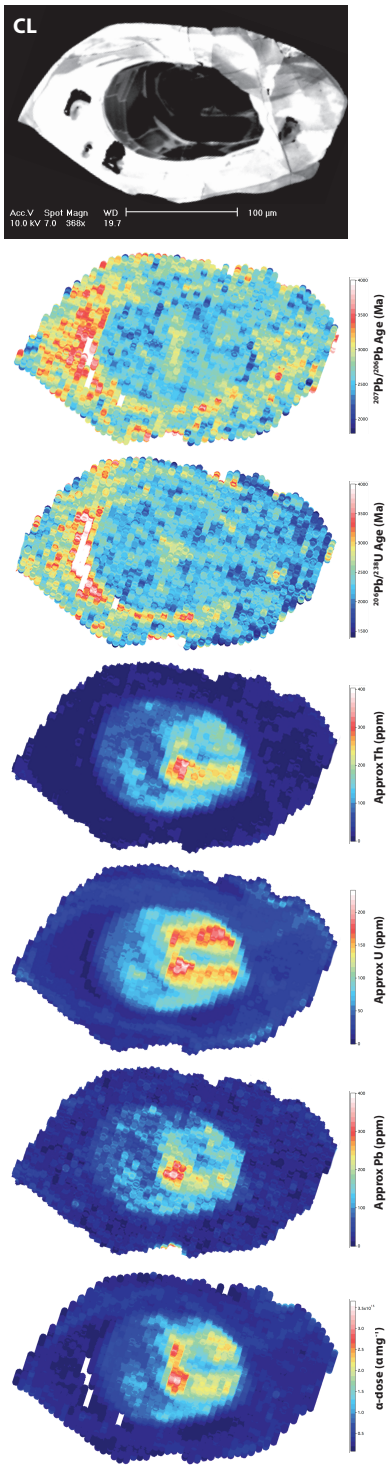






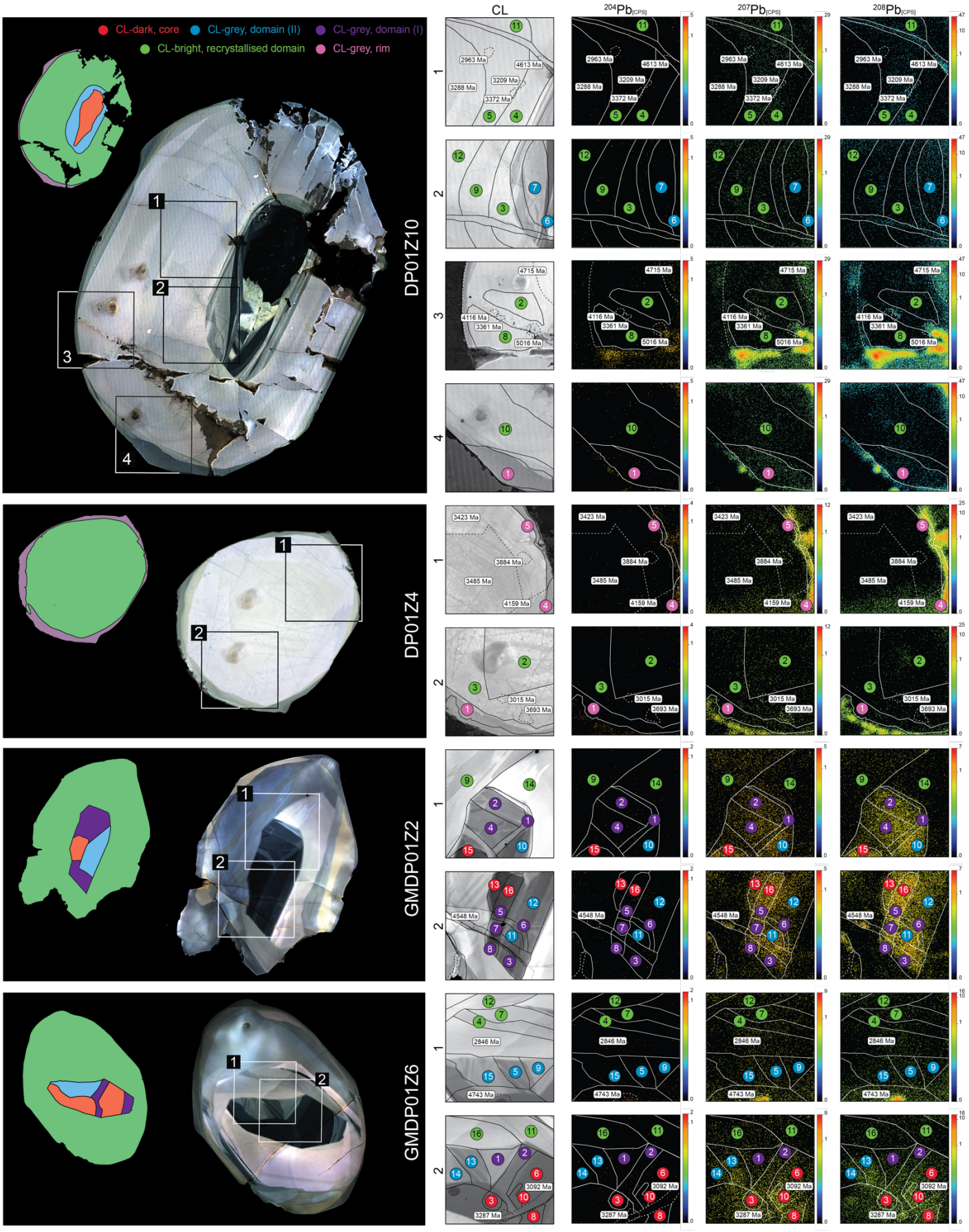
4.15.2. Preliminary LA-ICP-MS mapping

Preliminary LA-ICP-MS mapping was conducted on sample GMDP01Z2 prior to the latest round of analysis by the CL, raman, EBSD and SII as discussed in this contribution. Therefore, they represent 2-D maps of a crystal surface plane which has since been polished away. LA-ICP-MS mapping was conducted using a Teledyne Photon Machines Excite (193 nm excimer Ar-F laser) equipped with a Helex 2-volume ablation cell, coupled to an Agilent 7900 at Trinity College Dublin. Analytical procedures for mapping broadly follow that of Ubide et al. (2015) and images depict $^{207}Pb/^{206}Pb$ age (Ma), $^{206}Pb/^{238}U$ age (Ma), Th concentration (ppm), U concentration (ppm), Pb concentration (ppm) and α-dose (α mg^{-1}).



4.15.3. Additional SII grids including isotopes of ^{204}Pb, ^{207}Pb and ^{208}Pb

A set of SII grids pertaining to samples; DP01Z10, DP01Z4, GMDP01Z2 and GMDP01Z6 is shown for isotopes ^{204}Pb, ^{207}Pb, ^{208}Pb. Highlighted in each case is the CL image which guided the selection of ROIs. ROIs are delineated by solid lines enclosing sub-domains in order of increasing ^{207}Pb/^{206}Pb age within the domain categorisation to which they belong, which is referenced by colour coding of the labels, henceforth used in all subsequent figures. The instance of anomalous ages corresponding to "hotspots", suspected fractures and/or domains variably affected by ^{204}Pb are enclosed by ROIs having dashed lines and have their apparent ^{207}Pb/^{206}Pb age (Ma) denoted nearby.


CL-dark, core
CL-grey, domain (II)
CL-grey, domain (I)
CL-bright, recrystallised domain
CL-grey, rim
CL
204Pb[CPS]
207Pb[CPS]
208Pb[CPS]
DP01Z10
DP01Z4
GMDP01Z2
GMDP01Z6

CHAPTER 5 Synthesis

Natural minerals are usually heterogeneous in their chemical and isotopic composition this is no less true for mineral chronometers in commonly used for uranium-lead (U-Pb) geochronology. These can often display varied isotopic and age distributions over just several micrometers in a single grain (e.g. Kovaleva et al., 2017; MacDonald et al., 2015; Seydoux-Guillaume et al., 2015; Kusiak et al., 2013; Reddy et al., 2007). Such small-scale heterogeneities necessarily require the high spatial resolution of micro-beam techniques such as secondary ion mass spectrometry (SIMS) and laser-ablation inductively coupled mass-spectrometry (LA-ICP-MS) to target domains of specific interest (e.g. Chew et al., 2017; Bellucci et al., 2016; Ubide et al., 2015). What is more, an understanding of processes enacting either non-stoichiometric sampling behaviour during analysis and/or geological processes responsible for open-system isotopic behaviour during a mineral's past are necessary for a meaningful appraisal of U-Pb age. To this end, the overarching aim of this Ph.D. is to expand our working knowledge of high-spatial resolution techniques and the mineral chronometers they interrogate (namely zircon).

The contribution of this thesis can be summarised into findings pertaining to; (1) the direct development of a novel method of zircon sampling by LA-ICP-MS in tandem with a data-reduction software add-on, which extends the limits of high-spatial depth resolution; (2) observations made at both the scale of analysis chiefly with respect to LA-ICP-MS and its interaction with zircon, which establishes a likely source of matrix-dependent bias present in U-Pb age determination by LA-ICP-MS; (3) operative processes within zircon at a sub-micrometer scales within fluid altered rocks, evidenced by high-spatial resolution ion imaging. Observations of phenomena at all scales investigated within this thesis contribution, advance an understanding of zircon elemental and structural behaviour under variable geological and artificial conditions, as well as informing zircon's behaviour in response to micro-beam techniques. Such findings will hence instruct the analytical parameters under which the zircon matrixes should be treated.

(1) It is demonstrated in Chapter 2, that by collating a fixed number of multiple single (1 Hz) laser shots, as part of an analysis, that the resultant excavated crater depth is reduced by up to 96.5 % when compared to conventional, high-frequency static LA-ICP-MS protocols (e.g Horstwood, 2008). The process can be conceptualised as a "slowing down" of a conventional high-frequency static analysis, whereby multiple 1 Hz shots were applied to the sample surface in delayed succession for a total of up to 10 and 30 shots. The standard large-volume laser cell operates in conjunction with a short wash-out interval to produce and maintain elevated signal intensities throughout the duration of analysis. Thus no modification of the standard equipment for both UP-213 laser ablation system or Nu Attom HR-ICP-MS was required.

The analytical procedure differs from other previous high-spatial depth resolution techniques (e.g. Cottle et al., 2012, 2009), in that a measurement resolution of each single-shot is not of primary concern, instead the primary concern was to achieve reproducible ratio determinations for a small volume of analyte material. The multi-shot protocol allows

reproducible ratio determinations to be made for as few as 10 shots which, when collated, produce age determinations which are accurate and often indistinguishable from those determined by ID-TIMS (i.e. < 1 % reproducibility, 2σ), for sample volumes as low as 704 ± 23 μm^2. The resulting craters were as shallow as 0.56 ± 0.02 μm and maintain an aspect ratio << 1, consequently 'downhole' fractionation effects are negligible and the probability of encountering mineral heterogeneities at depth is greatly reduced when compared to conventional high-frequency spot analyses.

(2) Chapter 3 of this thesis presents evidence towards a likely cause of zircon matrix-dependent bias, present in U-Pb age determination made by LA-ICP-MS. This bias becomes apparent in a comparison of mirrored halves of the same Plešovice zircon sample, in which one half has been subjected to an artificial annealing process at 1100 °C for 96 h. Laser sampling of the annealed half produces ages which are apparently younger than the accepted age by ~ 22 Ma (6.7 %). This systematic offset towards younger apparent ages is concomitant with observations of ablation craters which demonstrate; a poor approximation of the laser spot mask, sub-parallel crater walls, as well as a non-stoichiometric sampling evidenced by the measured of U-Pb ratios. These observations are made in direct comparison with counterpart analyses in the untreated sample half, which were made under near identical analytical conditions, across mirrored sampling locations and which share analogous underlying compositions.

It is proposed that the greater density of structural defects accrued by self-irradiation in the untreated sample half act as absorption centres for incident laser radiation (sensu. Becker and Tenzler, 2001), resulting in a higher effective optical opacity in the UV spectrum. This aids in a shallower optical penetration of laser radiation. The radiation damage defects also likely result in confinement of thermal transformation processes, due to an inefficient dissipation of heat away from the interacting volume. It is posited therefore, that structural defects present as a result of self-irradiation aid in laser-matter coupling resulting in a near-surface emission of ablation products. Ablation in the untreated sample generates smaller mean particle size relative to those produced by equivalent locations in the annealed sample matrix (as evidenced by proxy by U/Th), thus resulting in a more accurate determination of age (Guillong et al., 2003). The presence of lattice defects therefore exhibit control over the optical and thermo-physical properties of an given zircon matrix, which are intrinsic contributing factors for laser sampling and may contribute towards U-Pb age biases observed between LA-ICP-MS and benchmark ID-TIMS techniques.

(3) The final contribution of this thesis (Chapter 4), proposes a mechanism which might explain the anomalous distribution of apparent ages in complex poly-phase metamorphic zircons. The spurious apparent ages observed within these zircons are often decoupled from any obvious intra-crystalline textural context and the derived apparent ages when viewed in isolation are meaningless within a wider geological context. Despite this, some discrete domains potentially retain diagnostic isotopic information which only becomes meaningful when integrated with

detailed textural, micro-structural and chemical observations. An integrated approach evidences a process of a fluid-catalysed recrystallisation in the wake of a CDR front, which operates to re-equilibrate radiation damage affected domains and in so doing initiates open-system behaviour by way of trace element mobilisation. A recognition of characteristic features associated with this reaction process allows for reacted and unreacted domains to be distinguished and for meaningful ages pertaining to discrete intra-crystalline domains to be determined from zircons which might otherwise be disregarded in a geochronological analysis of such rocks. Upper-intercept ages from unreacted domains potentially record protolith ages, whereas reacted and/or partially reacted domains may provide temporal constraints on the timing of the recrystallisation reaction, potentially contemporaneous with known hydrothermal events for the area.

5.1. FUTURE WORK

The analytical protocol as established in Chapter 2, is highly adaptable can be utilised in instances where shallow depth penetration is not of primary concern. By applying a greater number of subsequent single shots, the ratio determinations yielded would likely derive very precise age determinations as long as a crater aspect ratio of < 1 is maintained (Mank and Mason, 1999). A marked improvement to procedural efficiency would be envisioned if an automated application of successive spots for multiple locations could be programmed within the laser software. Furthermore, it would likely be beneficial to utilise the Nu Attom sector-field in tandem with a shorter wavelength (excimer; 193 nm) laser to improve laser-matter coupling. An improvement in ablative character, by way of greater absorption of laser radiation by target matrixes, should correlate with improved sensitivities for each single shot. Relatedly therefore, fewer shots may be necessary to achieve similar or better precision than that demonstrated within Chapter 2 for the same spot size, and would constitute a further improvement in depth resolution and sample throughput. Greater sensitivities brought about by an improved laser-matter coupling would also allow for smaller spot sizes to be used which would improve lateral spatial-resolution. The washout protocol and carrier gas flows could easily be amended to suit applications wherein a small volume (or 2-volume) laser cell are used.

In addition to modifications to the original equipment and/or automation of the procedure, future work might include a real-world application, which would seek to date unpolished zircon grains as well as other mineral chronometers (i.e. monazite in particular), contain thin outer rims which would otherwise be difficult to date. Due to the likelihood of surface common Pb contamination on unpolished grains, a rigorous cleaning protocol might have to be devised. The feasibility to conduct analysis on other isotope systems, trace elements and/or minerals has yet to be determined.

The adaptable nature of the NICE script used to define and collate incoming signal peaks makes the realisation of depth profiling possible. This would necessarily require modification of the baseline selection procedure, whereby baseline continuum sampling would have to be measured either side of a signal peak, rather than sub-section at the beginning of the TRA for the purposes of baseline subtraction and instrumental drift correction. Additionally, the collation function written into the NICE script could

either; be turned off entirely to allow each incoming signal peak to be measured (greater depth resolution at the expense of measurement precision) or instead the collation protocol could be amended to collate several smaller sub-sets of signal peaks during the duration of a single depth-profiling analysis for improved measurement precision (at the expense of shot-to-shot depth resolution). To generate depth resolution at the temporal-scale of a single incoming shot, a complete return to a stable baseline signal would have to be achieved, therefore the washout interval would necessarily have to be amended. In cases in which a sub-set of collated peaks was used a complete washout would only be necessary between a set of collated signal pulses. Shorter washout intervals could be achieved using an ultrafast washout cell geometry, suitable tubing diameters (e.g. PEEK (polyetheretherketone) tubing; internal diameter of 0.75 or 1.0 mm), and a rapid aerosol introduction system (e.g. the aerosol rapid introduction system, ARIS; Teledyne Photon Machines). The adaptor designs for rapid aerosol introduction promote laminar flow within the carrier gases and entrained aerosolised analyte are usually delivered directly into the plasma source (Chew et al. 2018), such systems thus deliver an undiluted packet of analyte ions for each laser shot promoting increased sensitivity.

The method explored in Chapter 2 utilised a sector-field single-collector instrument only, however it is likely that a similar protocol could be developed for use with more widely available and commonly used quadrupole instrumentation. A fast-switching quadrupole mass-spectrometer when used in tandem with an ultra-efficient transport setup as described above, as well as a shorter wavelength laser could be expected to achieve results similar to those described in Chapter 2, at much higher sample throughput. It would be necessary to modify existing mass-spectrometric collection software to replicate the data collection model outlined in Chapter 2.

Further work in light of observations made in Chapter 3, which establishes a potential matrix-dependent bias of U-Pb analysis of zircon with structural state, would ideally seek to include quantitative measurements of optical opacity at or near the 193 nm wavelengths used commonly in LA-ICP-MS. The the qualitative comparison of optical changes occurring in the visible spectrum of light (as described I Chapter 3) might not translate to equable changes as experienced by the absorption of UV spectra. Measurement of optical absorbance at the wavelengths used during analysis, might establish a direct correlation between mineral opacity and ablative character.

Furthermore, it would be useful to examine the mean particle sizes as generated by the two differentially treated sample halves, by use of an in-line particle filter such as used in Guillong et al. (2003). This too would establish the whether the observed fractionation of U/Th is a direct result of particle size fraction. If so, potential exists for quantifying the degree of sample-standard 'matrix matching' in respect of particle size fraction, perhaps by proxy of U/Th relative fractionation. Perhaps the most interesting future development which may stem from the observations made in Chapter 3, is for the potential development of sample pre-treatment by an external passive source of ionizing radiation (e.g. cobalt-60, γ-source) (Ioan et al., 2020), which may help to homogenise matrix responses to incoming laser radiation.

Future work with respect to the Lewisian zircons of Chapter 4, would necessarily require costly techniques capable of spatial-resolution < 2 μm, to investigate in more detail the instance of isolated enrichments of radiogenic Pb. This may follow similar procedures as those outlined for the 'nano-geochronology' conducted by atom probe tomography (APT) (e.g. Valley et al., 2015) or visualised by high-angle annular dark-field scanning transmission electron microscopy (HAAD-STEM) (e.g. Utsunomiya et al., 2004).

5.2. REFERENCES

Becker J. S. and Tenzler D., 2001. Studies of LA-ICP-MS on quartz glasses at different wavelengths of a Nd:YAG laser. Fresenius Journal of Analytical Chemistry, 370, 637-640.

Bellucci, J.J., Whitehouse, M.J., Nemchin, A.A., Snape, J.F., Pidgeon, R.T., Grange, M., Reddy, S.M., Timms, N., 2016. A scanning ion imaging investigation into the micron-scale U-Pb systematics in a complex lunar zircon. Chemical Geology, 438, 112-122.

Chew, D.M., Petrus, J.A., Kenny, G.G., McEvoy, N., 2017. Rapid high-resolution U–Pb LA-Q-ICPMS age mapping of zircon. Journal of Analytical Atomic Spectrometry, 32, 262-276.

Chew, D.M., Drost, K., Petrus, J.A., 2018. Ultrafast, > 50 Hz LA-ICP-MS spot analysis applied to U–Pb dating of zircon and other U-bearing minerals. Geostandards and Geoanalytical Research, 43, 39–60.

Cottle, J.M., Horstwood, M.S.A., Parrish, R.R., 2009. A new approach to single shot laser ablation analysis and its application to in situ Pb/U geochronology. Journal of Analytical Atomic Spectrometry, 24, 1355–1363.

Cottle, J.M., Kylander-Clark, A.R., Vrijmoed, J.C., 2012. U–Th/Pb geochronology of detrital zircon and monazite by single shot laser ablation inductively coupled plasma mass spectrometry (SS-LA-ICPMS). Chemical Geology, 332–333, 136–147.

Guillong M., Horn I. and Günther D., 2003. A comparison of 266 nm, 213 nm and 193 nm produced from a single solid state Nd:YAG laser for laser ablation ICP-MS. Journal of Analytical Atomic Spectrometry, 18, 1224-1230.

Horstwood, M.S.A., 2008. Data reduction strategies, uncertainty assessment and resolution of LA-(MC)-ICP-MS isotope data. In: Sylvester, P. (Ed.), Laser Ablation ICP-MS in the Earth Sciences: Current Practices and Outstanding Issues. Mineralogical Association of Canada, 283–303. (Short course, 40, 40).

Ioan, M.R., Tugulan, L.C., Zadehrafi, M., Olaru, C., Ormenisan, G., Ciobanu, S. and IOAN, G., 2020. Radiation induced absorption (RIA)–based dosimetry. Romanian Journal of Physics, 65, p.903.

Kusiak, M.A., Whitehouse, M.J., Wilde, S.A., Nemchin, A.A. and Clark, C., 2013. Mobilization of radiogenic Pb in zircon revealed by ion imaging: Implications for early Earth geochronology. Geology, 41(3), 291-294.

Kovaleva, E., Klötzli, U., Habler, G., Huet, B., Guan, Y., Rhede, D., 2017. The effect of crystal-plastic deformation on isotope and trace element distribution in zir- con: combined BSE, CL, EBSD, FEG-EMPA and NanoSIMS study. Chem. Geol. 450, 183–198.

MacDonald, J.M., Goodenough, K.M., Wheeler, J., Crowley, Q., Harley, S.L., Mariani, E. and Tatham, D., 2015. Temperature–time evolution of the Assynt Terrane of the Lewisian Gneiss Complex of Northwest Scotland from zircon U-Pb dating and Ti thermometry. Precambrian Research, 260, 55-75.

Mank, A.J.G., Mason, P.R.D., 1999. A critical assessment of laser ablation ICP-MS as an analytical tool for depth analysis in silica-based glass samples. Journal of Analytical Atomic Spectrometry, 14 (8), 1143–1153.

Reddy, S.M., Timms, N.E., Pantleon, W. and Trimby, P., 2007. Quantitative characterization of plastic deformation of zircon and geological implications. Contributions to Mineralogy and Petrology, 153(6), 625-645.

Seydoux-Guillaume, A.M., Bingen, B., Paquette, J.L. and Bosse, V., 2015. Nanoscale evidence for uranium mobility in zircon and the discordance of U–Pb chronometers. Earth and Planetary Science Letters, 409, 43-48.

Ubide, T., McKenna, C.A., Chew, D.M., Kamber, B.S., 2015. High-resolution LA-ICP- MS trace element mapping of igneous minerals: In search of magma histories. Chemical Geology, 409, 157–168.

Utsunomiya, S., Palenik, C.S., Valley, J.W., Cavosie, A.J., Wilde, S.A., Ewing, R.C., 2004. Nanoscale occurrence of Pb in an Archean zircon. Geochimica et Cosmochimica Acta, 68, 4679–4686.

Valley, J.W., Reinhard, D.A., Cavosie, A.J., Ushikubo, T., Lawrence, D.F., Larson, D.J., Kelly, T.F., Snoeyenbos, D.R. and Strickland, A., 2015. Nano-and micro-geochronology in Hadean and Archean zircons by atom-probe tomography and SIMS: New tools for old minerals. American Mineralogist, 100(7), pp.1355-1377.